Karodia, Sarah (2018) *CP violation and lifetime measurements of two-body charmless decays of B hadrons at LHCb*. PhD thesis.

CP Violation and Lifetime Measurements of Two-body Charmless Decays of B Hadrons at LHCb

Sarah Karodia

University of Glasgow | School of Physics & Astronomy

University of Glasgow
Department of Physics and Astronomy

Submitted in fulfilment of the requirements
for the degree of Doctor of Philosophy

September 2017

Abstract

This thesis presents lifetime measurements of charmless two-body decays of b hadrons, specifically the decay modes known as $B \to h^+h^{'-}$, where B refers to meson or baryon containing a b quark and $h^{(')}$ refers to a proton p, pion π or kaon K. Using the large data samples collected by the LHCb detector, the $B \to h^+h^{'-}$ channels with the largest branching fractions provide an opportunity to perform high-precision measurements of the properties of the decays. The leading-order processes in $B \to h^+h'^-$ decays are tree and penguin topologies, where the loop-dominated channels could be sensitive to non-standard model physics.

The $B^0_s \to K^+K^-$ mode is particularly interesting as it has a CP-even final state, as well as being dominated by penguin decay processes. The $B^0_s \to K^+K^-$ effective lifetime can be used to calculate the B^0_s decay-rate asymmetry $A_{\Delta\Gamma}$, which quantifies the amount of CP violation in the decay.

Using LHCb data with an integrated luminosity of $3\,\text{fb}^{-1}$ collected at centre of mass energies of $7\,\text{TeV}$ and $8\,\text{TeV}$, the lifetimes of the decays $B^0_s \to K^+K^-$, $B^0 \to K^+\pi^-$, $B^0_s \to \pi^+K^-$, $B^0 \to \pi^+\pi^-$, $\Lambda^0_b \to p\pi^-$ and $\Lambda^0_b \to pK^-$ are measured to be

$$\begin{aligned}
\tau_{B^0_s\to K^+K^-} &= 1.410 \pm 0.009 \text{ ps (stat)} \ \pm 0.011 \text{ ps (syst)},\\
\tau_{B^0\to K^+\pi^-} &= 1.504 \pm 0.006 \text{ ps (stat)} \ \pm 0.023 \text{ ps (syst)},\\
\tau_{B^0_s\to \pi^+K^-} &= 1.548 \pm 0.028 \text{ ps (stat)} \ \pm 0.023 \text{ ps (syst)},\\
\tau_{B^0\to \pi^+\pi^-} &= 1.495 \pm 0.012 \text{ ps (stat)} \ \pm 0.007 \text{ ps (syst)},\\
\tau_{\Lambda^0_b\to p\pi^-} &= 1.511 \pm 0.028 \text{ ps (stat)} \ \pm 0.012 \text{ ps (syst)},\\
\tau_{\Lambda^0_b\to pK^-} &= 1.477 \pm 0.022 \text{ ps (stat)} \ \pm 0.022 \text{ ps (syst)}.
\end{aligned}$$

All these lifetime measurements are compatible with the current world averages.

The decay-rate asymmetry is calculated to be

$$A_{\Delta\Gamma} = -0.975 \pm 0.092\ (stat) \pm 0.113\ (syst) \pm 0.082\ (ext),$$

which agrees with the standard model prediction.

A performance study measuring the photoelectron yield of the Ring Imaging Cherenkov (RICH) subdetector during 2012, 2015 and 2016 is also presented in this thesis. The RICH is used for particle identification and it distinguishes between pion, kaon and proton tracks. During the long shutdown between the 2012 and 2015 data taking periods, the aerogel in the RICH 1 detector was removed and the centre-of-mass energies of the proton-proton collisions increased from 7-8 TeV to 13 TeV. The photoelectron yield of RICH1 was found to increase by ~ 3 photoelectrons in 2015 and 2016 and the photoelectron yield of RICH2 remained the same. This increase in RICH1 was expected due to the increased path length of the tracks through the Cherenkov medium once the aerogel was removed. Overall the contribution of photoelectron yield to the performance of the RICH remains acceptable for continued data taking.

Acknowledgements

I would like to thank my supervisors, Paul Soler and Lars Eklund, the STFC for funding my PhD studies, and the University of Glasgow. I would also like to thank my LHCb Glasgow colleagues for the joy of working with them; especially Michael and Cameron who worked closely with me on the $B \rightarrow h^+h'^-$ analysis.

For all the time we spent together I would also like to thank my friends in Glasgow, especially Katie, Roddy and Marieke. For making my time at CERN memorable and for always being there for coffee, I thank Alyssa. For being an excellent office companion, my thanks to Patrick. Thank you, Karl, for your support and supply of crisps while this thesis was being written. For freinds not in Glasgow, my thanks to Becky for being there from the first day I moved to Scotland and a special thanks to Sarah for her constant support. Finally, my thanks to my parents for supporting me.

I would also like to wish good luck to the remaining LHCb Glasgow PhD Students, Iain, Murdo, Lauren and Dana.

Declaration

The research results presented in this thesis are the product of my own work. Appropriate references are provided when results of third parties are mentioned. The research presented here was not submitted for another degree in any other department or university.

Sarah Karodia

Preface

This thesis presents lifetime measurements of charmless two-body decays of b hadrons, $B_s^0 \to K^+K^-$, $B^0 \to K^+\pi^-$, $B_s^0 \to \pi^+K^-$, $\mathit{\Lambda}_b^0 \to p\pi^-$ and $\mathit{\Lambda}_b^0 \to pK^-$, using data collected by the LHCb detector in 2011 and 2012. A performance study of the photoelectron yields in the RICH sub-detector during the 2012, 2015 and 2016 data taking is also included. Chapter 1 discusses the theoretical aspects of particle physics that relate to the lifetime measurements. This includes a short description of the standard model, flavour physics and *CP* violation. This review was performed by the author, following standard text books and journal papers, where required. The physics implications of $B \to h^+h^{'-}$ lifetimes, in particular the $B_s^0 \to K^+K^-$ lifetime is also detailed. Chapter 2 discusses the LHCb detector, which is located at Large Hadron Collider. A description of each individual subdetector and an overview of the performance during 2011 and 2012 is included. The detector description was compiled by the author, following LHCb construction and performance papers. Chapter 3 presents study carried out by the author to measure the the photoelectron yields in the RICH detectors of LHCb from 2012, 2015 and 2016. The author performed the study, using software previously developed by Dr Indrek Sepp from Imperial College London, and adapted by the author. The photoelectron yields are key to the performance of the RICH and shows some change in the photoelectron yield in RICH 1 between 2012 and 2015, after removal of the aerogel radiator of RICH . The $B \to h^+h^{'-}$ lifetime analysis is the main contribution of the author and is discussed in the remainder of this thesis, which used the full LHCb run 1 dataset with an integrated luminosity of $3\,\mathrm{fb}^{-1}$. Chapter 4 describes the candidate event selection, including trigger, kinematic and particle identification selections, where the PID selection efficiencies were evaluated by Cameron Dean from the University of Glasgow. Chapter 5 describes the method used to measure lifetimes. This includes a description of how the the invariant mass spectrum of five final states is modelled, a description of how lifetime biasing detector effects are evaluated and a description of how the decay-time spectrum is modelled. The fitter software was developed by the author and Dr Michael Alexander from the University of Glasgow. Chapter 6 describes the systematic uncertainties of the measured $B \to h^+h^{'-}$ lifetimes. Chapter 7 presents the results. All work in these chapters is the author's work, except where acknowledged. Finally, Chapter 8 summarises the work presented in this thesis.

Contents

List of Tables

List of Figures

Chapter 1

Theory of Standard Model and Flavour Physics

1.1 Theory Introduction

This chapter describes the Standard Model of particle physics and the theory behind flavour physics. Motivation of b-hadron lifetime measurements is discussed in later chapters of this thesis. Section 1.2 gives a brief overview of the Standard Model of particle physics. Section 1.3 describes flavour physics in the quark sector, including the theoretical description of the CKM matrix and the unitary triangle, as well as an overview of CP violation and neutral meson mixing. Finally, Section 1.4 discusses the theory of charmless two body decays known as $B \to h^+h'^-$ and predominantly focuses on the $B_s^0 \to K^+K^-$ effective lifetime and its relationship to the CP-dependent variable $A_{\Delta\Gamma}$.

1.2 The Standard Model

The Standard Model (SM) is a theoretical framework that describes the fundamental particles of matter and the forces through which these particles interact. The first elementary particle discovered was the electron in 1897 by J.J Thomson. Theories modelling the microscopic behaviour of observed matter (and anti-matter) were developed in the early part of the 20th century, leading to the development of quantum mechanics. During the later half of the 20th century a quantum field theory known as the SM was developed to describe all known particle interactions, except for gravity (electromagnetic, strong and

Generation	Quarks			
	Type	Mass [MeV/c^2]	Electric Charge [e]	I_3
1^{st}	Up, u	$2.2^{+0.6}_{-0.4}$	$+\frac{2}{3}$	$+\frac{1}{2}$
	Down, d	$4.7^{+0.5}_{-0.4}$	$-\frac{1}{3}$	$-\frac{1}{2}$
2^{nd}	Charm, c	$(1.27 \pm 0.03) \times 10^3$	$+\frac{2}{3}$	$+\frac{1}{2}$
	Strange, s	96^{+8}_{-4}	$-\frac{1}{3}$	$-\frac{1}{2}$
3^{rd}	Top, t	$(173.21 \pm 0.51) \times 10^3$	$+\frac{2}{3}$	$+\frac{1}{2}$
	Bottom, b	$(4.18^{+0.04}_{-0.03}) \times 10^3$	$-\frac{1}{3}$	$-\frac{1}{2}$

Table 1.1: Quark content of the standard model. I_3 is the z component of the weak isospin of the left-handed field. All values are from [8].

weak interactions). Since then, all fundamental particles predicted by the SM have been observed, including the most recently discovered particles, the Z and W bosons in 1983 by the UA1 collaboration [1, 2], the top quark in 1995 by the CDF and D0 collaborations [3, 4] the tau neutrino ν_τ in 2000 by the DONUT collaboration [5] and the Higgs boson in 2012 by the ATLAS [6] and CMS [7] collaborations.

1.2.1 Particle Content

The elementary particles in the SM are split into two groups, fermions and bosons. Fermions have intrinsic angular momentum, normally called spin, of $\frac{1}{2}$ and bosons have a spin of integer value. For each particle in the SM there exists an antiparticle, which has the same mass as the corresponding particle and the sign of the internal quantum numbers (e.g charge) reversed. A neutral elementary particle can be its own antiparticle. The transformations parity P relates a particle to its mirror image by exchanging the coordinate $\vec{r}$ with respect to $-\vec{r}$ and charge conjugation transformation C relates a particle to its anti-particle, as described in Section 1.3.

The fermions which interact via strong and electroweak forces are known as quarks and the fermions which do not interact via the strong force are known as leptons.

Fermions can be grouped into three generations shown in Table 1.1 and Table 1.2, where I_3 is the z component of the weak isospin of the left-handed field. As generation increases the mass of the fermions becomes larger, but the quantum numbers remain the same, excluding flavour. Quarks carry a flavour quantum number, which is dependent on

Generation	Leptons			
	Type	Mass [MeV/c^2]	Electric Charge [e]	I_3
1st	Electron, e	0.511	-1	$-\frac{1}{2}$
	Electron-neutrino, ν_e	$< 2 \times 10^{-6}$	0	$+\frac{1}{2}$
2nd	Muon, μ	105.65	-1	$-\frac{1}{2}$
	Muon-neutrino, ν_μ	< 19	0	$+\frac{1}{2}$
3rd	Tau, τ	1776.86 ± 12	-1	$-\frac{1}{2}$
	Tau-neutrino, ν_τ	< 18.2	0	$+\frac{1}{2}$

Table 1.2: Lepton content of the standard model. I_z is the z component of the weak isospin of the left-handed field. All values are from [8].

the quark type. The up and down quark flavour quantum number is I_3 with $I_3 = +\frac{1}{2}$ for up and $I_3 = -\frac{1}{2}$ for down. The other four quarks have an individual flavour quantum number (charm, strangeness, topness and bottomness) with a value of +1 for charm and top, and −1 for strange and bottom. Quark flavour is conserved for all interactions apart from the weak interaction.

Quarks carry a colour charge as they can interact via the strong force. The colour of a quark can be red, green or blue and anti-quarks colour can be anti-red, anti-green or anti-blue. Individual quarks do not exist as free particles, they only exist in colour-neutral states, this is known as colour confinement [9]. Mesons are bound states of a quark and anti-quark pair, an example of a meson is the B^0 which contains a $\bar{b}$ and d quark. Baryons are bound states of three quarks/anti-quarks, an example of a baryon is the proton which contains uud quarks.

Leptons also have a flavour quantum number which is associated to the generation. The first generation leptons (e^- and ν_e) have electron-number of +1, the second generation leptons (μ^- and ν_μ) have muon-number of +1 and the third generation leptons (τ^- and ν_τ) have tau-number of +1. Lepton flavour is conserved in all interactions except neutrino oscillations.

Bosons have a spin of either 1 or 0, shown in Table 1.3, again I_3 is the z component of the weak isospin of the left-handed field and $I_3 = 0$ is a right-handed field.

The photon (γ) mediates the electromagnetic force. All particles that are electrically charged experience the electromagnetic force. As the photon has a neutral charge and is massless, self-coupling is not observed and the photon is able to travel an infinite distance

Bosons				
Type	Mass [GeV/c^2]	Electric Charge [e]	Spin	I_3
Photon, γ	0	0	1	0
$W^\pm$	80.385 ± 0.015	±1	1	±1
Z^0	91.1876 ± 0.0021	0	1	0
Gluon, g	0	0	1	0
Higgs, H^0	$125.09 \pm 0.21 \pm 0.11$	0	0	0

Table 1.3: Boson content of the standard model. I_z is the z component of the weak isospin of the left-handed field. All values are from [8].

and the range of the electromagnetic force is infinite.

The $W^\pm$ and Z^0 bosons mediate the electroweak force, these bosons couple to all fermions. As the $W^\pm$ and Z^0 bosons have relatively large mass, the interaction range is finite. The electroweak force acts with a range of order 10^{-18} m [8].

The gluon g mediates the strong force. Particles which have colour charge experience the strong force. Despite the fact that gluons are massless, the range of the strong force is finite due to gluons containing colour charge. This property means that gluons self-interact [9]. As mentioned previously, colourless free particles do not exist and free gluons are not found in nature, in-fact eight coloured gluon states exist. The strong force range is of order 10^{-15} m [8].

In the early formulations of the SM the $W^\pm$ and Z^0 bosons were massless, this is known to be incorrect. The mass of these bosons comes from the breaking of electroweak symmetry of the SM, which is caused by the Higgs mechanism [10, 11]. The mechanism leads to the existence of a massive neutral scalar boson, which is the Higgs boson H^0. This prediction was recently confirmed with the discovery of the Higgs boson [6, 7].

1.2.2 Mathematical Formalism of the SM

The Standard Model as a Gauge Theory

The SM [8] can be described as the gauge group SU(3) × SU(2) × U(1). An SU(n) gauge group can be used to represent an interaction with $n^2 - 1$ gauge bosons. The SU(3) gauge group describes Quantum Chromodynamics (QCD) with eight gluons mediating the strong force. The SU(2) × U(1) gauge group describes electroweak theory (EW) interacting via the photon, $W^{\pm}$ and Z^0 bosons. In this model, the electromagnetic and weak forces are unified.

The Standard Model Lagrangian

The SM Lagrangian is invariant under local transformations of the gauge group SU(3) × SU(2) × U(1). The Lagrangian of the Standard model can be written as

$$\mathcal{L}_{SM} = \mathcal{L}_{\text{fermion kinetic}} + \mathcal{L}_{\text{boson kinetic}} + \mathcal{L}_{\text{Higgs}} + \mathcal{L}_{\text{Yukawa}}. \tag{1.1}$$

Equation 1.1 separates the kinetic terms of the fermions and bosons, as well as Yukawa couplings that give fermions mass and a Higgs field coupling giving bosons mass.

The Lagrangian of a particle in the SM depends on its spin. A spin-half particle with field ψ has a Lagrangian

$$\mathcal{L} = \overline{\psi} i \gamma^{\mu} D_{\mu} \psi. \tag{1.2}$$

The fermion kinetic term of Equation 1.1 follows the form of this Lagrangian with additional terms from each fermion. The covariant derivative $D_{\mu} = \partial_{\mu} + ig\boldsymbol{V}_{\mu}$, where $\boldsymbol{V}_{\mu} = V_{\mu}^{A} T^{A}$, with V_{μ} as vector fields and T_{μ} as generators of the algebra of the gauge group.

A spin 0 particle, such as the Higgs boson, with field ϕ has a Lagrangian

$$\mathcal{L} = \frac{1}{2} D_{\mu}\phi D^{\mu}\phi - \frac{1}{2} m^2 \phi^2 - \frac{\lambda}{4!}\phi^4. \tag{1.3}$$

A non-zero integer spin particle with field A_{μ} has a Lagrangian

$$\mathcal{L} = -\frac{1}{4} F_{\mu\nu} F^{\mu\nu}, \tag{1.4}$$

where $F_{\mu\nu} = \partial_{\mu} A_{\nu} - \partial_{\nu} A_{\mu}$ is the field strength.
Similar to the fermion kinetic term, the boson kinetic term of 1.1 follows this form with a term for each boson.

Fermion mass term are absent in Equation 1.1 but are generated when introducing the scalar ‘Higgs’ field. This leads to fermion masses determined by the Yukawa interaction, which is described later. The Higgs term arises from equation 1.3, where the boson masses come from couplings between the bosons and the Higgs.

1.2.3 Limitations of the SM

The SM is extremely successful at accurately predicting the behaviour of fundamental particles, although it has its limitations. Some of the main areas where the SM does not match observations in nature are:

- In the most basic SM, neutrinos have no mass, this is contradicted by experimentally observed neutrino oscillations [12].
- The large observed excess of matter compared to antimatter is not consistent with the predictions of the SM.
- Astronomical and cosmological evidence suggests that the particles described in the SM can only account for 5% of the universe [13]. The remaining universe is thought to be comprised of dark matter and dark energy, the composition and existence of which is unexplained by the SM.

1.3 Flavour Physics and *CP* Violation

Flavour Physics describes the interactions between the different species or 'flavours' of quarks and leptons. This section details Flavour Physics in the quark sector, including a description of neutral meson mixing which is relevant in the lifetime analysis in this thesis.

1.3.1 Discrete Symmetries

The discrete symmetries important in particle physics are:

- Charge conjugation, C, reverses the sign of all the internal quantum numbers, i.e. changing a particle into its antiparticle.
- Parity, P, reflects the spatial coordinates of a particle.
- Time reversal, T, reverses the time coordinate of a particle; $(t \to -t)$.

The electromagnetic and strong interactions are C-symmetric and P-symmetric, but the weak interaction violates C and P individually [14]. The symmetry of the combined operator CP is also violated in weak interactions, this has been observed in the K and B systems [15, 16, 17, 18]. The CPT theorem states that any Lorentz invariant quantum field theory is invariant under the operation CPT, therefore T violation implies CP violation. The CPT symmetry is thought to be a fundamental symmetry of nature [9]. Consequences of the CPT theorem are that a particle and its antiparticle have the same mass and lifetime. As mentioned earlier, there is an asymmetry between matter and antimatter content in the universe which suggests that matter and antimatter interact differently on a fundamental level. This is known to be the case for the weak interaction, which only couples to left-handed fermions and right-handed anti-fermions. The weak interaction is not symmetric under the transformation CP and this asymmetry is referred to as CP asymmetry. The CPT implies that there must be a T asymmetry and time dependent analyses provide channels to measure CP asymmetries.

1.3.2 The CKM Matrix

The Lagrangian that describes the mass of the quarks can be written as

$$\mathcal{L}_{quark\ masses} = -[Y_d]_{ij}\overline{q_{Li}}\Phi d_{Rj} - [Y_u]_{ij}\overline{q_{Li}}\epsilon_{jk}\Phi^* u_{Rk} + \text{h.c.}, \tag{1.5}$$

where Y is the Yukawa coupling, which is a 3×3 matrix in flavour space, i and j are the generation labels, q_L are left handed quark doublets, d_R and u_R are right handed down and up-type quark singlets, Φ is the Higgs field, ϵ is a 2×2 antisymmetric tensor and h.c. stands for the Hermitian conjugate. The Yukawa coupling matrix has non-zero off-diagonal elements which causes mass mixing between quark generations. The interactions of first generation fermions are identical to interactions of second and third generations. This implies that it is possible to rotate the flavour eigenstates into the mass eigenstates, and is achieved by diagonalising Y. For three generations, the quark mixing matrix is named the Cabibbo-Kobayashi-Maskawa (CKM) matrix [19, 20], V_{CKM}. Mass eigenstates (d, s, b) are related to flavour eigenstates (d', s', b'):

$$\begin{pmatrix} d' \\ s' \\ b' \end{pmatrix} = V_{CKM} \begin{pmatrix} d \\ s \\ b \end{pmatrix}. \tag{1.6}$$

When the Higgs potential is at its minimum, Equation 1.5 gives mass terms for the quarks. The Higgs potential is given by

$$V(\Phi) = -\mu^2\Phi^*\Phi + \lambda|\Phi^*\Phi|^2, \tag{1.7}$$

where λ is the Higgs self-coupling parameter and μ is the mass.

At the minimum potential $\Phi^*\Phi = \frac{1}{2}\mu^2/\lambda$, the vacuum expectation value is expressed as

$$\langle\Phi\rangle = \frac{1}{\sqrt{2}}\begin{pmatrix}0\\ \mu^2/\lambda\end{pmatrix} = \frac{1}{\sqrt{2}}\begin{pmatrix}0\\ v\end{pmatrix}. \tag{1.8}$$

The choice of diagonalised $Y_{d,u}$ is achieved via

$$M_u = \frac{v}{\sqrt{2}}V_{L,u}Y_uV_{R,u}^\dagger \text{ and } M_d = \frac{v}{\sqrt{2}}V_{L,d}Y_dV_{R,d}^\dagger, \tag{1.9}$$

where M_q is a quark mass matrix and $V_{A,q}$ are the unitary matrixes that diagonalise the Yukawa matrices.

This transformation only affects the charged current of the weak interaction, the Lagrangian for this is

$$\mathcal{L}_{cc} = \frac{-g}{\sqrt{2}}\overline{u_L}\gamma^\mu(V_{L,d}V_{R,d}^\dagger)\overline{d_L}W_\mu. \tag{1.10}$$

This allows couplings of charged current $W^\pm$ interactions to the quarks to be expressed as

$$\frac{-g}{\sqrt{2}}(\overline{u_L}, \overline{c_L}, \overline{t_L})\gamma^\mu W_\mu^+ V_{CKM}\begin{pmatrix}d_L\\ s_L\\ b_L\end{pmatrix} + \text{h.c.}, \tag{1.11}$$

where V_{CKM} is the CKM matrix,

$$V_{CKM} = V_L^u V_L^{d\dagger} = \begin{pmatrix}V_{ud} & V_{us} & V_{ub}\\ V_{cd} & V_{cs} & V_{cb}\\ V_{td} & V_{ts} & V_{tb}\end{pmatrix}. \tag{1.12}$$

The CKM matrix can be parameterised by three mixing angles θ_{ij} and one phase

δ [21]:

$$V_{CKM} = \begin{pmatrix} c_{12}c_{13} & s_{12}c_{13} & s_{13}e^{-i\delta} \\ -s_{12}c_{23} - c_{12}s_{23}s_{13}e^{i\delta} & c_{12}c_{23} - s_{12}s_{23}s_{13}e^{i\delta} & s_{23}c_{13} \\ s_{12}s_{23} - c_{12}c_{23}s_{13}e^{i\delta} & -c_{12}c_{23} - s_{12}s_{23}s_{13}e^{i\delta} & c_{23}c_{13} \end{pmatrix}, \tag{1.13}$$

where $c_{ij} \equiv \cos\theta_{ij}$, $s_{ij} \equiv \sin\theta_{ij}$. In the SM the complex phase δ is the cause of CP-violation in flavour physics of the quark sector [21].

The unitarity of the CKM matrix introduces the constraints $\sum_i V_{ij}V^*_{ik} = \delta_{jk}$ and $\sum_j V_{ij}V^*_{kj} = \delta_{ik}$. The six cases that lead to a Kronecker delta value of zero can be represented as triangles in a complex plane. The most frequently used of these triangles, often called the unitary triangle, is

$$V_{ud}V^*_{ub} + V_{cd}V^*_{cb} + V_{td}V^*_{tb} = 0. \tag{1.14}$$

This triangle has sides of similar length, the less used triangles consist of one side significantly smaller than the other two. It is worth mentioning that equation 1.14 is generally associated with B^0_d decays and there is a similar triangle associated to B^0_s decays.

The angles of the unitarity triangle are given by:

$$\alpha = \arg\left(-\frac{V_{td}V^*_{tb}}{V_{ud}V^*_{ub}}\right), \tag{1.15}$$

$$\beta = \arg\left(\frac{V_{cd}V^*_{cb}}{V_{td}V^*_{tb}}\right), \tag{1.16}$$

$$\gamma = \arg\left(\frac{V_{ud}V^*_{ub}}{V_{cd}V^*_{cb}}\right). \tag{1.17}$$

The current fit of experimental measurements constraining the CKM unitary triangle is shown in Figure 1.1, where this global fit has been performed to all available measurements and assumes the unitarity of the CKM matrix. The current global fit gives the sum of the angles of the unitarity triangle $\alpha+\beta+\gamma = (183^{+7}_{-8})^\circ$ [8], which agrees with SM predictions.

1.3.3 Neutral Meson Mixing

It is possible for a meson containing a quark and anti quark of different flavour, i.e. $(q\overline{q}')$ to oscillate between particle and antiparticle states. The neutral mesons that can transition

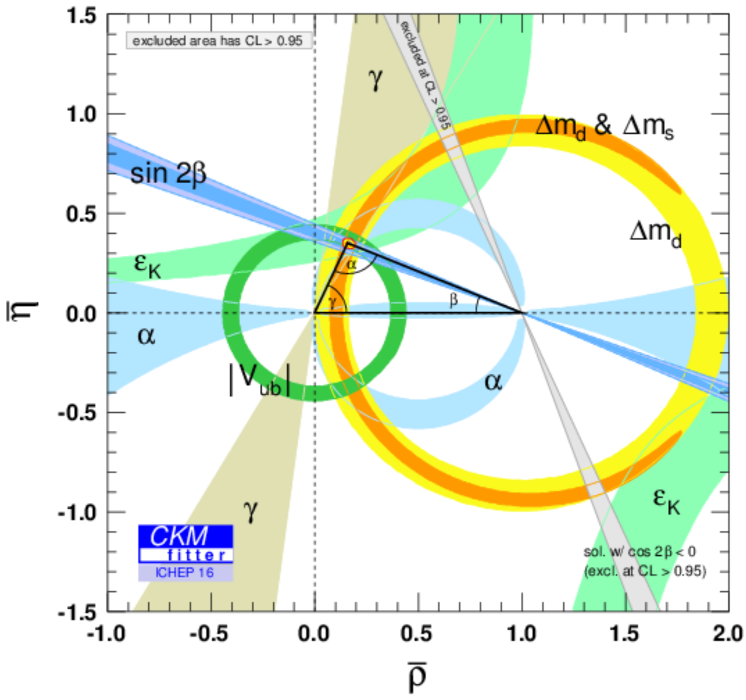

Figure 1.1: Current experimental status of the CKM unitarity triangle fit. The shaded areas identify the 95% CL regions, which can be seen to overlap around the global fit area. Reproduced from [22].

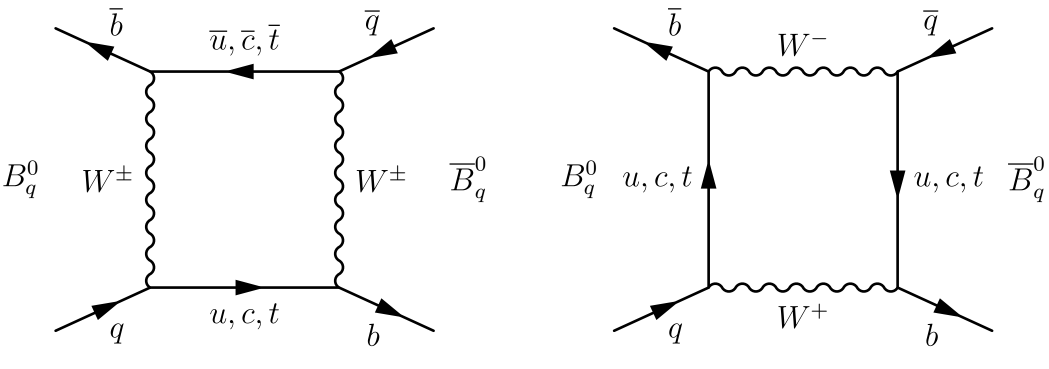

Figure 1.2: Leading order Feynman diagram for B^0_q-$\overline{B^0_q}$ mixing, where $q = (s, d)$.

into their antiparticle states via weak interactions are K^0 D^0 B^0_d and B^0_s mesons [23, 24, 25, 26]. This thesis will focus on mixing in the B^0_d and B^0_s systems.

Figure 1.2 shows the leading order Feynman diagrams for the neutral mixing in the

B system. These diagrams show the spontaneous transition from one state to the other, i.e. oscillation between the two states, known as B-$\overline{B}$ mixing. This behaviour can be represented by the Schrödinger equation

$$i\frac{d}{dt}\begin{pmatrix}|B_q^0(t)\rangle\\ |\overline{B_q^0}(t)\rangle\end{pmatrix} = \left(M_q - \frac{i}{2}\Gamma_q\right)\begin{pmatrix}|B_q^0(t)\rangle\\ |\overline{B_q^0}(t)\rangle\end{pmatrix}, \tag{1.18}$$

which describes the oscillations over time, where M_q is the mass matrix and Γ_q is the decay matrix. It can be shown by diagonalising $M_q - \frac{i}{2}\Gamma_q$ that there are two mass eigenstates, a heavy mass eigenstate $|B_H\rangle$ and a light mass eigenstate $|B_L\rangle$ with decay widths Γ_H, Γ_L and masses M_H, M_L respectively. The decay width difference is defined as

$$\Delta\Gamma_q = \Gamma_L - \Gamma_H. \tag{1.19}$$

It is possible to express the mass eigenstates $|B_H\rangle$ and $|B_L\rangle$ as a linear combination of the flavour eigenstates at time $t = 0$;

$$|B_L\rangle = p|B_q^0\rangle + q|\overline{B_q^0}\rangle, \tag{1.20}$$

$$|B_H\rangle = p|B_q^0\rangle - q|\overline{B_q^0}\rangle, \tag{1.21}$$

where $|p|^2 + |q|^2 = 1$ is required for normalisation.

CP Violation

As mentioned earlier, CP violation occurs in weak decays and enters the CKM matrix though the complex phase δ in Equation 1.13. Measurements of CP violation in the B and D systems are an important part of the LHCb physics program [27]. There are three categories of CP violation which are outlined in this section. Generic formulas of the decay amplitudes of a neutral meson B and its antiparticle $\overline{B}$ transitioning into the multi particle final state f and its charge conjugate state $\overline{f}$ are given by

$$A_f = \langle f|\mathcal{H}|B\rangle,\ A_{\overline{f}} = \langle\overline{f}|\mathcal{H}|B\rangle, \tag{1.22}$$

$$\overline{A}_f = \langle f|\mathcal{H}|\overline{B}\rangle,\ \overline{A}_{\overline{f}} = \langle\overline{f}|\mathcal{H}|\overline{B}\rangle, \tag{1.23}$$

where $\mathcal{H}$ represents the Hamiltonian operator of the weak interaction. It is worth noting the mesons B and $\overline{B}$ are distinguishable, for example B_d^0 and $\overline{B}_d^0$.

- Direct CP violation, also called CP violation in decay, exists if $B \to f$ and $\overline{B} \to \overline{f}$ have different decay rates and therefore

$$\left| \frac{A_f}{\overline{A}_{\overline{f}}} \right| \neq 1. \tag{1.24}$$

- Indirect CP violation, also called CP violation in mixing, occurs when the mixing rate $B \to \overline{B}$ is different to $\overline{B} \to B$. This gives the condition

$$|p/q| \neq 1. \tag{1.25}$$

- CP violation in interference between decays with and without mixing, i.e. when $B \to f$ and $B \to \overline{B} \to f$ interfere quantum mechanically. For this to occur the final state f is accessible from both B and $\overline{B}$ decays. The interference can be expressed as

$$\lambda_f \equiv \frac{q}{p}\frac{\overline{A}_f}{A_f}. \tag{1.26}$$

  This type of CP violation exists if $\Im(\lambda_f) \neq 0$.

1.4 Theory of Two-body Charmless B decays

This section contains a theoretical description of charmless two-body B decays, and details for the motivation of the $B_s^0 \to K^+K^-$ effective lifetime in particular. The theory in this section relates to the lifetime analysis discussed later in this thesis.

By describing a B decay as two-body and charmless, the mother particle could decay into any two hadrons containing no charm quarks. The description $B \to h^+h'^-$ narrows the possible decay channels being referred to. In this case a $B \to h^+h'^-$ decay has a mother particle B^0, B_s^0 or Λ_b^0 decaying into a two body final state which is a combination of protons p, pions π and kaons K. Overall there are ten possible $B \to h^+h'^-$ modes: $B^0 \to \pi^+\pi^-$, $B_s^0 \to \pi^+\pi^-$, $B^0 \to K^+\pi^-$, $B_s^0 \to \pi^+K^-$, $B^0 \to K^+K^-$, $B_s^0 \to K^+K^-$,

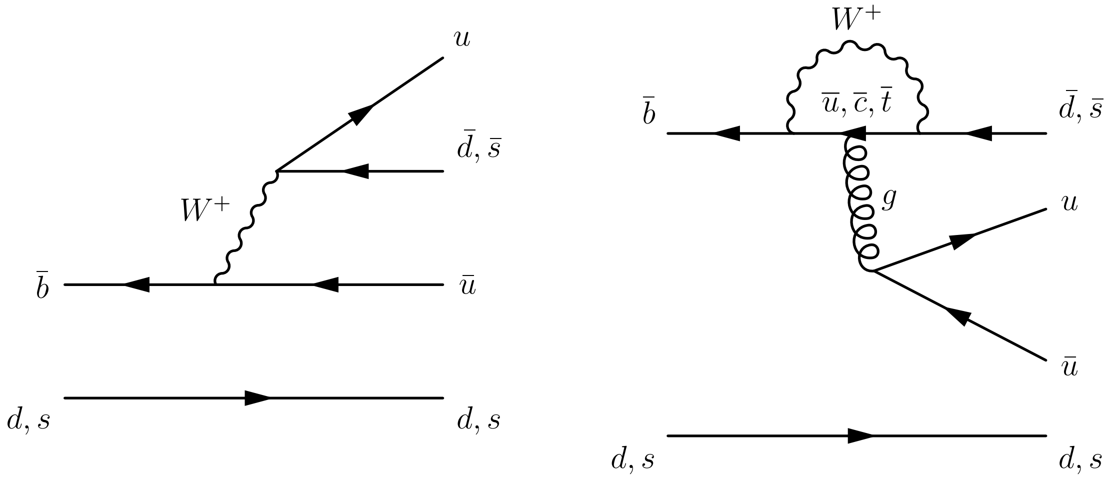

Tree

Penguin

Figure 1.3: Feynman diagrams of tree and penguin topologies of the decay $B \to h^+h'^-$, where the mother particle is either B_d^0, B_s^0.

$B^0 \to p\overline{p}$, $B_s^0 \to p\overline{p}$, $\Lambda_b^0 \to p\pi^-$ and $\Lambda_b^0 \to pK^-$. The antiparticles $\overline{B}^0$, $\overline{B}_s^0$ and $\overline{\Lambda}_b^0$ have similar decays. Nine of these decay modes have been observed, most recent of which are the $B^0 \to K^+K^-$, $B_s^0 \to \pi^+\pi^-$ and $B^0 \to p\overline{p}$ by the LHCb experiment [28, 29]. The channel that is currently unobserved is $B_s^0 \to p\overline{p}$.

For the $B \to h^+h'^-$ channels with the largest branching fractions, the leading order processes have tree and penguin topologies [30], Figure 1.3 shows these Feynman diagrams for the $B^0 \to \pi^+\pi^-$, $B^0 \to K^+\pi^-$, $B_s^0 \to \pi^+K^-$ and $B_s^0 \to K^+K^-$ modes. For the decays where the mother particle is a baryon, $\Lambda_b^0 \to p\pi^-$ and $\Lambda_b^0 \to pK^-$, the tree and penguin diagrams are similar. The dominant process is penguin decay for $B_s^0 \to K^+K^-$, however the tree decay is non negligible. As the penguin diagrams contain loops they provide a way for new physics to affect the system.

The $B_s^0 \to K^+K^-$ mode is particularly interesting as it can be used to constrain the B_s^0 mixing phase ϕ_s and the decay rate asymmetry $A_{\Delta\Gamma}$. If there are any contributions of physics beyond the SM effects in CP mixing they can be observed through the CP violation phase by $\phi_s = \phi_s^{SM} + \phi_s^{NP}$, where ϕ_s^{SM} is the standard model prediction and ϕ_s^{NP} is contributions to mixing from beyond SM processes, (NP stands for new physics).

When studying $B \to h^+h^{'-}$ decays there are two distinct types of final state; non-flavour specific i.e $f = \overline{f}$ and flavour specific $f \neq \overline{f}$. When formulating time-dependent variables these two categories are treated differently. $B^0 \to K^+\pi^-$ and $B_s^0 \to \pi^+K^-$ are examples of flavour specific decays and $B^0 \to \pi^+\pi^-$ and $B_s^0 \to K^+K^-$ are examples of non-flavour specific decays. The time-dependent decay rate $\Gamma_s[f,t]$ occurs when there is no distinction between the initial flavour, i.e untagged events. The decay width can be expressed as [27]

$$\begin{aligned}
\Gamma_s[f,t] &= \Gamma(B_s^0(t) \to f) + \Gamma(\overline{B_s^0}(t) \to f) \\
&= N_f[e^{-\Gamma_L t}|\langle f|B_L\rangle|^2 + e^{-\Gamma_H t}|\langle f|B_H\rangle|^2] \\
&\sim N_f|A_f|^2[1+|\lambda_f|^2]e^{-\Gamma t}\left\{\cosh\left(\frac{\Delta\Gamma_s t}{2}\right) + \sinh\left(\frac{\Delta\Gamma_s t}{2}\right) A_{\Delta\Gamma}\right\},
\end{aligned} \tag{1.27}$$

where N_f is the overall normalisation, λ_f is defined in Equation 1.26 and

$$A_{\Delta\Gamma} = \frac{2Re(\lambda_f)}{1+|\lambda_f|^2}. \tag{1.28}$$

The expression in equation 1.27 only holds true if $|q/p| = 1$, i.e. there is no CP violation in the mixing.

For flavour specific final state f the decay amplitude $\overline{A}_f = 0$ and therefore $\lambda_f = 0$. Equations 1.27 can simplify to

$$\Gamma_s[f,t] \sim N_f|A_f|^2 e^{-\Gamma t}\left\{\cosh\left(\frac{\Delta\Gamma_s t}{2}\right)\right\}. \tag{1.29}$$

This means any lifetime measurement of a non-flavour specific decay is a mixture of both the heavy and light mass eigenstates.

The variable $A_{\Delta\Gamma}$ provides a measure of the amount CP violation present in the decay. When no CP violation is present a CP-even final state, e.g. K^+K^-, will have $A_{\Delta\Gamma} = -1$ and for a CP-odd final state, e.g $J\psi f_0$, $A_{\Delta\Gamma} = +1$.

If the initial flavour of the mother particle is known, another quantity that can measure the CP asymmetries A_{CP} is defined as

$$\begin{aligned}
A_{CP}(B_s^0(t) \to K^+K^-) &= \frac{\Gamma(B_s^0(t) \to K^+K^-) - \Gamma(\overline{B_s^0}(t) \to K^+K^-)}{\Gamma(B_s^0(t) \to K^+K^-) + \Gamma(\overline{B_s^0})(t) \to K^+K^-)} \\
&= \frac{-C_f\cos(\Delta m t) + S_f\sin(\Delta m t)}{\cosh\left(\frac{\Delta\Gamma}{2}t\right) - A_{\Delta\Gamma}\sinh\left(\frac{\Delta\Gamma}{2}t\right)} \\
&\approx -C_f\cos(\Delta m t) + S_f\sin(\Delta m t),
\end{aligned} \tag{1.30}$$

where the CP asymmetry in the decay is

$$C_f = \frac{1 - |\lambda_f|^2}{1 + |\lambda_f|^2}, \tag{1.31}$$

and the CP asymmetry in mixing is

$$S_f = \frac{2\Im(\lambda_f)}{1 + |\lambda_f|^2}. \tag{1.32}$$

There is a unitary relation of the CP asymmetries

$$(S_f)^2 + (C_f)^2 + (A_{\Delta\Gamma})^2 = 1. \tag{1.33}$$

The approximation in equation 1.30 can be made due to the decay having a small width difference $\Delta\Gamma$ compared to the mass difference $\Delta m = m_{B_H} - m_{B_L}$. This is caused by the size of the elements in the Hamiltonian of the Schrödinger equation for the mixing and also means that the approximation $|p/q| = 1$ is valid. The argument for the time-dependent asymmetry in $B^0 \to \pi^+\pi^-$ is similar to the $B_s^0 \to K^+K^-$ channel just described. One difference is that $\Delta\Gamma$ for $B_s^0 \to \pi^+\pi^-$ is small and can be neglected in the experimental measurements. The decay $B^0 \to \pi^+\pi^-$ is the U-spin flavour symmetry partner of $B_s^0 \to K^+K^-$ though the exchange of d for s quarks. This results in the decays being topologically the same. The most recent measurements of C_f and S_f for $B_s^0 \to K^+K^-$ and $B^0 \to \pi^+\pi^-$ from LHCb are detailed in [31], where the results are

$$C_{\pi^+\pi^-} = -0.24 \pm 0.07 \pm 0.01, \tag{1.34}$$

$$S_{\pi^+\pi^-} = -0.68 \pm 0.06 \pm 0.01, \tag{1.35}$$

$$C_{K^+K^-} = 0.24 \pm 0.06 \pm 0.02, \tag{1.36}$$

$$S_{K^+K^-} = 0.22 \pm 0.06 \pm 0.02, \tag{1.37}$$

$$A^{\Delta\Gamma}_{K^+K^-} = -0.75 \pm 0.07 \pm 0.11. \tag{1.38}$$

1.4.1 $B \to h^+h^{'-}$ Lifetimes

Obtaining a measurement of a lifetime requires extraction of the decay time of particles created by the proton-proton collisions at the primary interaction point that decay at the secondary vertex. This is calculated by using the particle decay length and its momentum. The decay time is given by the equation

$$t = m\frac{\overrightarrow{p} \cdot \overrightarrow{d}}{|p^2|}, \tag{1.39}$$

where $\overrightarrow{d}$ is the decay length vector, $\overrightarrow{p}$ is the momentum of the B hadron and m is the reconstructed invariant mass. It should be noted that to acquire the momentum of a B hadron the reconstruction of all daughter particles is required.

The decay width in Equation 1.27 can be written as [32]

$$\Gamma_s[f,t] = Ae^{-\Gamma_L t} + Be^{-\Gamma_H t} = e^{-\Gamma t}\left[(A+B)\cosh\left(\frac{\Delta\Gamma_s t}{2}\right) + (B-A)\sinh\left(\frac{\Delta\Gamma_s t}{2}\right)\right], \tag{1.40}$$

where $A = 1 - A_{\Delta\Gamma}$ and $B = 1 + A_{\Delta\Gamma}$. This expression stays true for any B hadron decay with contributions from both heavy and light mass eigenstates. The value to which an unbinned maximum likelihood fit of a single exponential probability density function (PDF) fit onto a double exponential distribution [32] converges is given by the lifetime of $B_s^0 \to K^+K^-$ and can be expressed as

$$\tau_{K^+K^-} = \Gamma_f^{-1} = \frac{A/\Gamma_L^2 + B/\Gamma_H^2}{A/\Gamma_L + B/\Gamma_H}. \tag{1.41}$$

Therefore the effective lifetime can be expressed as

$$\frac{\tau_{K^+K^-}}{\tau_{B_s^0}} = \frac{1}{1-y_s^2}\left[\frac{1+2A_{\Delta\Gamma}y_s + y_s^2}{1+A_{\Delta\Gamma}y_s}\right] = 1 + A_{\Delta\Gamma}y_s + (2 - A_{\Delta\Gamma}^2)y_s^2 + \mathcal{O}(y_s^3))\ [33], \tag{1.42}$$

where

$$y_s = \frac{\Delta\Gamma_s}{2\Gamma_s}, \tag{1.43}$$

and

$$\tau_{B_s^0}^{-1} = \Gamma_s = \frac{\Gamma_H^{(s)} + \Gamma_L^{(s)}}{2}. \tag{1.44}$$

An experimental measurement of the effective lifetime $\tau_{K^+K^-}$ constrains $A_{\Delta\Gamma}$ and Γ_s.

Decay	Lifetime (ps)	Comments
$B_s^0 \to K^+K^-$	1.408 ± 0.017 [34]	CP-even
$B^0 \to K^+\pi^-$ and $B^0 \to \pi^+\pi^-$	1.520 ± 0.004 [34]	B^0 lifetime
$B_s^0 \to \pi^+K^-$	1.505 ± 0.005 [34]	flavour specific B_s^0 lifetime
$\Lambda_b^0 \to pK^-$ and $\Lambda_b^0 \to p\pi^-$	1.470 ± 0.010 [34]	Λ_b^0 lifetime

Table 1.4: Current world averages of $B \to h^+h'^-$ lifetimes

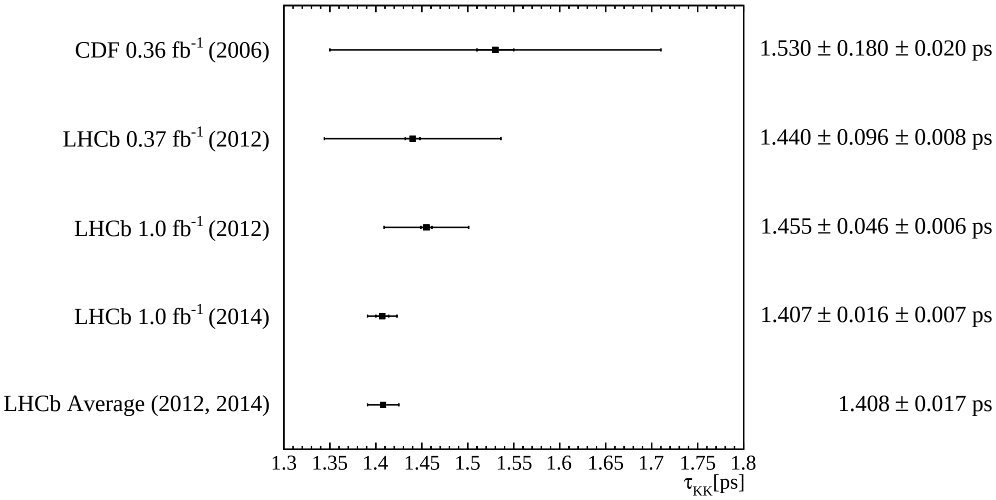

Figure 1.4: Illustration of available measurements of the $B_s^0 \to K^+K^-$ effective lifetime measurements [35, 36, 37, 38, 34].

1.4.2 Experimental Status

The current average $B \to h^+h'^-$ lifetime measurements are given in Table 1.4, where the $B_s^0 \to K^+K^-$ lifetime is the average of two independent LHCb measurements. Overall there has been four measurements of the $B_s^0 \to K^+K^-$ effective lifetime made, one by the CDF collaboration and three by LHCb, Figure 1.4 shows these measurements graphically and illustrates how the precision has improved over time.

The SM prediction on the $B_s^0 \to K^+K^-$ effective lifetime is

$$\tau_{K^+K^-}^{SM} = 1.395 \pm 0.020 \text{ ps [38]}, \tag{1.45}$$

and this gives a value of

$$A_{\Delta\Gamma}^{SM} = -0.972^{+0.014}_{-0.009}. \tag{1.46}$$

Using the most recent $B_s^0 \to K^+K^-$ effective lifetime measurement of $1.407 \pm 0.017\,\mathrm{ps}$ [38] with the LHCb measurements of $\Gamma_s = (0.661 \pm 0.004 \pm 0.006)\mathrm{ps}^{-1}$ and $\Delta\Gamma_s = (0.106 \pm 0.011 \pm 0.007)\mathrm{ps}^{-1}$ [39] gives

$$A_{\Delta\Gamma} = -0.87 \pm 0.18 \pm 0.013. \tag{1.47}$$

1.5 Summary

To summarise, this chapter has described the SM, a QFT commonly used to describe the strong, electromagnetic and weak forces. All observed elementary particles are predicted by the SM. Some of the behaviour of the elementary particles can be characterised with the SM but there are areas where this theory falls short. One of these areas is the observed matter-antimatter asymmetry of the universe. Searches for differences in the behaviour of matter and antimatter could explain the asymmetry, one method to do this is to measure CP violation. CP violation occurs in weak decays. There are three types of CP violation, direct CPV, indirect CPV and CPV in interference between decays with and without mixing. The $B_s^0 \to K^+K^-$ effective lifetime $\tau_{K^+K^-}$ can be used to measure the variable $A_{\Delta\Gamma}$, which is a measure of the amount CP violation that is present in the decay. $K^+K^-$is a CP-even final state which is expected to have a value of $A_{\Delta\Gamma} = -1$ if there is no CP violation. Later in this thesis is a description of an analysis measuring $\tau_{K^+K^-}$ on LHCb data, which enables to extract $A_{\Delta\Gamma}$.

Chapter 2

The LHCb Detector

2.1 The Large Hadron Collider at CERN

The Large Hadron Collider (LHC) [40] is located at the European Organisation for Nuclear Research (CERN), near Geneva, Switzerland. The collider lies underground at a mean depth of 100 m, in a circular tunnel with a circumference of 26.7 km. The tunnel was designed for and occupied by the Large Electron-Positron collider (LEP) [41] before the LHC. Construction of the tunnel occurred between 1983 -1988. The LHC was first started up in September 2008 but operations were delayed due to a devastating magnet quench in one of the LHC sectors [42]. The first physics run (run 1) took place from March 2010 to February 2013. The second physics run (run 2) started in June 2015 and is currently ongoing.

The LHC was designed to accelerate two proton beams in opposite directions to a centre-of-mass energy of 14 TeV. In run 1 the LHC collided protons with centre of mass energy $\sqrt{s} = 7$ TeV in 2010 and 2011, and $\sqrt{s} = 8$ TeV in 2012, with a 50 ns bunch spacing. For run 2 of the LHC the centre of mass energy was increased to $\sqrt{s} = 13$ TeV and 25 ns bunch spacing.

Before they reach the LHC, the protons travel through a series of lower energy accelerators shown in Figure 2.1. Hydrogen atoms are stripped of their electrons to create protons. These protons are firstly accelerated by Linac 2 which accelerates them to the energy of 50 MeV. The protons are then injected from Linac 2 into the Proton Synchrotron Booster (PSB), then the Proton Synchrotron (PS) and then the Super Proton Synchrotron (SPS). Each accelerator in the chain increases the proton energy. The SPS,

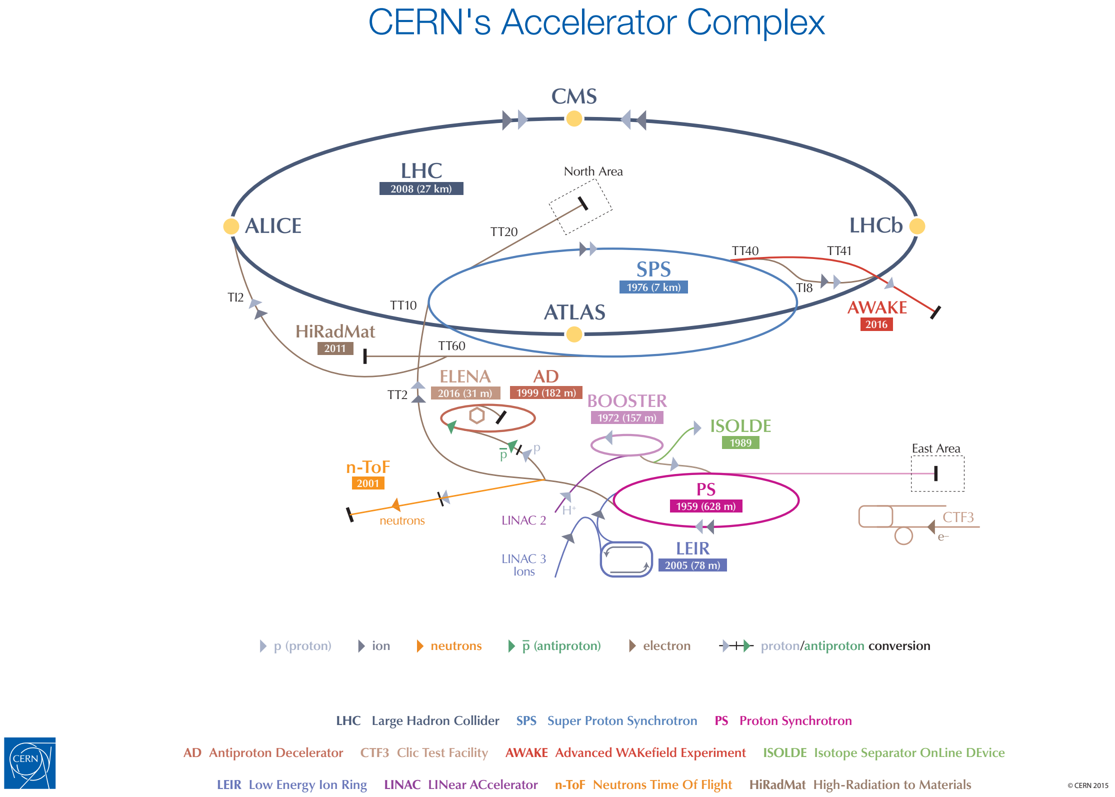

Figure 2.1: Layout of the LHC accelerator complex, reproduced from [43].

which brings the energy up to 450 GeV, injects the protons into the two beam pipes of LHC.

In the LHC the two high energy proton beams are kept in an ultrahigh vacuum and the beams are directed around the circular accelerator with superconducting electromagnets. The four main experiments, ALICE, ATLAS, CMS and LHCb are located at interaction points on the ring and two smaller experiments LHCf and TOTEM are at the side of interaction points. The LHC is also capable of accelerating heavy ions. ALICE [44] does research into quark-gluon plasma, this matter state is created through lead-ion collisions. ATLAS [45] and CMS [46] are general purpose detectors that share the same scientific goals. Their physics program includes Higgs Physics and searches for beyond Standard Model physics. LHCb [47] is designed to study heavy flavour physics and is discussed in the rest of this chapter. TOTEM [48] measures the total pp cross-section at the LHC and studies proton structure. LHCf [49] studies neutral particle production cross-sections at very forward regions of phase space.

2.2 The LHCb Detector

The LHCb detector [47] is a single arm forward spectrometer designed for the study of beauty (b) and charm (c) hadrons. The experiment focuses on flavour physics; primarily precision measurements of CP violation, and studies of rare decays [27].

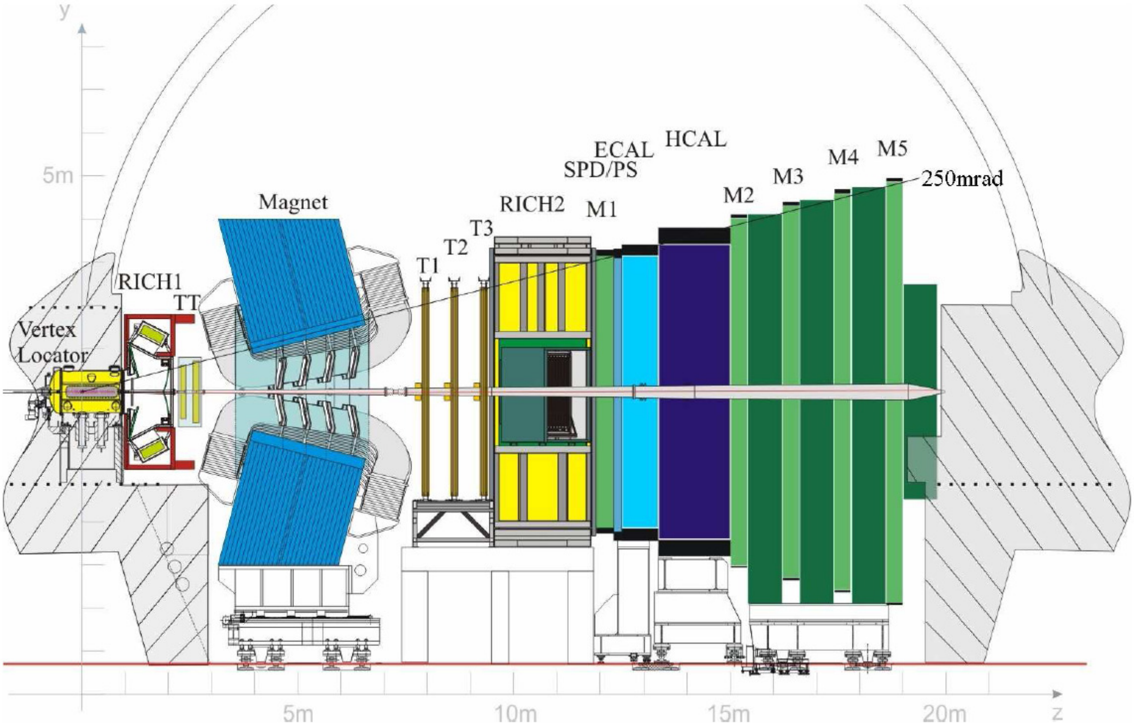

Figure 2.2: Side view of the LHCb detector, reproduced from [47].

The detector layout is shown in Figure 2.2, which also defines LHCb's right-handed coordinate system with the $z-$axis along the beam and the $y-$axis along the vertical direction.

The detector's geometry is designed around the fact that b and $\bar{b}$ hadrons are produced in symmetrical forward and backward cones, this is shown in Figure 2.3. The LHCb detector is designed to look at the particles in the forward region and $\sim 30\%$ of b quarks fall into the detector's acceptance region. The cross section of $b\bar{b}$ production is $75.3\,\mu$b and $154.3\,\mu$b in the LHCb acceptance for $\sqrt{s} = 7\,$TeV and $\sqrt{s} = 13\,$TeV respectively [51, 52]. The angular coverage ranges from approximately $10\,$mrad to 300 $(250)\,$mrad in the $x -$

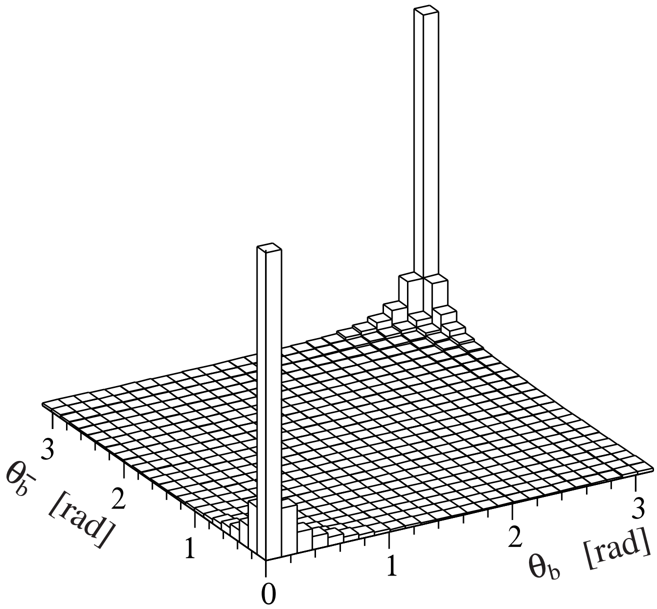

Figure 2.3: Angular production of $b\bar{b}$ from simulated pp collisions, relative to the beam line, at 14TeV. Reproduced from [50].

z $(y-z)$ plane. Only one direction is covered by the detector allowing for larger sub-detectors in the available cavern space. This means improved performance at the cost of detecting only half the b and $\bar{b}$ hadrons.

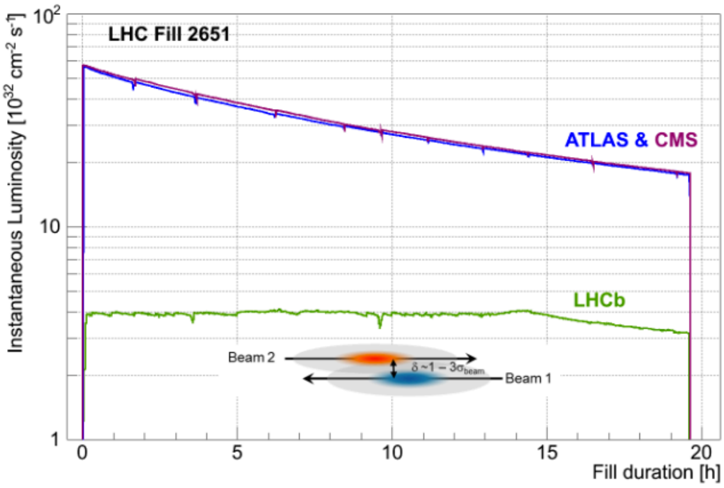

Figure 2.4: Instantaneous luminosity of LHC Fill 2651, reproduced from [53]. The LHCb luminosity is stable in a range of 5% for approximately 15 hours.

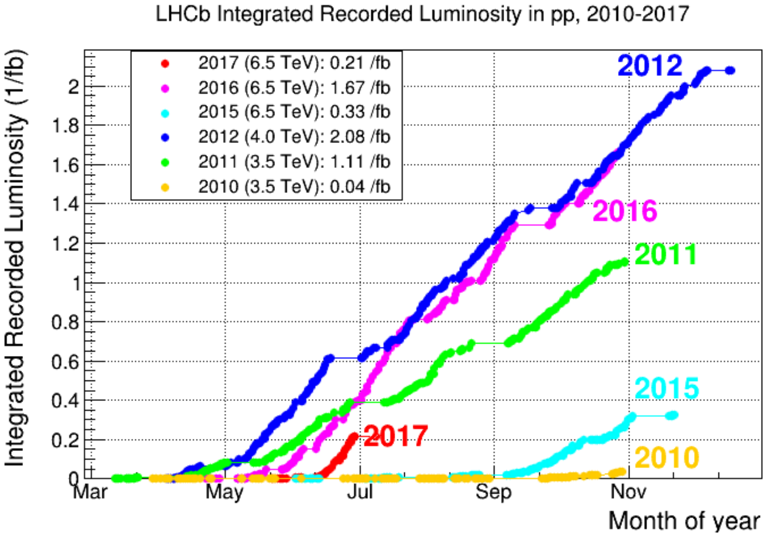

Figure 2.5: LHCb integrated luminosity in pp collisions recorded up to July 2017, reproduced from [54].

The LHCb performance is dependent on the number of interactions per bunch crossing. In 2011 LHCb demonstrated the detector can operate at luminosities of $3.5 \times 10^{32}\,\mathrm{cm}^{-2}\mathrm{s}^{-1}$, which is 1.75 times more than the designed luminosity. Luminosity levelling at the LHCb interaction point is achieved by a lateral displacement of the LHC proton beams. The instantaneous luminosity can be kept relatively stable for each fill, shown in Figure 2.4. The recorded integrated luminosity for LHCb during run 1 and run 2 is shown in Figure 2.5. Data from both run 1 and run 2 was used in the work presented in this thesis. The $B \to h^+ h'^-$ lifetime analysis described in this thesis in Chapters 5-7 uses data from 2011 and 2012. The photon yield studies in Chapter 3 uses data from 2012, 2015 and 2016.

The LHCb detector comprises of several specialised sub-detectors, as seen in Figure 2.2. The Vertex Locator (VELO), the Tracker Turicensis (TT) and 3 tracking stations (T1-T3) are the tracking systems. The VELO is the part of the detector closest to the beam, it is located upstream of the magnet, as is the TT. T1-T3 are located downstream of the magnet. Two Ring Imaging Cherenkov detectors (RICH1 and RICH2) provide particle identification. RICH1 is positioned behind the VELO and RICH2 is behind the T3. The electromagnetic calorimeter (ECAL) and hadronic calorimeter (HCAL) measure particle energy. The calorimetry systems are located after RICH2. There are five muon chambers (M1-M5) providing muon identification, M1 is placed before the calorimeter and M2-M5 are at the end of the detector.

2.2.1 The Vertex Locator (VELO)

The Vertex Locator [55] measures track coordinates close to the interaction region. The VELO can distinguish between a decay point of a long lived b or c hadron, known as the decay vertex (DV), and the location of the pp interaction, known as the primary vertex (PV). With positions of decay vertices, primary vertices and the measured momenta, the proper decay time of long lived particles can be calculated. This is key to physics analyses performed at the LHCb, including the lifetime measurement detailed in this thesis.

VELO Layout

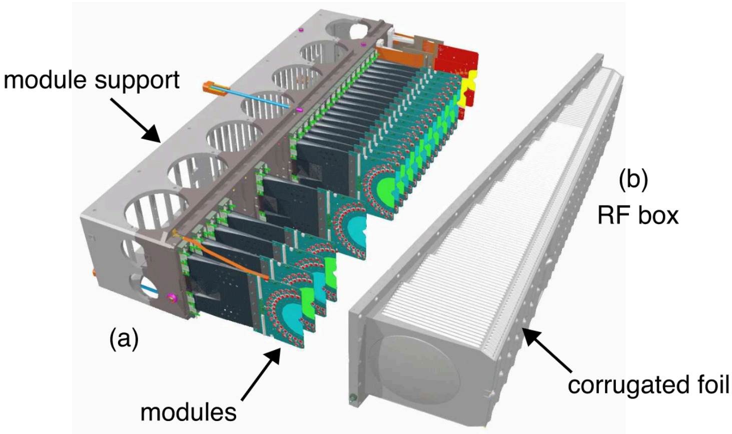

Figure 2.6: Diagram of the modules and module support for one half of the fully assembled VELO subdetector. Reproduced from [47].

The VELO consists of silicon-strip modules. It is made up of 42 modules that are positioned along the beam line in sets of two, shown in Figure 2.6. The sensors consist of approximately semicircular silicon wafers covered in aluminium strips. The VELO uses silicon with n-implants in n-bulk material with p-spray for the strip isolation. Each silicon module has two sensors; the R-sensor that measures the radial coordinate r, and the Φ-sensor that measures the azimuthal angle of the trajectory ϕ, illustrated in Figure 2.7. The z coordinate is determined from the positions of each sensor plane within the experiment. Pseudorapidity η is a measure of the angle of a particle's trajectory with respect to the

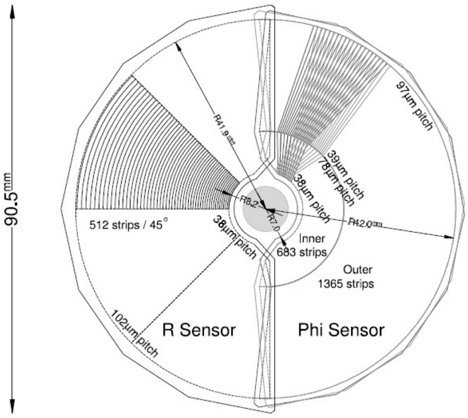

Figure 2.7: Sketch of R and Φ sensors in the VELO. Reproduced from [47].

beam axis and can be defined with the polar angle with respect to the beam axis θ as $\eta = -\ln(\tan(\frac{\theta}{2}))$. The VELO covers the pseudorapidity range $1.6 < \eta < 4.9$ and can detect particles produced at primary vertices in the range $|z| < 10.6\,\text{cm}$. The active area of both R-sensors and Φ-sensors has azimuthal angular coverage of 182°. An individual sensor has 2048 readout channels and the pitch increases from ∼40 μm at small radii to ∼90 μm at large radii.

The active regions of the VELO sensors start at a radial distance of 8 mm from the beam line. The beam radius is much smaller than this at injection. The VELO is designed to be retracted horizontally by 29 mm due to uncertainties of the beam trajectory at injection. These uncertainties are at their largest values at the start of each year when the LHC is re-commissioned after the winter shutdown as the risk of beam loss is at its highest and stable beams have not yet been achieved. The two halves of the VELO overlap when closed during stable beams, allowing full azimuthal angle coverage. Each time the VELO is closed the R-sensor alignment is required to have an accuracy smaller than 100 μm relative to the other half of the detector. This accuracy is needed as the trigger performance deteriorates with misalignments. The VELO alignment is checked after every fill.

The VELO is in a vacuum separated from the beam pipe vacuum by thin corrugated aluminium sheets. This is done to ensure a higher quality vacuum in the beam volume than the detector volume. The aluminium sheets also screen the VELO sensors from the electromagnetic interference induced by the bunched beam and provide a path for the mirror current of the beam. Each half of the VELO is contained in an aluminium box, known as an RF-box (shown in Figure 2.6), the inside surface of the box is known as the RF-foil.

Each module holds the sensors into the module support and the alignment between two sensors is accurate to less than 20 μm. The modules are built to be stable and have thermal management provided by a thermal path for the heat generated by the electronics and sensors to the cooling block. They consist of a thermal pyrolytic graphite core surrounded by carbon fibre. The temperature of the modules is maintained between -10 °C to 0 °C, this range is used as the measured temperature is dependent on the location on the module.

VELO Performance

The performance of the VELO [56] can be illustrated by the impact parameter resolution and the decay time resolution achieved during run 1. The impact parameter (IP) is defined as the distance of closest approach between a track and the PV. Tracks from decays of long-lived particles such as b and c hadrons have larger IPs than tracks originating from the PV due to displaced decay vertices from the interaction point. Requirements on the IP are very effective at removing backgrounds, therefore the ability to measure IP at high precision is important. The IP can be parameterised to IP in the plane perpendicular to the beam given by the projections along the x and y axes, IP$_x$ and IP$_y$.

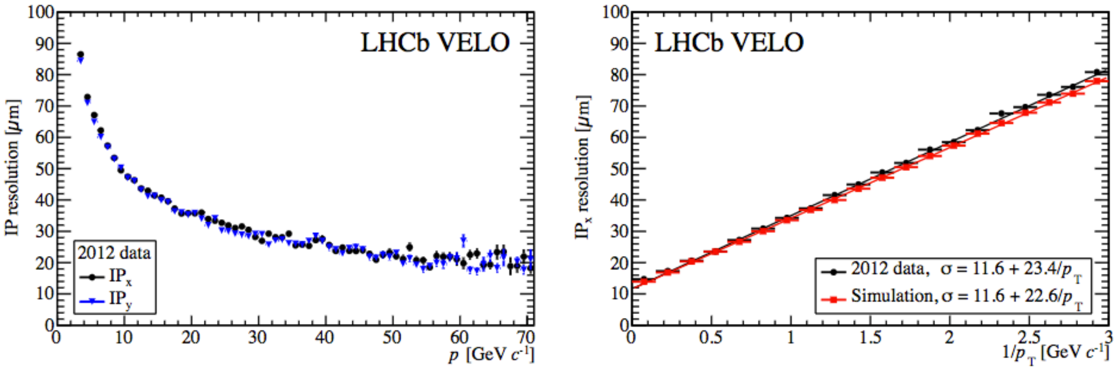

Figure 2.8: (Left) IP$_x$ and IP$_y$ as a function of momentum p. (Right) IP$_x$ as a function of $\frac{1}{p_T}$. Reproduced from [56].

Figure 2.8 shows IP resolution versus momentum. For IP$_x$ and IP$_y$ the resolution is identical, which is expected. The VELO achieves high IP resolutions of $< 35\mu$m for particles with $p_T > 1\,\mathrm{GeV}/c$, which is consistent with the simulations.

The decay time resolution is key to high-precision lifetimes, such as the $B \to h^+h^{'-}$ lifetime analysis described in this thesis. In the rest frame of a particle, the decay time is given by the expression

$$t = \frac{ml}{p}, \tag{2.1}$$

where m is the particle mass, l is the reconstructed decay length and p is the particle momenta. The decay time is evaluated by a vertex fit, which ensures the decay vertex originates from the primary vertex. The decay time resolution is dominated by the resolution of l at relatively small decay times. At decay times significantly larger than the b hadron lifetimes it is dominated by the momentum resolution, which is determined from the TT and T1-T3. This means that the momentum resolution does not affect the decay time precision in the VELO for the b hadron lifetimes in the lifetime analysis presented later in this thesis.

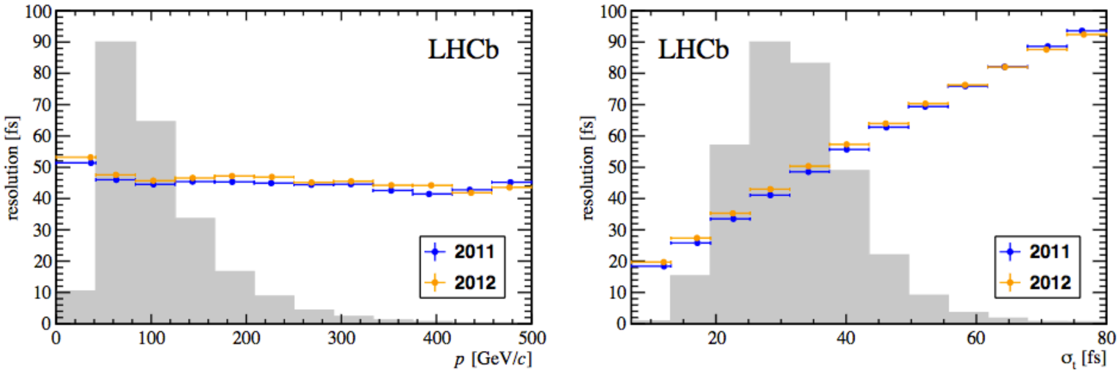

Figure 2.9: (Left, points) Decay time resolution as a function of momentum. (Right, points) Decay time resolution as a function of estimated decay time uncertainty. (Left, grey) Distribution of momentum with arbitrary scale. (Right, grey) distribution of estimated decay time uncertainty with arbitrary scale. Reproduced from [56].

The decay time resolution is shown to be independent of the momentum in Figure 2.9. A linear dependence of the decay time resolution with the estimated decay time uncertainty is expected and is also shown in Figure 2.9. The decay time resolution for the

VELO is on average $\sim 50\,\mathrm{fs}$.

2.2.2 The Ring Imaging Cherenkov Detectors (RICH)

LHCb has two Ring Imaging Cherenkov detectors, RICH 1 and RICH 2 [57], which perform charged track particle identification (PID). These detectors provide separation between pions, kaons, protons, electrons and muons. Located upstream of the magnet, RICH 1 covers a low momentum range between 1-60 GeV/c. RICH 2, which is located downstream of the magnet, covers a higher momentum range of 15-100 GeV/c.

When a charged particle travels throughout the dielectric material in the RICH, a cone of light is emitted, which is seen as a ring image projected onto the photon detectors. The Cherenkov angle θ_C is the opening angle of the cone of light emitted by the particle about its direction of motion. θ_C is dependent on the refractive index of the dielectric medium n and the velocity of the charged particle v,

$$\cos\theta_C = \frac{1}{n\beta}, \text{ where } \beta = \frac{v}{c} = \frac{pc}{\sqrt{m^2c^4 + p^2c^2}}, \tag{2.2}$$

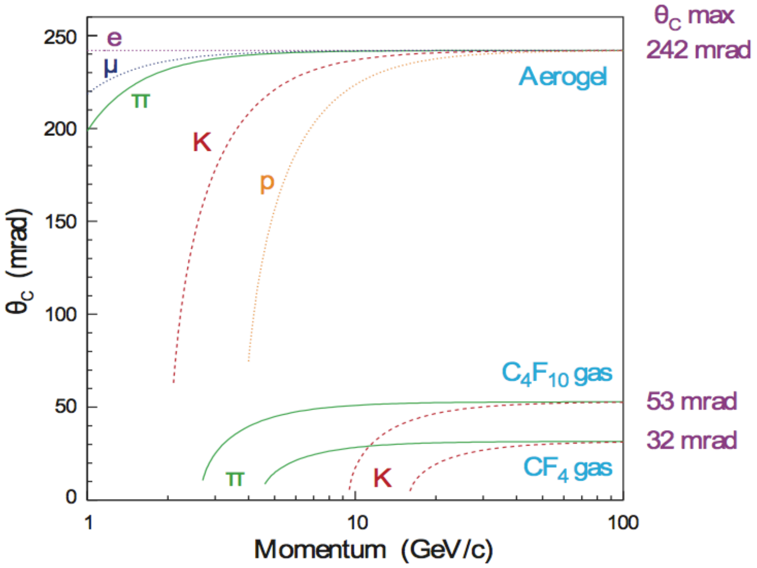

Figure 2.10: Cherenkov angle θ_C against particle momentum for the RICH radiators, reproduced from [47].

where c is the speed of light in a vacuum, m is the particle mass and p is the particle momentum. The dependence of particle momentum for different particle species passing through different dielectric mediums, known as radiators, is shown in Figure 2.10. Three radiators were used in the RICH during run 1, CF_4, C_4F_{10} and aerogel. The aerogel was removed in the operational shut down between runs 1 and 2. The PID of a particle can be determined via the ring radius and its momentum.

There is a lower and upper momentum limit that the RICH is able to identify a track species, known as the threshold momentum and saturation momentum respectively. The threshold momentum is when $n\beta = 1$, no Cherenkov light is emitted below this. The saturation momentum is where $p \gg mc$, at this momentum θ_C is at its saturation angle θ_{sat},

$$\cos\theta_{sat} = \frac{1}{n}. \tag{2.3}$$

RICH Layout

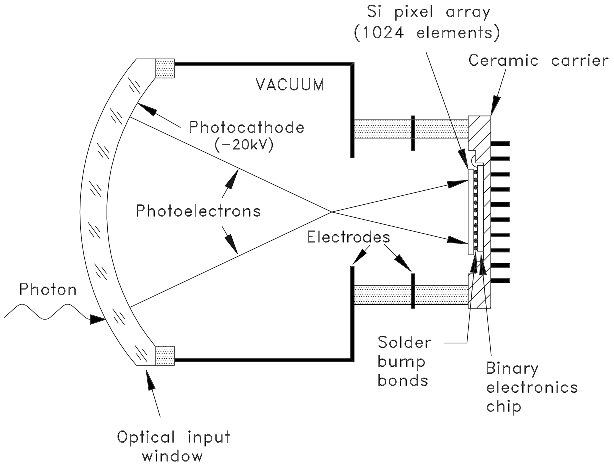

Figure 2.11: Schematic layout of a HPD in the RICH, reproduced from [47].

In the RICH, a combination of flat and spherical mirrors is used to focus the Cherenkov light onto Hybrid Photon Detectors (HPDs). The HPDs consist of a vacuum tube with a spherical quartz entrance window. The quartz window has a photocathode inner surface coating. The interaction between this coating and a photon results in the generation of a photoelectron. An electric potential of $\sim$ 10 to 20 kV accelerate the photoelectrons onto silicon pixel detectors. The silicon in each HPD has 1042 pixels and each pixel is $500 \times 500\,\mu\text{m}^2$ in size, requiring the entrance window to be $2.5 \times 2.5\,\text{mm}^2$. The HPDs are designed to detect single photons of wavelengths between 200-600 nm and are encompassed by an iron shield allowing them to be operational in the magnetic field. Figure 2.11 shows the schematic layout of a HPD. RICH 1 has 196 HPDs and RICH 2 has 288 HPDs.

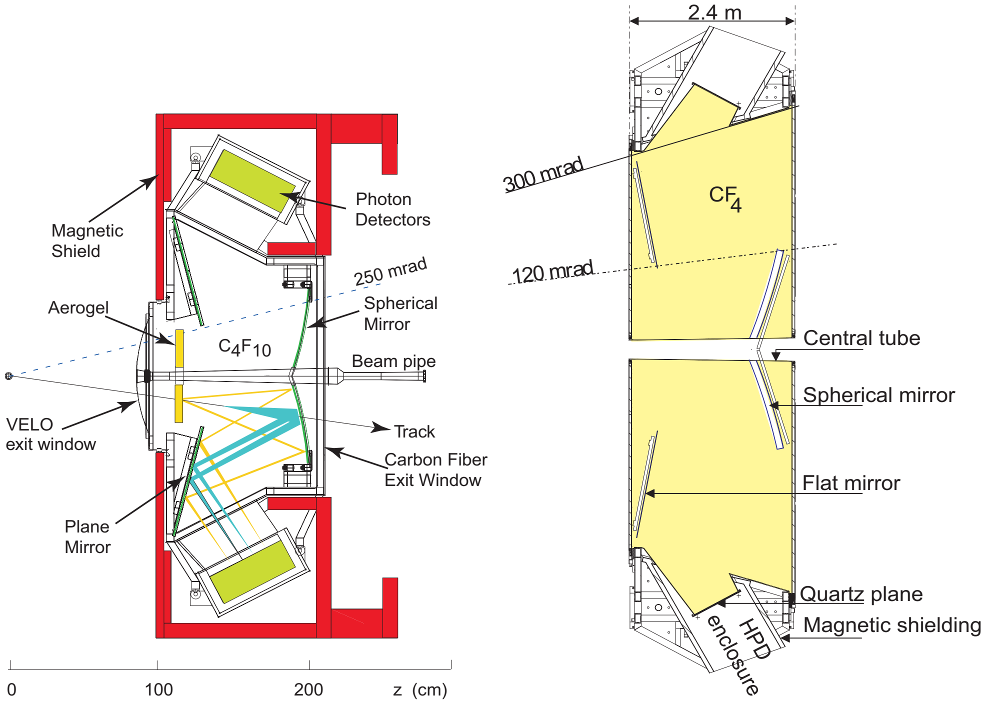

Figure 2.12: Schematic layout of a (left) RICH 1 and (right) RICH 2, reproduced from [47].

Figure 2.12 shows the layout of both RICH detectors. The optical systems of both RICH detectors contain tilted spherical primary mirrors, secondary flat mirrors and photon detectors containing HPDs. Located close to the interactive region, RICH 1 is divided vertically into two halves (Up and Down) around the beam pipe as a requirement of the magnetic shielding, it has 4 spherical mirror and 16 flat mirror segments. RICH 1 has an angular acceptance of 25-300 (250) mrad in x-y (x-z). RICH 2 is located downstream from the magnet and is divided horizontally (A and C) around the beam pipe and has 56 spherical mirror and 40 flat mirror segments. RICH 2 has an angular acceptance of 15-100 (120) mrad in x-z (x-y). The mirrors in the RICH have reflectivity of approximately 90%.

The refractive index of C_4F_{10} in RICH 1 is n = 1.0014 and CF_4 in RICH 2 is n = 1.0005 at a temperature of 0° C and pressure of 101325 Pa. The refractive index of the aerogel is approximately n $\simeq$ 1.03. The aerogel was designed to detect particles at the low momentum range of 2 - 10 GeV/c.

RICH performance

The performance of the RICH [58] can be evaluated by studies of the Cherenkov angle resolution, the particle identification performance and the photoelectron yield. Chapter 3 discusses the photoelectron yield in detail.

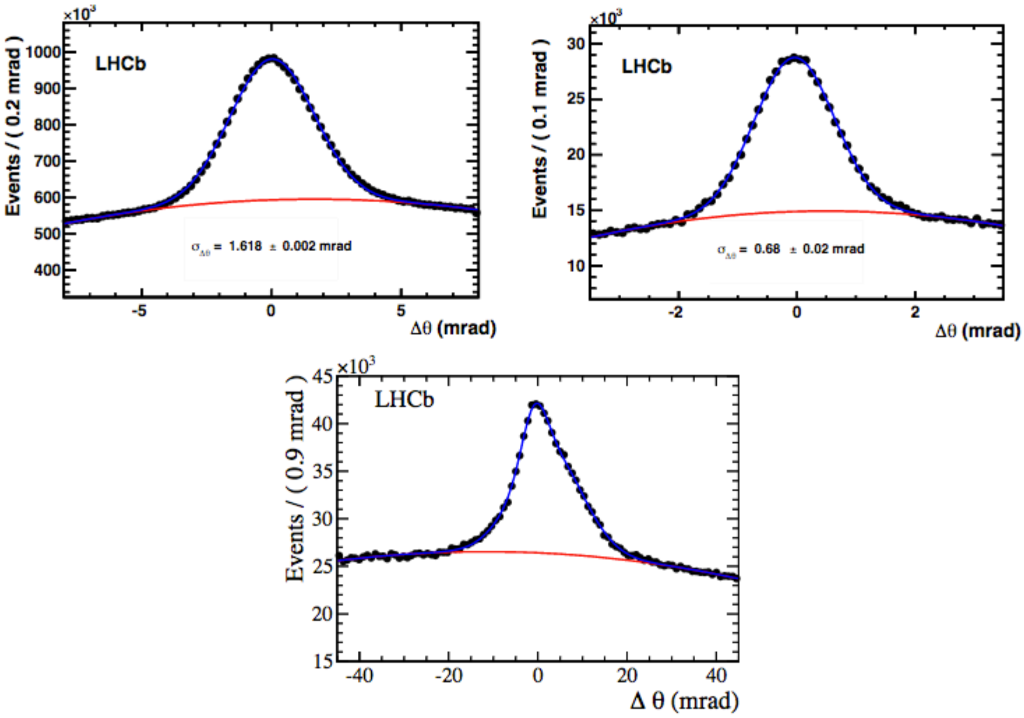

Figure 2.13: $\Delta\theta_C$ distributions for the (top left) RICH 1 gas, (top right) RICH 2 gas and (bottom) Aerogel for 2011 data. Reproduced from [53].

The resolution at which Cherenkov angles $\sigma(\theta_C)$ are measured in the RICH can be reconstructed by analysing Cherenkov rings for saturated tracks (i.e. when $p \gg mc$). Figure 2.13 shows the distributions of difference between the expected and measured Cherenkov angle $\Delta\theta_C$ for tracks with momentum above the saturation value. The expected Cherenkov angles are calculated with the momentum and refractive index of the radiators only.

The fits in Figure 2.13 give $\sigma(\theta_C)$ to be 1.618 mrad for the RICH 1 gas, 0.68 mrad for the RICH 2 gas and 5.6 mrad for the aerogel.

Discrimination between particle species is performed on event selections by using difference in log-likelihood between different hypotheses of a track. Given the likelihood

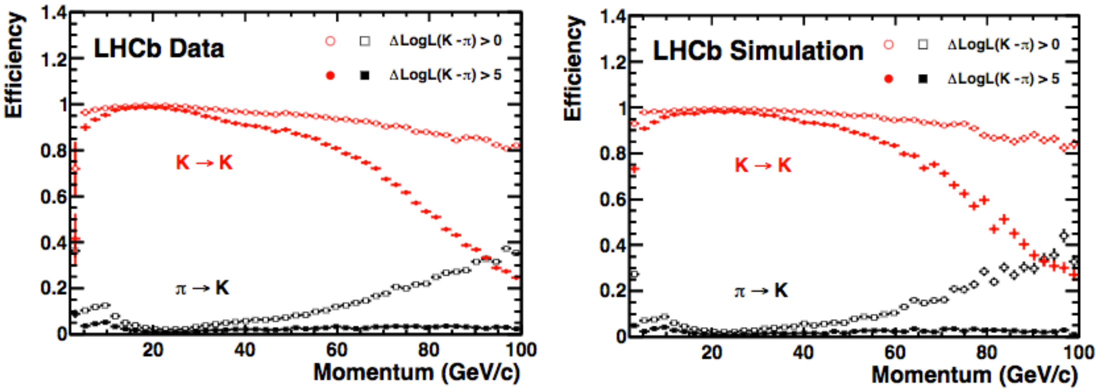

Figure 2.14: Kaon identification efficiency (red points) and pion misidentification efficiency (black points) against momentum for (left) data and (right) simulation. Reproduced from [53].

function $\mathcal{L}_K$ and $\mathcal{L}_\pi$ for a track to be a kaon or pion respectively, the log-likelihood of the kaon hypothesis minus the log-likelihood of the pion hypothesis for a given track is given by $DLL_{K\pi} = log(\mathcal{L}_K) - log(\mathcal{L}_\pi) = \Delta log(K - \pi)$. Data samples where the particle type can be identified from kinematic constraints alone and have no selections on RICH information are studied to test each of the different particle hypotheses to determine the RICH performance.

Figure 2.14 shows the kaon efficiency and misidentification rate of pions as kaons. At $\Delta log(K - \pi) > 0$ the kaon efficiency is 95% with a pion misidentification of 10% and at $\Delta log(K - \pi) > 5$ the kaon efficiency is 85% with a lower pion misidentification of 3%. The proton-pion and proton-kaon separation have also been evaluated in Ref [58].

2.2.3 The Magnet

The LHCb magnet [59] has an integrated magnetic field over the length of the magnet of 4 Tm to bend tracks of charged particles, allowing momentum to be calculated. A diagram of the magnet is shown in Figure 2.15, it consists of two conical saddle shaped coils located above and below the beam. The coils are made of Al-99.7. The magnet polarity is reversed during data taking to cancel any asymmetries in detector efficiency that can fake CP violation.

The integrated magnetic field is measured with a high relative precision of 10^{-4} and

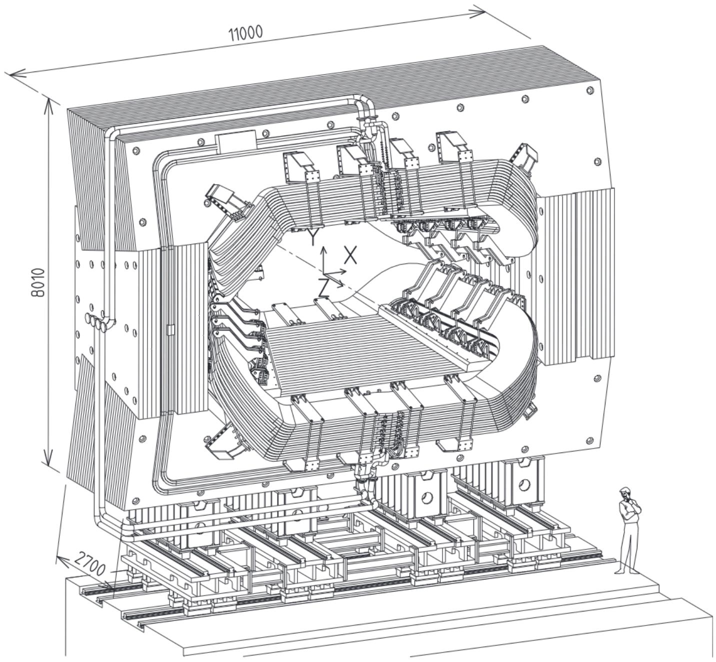

Figure 2.15: Diagram of LHCb Magnet with current and water connections (in mm). Reproduced from [47].

the B-field is measured with a precision of 2 mT. The field mapping was performed with a semi-automatic device made up of an array of Hall probes and is used to maintain the required momentum resolution of LHCb. The magnetic field is measured in the magnet, the VELO, the tracking stations and inside the magnetic shielding of both RICH detectors.

2.2.4 The Tracking System

The LHCb Tracking system consists of the VELO, the TT positioned upstream of the magnet and the T1-T3 positioned downstream of the magnet. The Silicon trackers are the TT and inner part of T1-T3, called the Inner Tracker (IT). The outer part of T1-T3, the outer tracker (OT) is a drift-time detector, which measures momentum by tracking charged particles.

The Silicon Tracker

Both the TT and IT use p^+-on-n silicon microstrip sensors with a strip pitch of $\sim$200 μm. The TT is located upstream of the dipole magnet. It has four detection layers, that

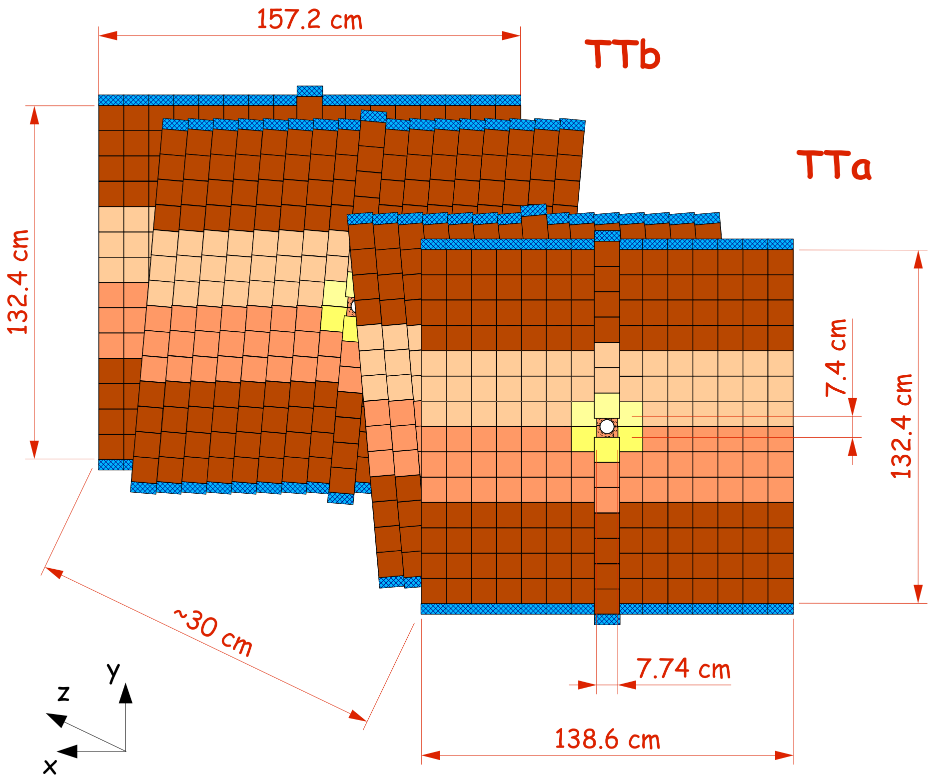

Figure 2.16: Layout of TT layers. Reproduced from [60].

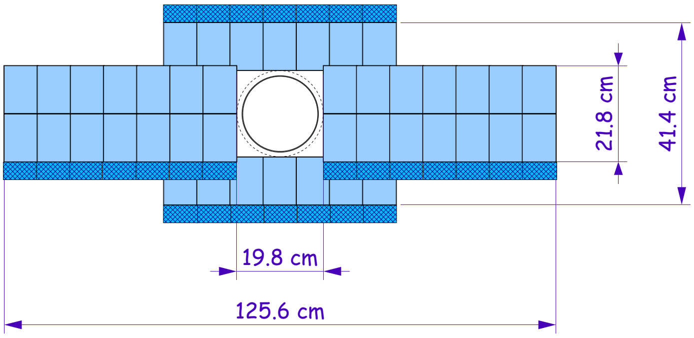

Figure 2.17: Layout of IT. Reproduced from [60].

are grouped into pairs, shown in Figure 2.16. The TT sensors are 9.64 cm wide, 9.44 cm long and 500 μm thick. The middle two layers of the TT have strips rotated by ±5° in the vertical plane, this helps to detect ambiguities in hits as well as improve pattern recognition. The IT is part of the downstream tracking system. The IT layout is shown in Figure 2.17, which shows the arrangement of the 4 detector layers. The IT sensors are 7.6 cm wide, 11 cm long and are either 320 μm or 410 μm thick. Each TT sensor has 512 readout channels and each IT sensor has 384 readout channels.

The Outer Tracker

The OT is an array of individual straw tube modules that surrounds the IT of each tracking station T1-T3. Each module consists of two layers of drift tube. The tubes have an inner diameter of 4.9 mm and are filled with a mixture of Argon (70%) and CO_2 (30%) gas. A gold-plated anode wire is located at the centre of the tubes and the inner layer of the tube wall made of Carbon-doped Kapton-XC acts as a cathode. The outer layer of the tube wall is Kapton-XC and aluminium. As a charged particle passes through the straw tubes the gas inside them becomes ionised. The drift time of the ionisation electrons traveling to the centre of the tubes is measured with respect to the beam crossing signal. The measured drift time is proportional to the distance between the path of the charged particle and the central wire. The gas combination inside the tubes results in electron drift times less than 50 ns. Overall the OT consists of 55000 single straw tubes.

Tracking system performance

The hit efficiency of the silicon tracker was measured with a pure sample of $J/\psi \to \mu^+\mu^-$ with track momentum > 10 GeV/c to minimise multiple scattering effects. This efficiency is defined as the ratio of the number of hits found and the number of hits expected and was measured to be greater than 99.7% for the TT and greater than 99.8% for the IT in 2011. The hit resolution is determined from the residuals of the measured hit position and the extrapolated track position when the hit is removed from the fit. The hit resolution of the TT is 52.6 μm for 2011 and 53.4 μm for 2012. The hit resolution of the IT is 50.3 μm for 2011 and 54.9 μm for 2012 [53].

The average efficiency for a single straw tube in the OT is 99.2% [61], this value is for tracks in the central section of the straw tube, closer than 1.25 mm to the wire. Radiation damage could potentially decrease the efficiency, this was not observed over 2011 and 2012. The single hit resolution is defined as the distance between the extrapolated hit position, with the hit evaluated being removed from the prediction and the position calculated with the drift time. The single hit resolution for tracks with momentum over 10 GeV/c was measured to be 205 μm for run 1.

2.2.5 The Calorimeters

The Calorimetry system comprises of pad/preshower detectors known as the SPD and PS, followed by the electromagnetic calorimeter (ECAL) and then the hadronic calorimeter (HCAL). The ECAL measures the position and energy of electrons and photons and the HCAL measures the position and energy for hadrons. Information from the calorimeter systems is used in the particle identification and the LHCb L0 Trigger.

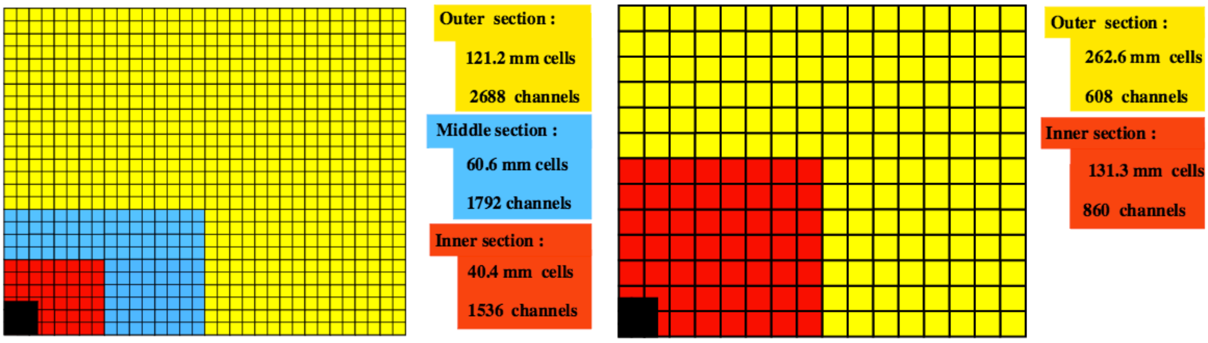

Figure 2.18: Diagram showing segmentation of the calorimeters. (Left) PS, SPD and ECAL, measurements are for ECAL. (Right) HCAL. Reproduced from [47].

All four calorimeter components consist of alternating scintillating pads and metal absorption material. When a particle is stopped in the calorimeter its energy is deposited into the absorption material producing a shower of secondary particles which excite the scintillation material. Photons are then released by the scintillation material and this light is sent to photomultipliers (PMT) by wavelength-shifting fibres (WLS). The calorimeter system is segmented in the $x - y$ plane accounting for the larger particle density close to the beam pipe. The area of the segments increases further away from the beam pipe, shown in Figure 2.18.

ECAL Layout

The PS is included to separate out the high background of charged pions and the SPD separates out a neutral pion background before they enter the ECAL. Both PS and SPD are made up of 15 mm thick lead plates between two scintillator pads. The ECAL is located 12.5 m from the interaction point. It is built up of 2 mm lead and 4 mm scintillator material layers, overall there are 66 layers of each. The ECAL is 25 radiation lengths and is able to fully detect electromagnetic showers from high energy photons.

HCAL Layout

The HCAL uses iron as the absorption material. It has 1 cm thick iron layers and 3 mm thick scintillator tiles. The layers on the HCAL are parallel to the beam line. The resolution of the HCAL is lower than that of the ECAL and it is 5.6 interaction lengths thick.

Calorimeter performance

Electron identification can be achieved with information from the full calorimeter system only. Using $J/\psi \to e^+e^-$ events from 2011 data, the electron identification efficiency has been found to be $(91.9 \pm 1.3)\%$ with a π^0 misidentification rate of $(4.54 \pm 0.02)\%$ [53]. The electron efficiency increases when RICH systems are included.

Photon-neutral pion separation achieved with the ECAL was studied using a sample of $B^0 \to K^{*0}\gamma$ decays and a π^0 sample with the same selection as the photons. Particles with energies above 200 MeV/c were used. The photon identification efficiency was measured to be 95% with 45% of the misidentified π^0 candidates rejected [53].

2.2.6 The Muon System

The muon system consists of 5 muon stations (M1-M5), M1 is located before the ECAL and M2-M5 are at the end of the detector [62], shown in Figure 2.19. Iron absorbers of thickness 80 cm separate the outer muon stations. A minimum momentum of approximately 6 GeV/c is needed for a muon to cross all 5 stations. The inner part of M1 has 12 gas electron multiplier (GEM) detectors and the remaining stations contain 276 multiwire proportional chambers. The chambers contain a mixture of carbon dioxide, argon, and tetrafluoromethane gas.

The muon system is segmented in a similar way to the calorimeters. This segmentation is shown in Figure 2.20. The spatial resolution of M1-M3 is small along the x direction, this is used for track reconstruction and momentum measurements. M4 and M5 have a larger resolution as their purpose is particle identification. Overall, the muon system

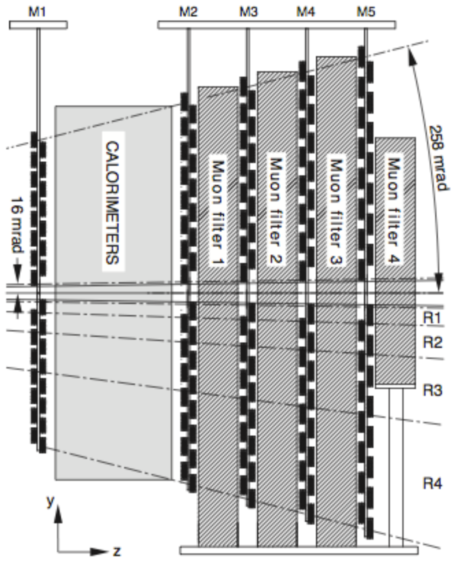

Figure 2.19: Side view of muon system, reproduced from [47].

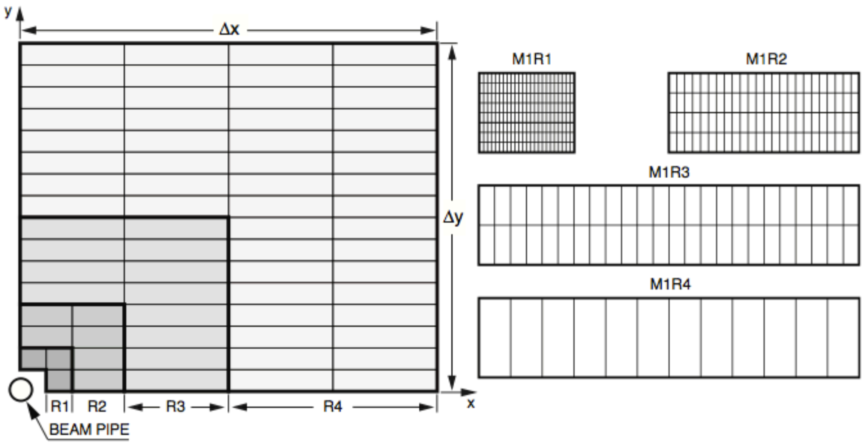

Figure 2.20: Diagram showing the segmentation of M1. (Left) shows the front view of a section of M1, each rectangle shows one chamber. (Right) shows the segmentation of the chambers, each rectangle shows one sensor pad. Reproduced from [47].

has 1380 chambers and covers a total area of 435 m^2. The inner angular acceptance is 20 (16) mrad and the outer angular acceptance is 306 (258) mrad in the bending (non-bending) plane.

Muon system performance

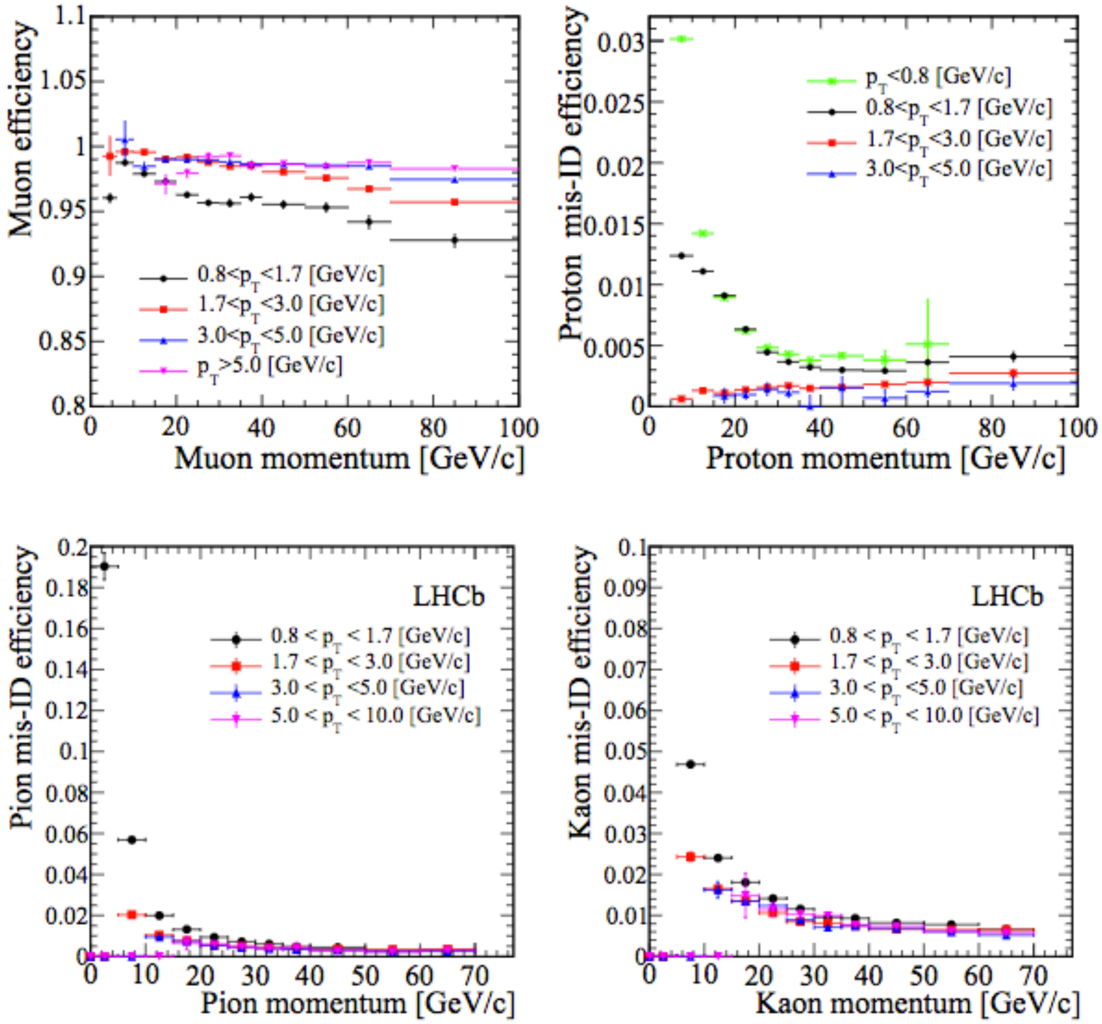

Figure 2.21: (Top left) efficiency of muon selection versus momentum. (Top right) muon-proton misidentification versus momentum. (Bottom left) muon-pion misidentification versus momentum. (Bottom right) muon-kaon misidentification versus momentum. Reproduced from [53].

The muon performance was evaluated on data where only kinematic selections were applied. Muons from $J/\psi \to \mu^+\mu^-$ decays, protons from $\Lambda \to p\pi$ decays, kaons and pions from tagged $D^* \to D^0\pi^+$ with $D^0 \to K^+\pi^-$ decays were chosen to evaluate muon identification efficiency. The results of this study are shown in Figure 2.21, where a binary classification known as “IsMuon” is used to discriminate between particle species. IsMuon is evaluated based on the matching of hits on the muon system to the track extrapolation, this is dependent on the transverse momentum of the muon and therefore the number of muon stations the particle traverses through as seen in Figure 2.21. Inclusion of a muon or non-muon likelihood hypothesis is known to improve muon selection efficiency, studies on this are detailed in Reference [63].

2.2.7 The Trigger

The LHC bunch crossing rate of 40 MHz produces too many interactions to be saved on disk. The job of the Trigger is to decide which events are kept, this is implemented such that only pp interactions interesting to physics analyses are saved. The rate of $b\bar{b}$ pairs expected to be observed from visible pp interactions by the LHCb spectrometer is 100 kHz and the rate that these events can be written to storage is 2-5 kHz. The LHCb experiment achieves this reduction with a two level trigger system, Level 0 (L0) and High Level Trigger (HLT).

L0 trigger

The Level 0 trigger is a hardware trigger, its main purpose is the reduction of the LHC bunch crossing rate (40 MHz) to a rate which the detector electronics are able to read out (1 MHz). L0 achieves this with three pieces of information; the highest reconstructed transverse energy of a hadron, electron and photon clusters in the calorimeters (Level 0 calorimeter trigger), the two highest transverse momentum muons observed in the muon chambers (Level 0 muon trigger). This information is passed onto a decision unit (Level 0 DU) which makes the final decision.

HLT trigger

The High Level Trigger is a software trigger that is run at the Event Filter Farm (EFF). All events that passed the L0 trigger are processed by the HLT. During run 1 there were two stages, firstly HLT1, which reconstructs particles in the VELO and Tracking stations and is dependent on which information leads L0 to accept the event. The second stage, HLT2 performs full event reconstruction. It applies selections based on chosen specific ‘explicit’ and general ‘inclusive’ decays and has multiple lines allowing LHCb to perform a wide range of different measurements. During run 1 the HLT1 reduced the rate to approximately 30 kHz and HLT2 lowers the rate further to approximately 2 kHz. Events that pass HLT2 are written to storage.

2.2.8 Data Processing and Simulation

To perform physics analyses the raw data passes the trigger and is reconstructed offline. This is accomplished using the software packages Brunel [64] and DaVinci [65]. Firstly the Brunel package is run on raw hits and clusters in the detector. Primary vertices are reconstructed and the PID of each track is evaluated using information from the RICH, calorimeters and muon systems. The output of Brunel is very large, approximately twice the size of the raw data. To save disk space, only events that pass a preselection known as 'stripping' are stored in a fully reconstructed format. The second stage is performed with DaVinci, which evaluates sets of tracks under different hypotheses to determine if they originated directly from the decay by a single mother particle, or if they can be reconstructed as several daughter particles. Stripping lines select decay channels or candidate particles of physics interest and the output is stored on disk. DaVinci can be rerun on this data by end users with tighter selections to produce data files containing relevant information for a specific analysis.

In physics analyses and many performance studies, simulated events are used. These simulations are used to perform systematic studies, to provide verification of the analysis method and to determine the selection efficiencies and background rejection performance. The proton-proton collisions are generated with Pythia [66] and the particle decays and distributions are modelled with EvtGen [67]. The primary event generation and the decay simulation is then used with the package Geant4 [68, 69] to produce full simulation interactions of particles within the LHCb detector. Simulated data is produced in the same format as the raw data from collisions. Both the Brunel and DaVinci packages can be used on the simulated data.

2.3 Summary

To summarise, this chapter has described the LHCb detector, a forward spectrometer designed for the study of flavour physics of b and c quarks. The tracking of particle trajectories is evaluated with information from the VELO, the TT and the tracking stations (T1-T3). Particle identification is evaluated with information from the RICH, the calorimeter and the muon stations. The dipole magnet, which bends the trajectory of charged particles as they traverse through the detector, allows the momentum of charged particles to be measured. The performance of individual subdetectors was evaluated for run 1 LHCb data. The trigger ensures that only proton-proton events that are relevant for the physics analyses are stored to disk.

Chapter 3

RICH Performance Studies

3.1 Introduction

With the increase in centre of mass energy for run 2, studies on the number of photons detected by the RICH HPDs provides an opportunity to monitor how the performance of the RICH changes over time and can be used to verify that the detector is operating as expected. One such study is to measure the RICH photoelectron yield N_{pe}, which is defined as the mean number of detected Cherenkov photons emitted by a charged track passing through the radiator. The photoelectron yield N_{pe} is key to the performance of the RICH detector as it contributes to the particle identification (PID) algorithm. Changes in N_{pe} could be caused by variations in the reflectivity of the mirrors and the RICH radiator medium transparency. This section describes measurements of N_{pe} with LHCb data from both run 1 and run 2.

As well as the increase in the centre of mass energy, $\sqrt{s}$, the aerogel in the RICH 1 subdetector was removed for run 2, which will affect N_{pe} and motivates comparisons with run 1 results. The aerogel was described previously in Section 2.2.2. The aerogel was removed since the aerogel particle identification performance is reduced for large track multiplicity events [70], which are more frequent at high $\sqrt{s}$. The volume of gas radiator in RICH 1 located between the VELO exit window and the location where the aerogel was placed did not yield Cherenkov photons in run 1, but this volume is now usable for run 2.

The variation of N_{pe} over time is also studied as any loss in PID performance could be explained by variations in N_{pe}. Finally, the mirrors of the top half of RICH 1 are known to be covered in a small amount of dust, the origin of which is unknown. This has the potential to reduce the value of N_{pe} and studies separating the two halves of RICH 1 are detailed in this chapter. The two halves of RICH 2 are also split, as the detector is assumed to be symmetrical and differences between the left and right side of the detector would be highlighted.

3.2 Method

A statistical method was used to calculate N_{pe}. This method used the variable $\Delta\theta_C$, which is the difference between the measured and expected Cherenkov angle. $\Delta\theta_C$ is defined by

$$\Delta\theta_C = \theta_C - \theta_{exp}, \tag{3.1}$$

where θ_C is the measured angle between a charged particle's track and photon candidate observed as a HPD hit. The expected Cherenkov angle for the charged particle, θ_{exp}, is calculated using equation 2.2.

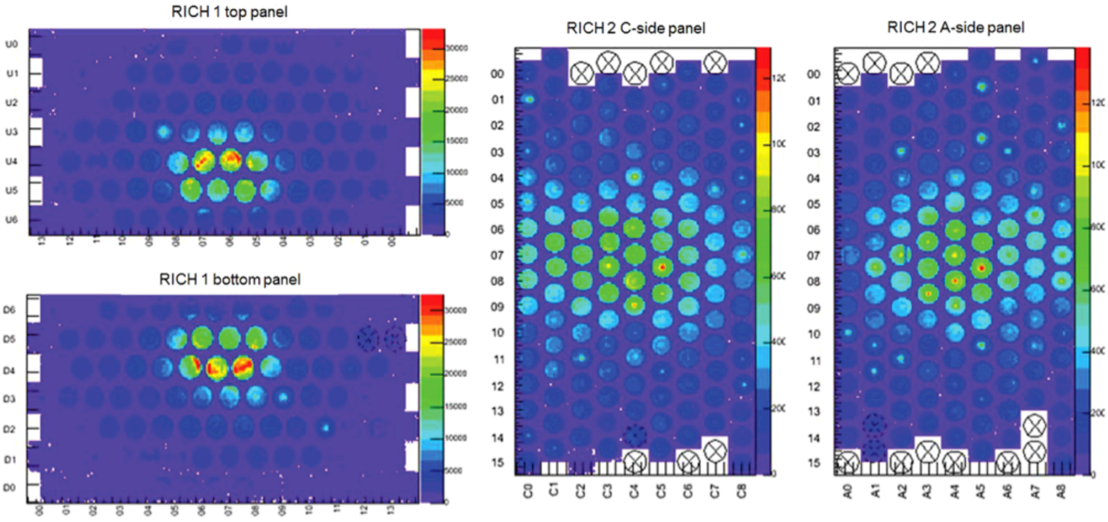

Figure 3.1: Typical HPD hit distribution for 2012 data collection for (left) RICH 1 and (right) RICH 2. The colour scale represents the number of hits, where areas with the highest occupancy are in red and areas low occupancy/no hits are shown in purple. Reproduced from [71].

The method exploits the fact that Cherenkov photons correctly assigned to a charged particle track will form a $\Delta\theta_C$ distribution that is Gaussian with a mean of zero and width that equals the resolution of the measured θ_C distribution. Backgrounds that come from incorrect track - HPD hit assignments form a smooth background and are non-peaking. The $\Delta\theta_C$ for each individual track is then fitted with a Gaussian signal with mean zero, width set to the resolution of θ_C, and a linear background; the signal area under this individual fit gives the individual track N_{pe}. In these individual track fits the width is fixed due to limited statistics. Alignment studies have shown that the track θ_C resolution is independent of the HPD position, (HPD planes are shown in Figure 3.1), allowing the aggregate $\Delta\theta_C$ distribution width to be used as the resolution [58]. Individual track background is dependent on HPD position and needs to be evaluated on a track by track basis. The overall N_{pe} is the mean of the individual N_{pe} distribution.

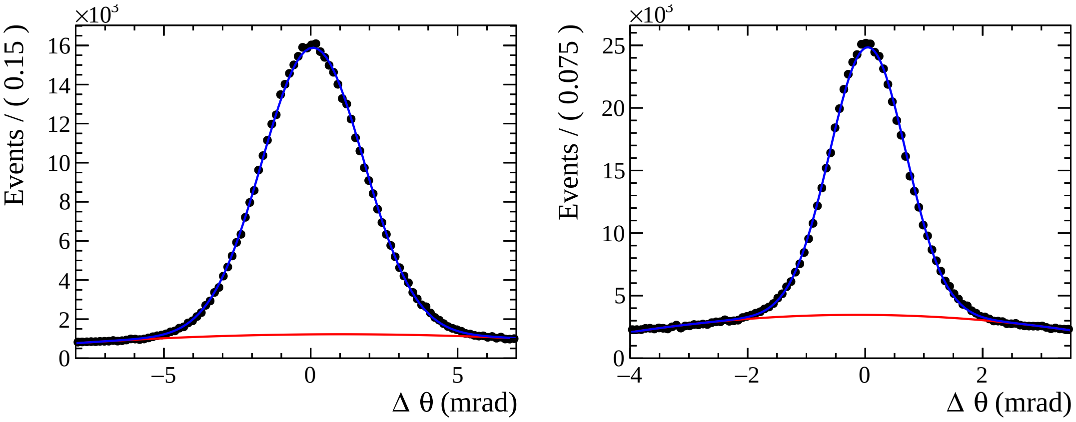

Figure 3.2: Aggregate $\Delta\theta_C$ distributions for 2012 $pp \to pp\mu^+\mu^-$ data. (Left) RICH 1, $\sigma = 1.731 \pm 0.004\,\text{mrad}$. (Right) RICH 2, $\sigma = 0.652 \pm 0.001\,\text{mrad}$.

The aggregate $\Delta\theta_C$ distribution is fitted with a Gaussian signal centred at zero and a polynomial background; the width of this Gaussian is the resolution with which θ_C is measured. Examples of aggregate $\Delta\theta_C$ distributions are shown in Figure 3.2 where the fit described previously is shown in blue. Figure 3.3 shows examples of individual track fits. The signal fit can have a negative yield. This happens when background fluctuations in the upper and lower $\Delta\theta_C$ sidebands are greater than those in the signal region and the effect is compensated when these fluctuations enhance the signal yield in other tracks. In these cases were a track has a negative yeild, the photon yield is compatible with zero photons, within the statistical error of the fit.

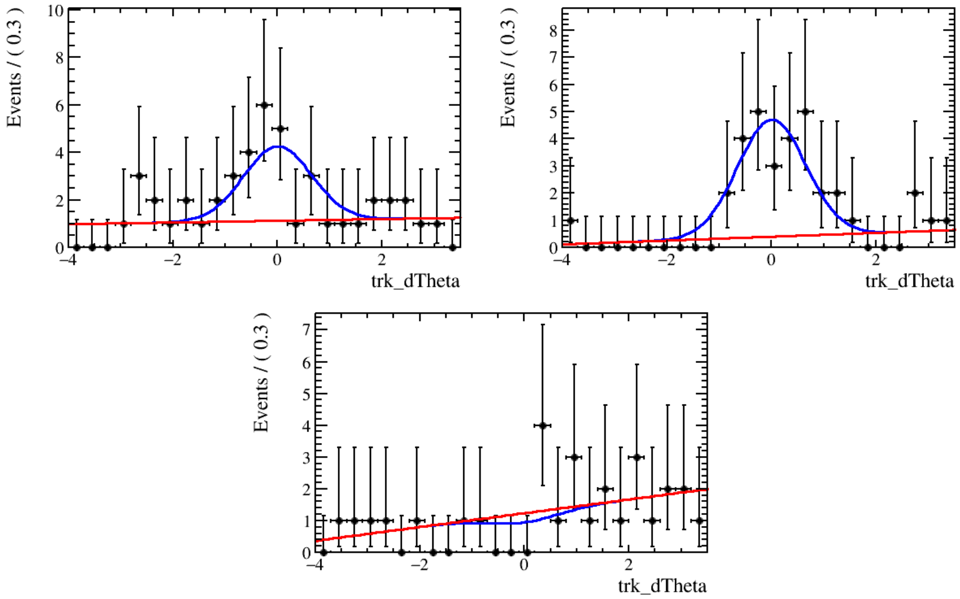

Figure 3.3: Examples of individual track fits of $\Delta\theta_C$, where the x-axis represents $\Delta\theta_C$ (mrad). These fits are for RICH 1 gas.

3.3 Data Sample

Two categories of events are used for the measurement of N_{pe}.The first category contains low track multiplicity muon events from the diffractive scattering process $pp \to pp\mu^+\mu^-$ [73, 74]. Since they have significantly lower charged track multiplicities than typical events used in physics analyses, the $pp \to pp\mu^+\mu^-$ events have very low HPD backgrounds. The second event category are observed more frequently during data collection and consist of the D^* tagged $D^0 \to K^-\pi^+$ events. These consist of $D^{*+} \to D^0\pi^+$ or $D^{*-} \to \overline{D}^0\pi^-$ to tag the flavour of the D meson by the charge of the pion, with a subsequent decay to $D^0 \to K^-\pi^+$ or $\overline{D}^0 \to K^+\pi^-$ to identify the kaon. These events have higher HPD backgrounds than $pp \to pp\mu^+\mu^-$ events. Figure 3.4 shows typical RICH 1 event displays for both categories of events, where the difference in number of charged tracks present can be seen. Kaons from the $D^0 \to K^-\pi^+$ events are not used as the available data had PID requirements based on the RICH information of the K track which could bias N_{pe} results.

In both cases only saturated tracks are used, i.e. $\theta_C \sim \theta_{sat}$. This is done to minimise the uncertainty on θ_{exp} which arises from the measured track momentum. For both muons

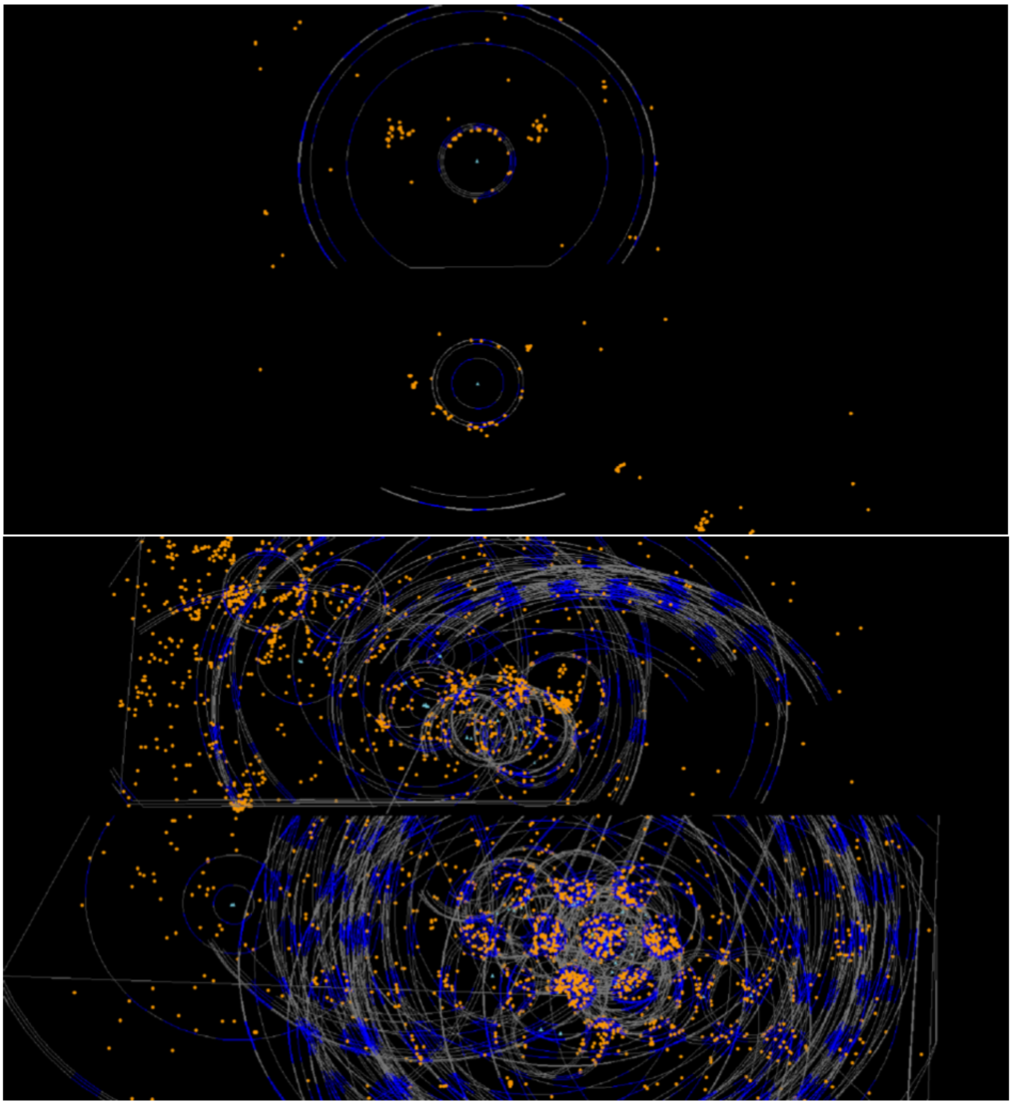

Figure 3.4: Event displays of RICH 1 HPDs taken from the 2011 data run. Orange dots represent HDP hits, light blue triangles in the centre of rings represent the position of the charged tracks, and the lines represent expected rings from a pion, kaon or proton PID hypothesis. The blue lines show where the active HPD areas overlap with ring hypothesis. (Top) A typical $pp \to pp\mu^+\mu^-$ event, (bottom) a typical $pp \to D^{*+}(D^0(\to K^-\pi^+)\pi^+)X$ event. Reproduced from [72]

and pions the saturation momentum for C_4F_{10} (in RICH 1) is 25 GeV/c and for CF_4 (in RICH 2) it is 40.4 GeV/c.

The low multiplicity muon tracks from $pp \to pp\mu^+\mu^-$ decays are selected by requiring that no primary pp primary collision vertex is reconstructed i.e. the number of PVs, $nPV = 0$. The muon production vertex is required to be located within ±1.5 mm of the detector in the $x - y$ plane. Both muons have a selection on the PID variable DLL_{μ}, which is the log-likelihood of the muon track hypothesis minus log-likelihood of the pion track hypothesis. The variable DLL_{μ} only uses PID information from the muon systems to determine a track hypothesis and the selection for this is $DLL_{\mu} > 3$. The muons also have a requirement on the fraction of the area that their Cherenkov ring projects onto active HPD pixels, which is described as geometric efficiency, $\epsilon_{geom} > 0.5$, the track fit χ^2 per degree of freedom $\chi^2/ndof < 2$ and the probability that the track is a ghost is less than 0.5.

The pions used in this study are from $D^{*+} \to D^0(\to K^-\pi^+)\pi^+$ [75] decays, where the pion selected originates from the D^0 decay and the other pion from the D^{*+} decay is a low momentum pion referred to as a 'slow' pion, which is not used for the measurement and is used to tag the flavour of the D^0. The kaons and pions from the $D^0 \to K^-\pi^+$ decay are required to have a good quality decay vertex fit. The full list of selections on this data is found in Appendix A. The pion tracks have a requirement of $\chi^2/ndof < 2$ and the probability that the track is a ghost less than 0.5.

3.4 Rich Photoelectron Yield Results

The photoelectron yield N_{pe} was measured with samples of 2012 (after July), 2015 and 2016 $pp \to pp\mu^+\mu^-$ data. N_{pe} is also measured with samples of 2012 (after July), 2015 data and 2012 MC for the D^* tagged $D^0 \to K^-\pi^+$ events. The muon events are used to study the time dependence and the effect of separating the HPD boxes of the RICH on the photoelectron yield.

3.4.1 Low Multiplicity Muon Events

RICH 1 Results

The photoelectron yield for RICH 1 was measured for samples of 2012, 2015 and 2016 muon data, where the individual track N_{pe} distributions are shown in Figure 3.5. The mean of the distributions give the overall photoelectron yields of $N_{pe}^{2012} = 21.79 \pm 0.06$, $N_{pe}^{2015} = 24.20 \pm 0.07$ and $N_{pe}^{2016} = 23.54 \pm 0.04$ for 2012, 2015 and 2016 data respectively

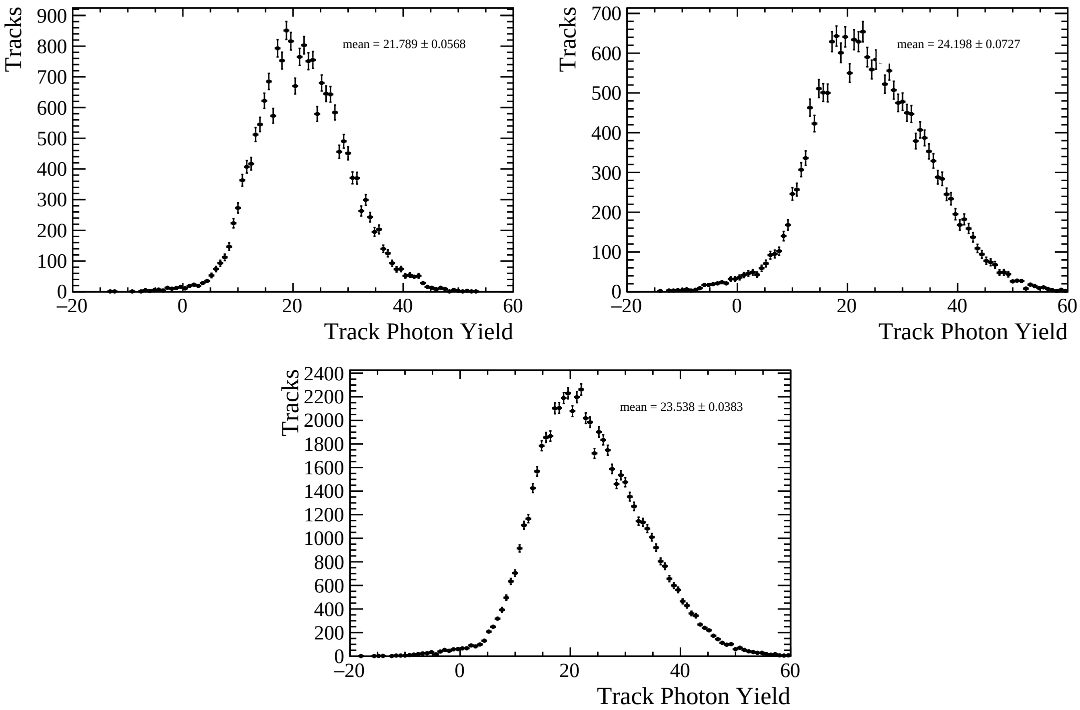

Figure 3.5: C_4F_{10} track N_{pe} distributions for $pp \to pp\mu^+\mu^-$ data. (Top left) Results for 2012 data with individual track resolution $\sigma = 1.73$ mrad. (Top right) Results for 2015 data with individual track resolution $\sigma = 1.76$ mrad (Bottom) Results for 2016 data with individual track resolution $\sigma = 1.68$ mrad.

from muon tracks in RICH 1, all quoted errors are statistical. The differences in the distributions of the individual track N_{pe} highlighted are in Figure 3.6, where the histograms are overlaid. The shape of the RICH 1 N_{pe} distribution is significantly different between run 1 and run 2 data. There is an increase by a factor of ~ 4 in the number of individual tracks with yields above 35. The difference in shape is caused by the removal of the aerogel radiator in RICH 1 during the long shut down between 2012 and 2015 data taking periods. This increases the average track length in the C_4F_{10} gas, thereby increasing the average number of photoelectrons which is seen in the results.

The ratio of the effective radiator length of the C_4F_{10} in RICH 1, L^{2015}/L^{2012}, where L is the average effective radiator length, is expected to be approximately the same as the ratio $N_{pe}^{2015}/N_{pe}^{2012}$. The lengths $L^{2012} = 95\,\text{cm}$ and $L^{2015} \approx 120\,\text{cm}$ [76]. Note that L^{2015} is only approximate as the boundary between the VELO exit window and RICH 1 is curved.

These lengths give $L^{2015}/L^{2012} \approx 1.26$ and for the muon data $N_{pe}^{2015}/N_{pe}^{2012} = 1.11$. The increase change in length should produce an increase in N_{pe}, which is observed.

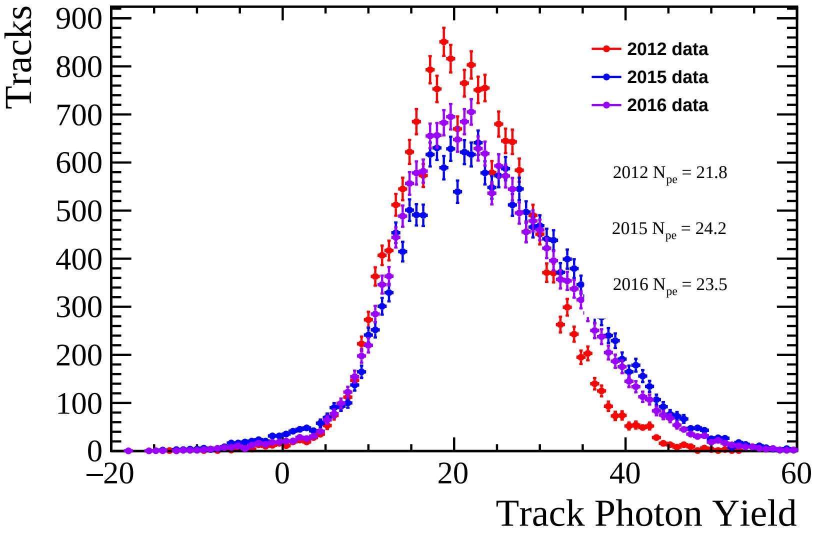

Figure 3.6: C_4F_{10} track N_{pe} distributions for $pp \rightarrow pp\mu^+\mu^-$ data, where the 2012, 2015 and 2016 distributions are overlaid to highlight differences. In this figure the 2015 and 2016 histograms are scaled to match the number of events in the 2012 sample.

RICH 2 Results

The photoelectron yield for RICH 2 was measured for samples for 2012, 2015 and 2016 muon data, where the individual track N_{pe} distributions are shown in Figure 3.7. The mean of the distributions give the overall photoelectron yields of $N_{pe}^{2012} = 14.28 \pm 0.04$, $N_{pe}^{2015} = 13.83 \pm 0.04$ and $N_{pe}^{2016} = 13.08 \pm 0.02$ for 2012, 2015 and 2016 data respectively from muon tracks in RICH 2, all quoted errors are statistical. The differences in the distributions of the individual track N_{pe} highlighted are in Figure 3.8, where the histograms are overlaid. Slight differences in the RICH 2 distributions of the individual track N_{pe} are observed in the lower end of the distribution tail. One possible cause of this is larger fluctuations in the HPD background during higher energy runs. The average number of photoelectrons in RICH 2 reduces between 2012 and 2016, this could be due to HPD ageing.

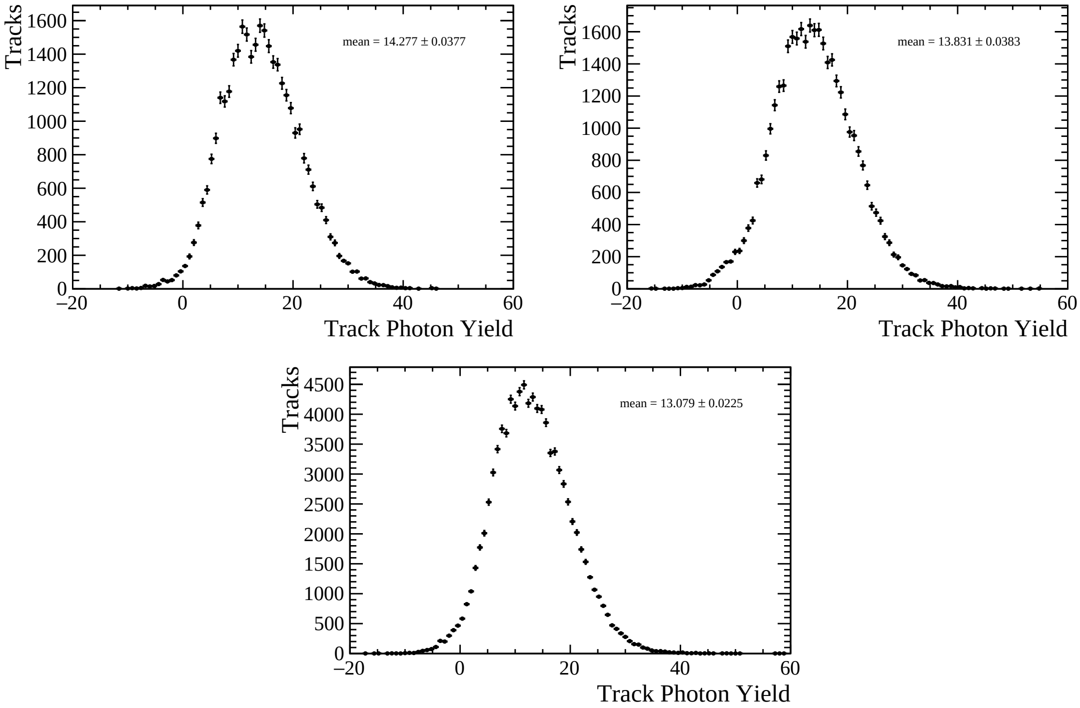

Figure 3.7: CF_4 track N_{pe} distributions for $pp \to pp\mu^+\mu^-$ data. (Top left) Results for 2012 data with individual track resolution $\sigma = 0.65\,\mathrm{mrad}$. (Top right) Results for 2015 data with individual track resolution $\sigma = 0.65\,\mathrm{mrad}$. (Bottom) Results for 2016 data with individual track resolution $\sigma = 0.63\,\mathrm{mrad}$.

3.4.2 High Multiplicity Pion Events

RICH 1 Results

The photoelectron yield for RICH 1 was measured for samples of 2012 data, 2015 data and 2012 MC for pion tracks from D^* tagged $D^0 \to K^-\pi^+$ events, where the individual track N_{pe} distributions are shown in Figure 3.9. The mean of the distributions give the overall photoelectron yields of $N_{pe}^{2012} = 19.85 \pm 0.03$, $N_{pe}^{2012MC} = 19.80 \pm 0.08$ and $N_{pe}^{2015} = 22.61 \pm 0.02$ for 2012 data, 2012 MC and 2015 data respectively from pion tracks in RICH 1, all quoted errors are statistical. The 2012 data and MC agree with each other within 1 standard deviation. Overall the pion track N_{pe} is lower than the muon track result, this is to be expected as no geometric efficiency requirement was applied to the D^* data set. The dependence of track multiplicity on N_{pe} in RICH 1 is shown in Figure 3.10, where the photon yield is measured as a function of the multiplicity in the SPD. The

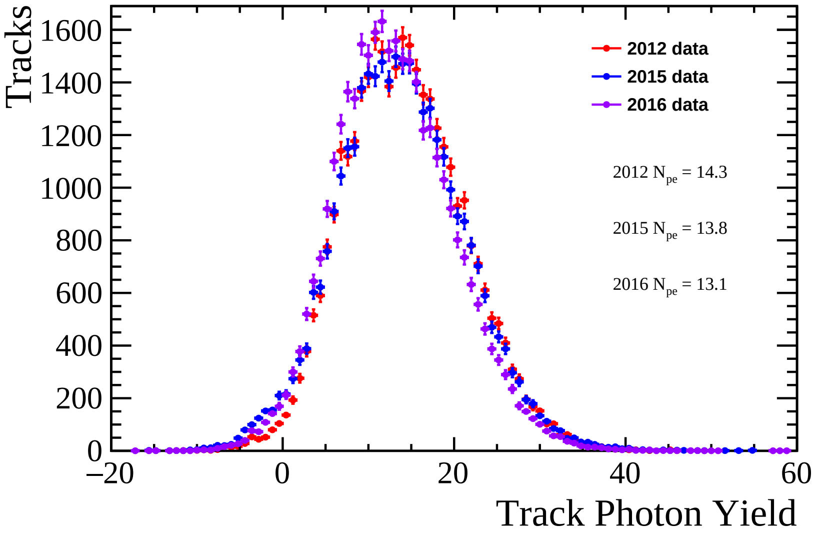

Figure 3.8: CF_4 track N_{pe} distributions for $pp \rightarrow pp\mu^+\mu^-$ data, where the 2012, 2015 and 2016 distributions are overlaid to highlight differences. In this figure the 2015 and 2016 histograms are scaled to match the number of events in the 2012 sample.

distribution is approximately flat for run 1 data, which agrees with the run 1 MC. For run 2 the photoelectron yield reduces linearly with increasing multiplicity. Linear fits to these distributions are detailed in Appendix B. This suggests that for run 2, at higher multiplicity, the photon background increases causing a reduction in N_{pe}, this is seen in run 2 but not run 1 due to increased centre of mass energies and the removal of the aerogel.

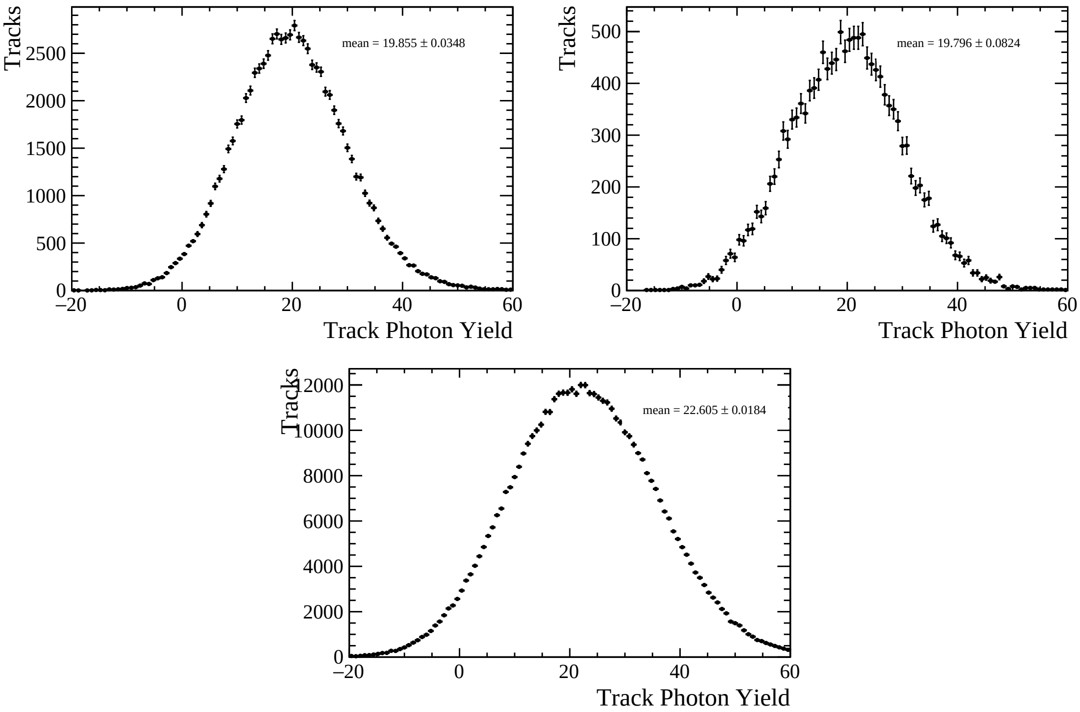

Figure 3.9: C_4F_{10} track N_{pe} distributions for D^* tagged $D^0 \to K^-\pi^+$ data. (Top left) Results for 2012 data with individual track resolution $\sigma = 1.57\,\text{mrad}$. (Top right) Results for 2012 MC with individual track resolution $\sigma = 1.57\,\text{mrad}$. (Bottom) Results for 2015 data with individual track resolution $\sigma = 1.67\,\text{mrad}$.

RICH 2 Results

The photoelectron yield for RICH 2 was measured for samples of 2012 data, 2015 data and 2012 MC for pion tracks from D^* tagged $D^0 \to K^-\pi^+$ events, where the individual track N_{pe} distributions are shown in Figure 3.11. The mean of the distributions give the overall photoelectron yields of $N_{pe}^{2012} = 13.74 \pm 0.04$, $N_{pe}^{2012MC} = 14.39 \pm 0.09$ and $N_{pe}^{2015} = 12.01 \pm 0.02$ for 2012 data, 2012 MC and 2015 data respectively from pion tracks in RICH 2, all quoted errors are statistical. Similarly to the RICH 1 results the overall pion track N_{pe} is lower than the muon track result due to no geometric efficiency requirement on the D^* data sample. The dependence of track multiplicity on N_{pe} in RICH 2 is shown in Figure 3.12, where the charged track multiplicity is measured as the multiplicity in the SPD. The distribution is approximately flat for both run 1 and run 2 data and again the linear fits to these distributions are detailed in Appendix B. The run 1 MC also has an

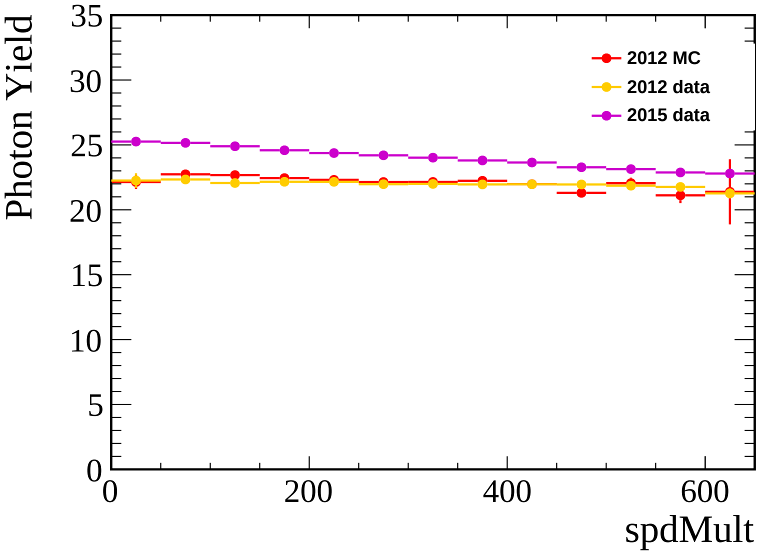

Figure 3.10: Charged track multiplicity dependence on C_4F_{10} N_{pe} from 2012 data, 2015 data and 2012 MC from pion tracks from D^* tagged $D^0 \rightarrow K^-\pi^+$ events.

approximately flat distribution.

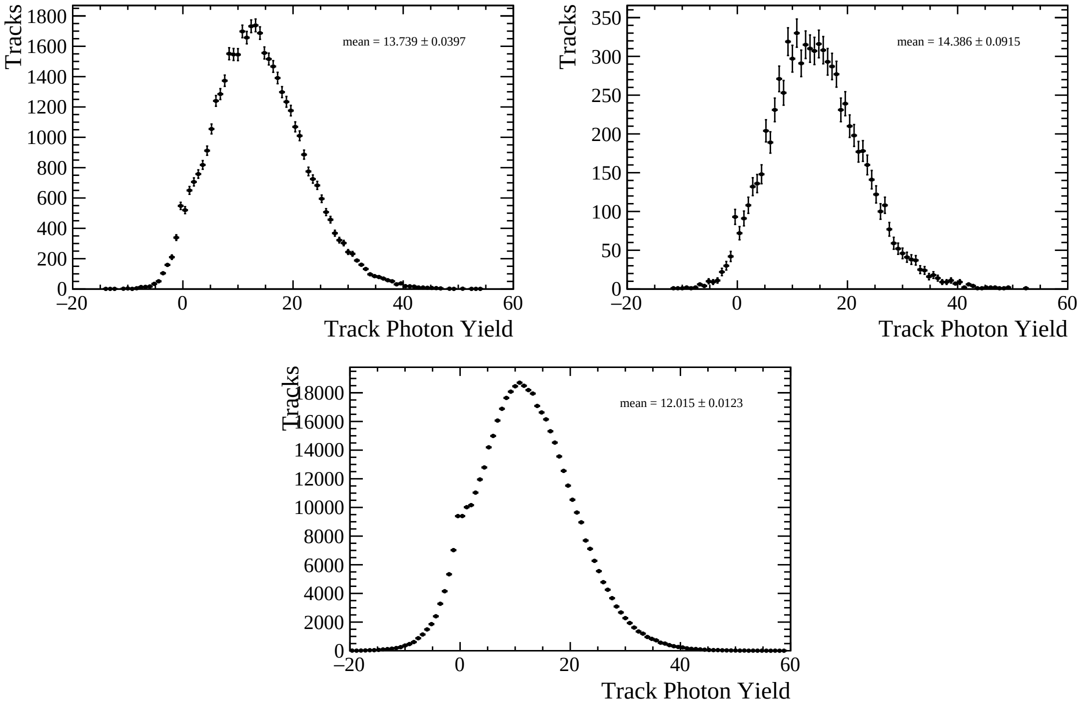

Figure 3.11: CF_4 track N_{pe} distributions for D^* tagged $D^0 \to K^-\pi^+$ data. (Top left) Results for 2012 data with individual track resolution $\sigma = 0.58\,\text{mrad}$. (Top right) Results for 2012 MC with individual track resolution $\sigma = 0.62\,\text{mrad}$. (Bottom) Results for 2015 data with individual track resolution $\sigma = 0.59\,\text{mrad}$.

3.4.3 N_{pe} Time Variation

The photoelectron yield variation over time is shown in Figures 3.13-3.15. These N_{pe} measurements are from $pp \to pp\mu^+\mu^-$ events. Individual track N_{pe} is binned in the variable run number, where each LHCb run is given a consecutive number and only physics $p-p$ collision runs with stable beams are included.

2012 data taking occurred during April to December, N_{pe} during the runs at the beginning of the year ($\sim 111100-120000$) is less than the runs later on in the year. This increase in N_{pe} is due to an adjustment of the reference voltage of the HPD pixel readout chips and deliberately carried out as the PID performance of the RICH had decreased compared to the performance during 2011. The cause of this loss in PID performance is unknown. The effect of the adjustment was to increase N_{pe} after July. The LHCb PID performance at a 95% K ID efficiency caused the $K \to \pi$ misidentification rate to

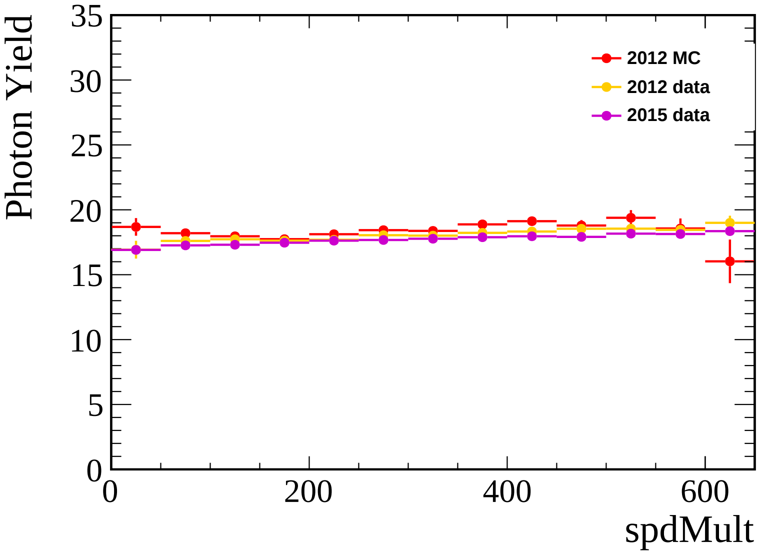

Figure 3.12: Charged track multiplicity dependence on CF_4 N_{pe} from 2012 data, 2015 data and 2012 MC from pion tracks from D^* tagged $D^0 \to K^-\pi^+$ events.

decrease from 12% to 8% after the adjustment in July. The effect of the adjustment can be seen best in the 2012 RICH 1 data where N_{pe} $\sim$ 20 before the adjustment and N_{pe} $\sim$ 22 subsequently.

2015 data taking occurred during August-November of that year and 2016 data taking occurred during April-November of that year. During both years in run 2 the N_{pe} is roughly flat. There are some small variations over time, these could be due to a variety of reasons, one of which is the pressure of the gas in the RICH.

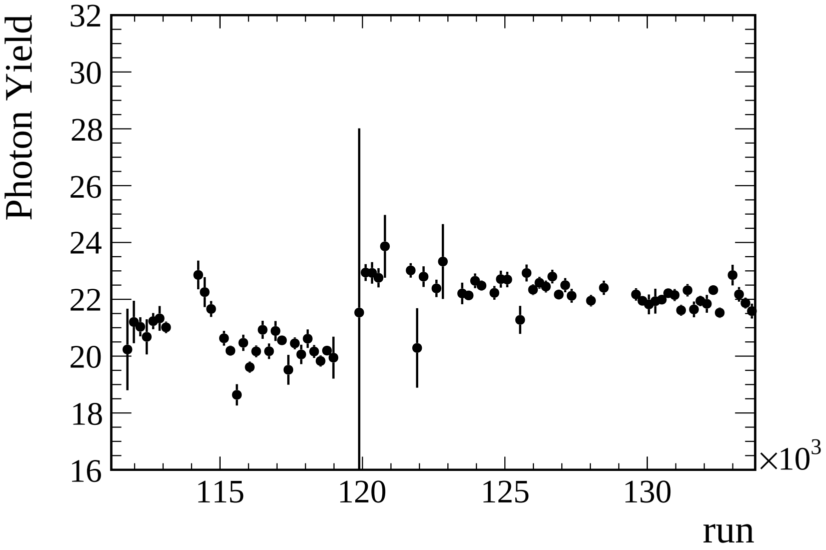

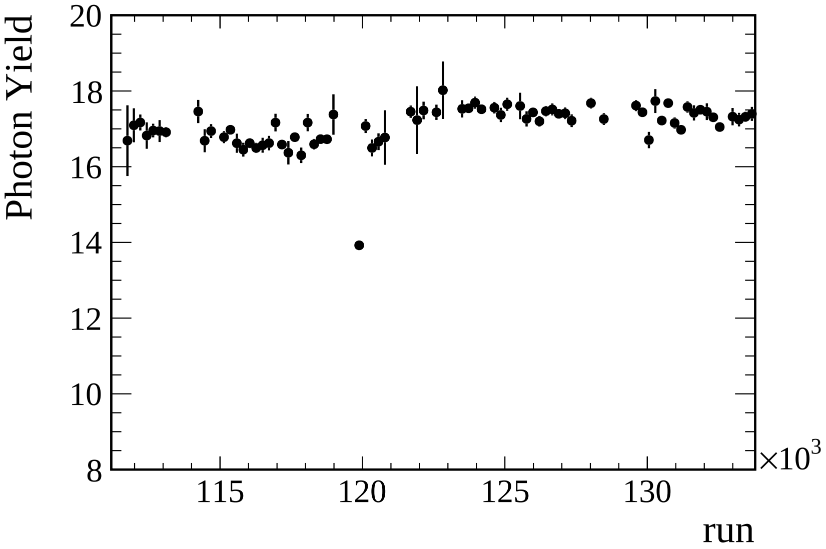

Figure 3.13: Time dependence on N_{pe} during 2012. (Top) C_4F_{10} radiator in RICH 1. (Bottom) CF_4 radiator in RICH 2.

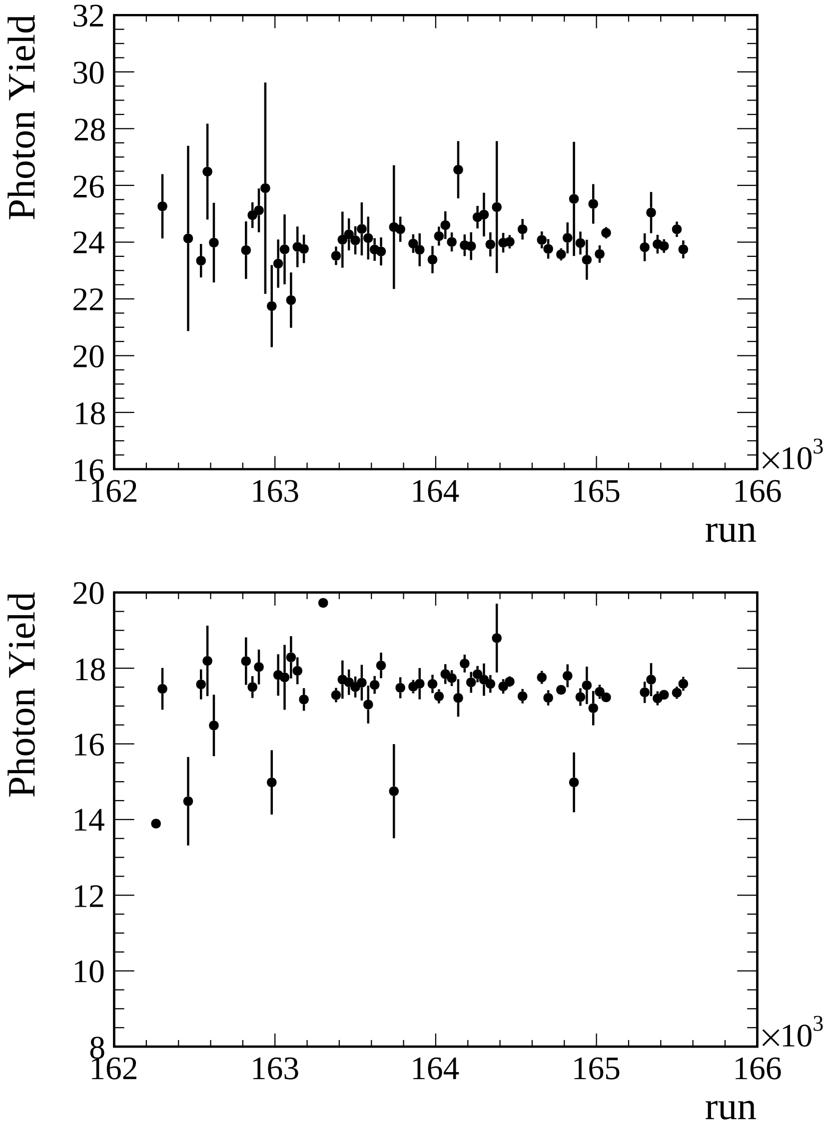

Figure 3.14: Time dependence on N_{pe} during 2015. (Top) C_4F_{10} radiator in RICH 1. (Bottom) CF_4 radiator in RICH 2.

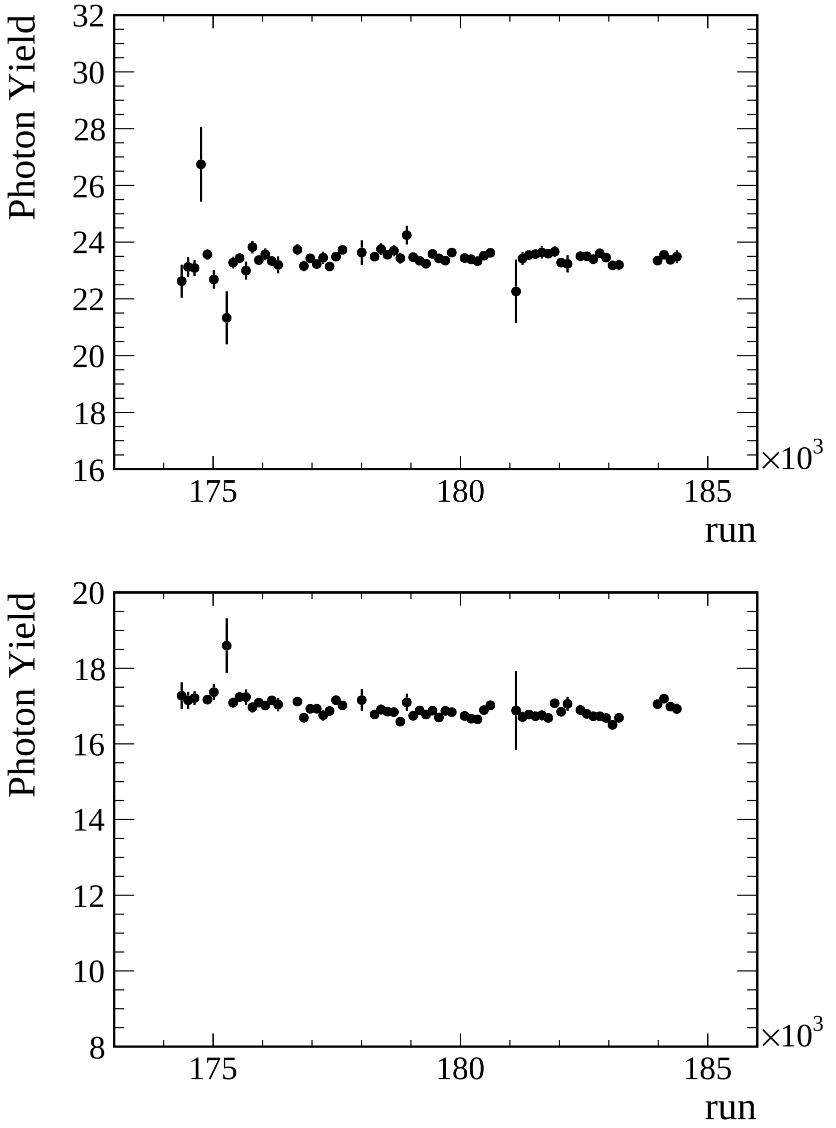

Figure 3.15: Time dependence on N_{pe} during 2016. (Top) C_4F_{10} radiator in RICH 1. (Bottom) CF_4 radiator in RICH 2.

3.4.4 Separation of HPD Boxes

RICH 1 Results

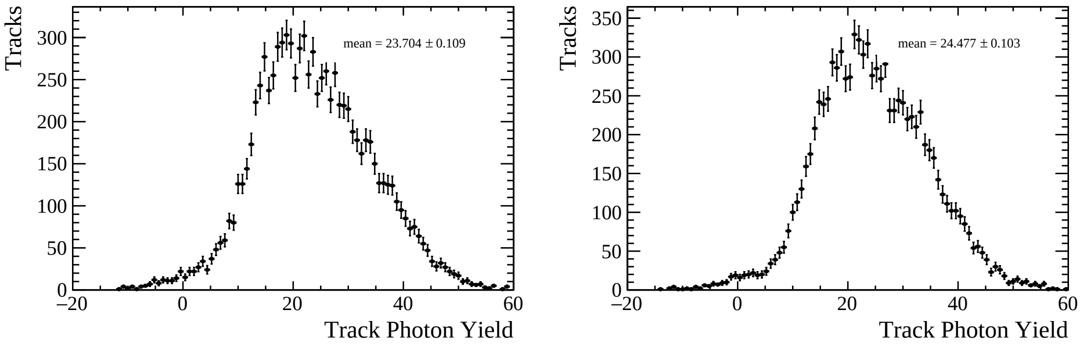

Figure 3.16: Individual RICH 1 HPD box N_{pe} distributions for 2015 $pp \to pp\mu^+\mu^-$ data. (Left) Results for the Up HPD box with individual track resolution $\sigma = 1.84\,\mathrm{mrad}$. (Right) Results for Down HPD box with individual track resolution $\sigma = 1.65\,\mathrm{mrad}$.

The photoelectron yield for the individual HPD boxes in RICH 1 was measured to be 23.70 ± 0.11 and 24.48 ± 0.10 for the Up and Down box respectively. This is shown in Figure 3.16. The mirrors on the Up box have a small amount of dust on their surface, and the small difference in N_{pe} can be seen.

RICH 2 Results

The photoelectron yield for the individual HPD boxes in RICH 2 was measured to be 13.42 ± 0.06 and 13.49 ± 0.05 for the A and C box respectively. This is shown in Figure 3.17. The two N_{pe} measurements agree within 1 standard deviation illustrating the left-right symmetry of RICH 2.

3.5 Summary

To summarise, this chapter has described the analysis method and the results for measurements of the photoelectron yields of the RICH using run 1 and run 2 data. Tables 3.1-3.2 show all the N_{pe} results for both run 1 and run 2 pp collisions. N_{pe} from pion tracks originating from D^* tagged $D^0 \to K^-\pi^+$ events are listed with and without the geometric

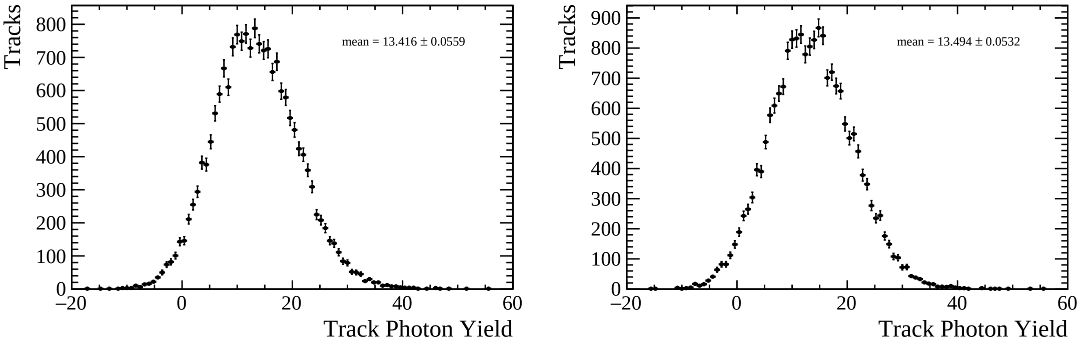

Figure 3.17: Individual RICH 2 HPD box N_{pe} distributions for 2015 $pp \to pp\mu^+\mu^-$ data. (Left) Results for the A HPD box with individual track resolution $\sigma = 0.65$ mrad. (Right) Results for C HPD box with individual track resolution $\sigma = 0.65$ mrad.

Track Species	Run Year	Photoelecton Yeild, N_{pe}
μ	2012 data	21.79 ± 0.06
μ	2015 data	24.20 ± 0.07
μ	2016 data	23.54 ± 0.04
π	2012 data	19.86 ± 0.03
π with $\epsilon_{geom} > 0.5$	2012 data	21.39 ± 0.04
π	2012 MC	19.80 ± 0.08
π with $\epsilon_{geom} > 0.5$	2012 MC	21.77 ± 0.09
π	2015 data	22.61 ± 0.02
π with $\epsilon_{geom} > 0.5$	2015 data	26.94 ± 0.02

Table 3.1: Comparison of C_4F_{10} RICH 1 N_{pe} measurements for different track types and different data taking years. All quoted errors are statistical.

efficiency requirement. All the results from muon tracks have $\epsilon_{geom} > 0.5$ applied. For the 2012 high track multiplicity pion events both Monte Carlo and data measurements are studied, the photon yield results agree with each other, in particular for RICH 1 where they are within 1 standard deviation from each other. A study on the time dependence of the photoelectric yield was performed, which showed no drop in N_{pe} over an extended time period for run 2. For the 2015 low-multiplicity muon tracks, the boxes of both RICH 1 and RICH 2 where analysed independently. N_{pe} for the Up and Down HPD boxes in RICH 1 show a small variation and N_{pe} for the A and C HPD boxes in RICH 2 showed no appreciable difference.

The RICH 1 N_{pe} measurement increased between run 1 and run 2 by ~ 3 photoelec-

Track Species	Run Year	Photoelecton Yeild, N_{pe}
μ	2012 data	14.28 ± 0.04
μ	2015 data	13.83 ± 0.04
μ	2016 data	13.08 ± 0.02
π	2012 data	13.74 ± 0.04
π with $\epsilon_{geom} > 0.5$	2012 data	15.31 ± 0.04
π	2012 MC	14.39 ± 0.09
π with $\epsilon_{geom} > 0.5$	2012 MC	15.76 ± 0.10
π	2015 data	12.02 ± 0.01
π with $\epsilon_{geom} > 0.5$	2015 data	13.45 ± 0.01

Table 3.2: Comparison of CF_4 RICH 2 N_{pe} measurements for different track types and different data taking years. All quoted errors are statistical.

trons and the RICH 2 N_{pe} measurement remains approximately the same between run 1 and run 2. The photoelectron yield directly affects the LHCb PID algorithm, the results of this study suggest that there should be no deterioration on the PID performance caused by N_{pe}.

Monitoring of the photoelectron yield is needed to continue for the remainder of run 2 and for the high luminosity upgrade. A study similar to this one, which measures N_{pe} with processed offline data, or with live online monitoring at the LHCb control room will be required for 2017 and 2018 data taking. The levels of dust on RICH 1 mirrors could increase, therefore studies on the individual HPD boxes must also continue.

Chapter 4

$B \to h^+h^{'-}$ Event Selection

4.1 Introduction

The analysis described in this chapter uses the combined 2011 and 2012 (run 1) LHCb data sets, which have a total integrated luminosity of 3 fb^{-1}. To be able isolate $B \to h^+h^{'-}$ events from the full data set selections are applied onto the data. These selections are described in this chapter.

4.2 Trigger

Selection Type	Selection
$h^{\pm}$ daughter	Impact parameter, $IP > 2mm$ $\chi^2/ndf < 3$
$h^+h'^-$ combination	4700 MeV/c^2 $< m_{comb} <$ 5900 MeV/c^2
B mother	$p_T > 1200$ MeV/c $\tau_B > 0.6$ ps $IP < 0.12$mm

Table 4.1: Requirements in the second level software trigger for the `HLT2B2HH` line used to select $B \to h^+h^{'-}$ candidates.

The LHCb trigger system was described in section 2.2.7. In general, all triggered events can be split into two categories, triggered on signal (TOS) or triggered independent of signal (TIS). If the event is TOS then the event is triggered only if particles that belong to the signal candidates are present and if the event is TIS then it passes the trigger without particles in the signal candidates. There are three trigger stages L0, HLT1 and HLT2. As the data taking progressed, the trigger definitions where modified slightly to account for variations in running conditions, therefore it is worth noting that some of the numbers quoted for the trigger selections in the section were varied slightly over time. A full description of the trigger conditions used for Run 1 is in Reference [77].

For the $B \to h^+h^{'-}$ candidate to be selected, the triggers chosen are:

$$\begin{gathered}(\texttt{L0Global\_TIS} = 1 \text{ OR } \texttt{L0Hadron\_TOS} = 1) \\ \texttt{AND} \\ \texttt{HLT1TrackAllL0\_TOS} = 1 \\ \texttt{AND} \\ \texttt{HLT2B2HHDecisionL0\_TOS} = 1,\end{gathered}$$

where the L0 trigger line `L0Global` selects events that pass any of the multiple L0 triggers. `L0Hadron` selects decays with hadronic final states, its criteria requires SPD multiplicity < 600 and hadron transverse energy $E_T > 3620\,\text{MeV}$. To simplify the detector acceptance correction, a single HLT1 and HLT2 line combination was chosen. The `HLT1TrackAllL0` line evaluates a single high momentum track originating from a heavy particle (B, D, τ), the selections are: VELO missing hits < 3, the number of hits in the track > 16, track momentum $p > 3\,\text{GeV}/c$, the track transverse momentum, $p_T > 1.6\,\text{GeV}/c$ and the χ^2 per degree of freedom of the track fit, $\chi^2/ndof < 2$. The `HLT2B2HHDecisionL0` is designed to select two-body charmless hadronic decays, the selections are given in table 4.1.

4.3 Stripping

The next selection stage is a pre-selection known as Stripping, which was previously mentioned in 2.2.8, in LHCb this is performed centrally for several categories of decays to optimise use of computing resources. The Stripping line used for the $B \to h^+h^{'-}$ lifetime analysis is called `Hb2Charged2BodyB2Charged2BodyLine` and the selections are listed in Table 4.2. The selections include requirements on the invariant mass and transverse momentum of the mother particle (the b hadron), daughter transverse momentum and ghost probability of daughter tracks. There are also selections that are know to affect decay time acceptance such as the selection requiring a mother decay time of greater than 0.6 ps.

Selection Type	Selection
Daughter Selections	$\min(p_T^{h^+}, p_T^{h'^-}) > 1100$ MeV/c $\min(IP(h^+), IP(h'^-)) > 0.15$ mm `OR` $\min(IP\chi^2(h^+), IP\chi^2(h'^-)) > 100$ $\max((\text{Track } \chi^2/\text{nDOF})^{\text{h}^+}, (\text{Track } \chi^2/\text{nDOF})^{\text{h}'^-}) < 3$ $\max((\text{Track GhostProb})^{\text{h}^+}, (\text{Track GhostProb})^{\text{h}'^-}) < 0.8$
Combination Selections	4600 MeV/c$^2 < m_{comb} < 6000$ MeV/c^2 $\max(IP(h^+), IP(h'^-)) > 0.27$ mm `OR` $\max(IP\chi^2(h^+), IP\chi^2(h'^-)) > 200$ $\max(p_T > 2700$ MeV/$c)$ DOCA < 0.08 mm
Mother Selections	4800 MeV/c$^2 < m_B < 5800$ MeV/c^2 $p_T^B > 1200$ MeV/c $\tau_B > 0.6$ ps $IP(B) < 0.08$ mm OR $IP\chi^2(B) < 12$

Table 4.2: Selection requirements of the `Hb2Charged2BodyB2Charged2BodyLine` stripping line for $B \to h^+h^{'-}$ candidates. Impact parameter, IP, is the minimum distance of the track to a primary vertex (PV) and $IP\chi^2$ is the χ^2 of the impact parameter. DOCA stands for distance of closest approach between two particles and GhostProb is the probability the track is a ghost track.

4.4 Offline Selection

After the data passed the trigger and stripping selections, an offline selection is applied to the events, increasing the significance of the $B \to h^+h^{'-}$ signal against background. The offline selection consists of a kinematic selection and particle identification (PID) selections. The kinematic selection described in Section 4.4.2 was optimised to select $B_s^0 \to K^+K^-$ candidates on 2012 data. The particle identification (PID) selection separates between the final states, i.e. K^+K^-, $K^+\pi^-$, $\pi^+\pi^-$, $p\pi^-$and pK^- allowing individual $B \to h^+h^{'-}$ channels to be accessed. The kinematic differences between the $B \to h^+h^{'-}$ decay modes are small and hence the same selection was applied to all decay modes.

The PID selections were optimised first and then the kinematic selection was performed. This was done to improve the kinematic selections by evaluating only candidates that pass the K^+K^- PID requirements. After this, the PID selection efficiencies were re-evaluated with the kinematic selections also applied.

4.4.1 Particle Identification Selection

Particle identification (PID) selections were applied to the data to separate between the daughter particles of the final states.

DLL is the difference in log-likelihood of a particle species hypothesis, i.e. $DLL_{K\pi}$ is the log-likelihood of the kaon hypothesis minus the log-likelihood of the pion hypothesis. A data-driven approach was used to evaluate the efficiencies of PID selections, which uses calibration data samples of pure kaons, pions, protons, muons and electrons [78]. This is done as PID variables are known to be modelled inaccurately in Monte Carlo. The cause of the inaccuracy in MC in unknown. PID variables such as DLL can be parameterised by other variables, such as track momentum, which are modelled well by MC. By binning a calibration sample in these well modelled variables the efficiency of a PID selection on a track in the MC sample can be determined.For the $B \to h^+ h^{'-}$ analysis the variables used to parameterise the PID variable DLL were track momentum p and pseudorapidity η. The PID selections used to separate between final states are in Table 4.3, these selections are applied on both 2012 and 2011 data. The efficiencies ϵ of these selections predicted by the calibration datasets are given in Tables 4.4-4.6, where ω represents the probabilities of misidentified two-body backgrounds predicted using the calibration data samples and k represents scaling factors that link the signal fraction to the misidentified background rates.

The scaling factors were calculated with the expression

$$k_{hh'}^{background} = \frac{f_{background}}{f_{signal}} \frac{\mathcal{B}_{background}}{\mathcal{B}_{signal}} \frac{\omega_{hh'}^{background}}{\varepsilon_{hh'}^{signal}}, \tag{4.1}$$

where $signal$ stands for signal channel, $background$ stands for background channel, f is the hadronisation fraction of the mother particle in the decay, $\mathcal{B}$ is the branching fraction of the decay, $\omega^{background}$ is the misidentification probability and ε^{signal} is the signal efficiency in the hh' final state hypothesis. These numbers were determined with 2012 MC.

Final State	Track Hypothesis	Selection
K^+K^-	Kaon	$DLL_{K\pi} >$ 5.0
		$DLL_{Kp} >$ 0.0
		$DLL_{Ke} >$ 0.0
		$DLL_{K\mu} >$ -1.0
$K^+\pi^-$	Kaon	$DLL_{K\pi} >$ 5.0
		$DLL_{Kp} >$ 0.0
		$DLL_{Ke} >$ 0.0
		$DLL_{K\mu} >$ -1.0
	Pion	$DLL_{K\pi} <$ -4.0
		$DLL_{p\pi} <$ 3.0
		$DLL_{e\pi} <$ 0.0
		$DLL_{\mu\pi} <$ 1.0
$\pi^+\pi^-$	Pion	$DLL_{K\pi} <$ -4.0
		$DLL_{p\pi} <$ 3.0
		$DLL_{e\pi} <$ 5.0
		$DLL_{\mu\pi} <$ 5.0
pK^-	Proton	$DLL_{p\pi} >$ 3.0
		$DLL_{pK} >$ 5.0
		$DLL_{pe} >$ 0.0
		$DLL_{p\mu} >$ 0.0
	Kaon	$DLL_{K\pi} >$ 5.0
		$DLL_{Kp} >$ 0.0
		$DLL_{Ke} >$ 0.0
		$DLL_{K\mu} >$ -1.0
$p\pi^-$	Proton	$DLL_{p\pi} >$ 3.0
		$DLL_{pK} >$ 9.0
		$DLL_{pe} >$ 0.0
		$DLL_{p\mu} >$ 0.0
	Pion	$DLL_{K\pi} <$ -4.0
		$DLL_{p\pi} <$ 3.0
		$DLL_{e\pi} <$ 5.0
		$DLL_{\mu\pi} <$ 5.0

Table 4.3: The PID selections applied to the LHCb Run 1 data sample.

$B_s^0 \to K^+K^-$	
Channel	
ε [%]	
$B_s^0 \to K^+K^-$	56.03 ± 0.07
ω [%]	
$\pi^+\pi^-$	0.029 ± 0.0006
$K^+\pi^-$	1.26 ± 0.02
pK^-	2.44 ± 0.39
$p\pi^-$	0.0529 ± 0.0090
k	
$B_s^0 \to \pi^+K^-$	0.50 ± 0.06
$B_s^0 \to \pi^+\pi^-$	(1.59 ± 0.41)x10^{-3}
$B^0 \to K^+\pi^-$	6.85 ± 0.62
$B^0 \to \pi^+\pi^-$	(4.13 ± 0.41)x10^{-2}
$\Lambda_b^0 \to pK^-$	1.78 ± 0.45
$\Lambda_b^0 \to p\pi^-$	0.030 ± 0.008

$B^0 \to K^+\pi^-$	
Channel	
ε [%]	
$B^0 \to K^+\pi^-$	54.44 ± 0.13
ω [%]	
$\pi^+\pi^-$	1.19 ± 0.02
K^+K^-	0.91 ± 0.02
pK^-	1.14 ± 0.71
$p\pi^-$	2.33 ± 0.38
k	
$B_s^0 \to \pi^+K^-$	7.28 ± 0.82
$B_s^0 \to \pi^+\pi^-$	(4.48 ± 0.82)x10^{-2}
$B_s^0 \to K^+K^-$	1.12 ± 0.07
$B^0 \to \pi^+\pi^-$	1.12 ± 0.04
$\Lambda_b^0 \to pK^-$	0.31 ± 0.23
$\Lambda_b^0 \to p\pi^-$	0.50 ± 0.13

Table 4.4: (Left)$B_s^0 \to K^+K^-$ PID efficiencies and (right) $B^0 \to K^+\pi^-$ PID efficiencies, where ϵ is the signal efficiency, ω is the probability misidentified two-body backgrounds agree and k represents a scaling factor that links ϵ and ω.

$B^0 \to \pi^+\pi^-$	
Channel	
ε [%]	
$B^0 \to \pi^+\pi^-$	59.76 ± 0.14
ω [%]	
K^+K^-	(1.70 ± 0.08)x10^{-2}
π^+K^-	0.97 ± 0.03
pK^-	(3.67 ± 5.81)x10^{-2}
$p\pi^-$	2.01 ± 1.62
k	
$B_s^0 \to K^+K^-$	(3.58 ± 0.39)x10^{-2}
$B_s^0 \to \pi^+K^-$	0.45 ± 0.06
$B_s^0 \to \pi^+\pi^-$	3.84 ± 1.00
$B^0 \to K^+\pi^-$	6.24 ± 0.35
$\Lambda_b^0 \to pK^-$	(3.27 ± 5.22)x10^{-2}
$\Lambda_b^0 \to p\pi^-$	1.50 ± 1.24

Table 4.5: $B^0 \to \pi^+\pi^-$ PID efficiencies, where ϵ is the signal efficiency, ω is the probability misidentified two-body backgrounds agree and k represents a scaling factor that links ϵ and ω.

$\Lambda_b^0 \to p\pi^-$	
Channel	
ε [%]	
$\Lambda_b^0 \to p\pi^-$	61.95 ± 0.93
ω [%]	
K^+K^-	$(1.03 \pm 0.03) \times 10^{-2}$
π^+K^-	0.63 ± 0.02
$\pi^+\pi^-$	2.09 ± 0.01
pK^-	1.06 ± 0.04
k	
$B_s^0 \to K^+K^-$	0.102 ± 0.012
$B_s^0 \to \pi^+K^-$	0.66 ± 0.16
$B_s^0 \to \pi^+\pi^-$	0.60 ± 0.14
$B^0 \to K^+\pi^-$	8.84 ± 1.66
$B^0 \to \pi^+\pi^-$	15.16 ± 2.14
$\Lambda_b^0 \to pK^-$	1.14 ± 0.56

$\Lambda_b^0 \to pK^-$	
Channel	
ε [%]	
$\Lambda_b^0 \to pK^-$	66.60 ± 0.98
ω [%]	
K^+K^-	1.95 ± 0.02
π^+K^-	2.89 ± 0.02
$\pi^+\pi^-$	0.063 ± 0.001
$p\pi^-$	1.50 ± 0.04
k	
$B_s^0 \to K^+K^-$	14.38 ± 2.02
$B_s^0 \to \pi^+K^-$	2.33 ± 0.5
$B_s^0 \to \pi^+\pi^-$	$(1.41 \pm 0.31)\mathrm{x}10^{-2}$
$B^0 \to K^+\pi^-$	31.02 ± 5.69
$B^0 \to \pi^+\pi^-$	0.34 ± 0.04
$\Lambda_b^0 \to p\pi^-$	1.11 ± 0.50

Table 4.6: (Left) $\Lambda_b^0 \to p\pi^-$ PID efficiencies and (right)$\Lambda_b^0 \to pK^-$ PID efficiencies, where ϵ is the signal efficiency, ω is the probability misidentified two-body backgrounds agree and k represents a scaling factor that links ϵ and ω.

4.4.2 Kinematic Selection

A kinematic selection is applied to the data via the use of a multivariate algorithm (MVA). The Root package TMVA [79] was used to test and optimise multivariate analysis methods and to determine an optimum selection for the 2012 data. Although the MVA was trained on 2012 data it was also applied to the 2011 data as there is negligible difference in the kinematics of these two datasets.

The TMVA package contains many supervised learning algorithms including a rectangular cut optimisation, a projective likelihood, linear discriminant analysis, non-linear discriminate analysis, boosted decision trees [80, 81] and artificial neural networks. The process for using all algorithms in the package is the same. Firstly, a classification stage is used with an input predicted signal and predicted background followed by an application stage, where the trained output is applied to data.

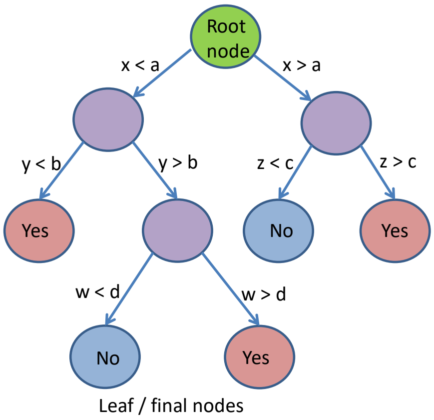

Figure 4.1: Graphical representation of a decision tree. A binary decision is made at each node until the final decision of yes or no is reached.

A gradient boosted decision tree (BDTG [80, 81]) was chosen for the kinematic selection of the $B \to h^+h^{'-}$ lifetime analysis. Decision trees are a common tool in multivariate analysis, they use a tree like structure shown in Figure 4.1. Starting from a root node, a binary decision is made based on the training of the decision tree. After a series of decisions and intermediate nodes, the algorithm reaches the final nodes (or leaf nodes), which represent the final classification, i.e. signal or background, yes or no. A boosted decision tree (BDT) is made up of many decision trees known as a forest of decision trees. Each decision tree uses a binary structure to classify a data sample and multiple decision trees in the forest reduce effects of fluctuations in the training sample. This is achieved by each tree being trained on the same sample and then combined to form a single classification method. The gradient boosting technique is fully described in Reference [79].

For the $B \rightarrow h^+h^{'-}$ lifetime analysis, the training data consisted of two samples; a signal and a background data set. The signal data set was LHCb 2012 Monte Carlo (MC12) $B_s^0 \rightarrow K^+K^-$ simulated events, a description of LHCb MC is in section 2.2.8. The background data sample was of a sample of the 2012 LHCb data. The background data sample was the upper mass sideband ($5500\,\text{MeV}/c < m_B < 5800\,\text{MeV}/c$) of the data which was reconstructed under the K^+K^- final state hypothesis and therefore outside the $B_s^0 \rightarrow K^+K^-$ signal peak range. The lower mass sideband was not used, as it is known to contain physics backgrounds. Both signal and background data sets have the trigger and stripping selections applied. In addition, the PID selection for the K^+K^- final state of $DLL_{K\pi}$ >5, DLL_{Kp} >0, DLL_{Ke} >0 and $DLL_{K\mu}$ >-1 are also applied onto the daughter particles of both samples.

Eight input variables where chosen to train the BDTG, their distributions are shown in Figure 4.2. The variables are:

1. the log distribution of the mother $IP\chi^2$ (labelled B_s0_IPChi2_Log_var);
2. the cosine of the angle between the flight path and the momentum vector of the reconstructed the B_s^0 (labelled B_s0_DIRA_var);
3. the distribution of the minimum daughter particle transverse momentum p_T found by comparing the K^+ and K^- and selecting the lowest p_T, $\min((p_T^{K^+}), (p_T^{K^-}))$ (labelled daughter_minPT_var);
4. the log distribution of the minimum daughter $IP\chi^2$ found from $\min(\, (IP\chi^2)^{K^+}, (IP\chi^2)^{K^-})$ (labelled daughter_minIPchi2_Log_var);
5. the log distribution of the minimum Trackχ^2/nDOF for the daughter is obtained from $\min(\, (\text{Track}\chi^2/\text{nDOF})^{\text{K}^+}, (\text{Track}\chi^2/\text{nDOF})^{\text{K}^-})$ (labelled daughter_minTrack_Log_var);
6. the distribution of the maximum daughter p_T found with $\max((p_T^{K^+}), (p_T^{K^-}))$ (labelled daughter_maxPT_var);

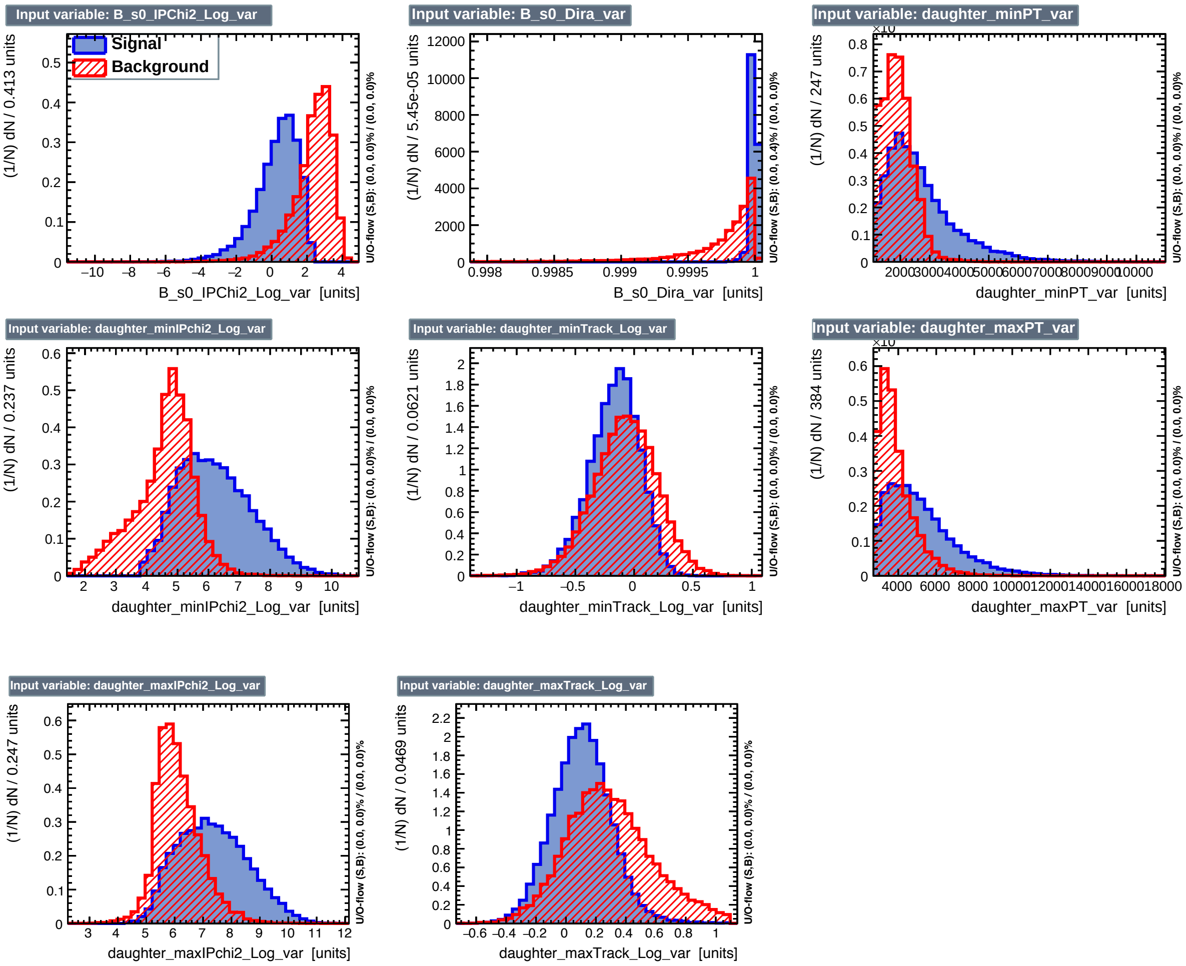

Figure 4.2: Signal (blue) and background (red) kinematic variable distributions used in TMVA training.

7. the log distribution of the maximum daughter $IP\chi^2$ found from max($(IP\chi^2)^{K^+}, (IP\chi^2)^{K^-}$) (labelled daughter_maxIPchi2_Log_var);

8. the log distribution of the maximum Trackχ^2/nDOF for the daughter is obtained from max($(\text{Track}\chi^2/\text{nDOF})^{\text{K}^+}, (\text{Track}\chi^2/\text{nDOF})^{\text{K}^-}$) (labelled daughter_maxTrack_Log_var).

Figure 4.3 shows the percentage correlations between input variables used to train the BDTG, where the variables are listed in the same order as described previously.

To avoid the bias created when the same data is used in the classification and ap-

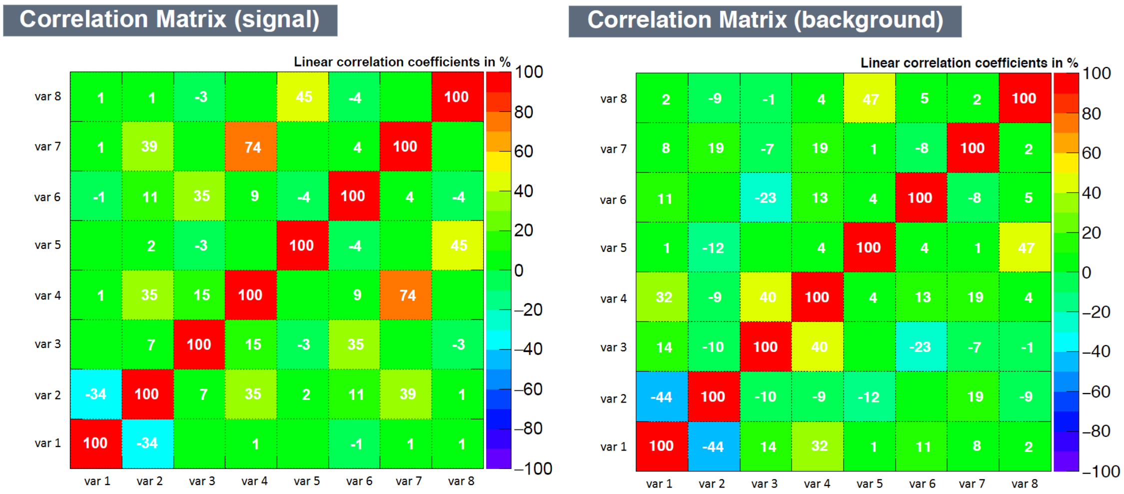

Figure 4.3: Percentage correlations between the input variables in the (left) the signal data set and (right) the background data set.

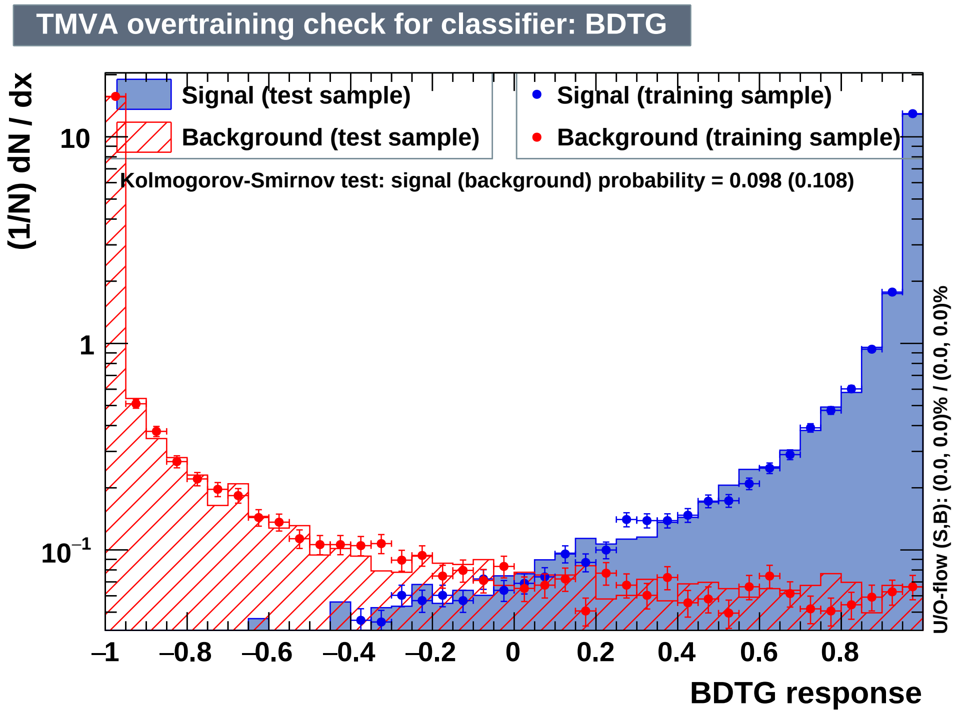

Figure 4.4: Normalised probability distributions of the signal (blue) and the background (red) BDTG response.

plication of a multivariate algorithm; the data sets were split in two by even/odd event number. One half is used in the training of the MVA methods and this trained classifier was then applied on the other half of the data and vice versa. This approach means that none of the data needed to be discounted in the rest of the analysis. The response from the BDTG is seen in Figure 4.4, which shows no overtraining.

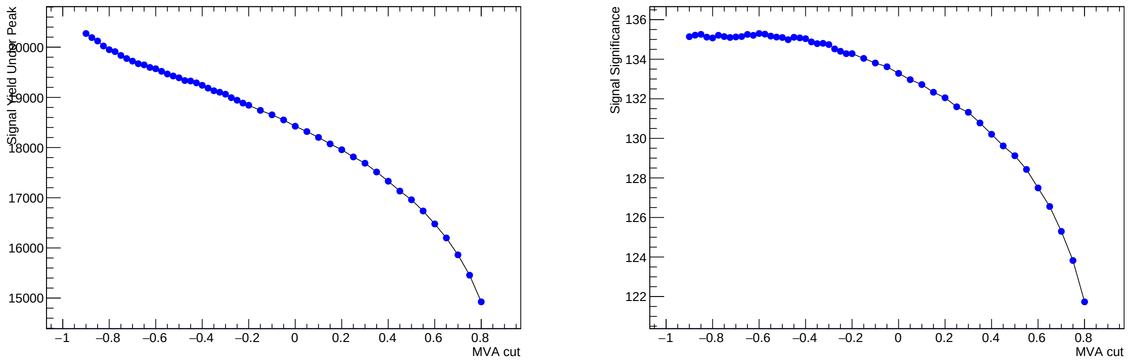

Figure 4.5: Signal yield (left) and signal significance (right) over varying selection on MVA response.

To optimise the selection, a figure of merit is used to calculate how clean the signal is, this is the signal significance

$$\text{Signal significance} = \frac{\mathrm{S}}{\sqrt{\mathrm{S}+\mathrm{B}}}, \tag{4.2}$$

where S is the number of signal events and B is the number of background events in the mass range under the signal peak (this is $+60\,\mathrm{MeV}/c$ and $-100\,\mathrm{MeV}/c$ around the mean of the mass signal peak). The optimal cut-off point is when the signal significance has a maximum value. Figure 4.5 shows how the signal yield (left) and signal significance (right) varied with selection on MVA response. The signal significance is approximately flat for selections on BDTG response between > -0.90 and > -0.40. To maximise the yield within this plateau whilst avoiding the edge a selection of > -0.80 was chosen. This selection was used for both even and odd event number MVAs as there are negligible differences in their responses.

The $B \to h^+h^{'-}$ invariant mass spectrum under the K^+K^-hypothesis for the 2012 data set resulting from a selection on the BDTG response alone is shown in Figure 4.6, with no PID selections and no requirements on the trigger decisions applied to this data.

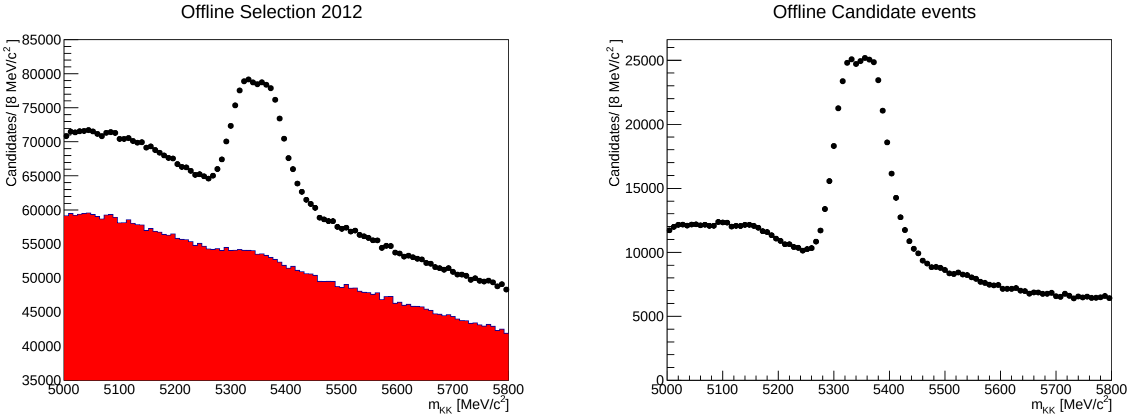

Figure 4.6: $B \rightarrow h^{+}h^{'-}$ invariant mass spectrum reconstructed as the $K^{+}K^{-}$final state, (left) before and (right) after the MVA selection is applied. On the left-hand plot candidates rejected by the selection on BDTG response of > -0.80 are illustrated red. These plots show the 2012 data set with no PID selections and no requirements on the trigger decisions.

4.5 Summary

To summarise, this chapter has described the event selection process used to select $B \rightarrow h^{+}h^{'-}$ candidates from the run 1 LHCb data set. This included a preselection and offline event selections. The offline event selections included trigger selections, kinematic selections with the use of a BDTG and particle identification selections to separate between final daughter states.

Chapter 5

Lifetime Determination Method

5.1 Introduction

In general the lifetime of a particle is described with an exponential distribution, but in practice this becomes more complicated due to experimental effects. A b hadron candidate event is selected based on a signal final state hypothesis and this leads to multiple backgrounds that dilute the signal purity. All backgrounds must be taken into account, this makes a lifetime measurement more complicated. In the $B \to h^+h^{'-}$ lifetime analysis, the invariant mass distributions are used to separate between the signal events and background events, this is discussed in Section 5.2. The reconstruction and selection efficiency varies with decay-time due to a bias introduced by event selections on the data sample and this is known as decay-time acceptance. The method used to evaluate this bias is discussed in Section 5.3. The decay-time distribution of $B \to h^+h^{'-}$ events is affected by resolution effects and detector acceptance effects. These effects are included into the fit of the decay-time distribution and this is discussed in Section 5.4. The fitter used in the $B \to h^+h^{'-}$ lifetime analysis is verified with data from a simplified MC generator or pseudo-experiments, and LHCb MC. This verification is discussed in Section 5.5.

5.1.1 Method of Lifetime Fitting

To measure the lifetime of a specific $B \to h^+h^{'-}$ channel, known as the signal channel, all background channels must be considered. To identify the signal candidates from the other events the invariant mass spectrum is used. The fit method has two components:

1. A fit of the invariant mass distribution with all possible backgrounds taken into account.
2. A fit of the decay-time distribution, where the fractions of the signal channel and background channels have been extracted from the results of the mass fit.

This method is performed by utilising a probably density function (PDF) parametrised by a set of observables to fit to a data sample. With the observables decay-time t, acceptance parameter A and mass of the particle m, a PDF can be written as

$$f(t, A, m) = f(t, A|m) \cdot f(m), \tag{5.1}$$

where the particle mass is the discriminating variable between the signal classes as it is independent of decay-time. The PDF $f(m)$ is found with the first part of the fit method. For a given data sample, a fit modelling the invariant mass spectrum can be made up of a sum of the individual components modelling each signal and background class. Therefore $f(m)$ can be expressed as

$$f(m) = \sum_{class} f(m|class) \cdot P(class), \tag{5.2}$$

where $f(m|class)$ is the mass PDF for an individual class and $P(class)$ is the probability of a candidate belonging to that class. With Bayes theorem, the probability of a signal candidate being in a class is

$$P(class|m) = \frac{f(m|class) \cdot P(class)}{f(m)}, \tag{5.3}$$

The first term of 5.1 can also be expanded

$$f(t, A|m) = \sum_{class} f(t, A|class) \cdot P(class|m). \tag{5.4}$$

The PDF describing the time can be written as

$$f(t, A|class) = f(t|A, class) \cdot f(A|class), \tag{5.5}$$

where $f(t|A, class)$ is the PDF of the decay-time given the acceptance function and class and $f(A|class)$ is the PDF of the acceptance function given the class.

The PDF for the lifetime fit becomes

$$f(t, A|m) = \sum_{class} f(t, A|class) \cdot f(A|class) \cdot \frac{f(m|class) \cdot P(class)}{f(m)}. \tag{5.6}$$

Equation 5.6 is used in the second part of the fit process, where the $P(class)$, $f(m|class)$ and $f(m)$ has been determined by a fit to the invariant mass spectrum, which is described in Section 5.2. After the acceptance function term, $f(A|class)$, is evaluated it is input into the decay-time fit. The acceptance function is detailed in Section 5.3 and the fit to the decay-time distribution is detailed in Section 5.4.

5.1.2 Maximum Likelihood Method for Parameter Optimisation

The mass and time fits are performed with an algorithm that is based on an un-binned maximum likelihood technique. For a PDF, $f(x)$, with multiple parameters, the maximum likelihood method chooses values of the parameters that maximises the likelihood function. The likelihood function can be written as

$$\mathcal{L}(\vec{\theta}; x_1, ..., x_N) = \prod_{i=1}^{N} f(x_i|\vec{\theta}), \tag{5.7}$$

where $\vec{\theta} = \{\theta_1, \theta_2, ...\}$ is a vector containing unknown parameters in a model and x_i represent the measured observables for a sample sized N.

The $B \rightarrow h^+h^{'-}$ analysis uses a modification of this method, where the logarithm of the likelihood function or log-likelihood function is maximised. The log-likelihood function can be written as

$$\ln \mathcal{L}(\vec{\theta}; x_1, ..., x_N) = \sum_{i=1}^{N} \ln f(x_i|\vec{\theta}). \tag{5.8}$$

The parameter optimisation is performed in the fits using the Minuit Package [82], which varies the parameter values then calculates the rate of change of the log-likelihood function to determining the parameter value that yields a maximum log-likelihood.

5.1.3 sWeights

The mass fit is used to discriminate between the signal and background classes in the time fit and this is achieved with candidate probability weightings. This is performed with the *sPlot* technique [83], which works by taking the discriminating variable, in this case the mass m, and determining the probability of a candidate belonging in a class for a control variable distribution. In this analysis the control variable is the decay-time t. The control variable and the discriminating variable are uncorrelated.

The log-likelihood for a data sample containing several classes can be written as

$$\ln \mathcal{L} = \sum_{e=1}^{N} \ln \Big\{ \sum_{i=1}^{N_s} N_i f_i(y_e) \Big\} - \sum_{i=1}^{N_s} N_i, \tag{5.9}$$

where N is the number of candidates in the sample, N_s is the number of different classes, N_i is the number if candidates expected in the i^{th} class, y is the set of discriminating, variables, y_e is the value of y for candidate e and f_i is the PDF of the i^{th} class.

A covariance matrix can be defined with the second derivative of the log-likelihood function:

$$\mathbf{V}_{nj}^{-1} = \frac{\partial^2(-\ln \mathcal{L})}{\partial N_n \partial N_j} = \sum_{e=1}^{N} \frac{f_n y_e f_j y_e}{(\sum_{k=1}^{N_s} N_k f_k(y_e))^2} \tag{5.10}$$

The final event weight, known as *sWeight* is defined as

$${}_s\mathcal{P}_n(y_e) = \frac{\sum_{j=1}^{N_s} \mathbf{V}_{nj} f_j(y_e)}{\sum_{k=1}^{N_s} N_k f_k(y_e)}. \tag{5.11}$$

If *sWeights* are used as a candidate weight when determining the distribution of a variable, they recover the original distributions of each signal class, provided that the control and discriminating variables are uncorrelated.

5.2 Fitting the Invariant Mass Spectrum

The invariant mass distributions for the final states K^+K^-, $K^+\pi^-$, $\pi^+\pi^-$, pK^- and $p\pi^-$ are fitted individually with maximum likelihood fits, which was described earlier. The fit to each invariant mass spectrum is performed on the combined 2011 and 2012 dataset. The parameters of the mass fits are listed in Appendix C.

5.2.1 Mass Model

Signal and background classes that contribute to each mass spectrum are included in the total fit to the invariant mass distribution. Some of the backgrounds lie directly underneath the $B \to h^+h^{'-}$ signals and need to be modelled accurately to ensure an accurate lifetime measurement. Because of this, Monte-Carlo data has been used to determine the shape of the mass models. The 2012 MC used is listed in Appendix D.

$B \to h^+h^{'-}$ Signal Classes

All $B \to h^+h^{'-}$ signal modes are modelled with a double crystal ball function (DCB) except the $B^0 \to K^+K^-$ signal. An individual crystal ball function [84] is given by the expression

$$f(x;\alpha,n,\overline{x},\sigma) = N \cdot \begin{cases} \exp(-\frac{(x-\overline{x})^2}{2\sigma^2}) & \text{if } \frac{x-\overline{x}}{\sigma} > -\alpha \\ A \cdot (B - \frac{x-\overline{x}}{\sigma}) & \text{if } \frac{x-\overline{x}}{\sigma} \leq -\alpha \end{cases}, \tag{5.12}$$

where

$$A = \Big(\frac{n}{|\alpha|}\Big)^n \cdot \exp\Big(-\frac{|\alpha^2|}{2}\Big)$$

$$B = \frac{n}{|\alpha|} - |\alpha|, \tag{5.13}$$

where μ is the mean of the Gaussian central component, σ is the width of the Gaussian central components and α and n are parameters of the power-law tail component. The DCB comprises of two crystal ball functions with a shared mean, μ, and sigma, σ. The DCB has tail components in the upper and lower regions around the central mass peak, $\alpha_{CBL}, n_{CBL}, \alpha_{CBH}$ and n_{CBH}, which are fixed to values determined by 2012 MC. Fits of DCB functions to 2011 MC data were also performed and these fits showed that the DCB parameters in 2012 MC and 2011 MC agreed to three standard deviations in most cases. Examples of fits to the simulated $B \to h^+h^{'-}$ MC data are shown in Figure 5.1, which show the radiative tails in the data where mass regions that are lower and higher than the central peak are well described by the fit. Mass distributions were fit with DCB functions for all $B \to h^+h^{'-}$ signal classes and the values of the fitted tail parameters are in Appendix D.

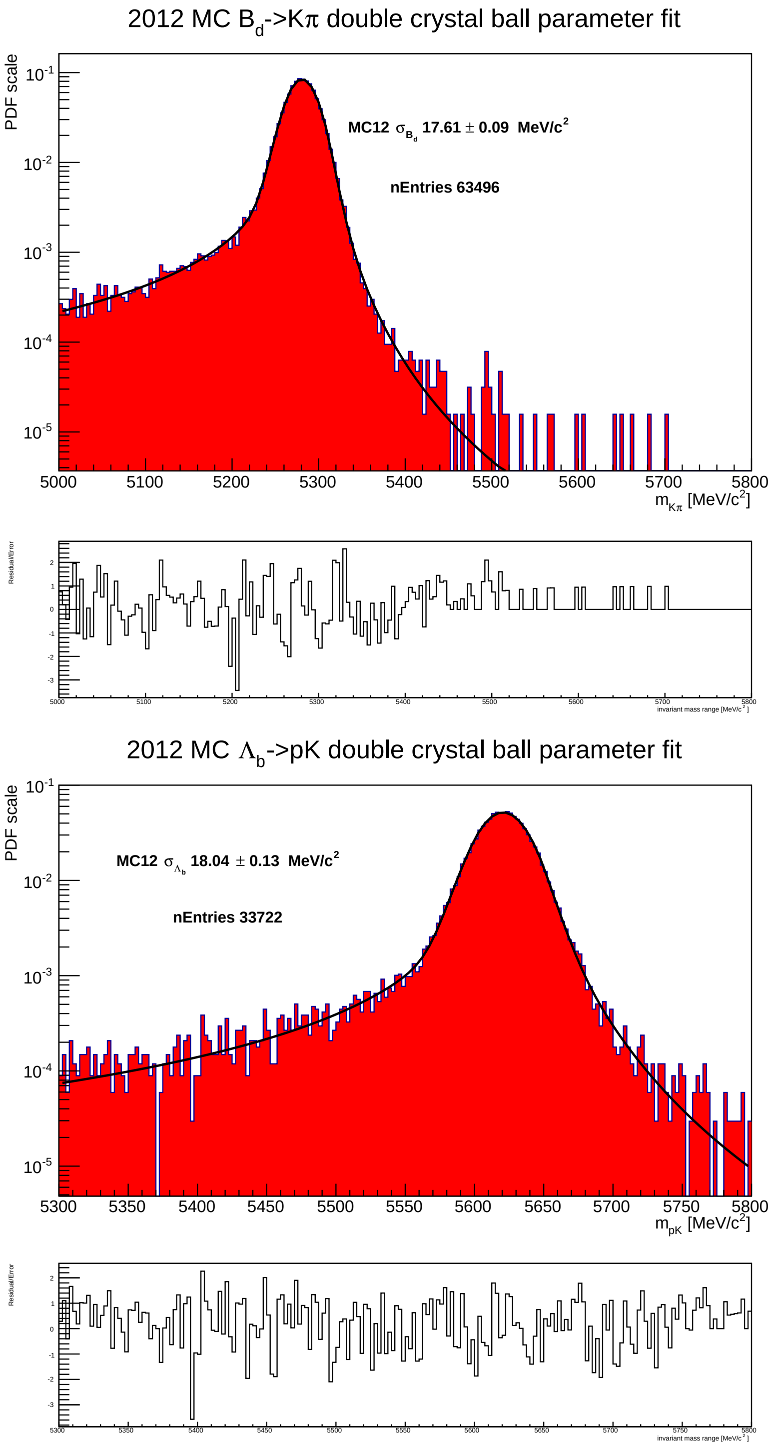

Figure 5.1: Mass distributions and residuals of double crystal ball functions fit to $B^0 \to K^+\pi^-$ and $\Lambda_b^0 \to pK^-$ 2012 MC after full event selection

Due to the small number of events expected for the $B^0 \to K^+K^-$ signal channel, this is treated differently to the other $B \to h^+h^{'-}$ signal channels. The $B^0 \to K^+K^-$ shape is modelled with a non parametric shape extracted from MC.

Misidentified Two-body Backgrounds

The two-body backgrounds arise from $B \to h^+h^{'-}$ candidates when one or more final state particle has a misidentified PID assignment. In the invariant mass fit, these backgrounds are modelled with non-parametric distributions where the shapes are extracted from 2012 MC. The MC is reconstructed under the signal channel hypothesis and has the full event selection applied for the signal channel final state. The selected MC distributions are smeared to create a smooth PDF to model the misidentified mass shapes. The smearing is performed with the kernel method [85], which is described in more detail later in Section 5.4.1

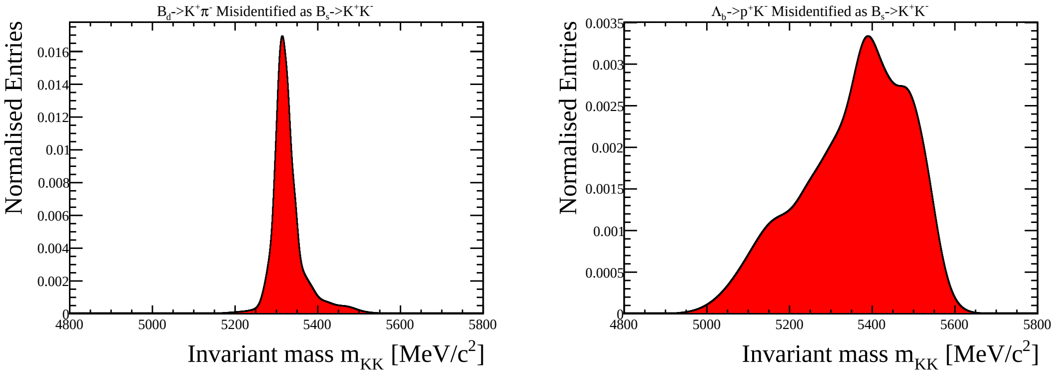

Figure 5.2: Examples of kernelised histograms for misidentified two-body backgrounds where the shapes are extracted from MC 2012. These distributions are used to create the PDFs that model two-body backgrounds in the invariant mass fits. (Left) shows $B^0 \to K^+\pi^-$ misidentified as $B_s^0 \to K^+K^-$ and (right) shows $\mathit{\Lambda}_b^0 \to pK^-$ misidentified as $B_s^0 \to K^+K^-$.

Examples of a smooth misidentified PDF are shown in Figure 5.2. The only shape parameter that these template distributions have is the offset that shifts their mass to account for a shift in the LHCb mass scale. The offset is defined as the difference between the mean of the $B \to h^+h^{'-}$ signal channel peak and the PDG value [8] of the b hadron mass. (The B_d^0, B_s^0 and Λ_b^0 masses are $5279.63 \pm 0.15\,\text{MeV}/c^2$, $5366.89 \pm 0.19\,\text{MeV}/c^2$ and $5619.58 \pm 0.17\,\text{MeV}/c^2$ respectively [8].)

Partially Reconstructed Backgrounds

The shape of three-body backgrounds, which are partially reconstructed with one final state missing and a possible particle identification, are modelled with a combination of MC 2012 samples. The list of MC samples used is in Table 5.1, which includes all decay modes for which there was available MC samples for decays that could contaminate the mass spectrum if they are partially reconstructed as a two-body decay mode, in combination with a particle misidentification. The decays are reconstructed under the final state and have passed the full event selection. The contribution of each decay is then weighted with their hadronisation fraction, which is listed in Appendix E, branching ratios and the sample size before selections, where these values used are listed in Appendix F.

The list of three-body decays that could contribute to the $\pi^+\pi^-$, $p\pi^-$ and pK^- spectrum is larger than that of the K^+K^- and $K^+\pi^-$ spectrum. This is because possible three-body background contributions were studied in the previous measurement of the $B^0_s \to K^+K^-$, $B^0 \to K^+\pi^-$ and $B^0_s \to \pi^+K^-$ lifetime [38] and only three-body decay that were known to contribute were considered.

The distributions of the weighted partially reconstructed MC are shown in Figure 5.3, where the fitted PDFs are either an exponentially modified Gaussian distribution or two exponential distributions. The exponentially modified Gaussian function is the sum of a Gaussian and an exponential and is given by the equation

$$f(x;\mu,\sigma,\lambda) = \frac{\lambda}{2} e^{\frac{\lambda}{2}(2x+\lambda\sigma^2-2\mu)} \cdot \mathrm{Erfc}\Big(\frac{x+\lambda\sigma^2-\mu}{\sqrt{2}\sigma}\Big), \tag{5.14}$$

where μ is the Gaussian mean, σ in the Gaussian sigma and λ is the decay rate of the exponential. The error function is defined as

$$\mathrm{Erfc}(x) = \frac{2}{\sqrt{\pi}} \int_0^x e^{-t^2} dt. \tag{5.15}$$

For the K^+K^-, $K^+\pi^-$, $\pi^+\pi^-$, $p\pi^-$ and pK^- invariant mass spectrum the function chosen to fit each of the partially reconstructed distributions is based on the spread of the data points. These functions are unable to model all the features of the weighted distributions. The parameters of these functions are taken from the fits shown in Figure 5.3 and fixed in the mass fits of the data samples. The distributions are strongly dependent on availability and size of the MC samples and there could be decays that affect the $B \to h^+h^{'-}$ mass spectrum that have not been included in this study.

Decay mode	K^+K^-	$K^+\pi^-$	$\pi^+\pi^-$	$p\pi^-$	pK^-
$B^0 \to \pi^+\pi^-\pi^0$	<0.01%	12.37%	93.79%	1.56%	<0.01%
$B^0 \to K^+\pi^-\pi^0$	2.34%	75.25%	0.29%	0.01%	25.30%
$B^0 \to K^+K^-\pi^0$	2.29%	-	-	0.05%	0.89%
$B^0 \to K^0_s\pi^+\pi^-$	-	-	<0.01%	<0.01%	<0.01%
$B^0 \to K^0_s K^\mp\pi^\pm$	-	-	<0.01%	<0.01%	<0.01%
$B^0 \to K^0_s K^+K^-$	-	-	-	<0.01%	<0.01%
$B^+ \to \pi^+\pi^-\pi^+$	-	1.67%	5.92%	0.14%	1.36%
$B^+ \to \pi^+\pi^-K^+$	0.11%	3.56%	<0.01%	<0.01%	7.20%
$B^+ \to \pi^+K^-K^+$	0.43%	-	<0.01%	<0.01%	1.17%
$B^+ \to K^+K^-K^+$	<0.01%	-	-	<0.01%	<0.01%
$B^+ \to p\overline{p}\pi^+$	-	-	<0.01%	<0.01%	<0.01%
$B^+ \to p\overline{p}K^+$	-	-	-	<0.01%	<0.01%
$B^0_s \to K^-\pi^+\pi^0$	0.07%	7.16%	0.01%	<0.01%	<0.01%
$B^0_s \to K^+K^-\pi^0$	94.75%	-	-	<0.01%	10.08%
$B^0_s \to K^0_s\pi^+\pi^-$	-	-	<0.01%	<0.01%	<0.01%
$B^0_s \to K^0_s K^+K^-$	-	-	-	<0.01%	<0.01%
$B^0_s \to K^0_s K^\mp\pi^\pm$	-	-	<0.01%	<0.01%	<0.01%
$\Lambda^0_b \to \Lambda^+_c\pi^-$	-	-	-	97.11%	53.96%
$\Lambda^0_b \to pK^-\eta$	-	-	-	<0.01%	0.02%
$\Lambda^0_b \to pD^0\pi^-$	-	-	-	1.13%	<0.01%
$\Lambda^0_b \to pD^0K^-$	-	-	-	<0.01%	<0.01%

Table 5.1: Percentage contributions of decay channels in the partially reconstructed three-body background in the K^+K^-, $K^+\pi^-$, $\pi^+\pi^-$, $p\pi^-$and pK^- mass spectrum.

Combinatorial Background

The combinatorial background is modelled with a first degree polynomial. The gradient of this polynomial, ∇_{comb}, is left to float in all mass fits and the PDF is normalised over the mass range of each fit.

5.2.2 Fractions of Signal and Background Classes

In the invariant mass fit, the fractions of the $B \to h^+h^{'-}$ signal classes and fractions of the partially reconstructed backgrounds are free to float. The two-body misidentified backgrounds are constrained with a Gaussian dependency. The fraction of the combinatorial background in each fit is dependent on the fraction of all the other signal and background classes. It is defined as

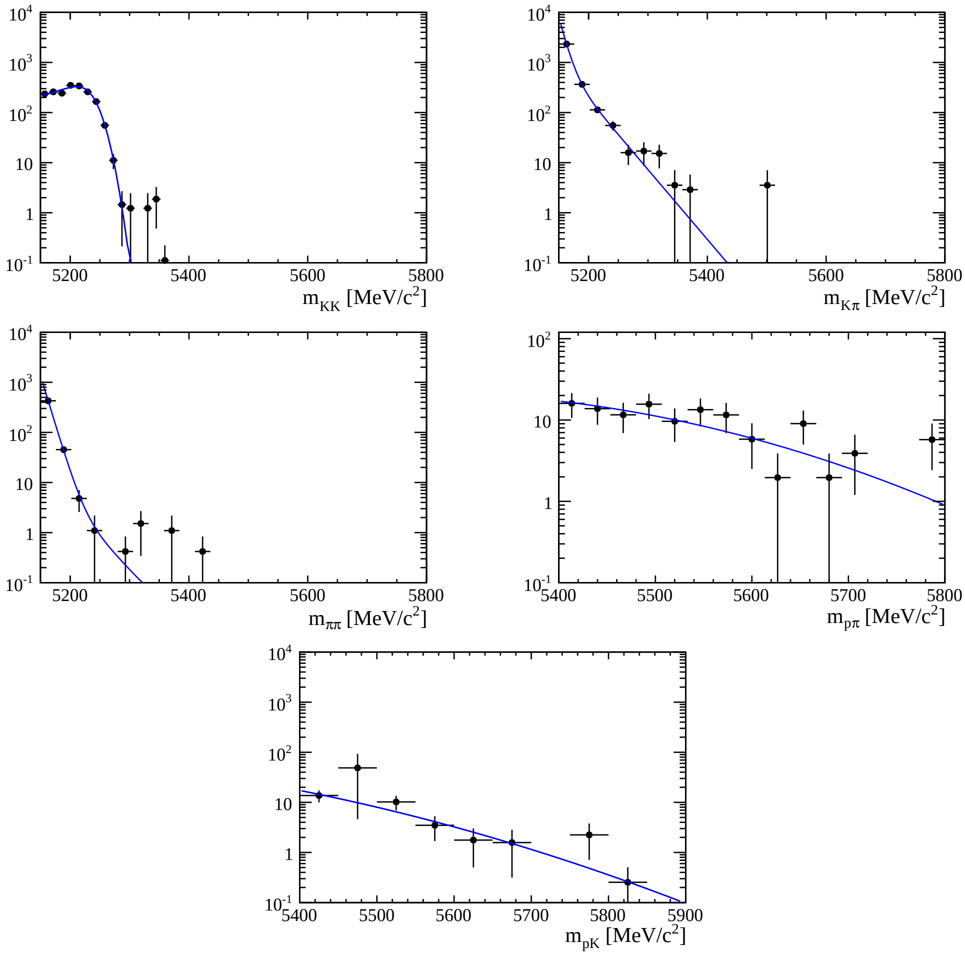

Figure 5.3: Weighted three-body MC 2012 that could contribute to the partially reconstructed backgrounds. The blue lines represent fits to the distributions.

$$f_{comb} = 1 - \sum f_{class}, \tag{5.16}$$

where f_{class} is the fraction of the other signal and background classes. This ensures that the total fractions of all signal and background classes is equal to one.

The Gaussian constraints on the misidentified backgrounds are centred around a predicated value that is calculated as the product of $B \to h^+h^{'-}$ signal channel fraction and a predicted misidentified background rate k. This scaling factor k is related to the signal channel fractions and the misidentified background fraction by the expression

$$f^{hh'}_{background} = f_{signal} \times k^{background}_{hh'}, \tag{5.17}$$

where hh' is the final state hypothesis, $f^{hh'}_{background}$ is the fraction of the background channel reconstructed under the hh' hypothesis and f_{signal} is the fraction of signal.

In the invariant mass fits, a preliminary value of k is determined with a calibration package, which is described in Section 4.4.1. Once the yields of the signal classes are obtained from the invariant mass fits of all five final states, the misidentification rates can be recalculated to give more accurate values. An example of this method includes the misidentification rate of $\Lambda^0_b \to pK^-$ in the KK spectrum relative to the $B^0_s \to K^+K^-$ yield, which can be expressed as

$$\frac{N^{KK}_{\Lambda^0_b \to pK^-}}{N^{KK}_{B^0_s \to K^+K^-}} = \frac{N^{pK}_{\Lambda^0_b \to pK^-}}{N^{KK}_{B^0_s \to K^+K^-}} \times \frac{\omega^{\Lambda^0_b \to pK^-}_{KK}}{\epsilon^{\Lambda^0_b \to pK^-}_{pK}}, \tag{5.18}$$

where $N^{hh'}_{channel}$ is the number of events for a given channel for the hh' final particle mass spectrum, ω is the misidentification probability and ϵ is the signal class efficiency.

This recalculation is done twice for all final state mass distributions with the $B \to h^+h^{'-}$ signal fractions updated from the previous fit. This recalculation was iteratively performed to improve the fit. The results of the new misidentified background rates are in Table 5.2 with the second iteration results used as input of the starting values into the invariant mass fits.

The misidentification background Gaussian constraints can bias the *sWeight* calculations, to ensure that this does not occur, the mass fit is run twice. In the second mass fit, all the parameters of the model shapes are fixed to the values determined in the first fit. Furthermore, the Gaussian constraints on the misidentified backgrounds are removed and all signal and background fractions are free to float, apart from the combinatorial which remains defined by Equation 5.16. This allows the covariance matrix of the yields to be correct and sWeights are calculated accurately. The results of the mass fits can be seen in Section 7.2.

Misidentification rates used in the KK fit relative to the $B_s^0 \to K^+K^-$ signal yield.

	1st iteration	2nd iteration
$B^0 \to K^+\pi^-$	0.0701 ± 0.0013	0.0704 ± 0.0013
$B_s^0 \to \pi^+K^-$	0.0049 ± 0.0001	0.0049 ± 0.0001
$\Lambda_b^0 \to pK^-$	0.0083 ± 0.0013	0.0083 ± 0.0013

Misidentification rates used in the $K\pi$ fit relative to the $B^0 \to K^+\pi^-$ signal yield.

	1st iteration	2nd iteration
$B_s^0 \to K^+K^-$	0.0115 ± 0.0002	0.0115 ± 0.0002

Misidentification rates used in the $\pi\pi$ fit relative to the $B^0 \to \pi^+\pi^-$ signal yield.

	1st iteration	2nd iteration
$B^0 \to K^+\pi^-$	0.0672 ± 0.0015	0.0637 ± 0.0015
$B_s^0 \to \pi^+K^-$	0.0047 ± 0.0002	0.0045 ± 0.0001
$\Lambda_b^0 \to p\pi^-$	0.0045 ± 0.0027	0.0043 ± 0.0027

Misidentification rates used in the $p\pi$ fit relative to the $\Lambda_b^0 \to p\pi^-$ signal yield.

	1st iteration	2nd iteration
$B^0 \to K^+\pi^-$	0.1243 ± 0.0070	0.1222 ± 0.0043
$B^0 \to \pi^+\pi^-$	0.1538 ± 0.0070	0.1595 ± 0.0057

Misidentification rates used in the pK fit relative to the $\Lambda_b^0 \to pK^-$ signal yield.

	1st iteration	2nd iteration
$B^0 \to K^+\pi^-$	0.6393 ± 0.0137	0.6402 ± 0.0132
$B_s^0 \to \pi^+K^-$	0.0468 ± 0.0015	0.0470 ± 0.0014
$B_s^0 \to K^+K^-$	0.1582 ± 0.0037	0.1577 ± 0.0036

Table 5.2: Predicted contamination from $B \to h^+h^{'-}$ misidentified backgrounds expressed relative to main signal peak, calculated with $B \to h^+h^{'-}$ signal fractions extracted from the invariant mass fit. The two-body background channels that could potentially influence the mass spectrum but were found to have very small fractions and therefore were removed from the fits, are not listed in this table, but were considered.

5.3 Correcting for Lifetime Biasing Selections

Kinematic selections, such as requiring a minimum impact parameter (IP), are commonly used to select b hadron events due to the events having displaced decay vertices. This displacement is illustrated in Figure 5.4. These kinematic selections are often implemented in the Trigger and are also used in offline event selections as they are very effective at reducing the combinatorial backgrounds but introduce a bias in the decay-time as they favour long lived particles. To perform an accurate lifetime measurement this bias must be accounted for.

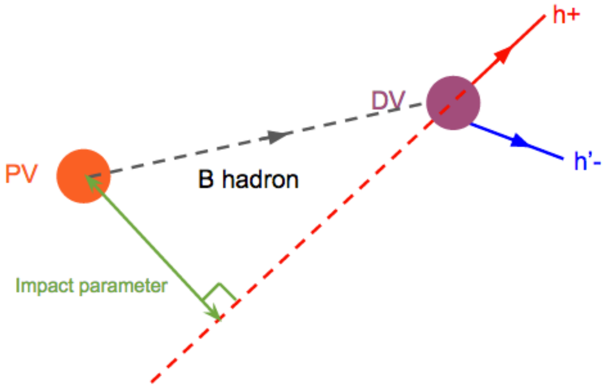

Figure 5.4: Diagram of a $B \to h^+h^{'-}$ event with the impact parameter for the daughter h^+ shown. The impact parameter is defined as the shortest distance between the extrapolated track and the PV.

The bias is modelled in the fitter with the acceptance function $A(t)$. The $B \to h^+h^{'-}$ lifetime analysis uses a method known as 'swimming' which evaluates the acceptance function of each event individually. The swimming method was initially developed by the NA11 experiment [86] and has since been used by DELPHI [87], CDF [88, 89] and LHCb [38, 90]. The method requires an artificial rerun of triggers and therefore works particularly well in LHCb due to the fact that the experimental decay-time biasing triggers are software based [91].

In a $B \to h^+h^{'-}$ event, the decay-time of the mother particle is independent of the kinematic properties of the daughter particles. The swimming algorithm takes advantage of this feature by artificially changing the mother particle decay-time by moving or 'swimming' the primary vertex forward and backwards along the mother particle's momentum vector. As the primary vertex is moved, the selection decision of the event is re-evaluated resulting in a time dependent acceptance function for the event. An example of this is shown in Figure 5.5, which illustrates how the acceptance changes with a selection on IP of the daughter particles. For a single event, the acceptance is a binary decision of yes or no and the points where the decision changes are called 'turning points' (TP).

The location of the turning points are firstly determined with a step size of 4 mm

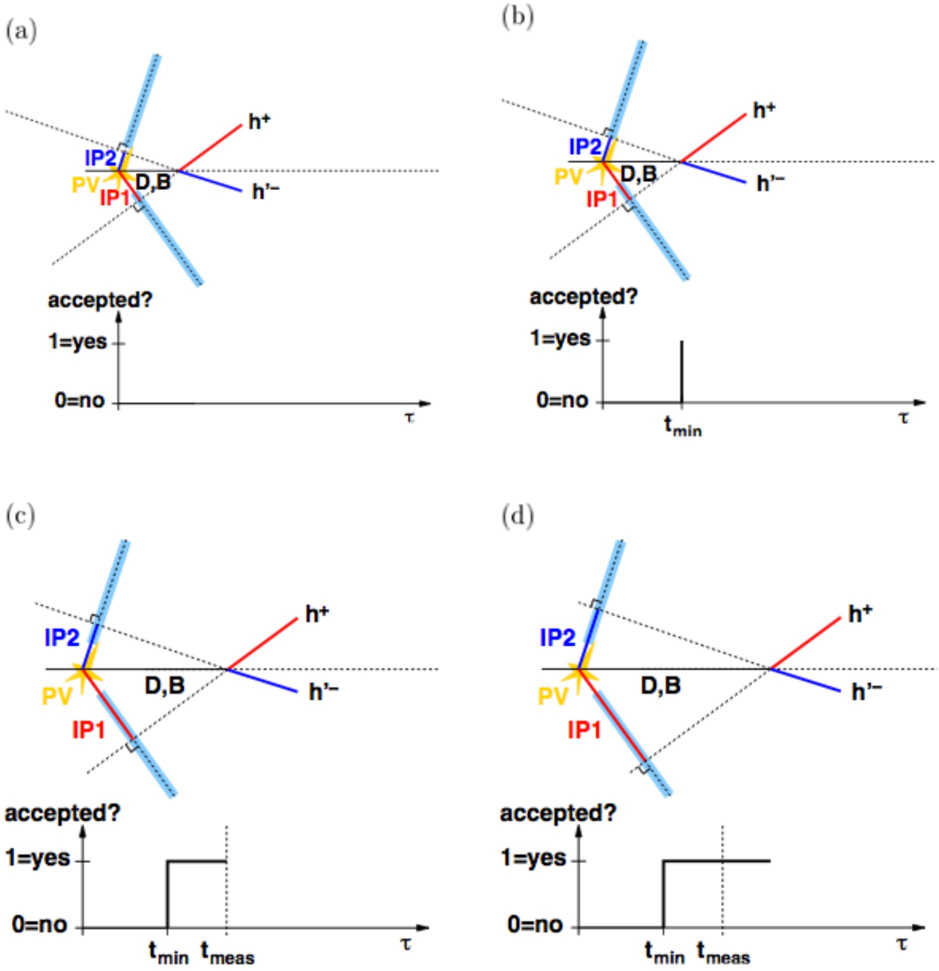

Figure 5.5: Diagram illustrating the swimming algorithm evaluation of decay-time acceptance for an event selection on minimum IP for a two body decay. The light blue regions represents the accepted daughter IP. This diagram shows how moving the primary/decay vertex affects the selection decision. (a) The negatively charged daughter particle h^- has an IP that is below the required minimum and the candidate fails the selection. (b) The negatively charged daughter particle h^- has an IP that is just large enough to be in the accepted region and the acceptance goes to one. This is known as a 'turning point'. (c) The candidate at its measured proper decay-time t_{meas}, where the acceptance is one. (d) The swimming algorithm continues to move the decay vertex to higher candidate decay-times and the candidate is still accepted. Reproduced from [92].

which is approximately half the length a b hadron flight path, once a change in decision is detected the step size is iteratively halfed until the location of the turning point is more precisely know. The precision of each turning point location is variable as the swimming algorithm takes into consideration both CPU time and accuracy.

The swimming determines intervals in decay-time where the event is either accepted or rejected and for each event the acceptance function can be described by the sum of top-hat and step functions. For a single event the PDF that describes decay-time, which was previously defined in equation 5.5, can be given by

$$f(t|A, class) = \frac{\frac{1}{\tau}e^{-t/\tau}A(t)}{\int_{-\infty}^{\infty}\frac{1}{\tau}e^{-t'/\tau}A(t')dt'}, \tag{5.19}$$

where τ is the lifetime of the decay and $A(t)$ is the acceptance function for the event. A top-hat function is expressed as

$$\begin{aligned} f_{tophat}(t) &= \begin{cases} 1 & t_{min} < t < t_{max} \\ 0 & \text{elsewhere,} \end{cases} \\ &= \Theta(t - t_{min})\Theta(t_{max} - t) \end{aligned} \tag{5.20}$$

where the accepted decay-times lie between t_{min} and t_{max} and $\Theta(t)$ is the Heaviside function [93]. This can be combined with Equation 5.19 to give the single event decay-time PDF as

$$f(t|A) = \begin{cases} \frac{\frac{1}{\tau}e^{-t/\tau}}{\int_{t_{min}}^{t_{max}}\frac{1}{\tau}e^{-t'/\tau}dt'} & t_{min} < t < t_{max} \\ 0 & \text{elsewhere.} \end{cases} \tag{5.21}$$

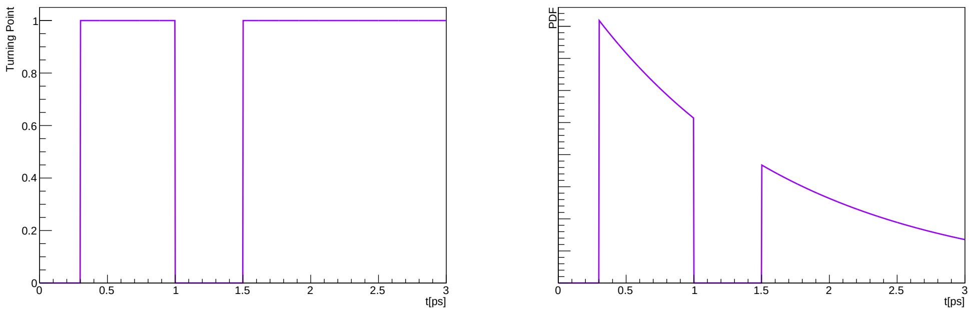

Figure 5.6: (Left) An example of acceptance intervals for a single event and (right) a decay-time PDF for the same single event.

An example of a single event acceptance function and decay-time PDF is shown in Figure 5.6. Multiple PVs can cause these individual event distributions to be more complicated and result in acceptance functions with more than three turning points, this does not affect the fitter performance. For a data sample, the individual acceptance functions are merged together resulting in the total acceptance distribution. In practice, a PV is moved over a range of ±600 mm. The swimming process can be very CPU intensive.

Incorporating the Acceptance Function into Decay-Time Fit

The acceptance function must be combined with the observed decay-time distribution for each signal and background class. The acceptance function $A(t)$ is determined with the swimming algorithm which produces a distribution that is the sum of multiple top hat functions. This acceptance function can be expressed in terms of the decay-time t, the number of turning points nTP and the proper decay-times of these turning points TP

$$A(t, nTP, TP_1 ... TP_{nTP}) = \sum_{n=1}^{nTP/2} \Theta(t - TP_{2n-1})\Theta(TP_{2n} - t). \tag{5.22}$$

Equation 5.19 which gives the PDF for a single event becomes

$$\begin{aligned} f(t|nTP, TP_1 ... TP_{nTP}, class) &= \frac{f(t|class)A(t, nTP, TP_1 ... TP_{nTP})}{\sum_{n=1}^{nTP/2} \int_{TP_{2n-1}}^{TP_{2n}} f(t'|class)dt'} \\ &= \frac{f(t|class)\sum_{n=1}^{nTP/2} \Theta(t - TP_{2n-1})\Theta(TP_{2n} - t)}{\sum_{n=1}^{nTP/2} \int_{TP_{2n-1}}^{TP_{2n}} f(t'|class)dt'}. \end{aligned} \tag{5.23}$$

where the denominator represents the probability that the candidate with given turning points passes the selection criteria.

Accounting for VELO track reconstruction efficiencies

The VELO track reconstruction [94] introduces an additional decay-time acceptance that is not accounted for in the previously described swimming method, and therefore needs to be accounted for independently. The VELO track finding procedure is more likely to reconstruct a track if it originates from the beamline (‘on-axis’). B hadrons are produced with transverse momentum and fly radially before decaying, so tracks originating from long-lived b hadron decays point away from the beamline ('off-axis') and have a lower reconstruction efficiency. The effect of this is an upper lifetime acceptance as a candidate with a larger decay-time is less likely to be reconstructed.

The efficiency is parameterised by a quadratic formula

$$\epsilon(DOCAz) = a(1 + c * DOCAz^2), \tag{5.24}$$

where $DOCAz$ is the distance of closest approach to the z-axis for a track and the parameters a and c have been determined from data. $DOCAz$ is defined by

$$DOCAz = \frac{|(\vec{d} - \vec{v}) \cdot (\vec{p} \times \vec{z})|}{|\vec{p} \times \vec{z}|}, \tag{5.25}$$

where $\vec{p}$ is the momentum of the final state track coming from a B-candidate which decays at point $\vec{d}$, $\vec{z} = (0, 0, 1)$ is defined as the z-axis and $\vec{v}$ gives the average position of the PVs in the event. $DOCAz$ can also be parametrised in terms of decay-time

$$DOCAz = p_0 + p_1 t. \tag{5.26}$$

The reconstruction efficiencies vary for each step of the selection process as different configurations of the software are used at HLT1, HLT2 and offline processing. The first part of the high-level trigger, HLT1, performs a 'fast' VELO reconstruction which has a larger bias than the regular VELO reconstruction algorithm.

To compensate for the effect of VELO-track reconstruction on the decay-time distribution each b hadron is weighted by

$$w = 1/\epsilon_B = 1/\prod_{i=1}^{n_{tracks}} \epsilon^i_{VELO}(DOCAz_i), \tag{5.27}$$

where ϵ_B is the efficiency of the b hadron and n_{tracks} is the number of daughter tracks.

When considering all the reconstruction stages of the event, the efficiency becomes

$$\epsilon_B = \epsilon_{offline}\, \epsilon_{HLT2|offline}\, \epsilon_{HLT1|HLT2\&offline}, \tag{5.28}$$

where $\epsilon_{offline}$ is the efficiency that the track was reconstructed offline, $\epsilon_{HLT2|offline}$ is the efficiency that the track was reconstructed in HLT2 assuming that it was reconstructed offline and $\epsilon_{HLT1|HLT2\&offline}$ is the efficiency that the track was reconstructed in HLT1 assuming that it was reconstructed offline and in HLT2. A $B \to h^+ h^{'-}$ candidate has two daughters and the previous equation becomes

$$\begin{aligned}\epsilon_B = &\epsilon_{offline,1}\,\epsilon_{HLT2|offline,1}\,\epsilon_{offline,2}\,\epsilon_{HLT2|offline,2}\times \\ &(\epsilon_{HLT1|HLT2\&offline,1} + \epsilon_{HLT1|HLT2\&offline,2} - \epsilon_{HLT1|HLT2\&offline,1}\,\epsilon_{HLT1|HLT2\&offline,2}),\end{aligned} \tag{5.29}$$

when the daughter particles are labelled 1 and 2 and both tracks are TOS at HLT1, or becomes

$$\epsilon_B = \epsilon_{offline,1}\,\epsilon_{HLT2|offline,1}\,\epsilon_{offline,2}\,\epsilon_{HLT2|offline,2}\,\epsilon_{HLT1|HLT2\&offline,1}, \tag{5.30}$$

when only one daughter is TOS at HLT1.

The parameters a and c defined in Equation 5.24 for offline, HLT2 and HLT1 were calculated with a data sample consisting of kaons collected during 2012 data taking and their values were determined in [95].

5.4 Fitting the Reconstructed Decay-Time Spectrum

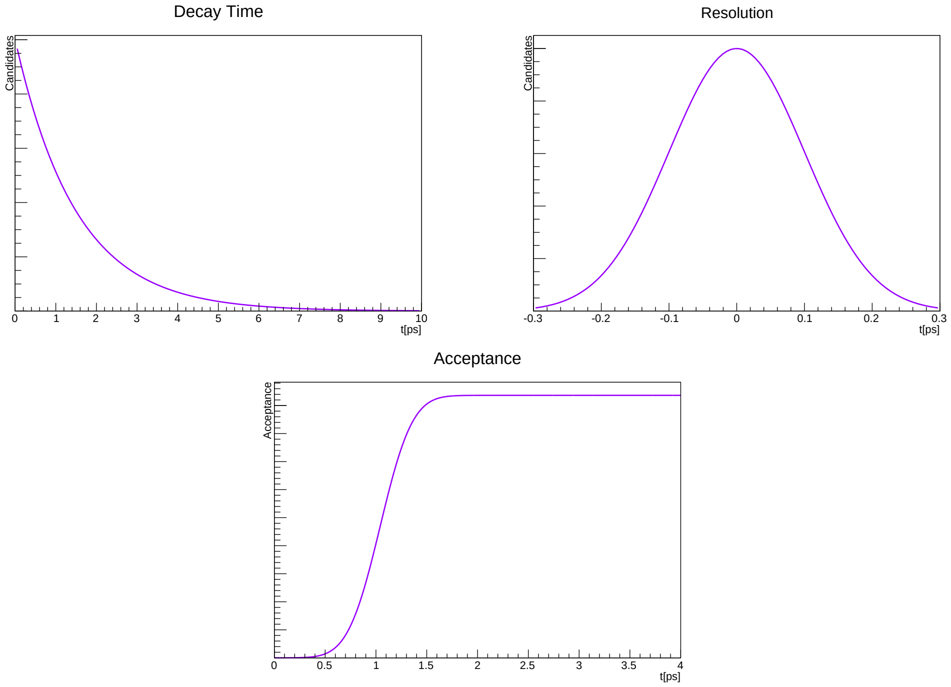

Figure 5.7: (Top left) An example of an unbiased decay-time distribution. (Top right) An example of a typical decay-time resolution distribution. (Bottom) An example of a typical decay-time acceptance distribution.

An unbiased decay-time spectrum follows an exponential distribution with the decay rate dependent on the particle lifetime τ, an example of which is shown in the top left plot of Figure 5.7. To fit the measured decay-time spectrum, experimental uncertainties and detector bias must be taken into account. The decay-time measurements have experimental uncertainties and this provides the resolution of the decay-time to be considered in the fit of the decay-time distribution. The resolution function can be described by a Gaussian distribution, an example of which is shown in the top right plot of Figure 5.7, where the Gaussian distribution is centred at zero. Finally, the time-dependent bias which was described previously must be incorporated into the fit. An example of a selection induced acceptance function is shown in the bottom plot of Figure 5.7. There is also an upper decay-time acceptance correction originating from track reconstruction efficiencies that is evaluated.

5.4.1 Lifetime Fitting

Detector Resolution Effects

To be able to perform a high-precision measurement of the lifetime, the resolution of the detector needs to be taken into account. For the LHCb detector the uncertainty on decay-time of b hadrons has been evaluated as $\approx 50\,\mathrm{fs}$ [96]. This is relatively small compared to the average decay-time of a b hadron

The decay-time resolution is a Gaussian function with a mean μ_t centred at zero and a width σ_t equal to the average detector uncertain on the measured value of the decay-times. It is written as

$$R(t, \sigma_t) = \frac{1}{\sqrt{2\pi}\sigma_t} e^{-\frac{t^2}{2\sigma^2}}. \tag{5.31}$$

This resolution function is convoluted with the previous single-event decay-time PDF to fit the measured decay-time distribution. For a signal event with a simplified acceptance function of a single step function, this convolution is

$$\begin{aligned} f(t|signal) &= \frac{1}{\tau} e^{-t/\tau} \Theta(t) \otimes R(t, \sigma_t) \\ &= \frac{1}{\tau} e^{-t/\tau} \Theta(t) \otimes \frac{1}{\sqrt{2\pi}\sigma_t} e^{-\frac{t^2}{2\sigma_t^2}} \\ &= \int_{-\infty}^{\infty} \frac{1}{\tau} e^{-t'/\tau} \Theta(t') \frac{1}{\sqrt{2\pi}\sigma_t} e^{-\frac{(t-t')^2}{2\sigma_t^2}} dt' \\ &= \frac{1}{\tau} e^{-t/\tau} e^{\frac{1}{2}\sigma_t^2/\tau^2} F\left(\frac{t}{\sigma_t} - \frac{\sigma_t}{\tau} \right), \end{aligned} \tag{5.32}$$

where $\Theta(t)$ is the Heaviside function describing the acceptance and $F(x)$ Gaussian cumulative frequency function which is defined as

$$F(x) = \frac{1}{\sqrt{2\pi}} \int_{-\infty}^{x} e^{-y^2/2} dy. \tag{5.33}$$

This can be extended for a two-turning point acceptance described by a top-hat function:

$$f(t|TP_1, TP_2, signal) = \frac{\frac{1}{\tau} e^{-t/\tau} e^{\frac{1}{2}\sigma_t^2/\tau^2} F(\frac{t}{\sigma_t} - \frac{\sigma_t}{\tau})}{N(TP_2, \tau, \sigma_t) - N(TP_1, \tau, \sigma_t)}, \tag{5.34}$$

Decay	Fixed Lifetime	Comments
$B_s^0 \to K^+K^-$	1.408 ± 0.017 [97]	
$B^0 \to K^+\pi^-$ and $B^0 \to \pi^+\pi^-$	1.520 ± 0.004 [97]	average B_d^0 lifetime
$B_s^0 \to \pi^+\pi^-$ and $B_s^0 \to \pi^+K^-$	1.511 ± 0.014 [97]	average B_s^0 lifetime
$\mathit{\Lambda}_b^0 \to pK^-$ and $\mathit{\Lambda}_b^0 \to p\pi^-$	1.467 ± 0.010 [97]	Λ_b^0 lifetime

Table 5.3: Lifetimes used in the fit for the misidentified backgrounds, these values are fixed in the fit.

where the denominator provides normalisation and the function $N(t)$ is given by

$$N(t, \tau, \sigma_t) = -e^{-t/\tau} e^{\frac{1}{2}\sigma_t^2/\tau^2} \left(F\left(\frac{t}{\sigma_t} + \frac{\sigma_t}{\tau}\right) - F\left(\frac{t}{\sigma_t}\right) \right). \tag{5.35}$$

Again, this can be modified for an acceptance function with multiple top-hat functions and the denominator of Equation 5.34 becomes

$$N_{tot} = \sum_{n=1}^{nTP/2} \left(N(TP_{2n}, \tau, \sigma) - N(TP_{2n-1}, \tau, \sigma) \right), \tag{5.36}$$

where the turning points are $\{TP_1, TP_2, ..., TP_{nTP}\}$.

Decay-Time Modelling of Misidentified Two-body Backgrounds

The two-body misidentified backgrounds are very small relative to the signal. These backgrounds do not have enough statistics to accurately model the decay-time distributions in the same way as the signal channels. Therefore, the lifetimes of these backgrounds are fixed to the best currently known values. The shapes used are the same as the signal channels, an exponential function convoluted with a Gaussian multiplied by the acceptance function. The values to which the misidentified backgrounds are fixed are listed in Table 5.3.

Decay-Time Modelling of Partial and Combinatorial Backgrounds with Non-parametric Lifetime PDFs

The decay-time distributions of the partially reconstructed and combinatorial backgrounds are modelled differently to the misidentified backgrounds, this analysis uses non-parametric models to fit these backgrounds. The difference between a parametric method and a non parametric method is that a parametric method assumes a model and aims to optimise the parameters of this model, whereas a non-parametric method is model-independent and optimises the function that estimate modelling a distribution directly.

The non-parametric method implementation combines two statistical methods, *sWeights* [83] and the kernel method [85]. The use of *sWeights* in this lifetime analysis were described previously in Section 5.1.3 and are used to identify these backgrounds in the decay-time spectrum. The kernel method is a technique that creates a smooth PDF to fit the background shapes.

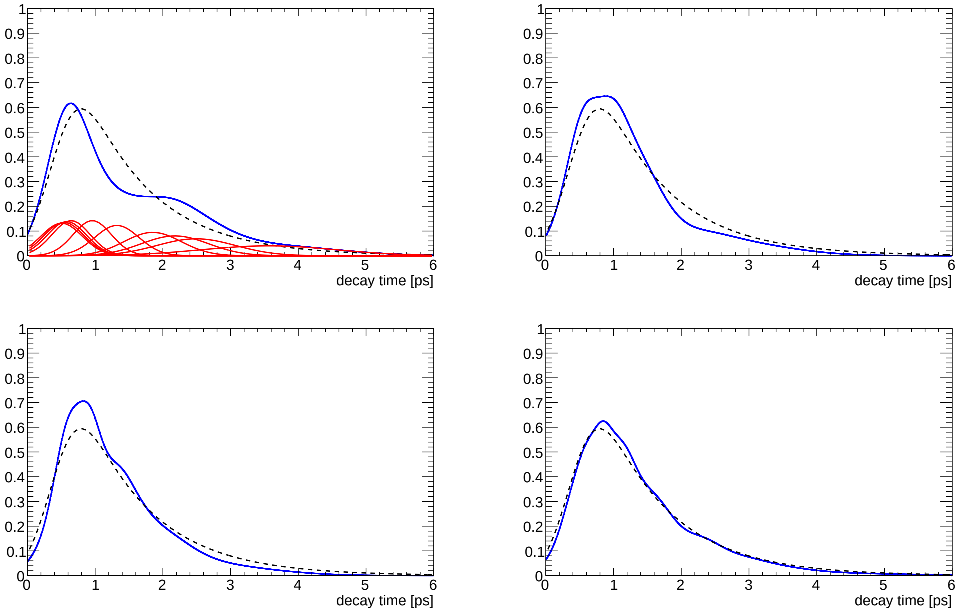

Figure 5.8: Diagram illustrating the use of the kernel method to create a smooth distribution. The data or 'true' distribution is shown in black, the individual kernels are shown in red and the kernel estimate of the distribution is shown in blue. (Top left) plot has 10 events, (top right) plot has 50 events, (bottom left) plot has 200 events and (bottom right) plot has 1000 events. Reproduced from [92].

As mentioned previously, the *sWeights* recovers the fraction contribution from each background. In a simplified version of the method, the recovered weight is filled into a histogram of decay-time. This simple method is limited by statistics and creates a distribution by binning a variable that causes a loss in the information associated to the shape of the distribution. The kernel method provides a way of smoothing the shape of the distribution. It uses individual Gaussian 'kernel' functions to build up a smooth distribution and the area of each kernel is the recovered weight for the corresponding event, this is shown in Figure 5.8. The events input to the kernel method to produce a non-parametric PDF have been determined based on the *sWeights* of each event. If the *sWeight* of an event predicts the event belongs to a specific background, in this case either the partial or combinatorial background, then an individual kernel is used to model this single event.

A generic kernel estimate of a function $f(x)$ can be expressed as

$$f(x) = \frac{1}{Nh}\sum_{i=1}^{N} K\Big(\frac{x - x_i}{h}\Big), \tag{5.37}$$

where $K(x)$ is the kernel function, h is the 'bandwidth' parameter that determines the width of the kernel function and N is the number of events in the sample. As a Gaussian function is used as the kernel function the parameter h is equivalent to the Gaussian width σ. The bandwidth defines the spread of the kernel function, an optimum value of h is generally not known. The adaptive kernel method determines a value of h for each candidate that is dependent on the function $f(x)$ [85]

$$h_i = \Big(\frac{4}{3N}\Big)^{1/5}\sqrt{\frac{\sigma}{f_0(x_i)}}, \tag{5.38}$$

where $f_0(x_i)$ is a best estimate of the parent distribution for each event x_i, in the analysis a histogram of the events is used as this estimate. In practice, the bandwidth of the estimate density function has minimal effect on the adaptive kernel bandwidth.

5.4.2 Blinding Procedure

The lifetime measurements are extracted with a blind analysis [98], which is an analysis that is performed without looking at the final results until completion of the analysis strategy and selections. This reduces the risk of experimental or human bias on the result. The blinding is achieved by scaling the measured $B \to h^+h^{'-}$ signal lifetimes that the fitter determines. Each $B \to h^+h^{'-}$ signal mode is scaled independently by scale factors that are randomly selected from a uniform distribution between 0.9 and 1.1, where the seeds used in each measured lifetime are different. The fitted value and its uncertainty are both scaled by this scale factor and this scaling is implemented internally into the fit. The results are unblinded once all the verifications are performed and the method is frozen.

5.5 Verification of Method

To verify that the fit method performs as expected and that no bias is introduced, the fit results of simplified simulations, known as pseudo-experiments, and full LHCb MC are examined. The verification with pseudo-experiments is performed with all signal and background modes included in a final-state mass spectrum. The verification on LHCb MC is performed with the main signal channel only.

5.5.1 Simplified Simulations

Many statistically independent pseudo-experiments are used to check that any floating parameters in the fitter converge to their correct values and that the statistical errors on these parameters are estimated accurately. In these simplified simulations only variables of interest to the lifetime measurement are generated, in this case the reconstructed mass, the decay-time, the turning point decisions, turning point lifetimes and daughter trigger decisions that are used in the fit, this ensures any observed biases are a result of the fit as opposed to reconstruction biases. The generation of the pseudo-experiments data for these data sets is significantly less CPU-intensive than producing full LHCb MC samples for this verification.

In all cases, the $B \to h^+h^{'-}$ signal fraction and partially reconstructed background fraction are generated with the values observed in data. The two-body background signal fractions are set to their expected yields, which are listed in Table 5.2. The total number of events in each individual data sample follows a Poisson distribution with a mean of 70000 events for the K^+K^-final state, 128000 events for the $K^+\pi^-$final state, 80000 events for the $\pi^+\pi^-$final state, 30000 events for the $p\pi^-$final state and 25000 events for the pK^-final state. The decay-time distributions are generated with two turning points, both sampled from a Gaussian distribution. The effects of the VELO track reconstruction bias are also included in these simulated data samples. Each final state mass hypothesis was checked with 1000 pseudo-experiments.

Each sample is fitted individually and the pull distributions of the fit results for the free parameters are evaluated. For a parameter that is allowed to float freely in the fit, the pull of the parameter is defined as

$$Pull = \frac{x - \mu}{\sigma}, \tag{5.39}$$

where x is the fit result of the parameter, μ is the true value of the parameter and σ is the error on the fit result.

If a fitter introduces no bias to the results, the pull distribution will follow a Gaussian function with a mean centred at zero and a a width of value one. Any deviation from zero on the mean value implies the fitter does not converge to the correct value. If the width of the pull distribution is smaller or larger than one the errors on the value are overestimated or underestimated.

The fits to these samples have the same configuration as the fit to the data, and the results of the lifetime pulls are shown in Figure 5.9, where the lifetime has been recovered with unbiased pulls. The pulls of the free parameters in the invariant mass distributions are in Appendix G. The simplified simulations show the fits to be unbiased and that they estimate the statistical uncertainties correctly, therefore no systematic uncertainty is assigned to the fitting procedure and no re-scaling of the uncertainties is applied.

5.5.2 LHCb MC

The fitter is also verified with the full LHCb MC. The full event selection is applied to all the MC samples. The acceptance function is determined in the same way as in data with the swimming algorithm used to evaluate the acceptance function of each candidate individually. The main signal class for each final daughter state was checked. Figures 5.10 shows the fits to the decay-time distributions and the resulting fitted lifetimes are listed in Table 5.4. Figure 5.11 shows the average acceptance distributions which were determined by the swimming method. There is a discrepancy between generated and fitted values which is not fully understood. To account for this, the difference in generated and fitted lifetimes is assigned as a systematic to each measured lifetime.

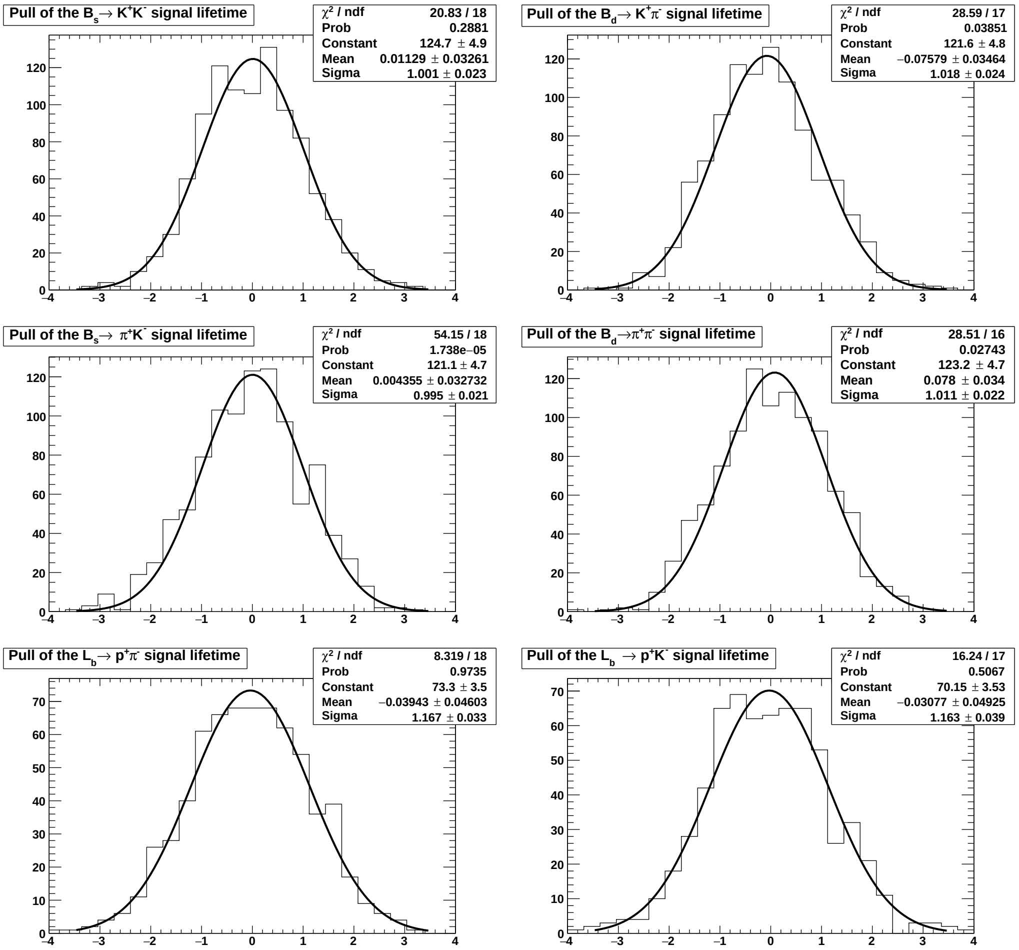

Figure 5.9: Pull distributions from the lifetime fitter for (top left) $\tau_{B_s^0\to K^+K^-}$, (top right) $\tau_{B^0\to K^+\pi^-}$, (middle left) $\tau_{B_s^0\to\pi^+K^-}$, (middle right) $\tau_{B^0\to\pi^+\pi^-}$, (bottom left) $\tau_{\Lambda_b^0\to p\pi^-}$ and (bottom right) $\tau_{\Lambda_b^0\to pK^-}$.

5.6 Summary

To summarise, this chapter has described the fit method used to measure $B\to h^+h^{'-}$ lifetimes, where firstly the invariant mass spectrum is fitted and these results are used to separate the signal and backgrounds in the decay-time spectrum. The decay-time fit takes into account detector acceptance effects, decay-time resolution and lifetime biassing reconstruction efficiencies. The decay-time acceptance is evaluated using a data-driven technique, which determines the individual candidate acceptance function, known as swimming. The fit method was checked with both simple simulations and full LHCb MC. The simplified simulations show the fitter is unbiased, the errors are evaluated ac-

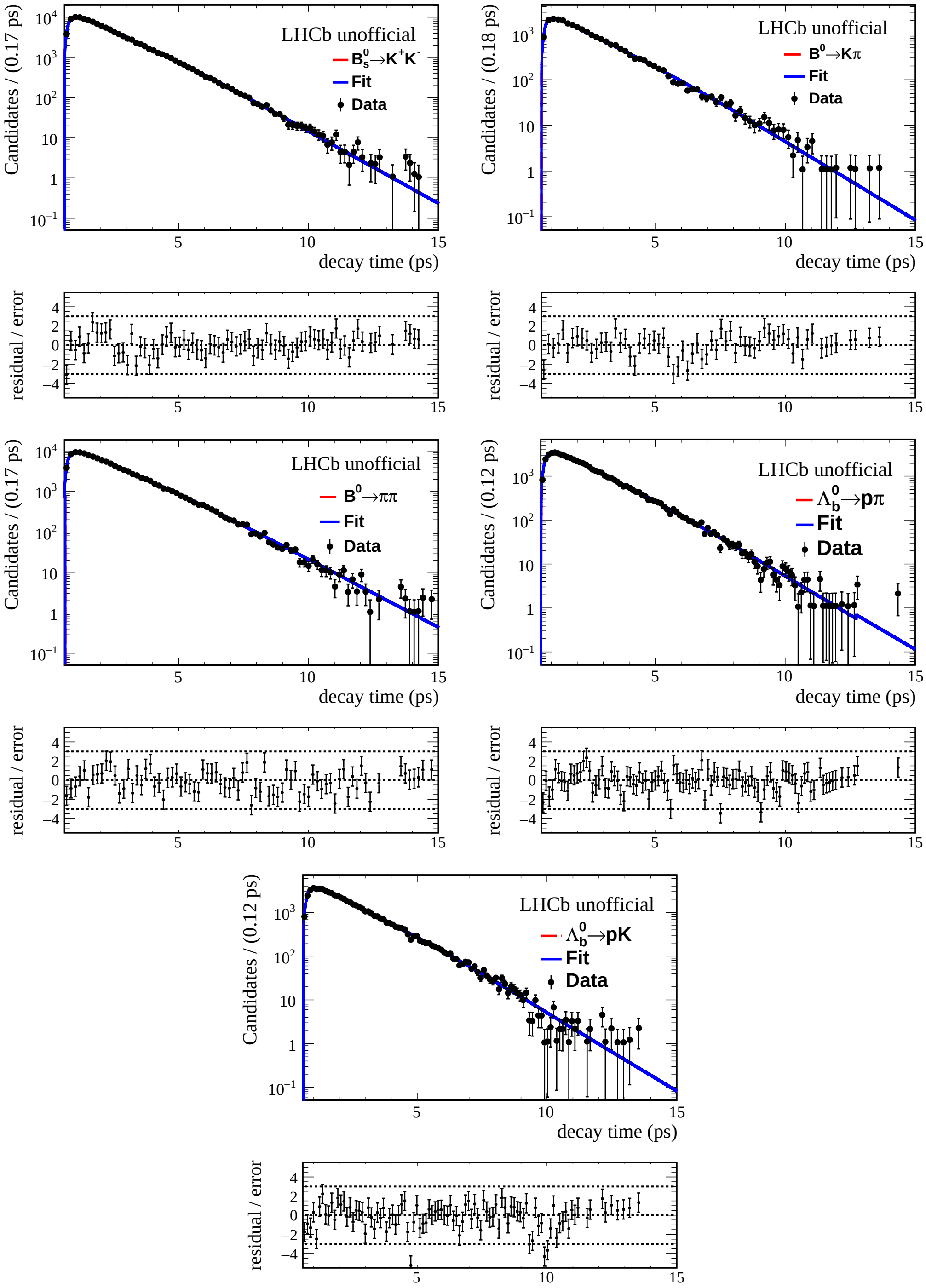

Figure 5.10: Lifetime fits and residuals of (top left) $B_s^0 \rightarrow K^+K^-$, (top right) $B^0 \rightarrow K^+\pi^-$, (middle left) $B^0 \rightarrow \pi^+\pi^-$, (middle right) $\Lambda_b^0 \rightarrow p\pi^-$ and (bottom) $\Lambda_b^0 \rightarrow pK^-$ 2012 MC. The black points represent the data points and the blue lines represent the fits.

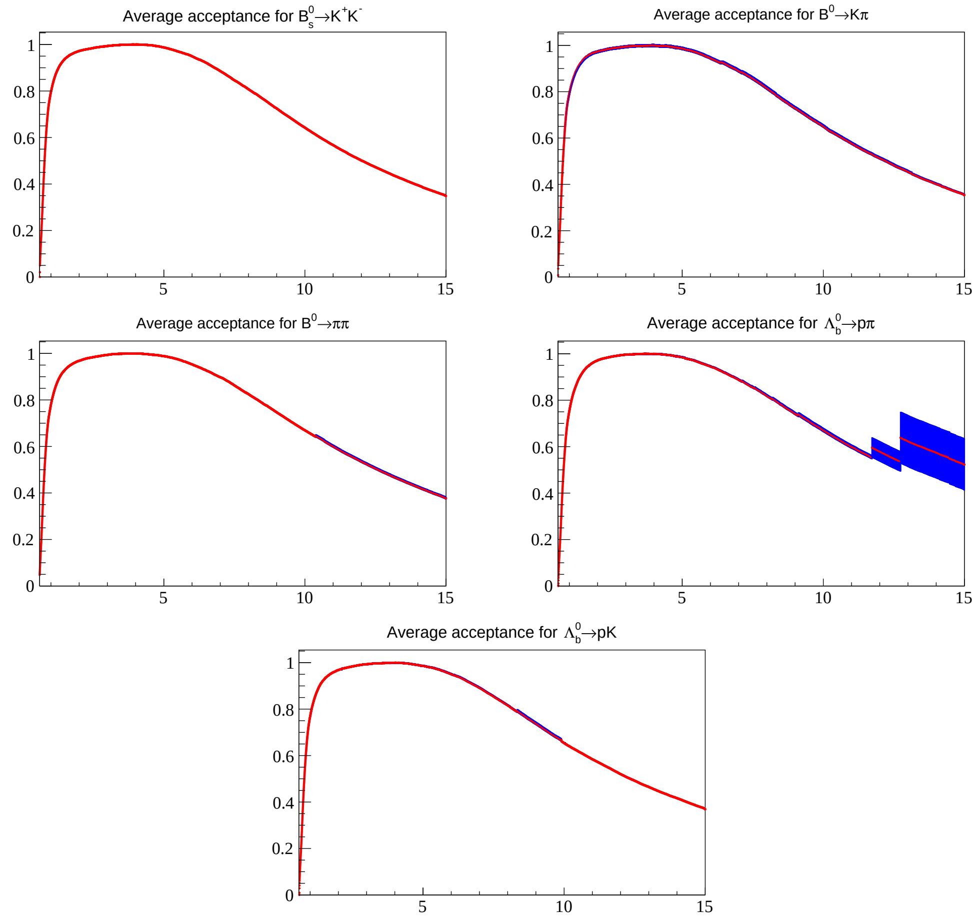

Figure 5.11: Acceptance functions of (top left) $B_s^0 \to K^+K^-$, (top right) $B^0 \to K^+\pi^-$, (middle left) $B^0 \to \pi^+\pi^-$, (middle right) $\Lambda_b^0 \to p\pi^-$ and (bottom) $\Lambda_b^0 \to pK^-$ 2012 MC. The red line represents the function and the blue area represents the statistical uncertainty on the function.

curately and no systematic error is induced by the fitter. The lifetimes produced by the fits to the LHCb MC samples do not agree with the known generated lifetimes of these samples and a systematic uncertainty is used to account for this.

2012 MC Signal channel	Fitted Lifetime (ps)	Generated Lifetime (ps)	No. of candidates in MC sample	Lifetime difference (fs)
$B_s^0 \to K^+K^-$	1.420 ± 0.004	1.431	111331	11 ± 4
$B^0 \to K^+\pi^-$	1.496 ± 0.011	1.519	11006	23 ± 11
$B^0 \to \pi^+\pi^-$	1.513 ± 0.005	1.519	108493	6 ± 5
$\Lambda_b^0 \to p\pi^-$	1.418 ± 0.006	1.425	53574	7 ± 6
$\Lambda_b^0 \to pK^-$	1.407 ± 0.006	1.425	56517	18 ± 6

Table 5.4: Comparison of fitted 2012 MC lifetime values compared to the generated values for the main $B \to h^+h^{'-}$ channels in each final state. Only statistical errors are shown. The last column lists the difference between the generated and fitted lifetime for each sample.

Chapter 6

Studies of Systematics Uncertainties

6.1 Introduction

Studies to determine the systematic uncertainties on the $B \to h^+h^{'-}$ lifetime measurements presented in this thesis are described in this section. The values of the systematic uncertainties induced from the method to evaluate the lifetime is determined with simplified simulations (pseudo-experiment data) and the combined 2012 and 2011 LHCb data samples.

6.2 Systematic Uncertainties in Mass Fitter

The systematic uncertainties introduced by the mass fitter are determined by varying fixed parameters by their uncertainties and in some cases by varying the function used to fit a background.

6.2.1 Modelling the $B \to h^+h^{'-}$ Signal

In the mass fitter, the tail parameters of the double Crystal Ball functions (DCB), n and α of each Crystal Ball, and the fraction between the 'high' and 'low' tail Crystal Balls, f, are fixed to values determined from MC. Each fixed parameter is evaluated individually using 1000 pseudo-experiment samples generated with a parameter varied up or down by 1σ of the value with which it is fixed in the nominal fit. The fitter is then run in the nominal fit configuration on these pseudo-experiment data samples and the difference in

Varied Mass Shape	Signal Lifetime	Lifetime uncertainty (fs)
$B_s^0 \to K^+K^-$	$\tau_{B_s^0 \to K^+K^-}$	1.18
$B^0 \to K^+\pi^-$	$\tau_{B^0 \to K^+\pi^-}$	0.20
$B^0 \to K^+\pi^-$	$\tau_{B_s^0 \to \pi^+K^-}$	3.05
$B_s^0 \to \pi^+K^-$	$\tau_{B^0 \to K^+\pi^-}$	0.48
$B_s^0 \to \pi^+K^-$	$\tau_{B_s^0 \to \pi^+K^-}$	0.95
$B^0 \to \pi^+\pi^-$	$\tau_{B^0 \to \pi^+\pi^-}$	0.38
$B_s^0 \to \pi^+\pi^-$	$\tau_{B^0 \to \pi^+\pi^-}$	0.34
$\Lambda_b^0 \to p\pi^-$	$\tau_{\Lambda_b^0 \to p\pi^-}$	1.53
$\Lambda_b^0 \to pK^-$	$\tau_{\Lambda_b^0 \to pK^-}$	1.62

Table 6.1: Systematic uncertainty from modelling the signal peaks. In this study the parameters in the $B^0 \to K^+\pi^-$ and $B_s^0 \to \pi^+K^-$ signal shapes are varied independently. The first column is the channel of the shape that is varied and the second column is the quantity that this systematic uncertainty is assigned to.

generated lifetime and fitted lifetime is taken as the systematic uncertainty. The largest deviation from the generated lifetime in this ensemble of pseudo-experiments is taken as the systematic uncertainty. The overall uncertainty from a signal model is the sum in quadrature of the shift in lifetime after varying all fixed parameters in the DCB function. The uncertainties on the $B \to h^+h^{'-}$ lifetimes from the signal mass shapes are given in Table 6.1

6.2.2 Modelling the Misidentified Backgrounds

The two-body misidentified backgrounds are shifted by an offset that is the difference between the fitted signal mean and the PDG value of the b hadron mass. To evaluate the uncertainty this introduces, 1000 pseudo-experiment data samples are generated with the offset varied up or down by the uncertainty on the fitted mean in the nominal fit. The fitter is run on these pseudo-experiment data samples with this signal mean fixed to the convergence fit value. The difference in generated lifetimes and fitted lifetime is taken as the systematic uncertainty and the results are in Table 6.2

6.2.3 Modelling the Partially Reconstructed Background

In the mass fitter, the parameters describing the shape of the partially reconstructed background are fixed to values determined from MC. The systematic uncertainty introduced

Signal	Lifetime uncertainty (fs)
$B_s^0 \to K^+K^-$	0.49
$B^0 \to K^+\pi^-$	0.18
$B_s^0 \to \pi^+K^-$	0.74
$B^0 \to \pi^+\pi^-$	0.64
$\Lambda_b^0 \to p\pi^-$	0.88
$\Lambda_b^0 \to pK^-$	0.87

Table 6.2: Systematic uncertainty from the two-body misidentified background offset parameter.

Signal	Lifetime uncertainty (fs)
$B_s^0 \to K^+K^-$	0.52
$B^0 \to K^+\pi^-$	0.13
$B_s^0 \to \pi^+K^-$	0.83
$B^0 \to \pi^+\pi^-$	0.92
$\Lambda_b^0 \to p\pi^-$	1.07
$\Lambda_b^0 \to pK^-$	1.13

Table 6.3: Systematic uncertainty from fixing parameters in partially reconstructed three-body backgrounds.

by fixing these parameters is determined in the same way as the fixed DCB parameters of the signal functions, described previously. The uncertainties on the $B \to h^+h^{'-}$ lifetimes from fixing the parameters in the function used to model the partially reconstructed three-body backgrounds are in Table 6.3

6.2.4 Modelling the Combinatorial Background

The function used to model the combinatorial background for all five mass spectrum can be varied from a linear function to an exponential function, where the decay rate of the exponential function is free to float. The observed shift in measured lifetime with the full LHCb run 1 dataset when the function shape changed is assigned as a systematic uncertainty and the values are listed in Table 6.4.

Signal	Lifetime uncertainty (fs)
$B_s^0 \to K^+K^-$	0.42
$B^0 \to K^+\pi^-$	0.19
$B_s^0 \to \pi^+K^-$	0.29
$B^0 \to \pi^+\pi^-$	0.76
$\Lambda_b^0 \to p\pi^-$	5.81
$\Lambda_b^0 \to pK^-$	10.9

Table 6.4: Systematic uncertainty from the function used to model the combinatorial backgrounds.

6.3 Systematic Uncertainties in Lifetime Fitter

The systematic uncertainties introduced by the decay-time fitter are determined by varying fixed parameters by their uncertainties and in some cases by varying the function used to fit a background.

6.3.1 Detector Resolution

To measure the uncertainty introduced by fixing the detector resolution to 50 fs, 1000 pseudo-experiment data samples are generated under nominal fit configurations. The fitter is then run on these data samples with the value that decay time resolution is varied to 40, 50 and 60 fs in the configuration. The uncertainty is found to be negligible in all cases.

6.3.2 VELO Track Reconstruction Efficiencies

The parameters that describe the effect of the VELO track reconstruction efficiencies are fixed in the fitter. Each fixed parameter is evaluated individually using 1000 pseudo-experiment data samples generated with a parameter varied up or down by 1σ of the value that is used in the nominal fit. The fitter is then run in the nominal fit configuration on these pseudo-experiment data samples and the difference in generated lifetime and fitted lifetime is taken as the systematic uncertainty. The largest deviation from the generated lifetime in this ensemble of pseudo-experiments is taken as the systematic uncertainty. The uncertainties on the $B \to h^+h^{'-}$ lifetimes from the VELO track reconstruction efficiencies are given in Table 6.5.

Signal	Lifetime uncertainty (fs)
$B_s^0 \to K^+K^-$	0.68
$B^0 \to K^+\pi^-$	0.43
$B_s^0 \to \pi^+K^-$	1.22
$B^0 \to \pi^+\pi^-$	1.45
$\mathit{\Lambda}_b^0 \to p\pi^-$	2.69
$\mathit{\Lambda}_b^0 \to pK^-$	3.84

Table 6.5: Systematic uncertainty from the accounting for the VELO track reconstruction efficiencies in the decay time fit.

Signal	Lifetime uncertainty (fs)
$B_s^0 \to K^+K^-$	0.52
$B^0 \to K^+\pi^-$	0.30
$B_s^0 \to \pi^+K^-$	0.32
$B^0 \to \pi^+\pi^-$	0.67
$\mathit{\Lambda}_b^0 \to p\pi^-$	0.74
$\mathit{\Lambda}_b^0 \to pK^-$	0.83

Table 6.6: Systematic uncertainty from the parametric functions used to model the misidentified two-body decay time.

6.3.3 Modelling the Misidentified Two-body Background with Parametric Functions

The lifetimes of misidentified two-body backgrounds are fixed to the best current known value [8]. The systematic uncertainty is determined by varying each fixed lifetime up or down by 1σ of the PDG value that is fixed in the nominal fit. 1000 pseudo-experiment data samples are generated for each variation and the fitter is run in the nominal fit configuration on these pseudo-experiment data samples. The difference in generated lifetime and fitted lifetime is taken as the systematic uncertainty. The overall uncertainty from these parametric decay time models is the sum in quadrature of the shift in lifetime after varying the lifetime of each function. The uncertainties on the $B \to h^+h^{'-}$ lifetimes from the parametric decay time shapes are given in Table 6.6.

Signal	Lifetime uncertainty (fs)
$B_s^0 \to K^+K^-$	1.06
$B^0 \to K^+\pi^-$	0.50
$B_s^0 \to \pi^+K^-$	0.83
$B^0 \to \pi^+\pi^-$	2.65
$\Lambda_b^0 \to p\pi^-$	7.53
$\Lambda_b^0 \to pK^-$	4.40

Table 6.7: Systematic uncertainty from the non-parametric functions used to model the misidentified two-body decay time.

6.3.4 Modelling of Partial and Combinatorial Backgrounds with Non-parametric Lifetime Functions

The parametric lifetime PDFs use the kernel method to create a smooth distribution. To measure the systematic uncertainty this introduces in the fit, the width of these Gaussian Kernels is varied with respect to the nominal, by having a kernel twice the size and half the size of the nominal kernel width. The largest variation in measured lifetime is taken as the uncertainty and the results given in Table 6.7.

6.3.5 Consistency Across Number of PV

The effect that incorrect primary vertex assignments or reconstruction has on the measured lifetime is evaluated by splitting the data samples by number of PV. The lifetime is measured data, which is blinded. The results of the fitter are shown in Figure 6.1. All fits on a data sample have the same blinding factor. The data samples are split into categories, decays with 1 PV, decays with 2 PVs and decays with greater than 2 PVs. The default selection without any selection on number of PVs is also measured. For the $B_s^0 \to K^+K^-$, $B^0 \to K^+\pi^-$ and $B_s^0 \to \pi^+K^-$ lifetimes all four measurements agree within 1σ and for the $B^0 \to \pi^+\pi^-$, $\Lambda_b^0 \to p\pi^-$ and $\Lambda_b^0 \to pK^-$ all measurements agree within 2σ. This validates the consistency of the lifetime as a function of the number of PVs and no further systematic error is assigned.

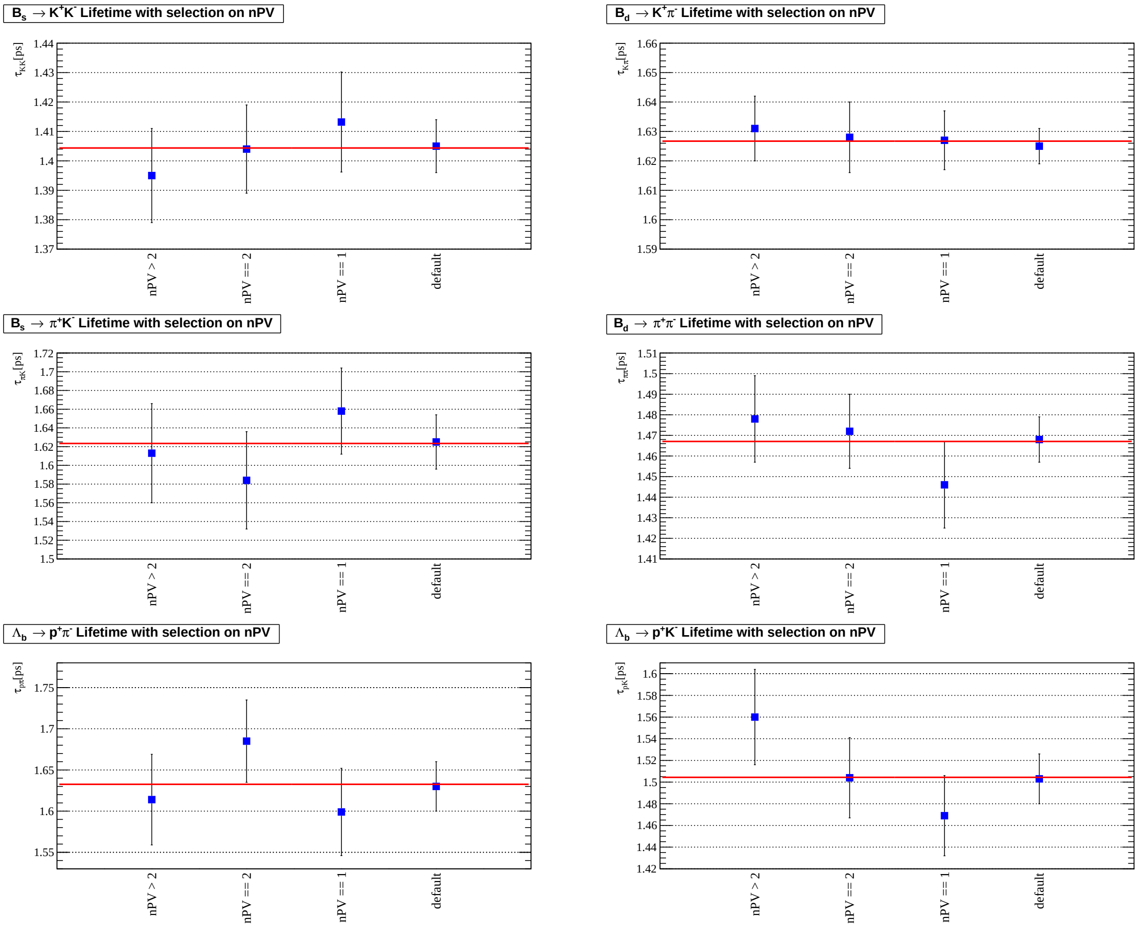

Figure 6.1: Fitted lifetime dependency on number of PV. The lifetimes are measured on the full data sample and the fits are performed blind. The red line represents a fit of constant lifetime to the data points. (Top left) $B^0_s \to K^+K^-$, (top right) $B^0 \to K^+\pi^-$, (middle left) $B^0_s \to \pi^+K^-$, (middle right) $B^0 \to \pi^+\pi^-$, (bottom left) $\Lambda^0_b \to p\pi^-$ and (bottom right) $\Lambda^0_b \to pK^-$.

6.3.6 Consistency Across L0 Trigger Categories

The effect of the L0 trigger on the measured lifetime is evaluated by splitting the data samples depending on whether an event passes the L0 trigger as TIS or as TOS. The L0 trigger selection used in the $B \to h^+h^{'-}$ lifetime measurements are in Section 4.2, where an event is selected if it passes either of the two L0 trigger conditions. The lifetimes are measured when the event passes `L0Global_TIS` only and `L0Hadron_TOS` only and the results are shown in Figure 6.2. All fits on a data sample have the same blinding factor. The default configuration is the configuration used in the nominal fit, (`L0Global_TIS` $=$

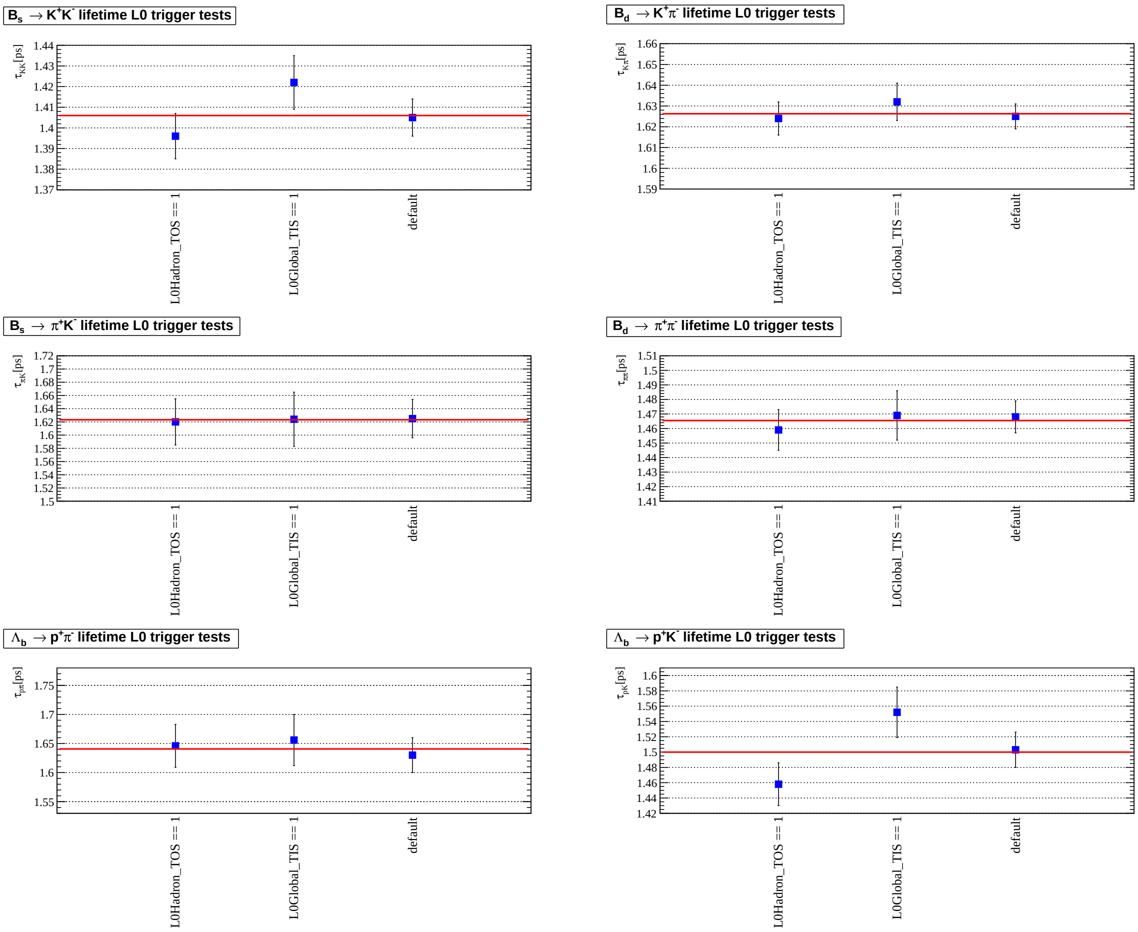

Figure 6.2: Fitted lifetime dependency in L0 trigger categories. The lifetimes are measured on the full data sample and the fits are performed blind. The red line represents a fit of constant lifetime to the data points. (Top left) $B_s^0 \to K^+K^-$, (top right) $B^0 \to K^+\pi^-$, (middle left) $B_s^0 \to \pi^+K^-$, (middle right) $B^0 \to \pi^+\pi^-$, (bottom left) $\Lambda_b^0 \to p\pi^-$ and (bottom right) $\Lambda_b^0 \to pK^-$.

`1 OR L0Hadron_TOS = 1)`. For the $B_s^0 \to K^+K^-$ and $\Lambda_b^0 \to pK^-$ lifetimes the measurements agree within 2σ and for the $B^0 \to K^+\pi^-$, $B_s^0 \to \pi^+K^-$, $B^0 \to \pi^+\pi^-$ and $\Lambda_b^0 \to p\pi^-$ the measurements agree within 1σ. This validates the consistency of the lifetime as a function of the trigger selection and no further systematic error is assigned.

2011		
Subset	Moore version	Run Number
1	v12r5	89489-90763
2	v12r6p1	90763-94385
3	v12r8	95946-100256
4	v12r9p1	101375-104414
2012		
Subset	Moore version	Run Number
5	v14r2	117098-118880
6	v14r6	119956-128492
7	v14r8	129534-129978
8	v14r9	130316-131983
9	v14r11	132104-133785

Table 6.8: Subsets of the 2011 and 2012 data split by Moore version.

6.3.7 Consistency Across Trigger Configurations

The effect of the trigger configuration used to select events during data taking is evaluated by splitting the data samples by Moore version. The Moore [99] software package is used in the trigger to perform fast event reconstruction. Table 6.8 lists the Moore version dependence on run number and the fitter is run on each sub-sample. The results are shown in Figure 6.3 where all fits on a data sample have the same blinding factor. All measurements agree within 2σ. This validates the consistency of the lifetime as a function of the trigger configurations and no further systematic error is assigned.

6.3.8 Consistency Across Magnet Polarity

The effect of the magnet polarity used to select events during data taking is evaluated by splitting the data samples each time the magnet polarity was changed during data taking. Table 6.9 lists the magnet polarity dependence on run number and the fitter is run on each sub-sample. The results are shown in Figure 6.4 where all fits on a data sample have the same blinding factor. All measurements agree within 2σ. This validates the consistency of the lifetime amongst magnet polarity settings and no further systematic error is assigned.

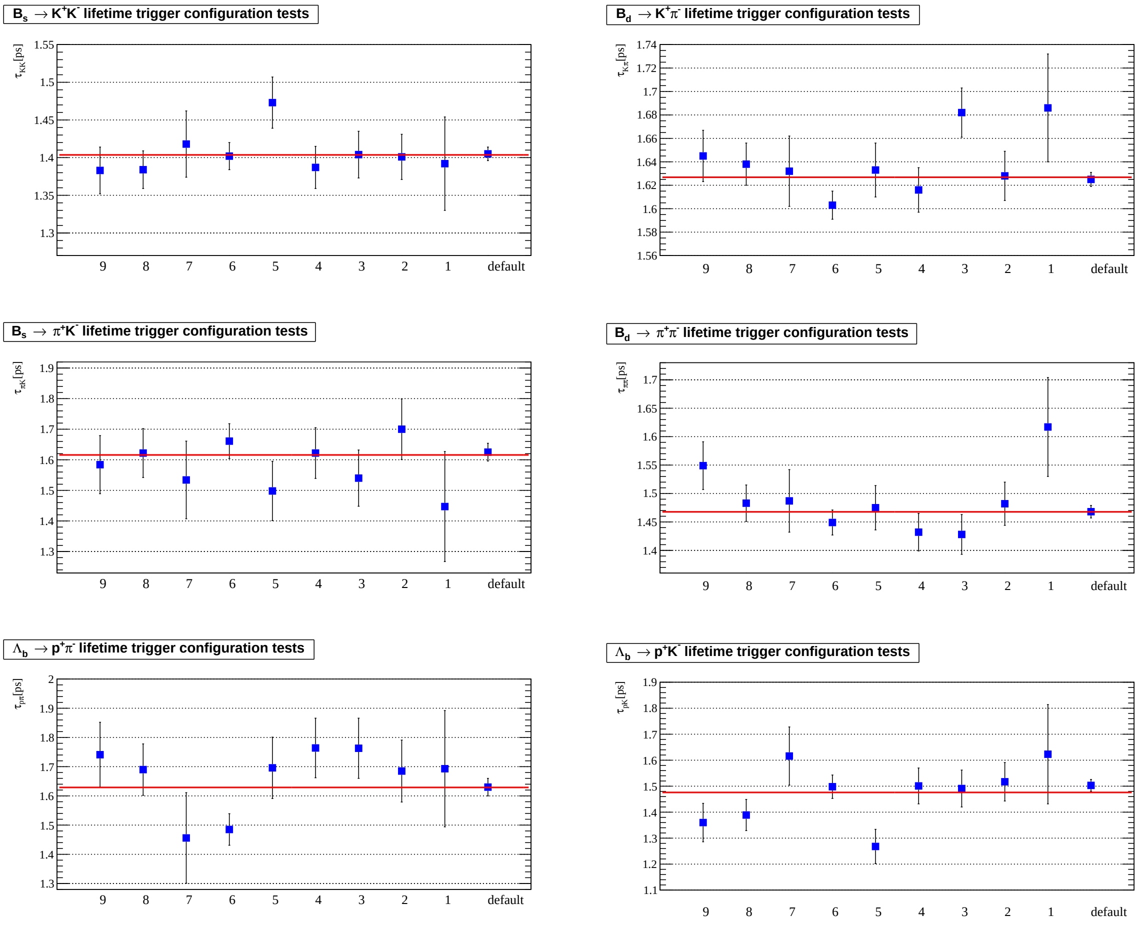

Figure 6.3: Fitted lifetime dependency on the trigger configuration. The lifetimes are measured on the full data sample and the fits are performed blind. The red line represents a fit of constant lifetime to the data points. (Top left) $B_s^0 \to K^+K^-$, (top right) $B^0 \to K^+\pi^-$, (middle left) $B_s^0 \to \pi^+K^-$, (middle right) $B^0 \to \pi^+\pi^-$, (bottom left) $\Lambda_b^0 \to p\pi^-$ and (bottom right) $\Lambda_b^0 \to pK^-$.

2011			
Subset	Magnet Polarity	Run Number	Date
1	Negative/Mag Up	86033-90207	1st March - 26th April
2	Positive/Mag Down	90319-93282	26th April - 11th June
3	Negative/Mag Up	93398-97028	11th June - 27th July
4	Positive/Mag Down	97114-98882	27th July - 17th August
5	Negative/Mag Up	98900-101862	17th August - 16th September
6	Positive/Mag Down	101891-102452	16th September - 28th September
7	Negative/Mag Up	102499-102907	28th September - 5th October
8	Positive/Mag Down	103049-103863	5th October - 22nd October
9	Negative/Mag Up	103936-104414	22nd October - 31st October
2012			
Subset	Magnet Polarity	Run Number	Date
10	Positive/Mag Down	114316-115464	2nd May - 16th May
11	Negative/Mag Up	115518-117103	16th May - 31st May
12	Positive/Mag Down	117192-118286	31st May - 11th June
13	Negative/Mag Up	118326-123803	11th June - 25th July
14	Positive/Mag Down	123910-125115	25th July - 11th August
15	Negative/Mag Up	125566-126680	11th August - 29th August
16	Positive/Mag Down	126824-128268	29th August - 12th September
17	Negative/Mag Up	128411-129978	12th September - 12th October
18	Positive/Mag Down	130316-130861	12th October - 24th October
19	Negative/Mag Up	130911-131940	24th October - 8th November
20	Positive/Mag Down	131973-133587	8th November - 4th December
21	Negative/Mag Up	133624-133785	4th December- 1st January

Table 6.9: Subsets of the 2011 and 2012 data split by magnet polarity changes.

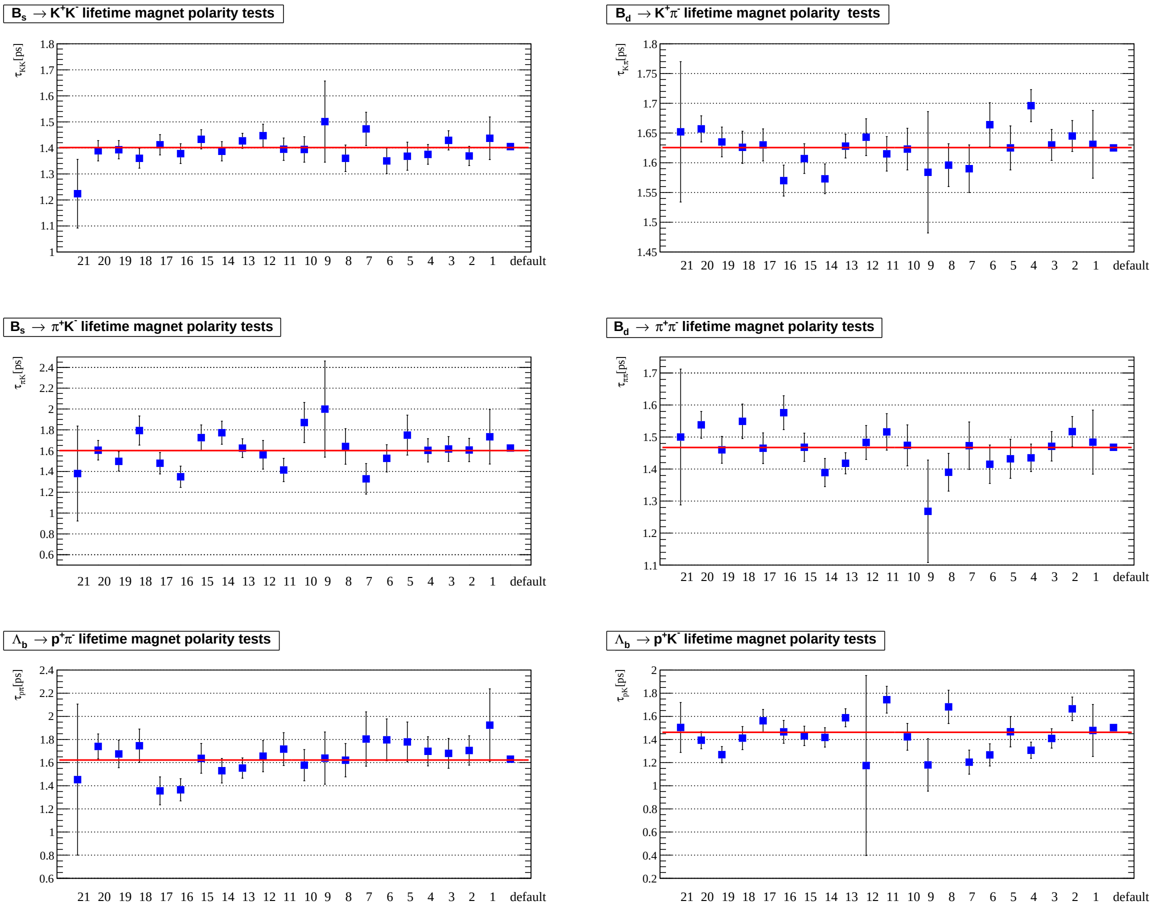

Figure 6.4: Fitted lifetime dependency on the magnet polarity. The lifetimes are measured on the full data sample and the fits are performed blind. The red line represents a fit of constant lifetime to the data points. (Top left) $B_s^0 \to K^+K^-$, (top right) $B^0 \to K^+\pi^-$, (middle left) $B_s^0 \to \pi^+K^-$, (middle right) $B^0 \to \pi^+\pi^-$, (bottom left) $\Lambda_b^0 \to p\pi^-$ and (bottom right) $\Lambda_b^0 \to pK^-$.

6.3.9 High Decay-Time Reconstruction Bias

High decay-time bias that is not accounted for by the acceptance correction comes from the finite length of the vertex locator. There is a requirement that a track must traverse at least three VELO segments in HLT1. This requirement means a reduction in the acceptance of very long lived b hadron candidates. The swimming method does not repeat the track reconstruction at each step and therefore the acceptance correction does not consider any bias due to this effect. An extra set of turning points determined from analytically computing the number of VELO stations a track passes through can be combined with the turning points from the swimming method to measure the bias. This was studied in [38] and found to have a negligible effect.

6.3.10 Absolute Decay-Time Scale

The systematic uncertainty on decay time scale arises from uncertainties in the longitudinal (z) scale of the detector and uncertainties in the overall momentum scale. The first effect is evaluated using a comparison of the track distributions in the VELO of the track-based alignment and survey data and the second is evaluated by the difference in the measured mass and the mass reference values [100] of well-known resonances. The second effect is determined by uncertainties on the overall momentum scale. As both the measured invariant mass and the measured momentum are used to determine decay-time, this effect becomes relatively small. Overall the uncertainty from the decay-time scale has been determined to be 0.028% of the measured lifetime [101].

6.3.11 B_c^+ Contribution in the K^+K^-Mass Spectrum

A fraction of all B_s^0 mesons will originate from the decay $B_c^+ \to B_s^0\pi^+$ [102], an upper limit on this fraction is 1% of all B_s^0 mesons. If this is not considered, it will cause an increase in the measured lifetime of the B_s^0. For a sample of B_s^0 mesons produced from the decay $B_c^+ \to B_s^0\pi^+$, the PDF becomes

$$\frac{1}{\tau_{B_s^0} - \tau_{B_c^+}} \cdot (e^{-t/\tau_{B_s^0}} - e^{-t/\tau_{B_c^+}}). \tag{6.1}$$

A single exponential fit to this distribution would measure a lifetime that is the mean of the observed decay-times. Assuming no detector acceptance and resolution effects, the single exponential fit would converge with a lifetime of $\tau_{B_s^0} + \tau_{B_c^+}$.

Introduction of a simple acceptance distribution with one turning point, i.e a step function with turn-on point at t_{min} gives

$$\hat{\tau} = t_{min} + \frac{\tau_{B_s^0}^2 \cdot e^{-t_{min}/\tau_{B_s^0}} - \tau_{B_c^+}^2 \cdot e^{-t_{min}/\tau_{B_c^+}}}{\tau_{B_s^0} \cdot e^{-t_{min}/\tau_{B_s^0}} - \tau_{B_c^+} \cdot e^{-t_{min}/\tau_{B_c^+}}}, \tag{6.2}$$

where $\hat{\tau}$ is the expected lifetime. Assuming no detector acceptance and resolution effects implies that $t_{min} = 0$. One can derive $\tau = \tau_{B_c^+} + \tau_{B_s^0}$ when $t_{min} = 0$ with Equation 6.2. The average value of $\tau_{B_c^+} = 0.507 \pm 0.009\,\mathrm{ps}$ [8].

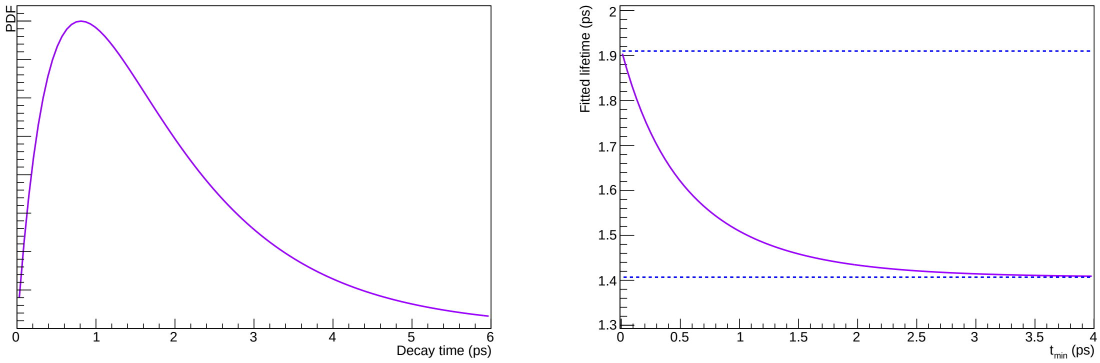

Figure 6.5: (Left) The lifetime PDF of a sample of B_s^0 mesons produced from the decay $B_c^+ \to B_s^0\pi^+$. (Right) The expectation value of the distribution when the acceptance is a step function with turn-on point t_{min}, subtracting t_{min}. The expectation value is the value of the convergence of a single exponential fit after correcting for the acceptance. The blue dashed lines are at $\tau_{B_s^0}$ and $\tau_{B_s^0} + \tau_{B_c^+}$.

Equation 6.2 goes to $\tau_{B_s^0} + \tau_{B_c^+}$ at $t_{min} = 0$ and goes to $\tau_{B_s^0}$ as the value of t_{min} increases, this is shown in Figure 6.5. The systematic uncertainty introduced by this effect is 1.83 fs, which was calculated with 1% $B_c^+ \to B_s^0\pi^+$ in the data sample and $t_{min} = 0.6\,\mathrm{ps}$. There is a known selection on decay-time of 0.6 ps in the stripping line which is the dominant contributor to the acceptance turn-on points.

6.3.12 Production Asymmetry Effect on $\tau_{B_s^0 \to K^+K^-}$

Equation 1.27 assumes that the production of B_s^0 and $\overline{B}_s^0$ mesons is equivalent at LHCb. In fact this is known to be false, the production of particles to antiparticles is asymmetric as the LHC collides protons. The production asymmetry, A_p, can be written as

$$A_p = \frac{R_{B_s^0} - R_{\overline{B}_s^0}}{R_{B_s^0} + R_{\overline{B}_s^0}} \tag{6.3}$$

where $R_{B_s^0}$ is the rate of B_s^0 production and $R_{\overline{B}_s^0}$ is the rate of $\overline{B}_s^0$ production at LHCb.

The expression for the time-dependent decay rate $\Gamma_s[f,t]$ including the production asymmetry is

$$\begin{aligned}\Gamma_s[f,t] &= \left(\frac{1+A_p}{2}\right)\Gamma(B_s^0(t) \to f) + \left(\frac{1+A_p}{2}\right)\Gamma(\overline{B_s^0}(t) \to f)\\ &= \frac{1}{2}N_f|A_f|^2(1+|\lambda_f|^2)e^{-\Gamma_s t}\Bigg\{ \cosh\left(\frac{\Delta\Gamma_s t}{2}\right) + \sinh\left(\frac{\Delta\Gamma_s t}{2}\right)A_{\Delta\Gamma}\\ &+ A_p\{C_f\cos(\Delta m t) + S_f\sin((\Delta m t)\}\Bigg\}.\end{aligned} \tag{6.4}$$

This can be written in terms of the heavy and light decay rates,

$$\begin{aligned}\Gamma_s[f,t] \simeq \frac{1}{4}N_f|A_f|^2(1+|\lambda_f|^2)\Bigg\{&(1-A_{\Delta\Gamma})e^{-\Gamma_L t} + (1+A_{\Delta\Gamma})e^{-\Gamma_H t}\\ &+ 2A_p e^{-\Gamma_s t}\{C_f\cos(\Delta m t) + S_f\sin((\Delta m t)\}\Bigg\}.\end{aligned} \tag{6.5}$$

Equation 6.5 has an oscillatory term that disappears as $A_p = 0$, when the decay time distribution can once again be written as a sum of two exponentials.

The $B_s^0 \to K^+K^-$ effective lifetime is

$$\tau_{B_s^0 \to K^+K^-} = \frac{\int_0^\infty t \cdot \Gamma_s[K^+K^-,t]dt}{\int_0^\infty \Gamma_s[K^+K^-,t]dt}, \tag{6.6}$$

when there are no detector acceptance and resolution effects. The numerator of Equation 6.6 becomes

$$\begin{aligned}\int_0^\infty t \cdot \Gamma_s[K^+K^-,t]dt =& N'\Bigg\{\frac{(1-A_{\Delta\Gamma})}{\Gamma_L^2} + \frac{(1+A_{\Delta\Gamma})}{\Gamma_H^2} \\ &+ 2A_p\left[C_f\frac{\Gamma_s^2-\Delta m^2}{(\Delta m^2+\Gamma_s^2)^2} + S_f\frac{2\Gamma_s\Delta m}{(\Delta m^2+\Gamma_s^2)^2}\right]\Bigg\},\end{aligned} \tag{6.7}$$

and the denominator becomes

$$\begin{aligned}\int_0^\infty \Gamma_s[K^+K^-,t]dt =& N'\Bigg\{\frac{(1-A_{\Delta\Gamma})}{\Gamma_L} + \frac{(1+A_{\Delta\Gamma})}{\Gamma_H} \\ &+ 2A_p\left[C_f\frac{\Gamma_s}{(\Delta m^2+\Gamma_s^2)^2} + S_f\frac{\Delta m}{(\Delta m^2+\Gamma_s^2)^2}\right]\Bigg\},\end{aligned} \tag{6.8}$$

where $N' \equiv \frac{1}{4}N_f|A_f|^2(1+|\lambda_f|^2)$. To calculate a numerical value of the effective lifetime with these expressions we need known values of the oscillation and CP asymmetry parameters. The values used are: $\Gamma_s = 0.664\,\text{ps}$, $\Delta\Gamma_s = 0.086\,\text{ps}$ and $\Delta m = 17.757\,\text{ps}$ from [34], $C_f = 0.236 \pm 0.06 \pm 0.02$ and $S_f = 0.216 \pm 0.06 \pm 0.02$ from [31]. The condition $C_f^2 + S_f^2 + A_{\Delta\Gamma}^2 = 1$ results in $A_{\Delta\Gamma} = 0.947 \pm 0.021$.

$$A_p = (-1.11 \pm 2.85 \pm 0.5)\% \quad \text{for} \quad \sqrt{s} = 7\,\text{TeV}, \tag{6.9}$$

$$A_p = (1.78 \pm 1.96 \pm 0.53)\% \quad \text{for} \quad \sqrt{s} = 8\,\text{TeV}. \tag{6.10}$$

These production asymmetries A_p were measured in [103] and the values are compatible with zero. The systematic uncertainty in the $B_s^0 \to K^+K^-$ effective lifetime is assigned as $\tau_{B_s^0\to K^+K^-}(A_p) - \tau_{B_s^0\to K^+K^-}(A_p = 0)$. Figure 6.6 shows the uncertainty as a function of production asymmetry. The measured values of A_p produce an uncertainty value of 0.73 fs, which is a weighted average of the 2011 and 2012 uncertainty.

6.4 Summary

To summarise, this chapter has described the systematic uncertainties of the measured $B \to h^+h^{'-}$ lifetimes. The method used to evaluate each individual source uncertainty has been described. Table 6.10 and Table 6.11 list all contributions that were studied,

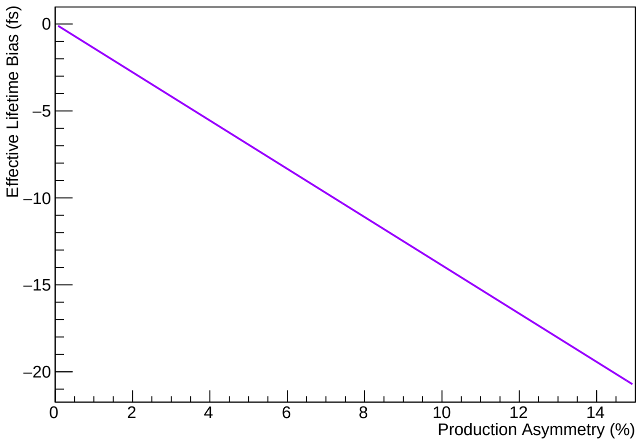

Figure 6.6: The uncertainty in the effective lifetime as a function of function of production asymmetry A_p.

Source	Lifetime uncertainty (fs)		
	$B_s^0 \to K^+K^-$	$B^0 \to K^+\pi^-$	$B_s^0 \to \pi^+K^-$
Method and verification	11	23	23
Mass Model	1.44	0.60	3.39
Detector Resolution	-	-	-
VELO Track Reconstruction Efficiencies	0.68	0.43	1.22
Parametric Lifetime Functions	0.52	0.30	0.32
Non-parametric Lifetime Functions	1.06	0.50	0.83
Absolute Decay Time Scale	0.39	0.42	0.44
Production Asymmetry	0.73	-	-
B_c^+ Contribution	1.83	-	1.83
Total	11.36	23.02	23.38

Table 6.10: Systematic uncertainty contributions for $B_s^0 \to K^+K^-$, $B^0 \to K^+\pi^-$ and $B_s^0 \to \pi^+K^-$ lifetime measurements.

as well as the overall systematic uncertainty derived from the quadratic sum of all the individual systematic uncertainties. All fitted values are in Appendix C.

Source	Lifetime uncertainty (fs)		
	$B^0 \to \pi^+\pi^-$	$\Lambda_b^0 \to p\pi^-$	$\Lambda_b^0 \to pK^-$
Method and verification	6	7	18
Mass Model	1.45	6.17	11.11
Detector Resolution	-	-	-
VELO Track Reconstruction Efficiencies	1.45	2.69	3.84
Parametric Lifetime Functions	0.67	0.74	0.83
Non-parametric Lifetime Functions	2.65	7.53	4.40
Absolute Decay Time Scale	0.42	0.43	0.42
Production Asymmetry	-	-	-
B_c^+ Contribution -	-	-	-
Total	6.73	12.32	21.96

Table 6.11: Systematic uncertainty contributions for $B^0 \to \pi^+\pi^-$, $\Lambda_b^0 \to p\pi^-$ and $\Lambda_b^0 \to pK^-$ lifetime measurements.

Chapter 7

$B \to h^+h^{'-}$ Results

7.1 Introduction

The results of the $B \to h^+h^{'-}$ lifetime measurement analysis is presented in this chapter. Section 7.2 contains the results of the mass fits, Section 7.3 contains the results of the decay-time fits and the decay-time acceptance functions used. Finally, Section 7.4.2 presents the resulting value of the decay asymmetry $A_{\Delta\Gamma}$ using the measured $B^0_s \to K^+K^-$ lifetime and the average values of the B^0 and Λ^0_b lifetimes.

7.2 Mass Fits Results

This section presents the results of the mass fits to the LHCb run 1 data sample. All candidates have passed the full event selections described in Chapter 4.1.

7.2.1 Mass fit to K^+K^- final state

The invariant mass spectrum of the K^+K^- final state hypothesis is fitted over a mass range of 5150 - 5800 MeV/c^2, which is shown in Figure 7.1. Candidates with decay time less than 0.6 ps and greater than 12 ps are not included in the fit. The total number of candidates in this fit is 44440 and the number of $B^0_s \to K^+K^-$ signal candidates are

$$N_{B^0_s \to K^+K^-} = 27849 \pm 201,$$

where the error is dependent on the signal fractions from the fit and the total number of candidates. The parameters of the fit are included in Appendix C.

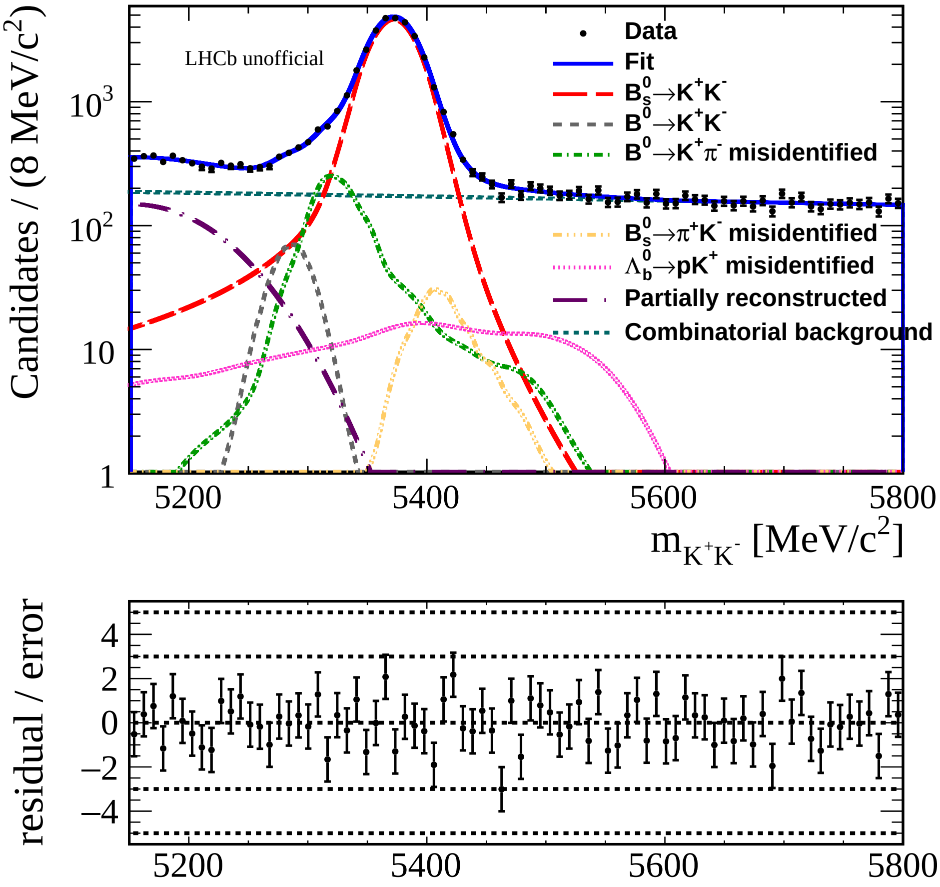

Figure 7.1: Mass distribution and fit to the K^+K^- invariant mass spectrum. The upper plot shows the fit to the mass spectrum in a log scale. The lower plot shows the binned residuals. The black points represent the data points and the blue line shows the full fit.

7.2.2 Mass fit to $K^+\pi^-$ final state

The invariant mass spectrum of the $K^+\pi^-$ final state hypothesis is fitted over a mass range of 5150 - 5800 MeV/c^2, which is shown in Figure 7.2. Candidates with decay time less than 0.6 ps and greater than 12 ps are not included in the fit. The total number of candidates in this fit is 128494, the number of $B^0 \to K^+\pi^-$ signal candidates are

$$N_{B^0 \to K^+\pi^-} = 78375 \pm 311,$$

and the number of $B_s^0 \to \pi^+ K^-$ signal candidates are

$$N_{B_s^0 \to \pi^+ K^-} = 5596 \pm 148.$$

The parameters of the fit are included in Appendix C.

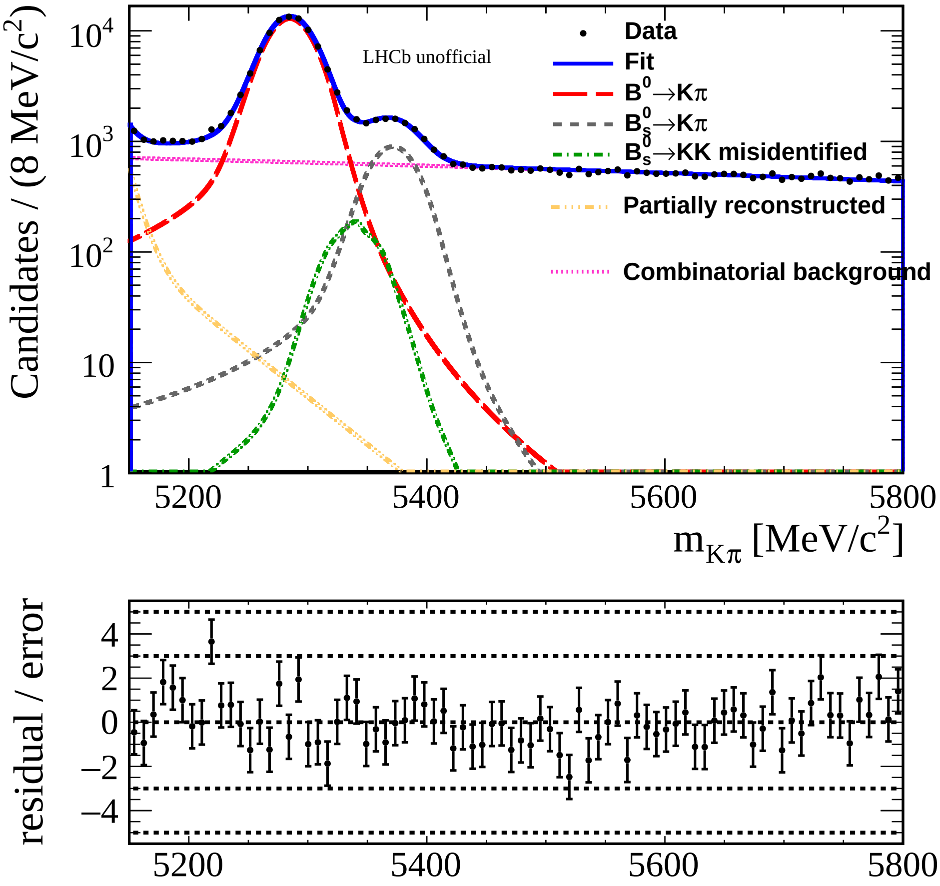

Figure 7.2: Mass distribution and fit to the $K^+\pi^-$ invariant mass spectrum. The upper plot shows the fit to the mass spectrum in a log scale. The lower plot shows the binned residuals. The black points represent the data points and the blue line shows the full fit.

7.2.3 Mass fit to $\pi^+\pi^-$ final state

The invariant mass spectrum of the $\pi^+\pi^-$ final state hypothesis is fitted over a mass range of 5150 - 5800 MeV/c^2, which is shown in Figure 7.3. Candidates with decay time less than 0.6 ps and greater than 12 ps are not included in the fit. The total number of candidates in this fit is 77871, the number of $B^0 \to \pi^+\pi^-$ signal candidates are

$$N_{B^0\to\pi^+\pi^-} = 22601 \pm 237,$$

and number of $B_s^0 \to \pi^+\pi^-$ candidates are

$$N_{B_s^0\to\pi^+\pi^-} = 835 \pm 123.$$

The parameters of the fit are included in Appendix C.

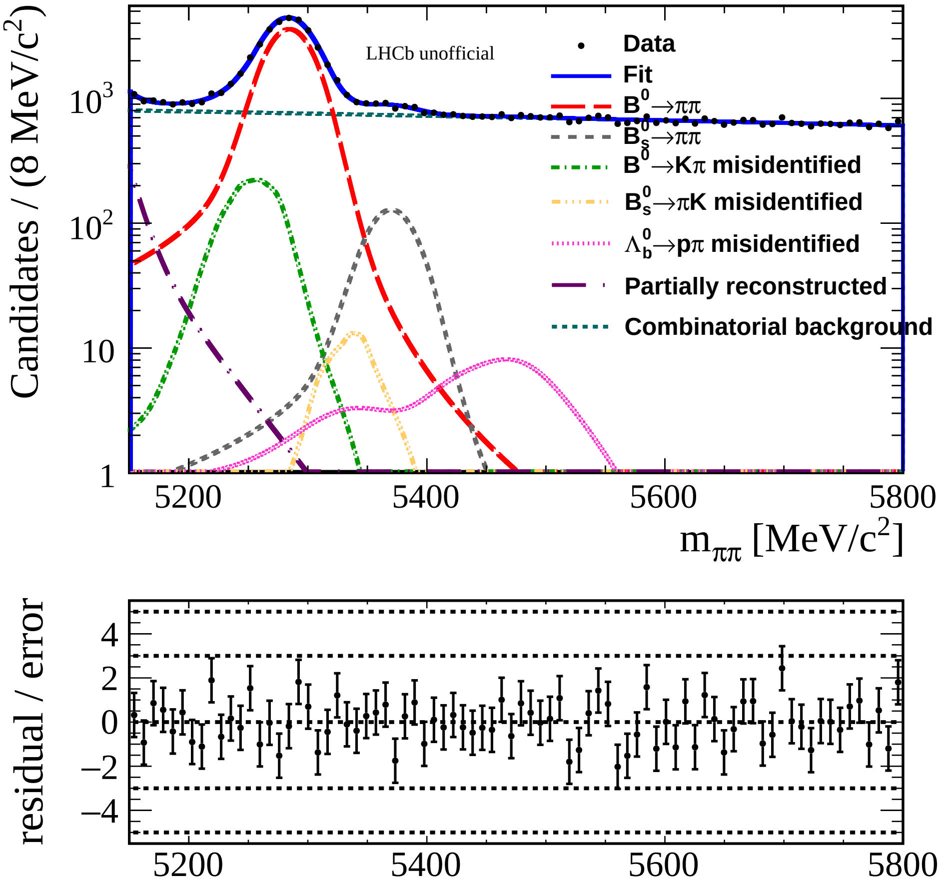

Figure 7.3: Mass distribution and fit to the $\pi^+\pi^-$ invariant mass spectrum. The upper plot shows the fit to the mass spectrum in a log scale. The lower plot shows the binned residuals. The black points represent the data points and the blue line shows the full fit.

7.2.4 Mass fit to $p\pi^-$ final state

The invariant mass spectrum of the $p\pi^-$ final state hypothesis is fitted over a mass range of 5400 - 5900 MeV/c^2, which is shown in Figure 7.4. Candidates with decay time less than 0.6 ps and greater than 10 ps are not included in the fit. The total number of candidates in this fit is 28407, the number of $\Lambda_b^0 \to p\pi^-$ signal candidates are

$$N_{\Lambda_b^0 \to p\pi^-} = 4319 \pm 106.$$

The parameters of the fit are included in Appendix C.

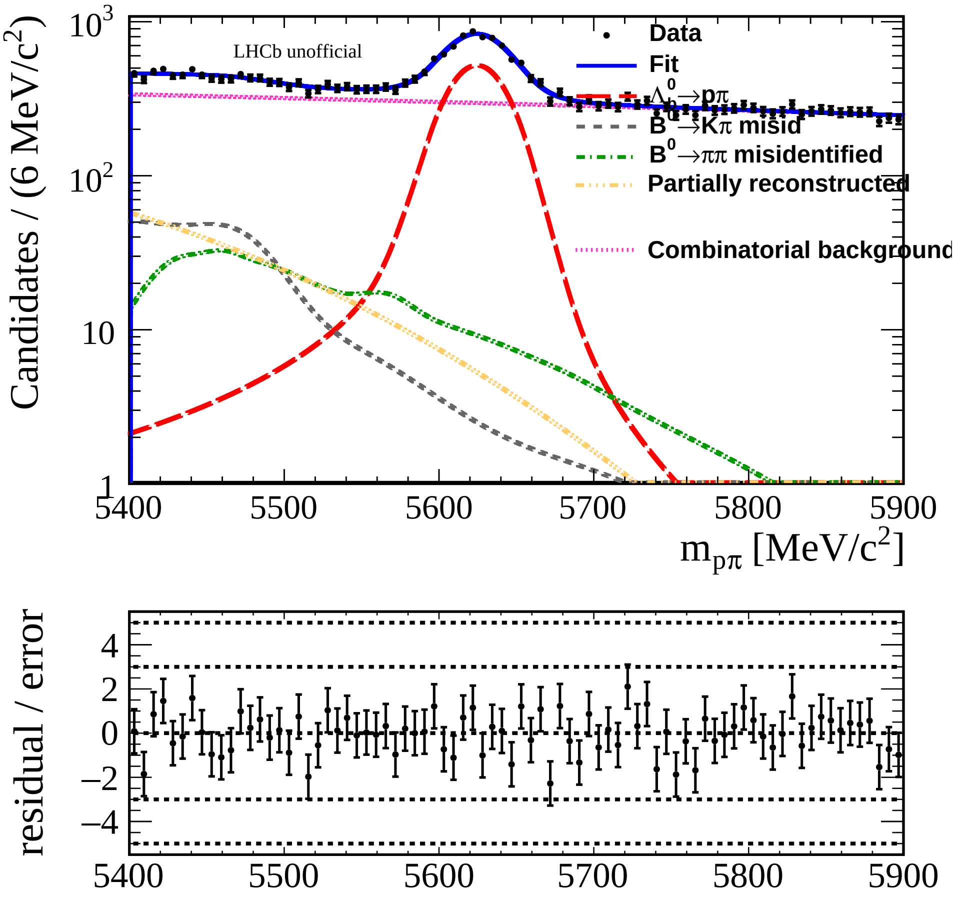

Figure 7.4: Mass distribution and fit to the $p\pi^-$ invariant mass spectrum. The upper plot shows the fit to the mass spectrum in a log scale. The lower plot shows the binned residuals. The black points represent the data points and the blue line shows the full fit.

7.2.5 Mass fit to pK^- final state

The invariant mass spectrum of the pK^- final state hypothesis is fitted over a mass range of 5400 - 5900 MeV/c^2, which is shown in Figure 7.5. Candidates with decay time less than 0.6 ps and greater than 10 ps are not included in the fit. The total number of candidates in this fit is 24470, the number of $\Lambda_b^0 \to pK^-$ signal candidates are

$$N_{\Lambda_b^0 \to pK^-} = 6002 \pm 123.$$

The parameters of the fit are included in Appendix C.

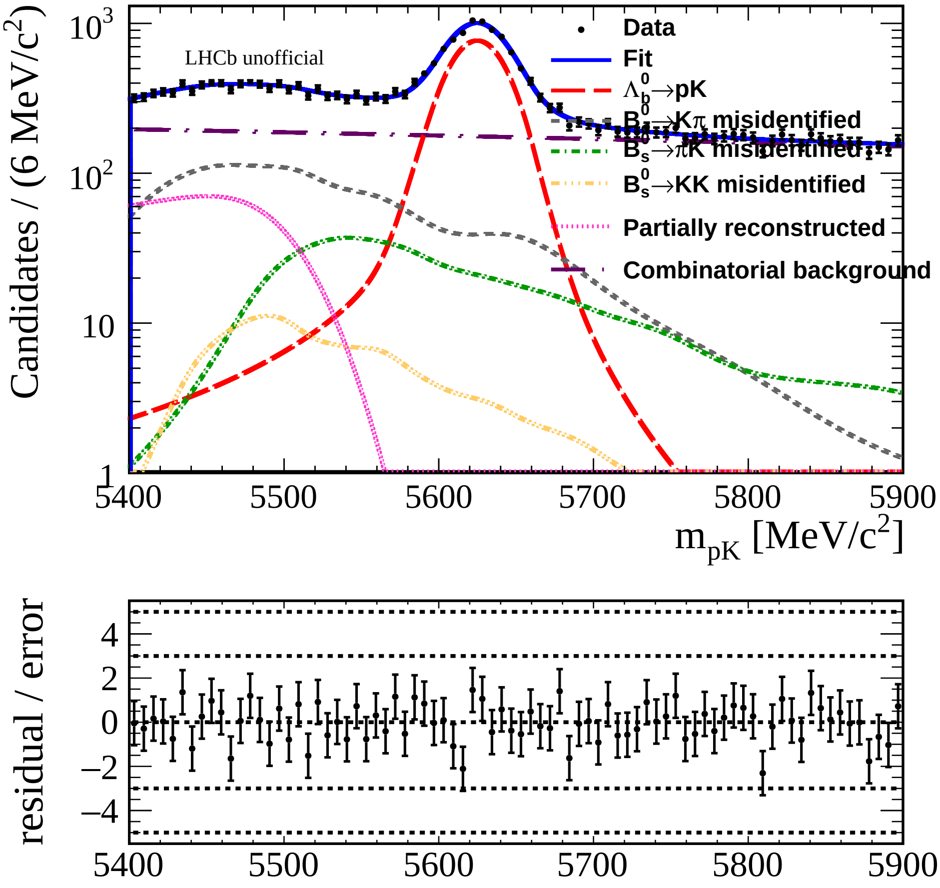

Figure 7.5: Mass distribution and fit to the pK^- invariant mass spectrum. The upper plot shows the fit to the mass spectrum in a log scale. The lower plot shows the binned residuals. The black points represent the data points and the blue line shows the full fit.

7.3 Lifetime Measurement Results

This section presents the results of the decay-time fits to the LHCb run 1 data sample. The decay-time acceptance for each individual candidate has been evaluated with the swimming method described in Chapter 5.1. The signal and background fractions have been recovered using the results of mass fits shown previously. Due to discrepancies between the fitted and generated lifetimes observed in the simulated data all measured lifetimes are systematics dominated.

7.3.1 Decay-time fit to the K^+K^- final state

The decay-time distribution of the K^+K^- final state candidates is fitted over a range of 0.6 - 12 ps, which is shown in Figure 7.6. The fit models the data very well apart from a small deviation in the first two decay-time bins. This fit measures the $B_s^0 \rightarrow K^+K^-$ lifetime as

$$\tau_{B_s^0 \rightarrow K^+K^-} = 1.410 \pm 0.009 \pm 0.011\text{ps}.$$

Figure 7.7 shows the acceptance functions for the signal and background channels in the K^+K^- distribution, which have been evaluated with the swimming algorithm.

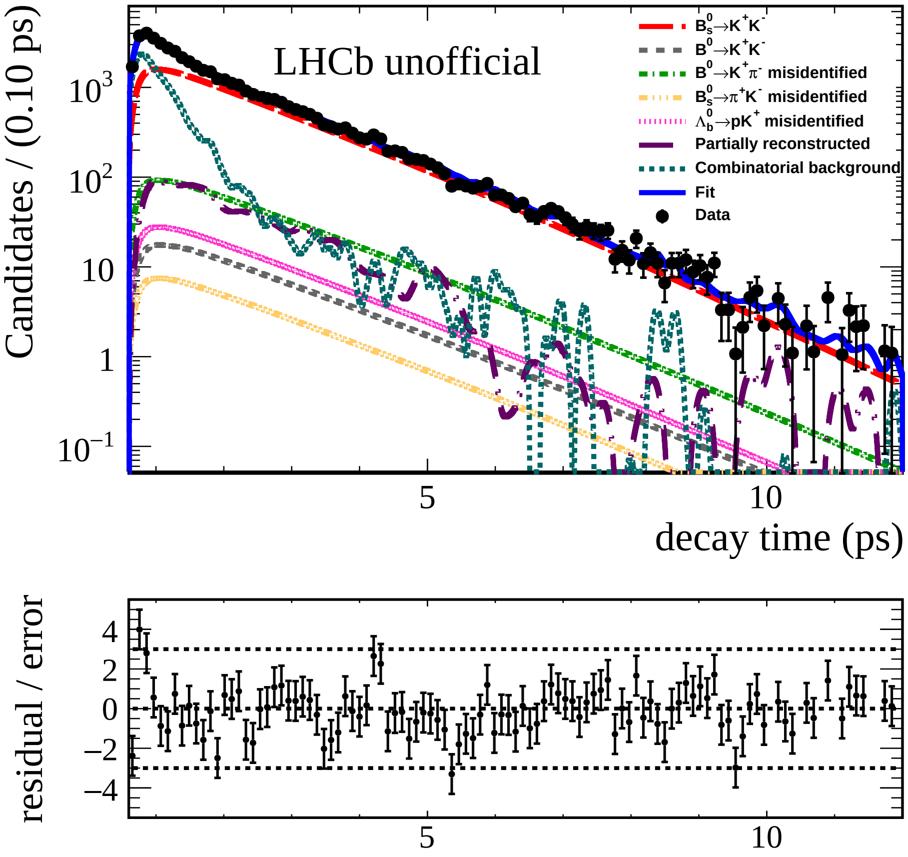

Figure 7.6: Decay-time distribution and fit to the K^+K^- final state. The upper plot shows the fit to the decay-time distribution in a log scale. The lower plot shows the binned residuals. The black points represent the data points and the blue line shows the full fit.

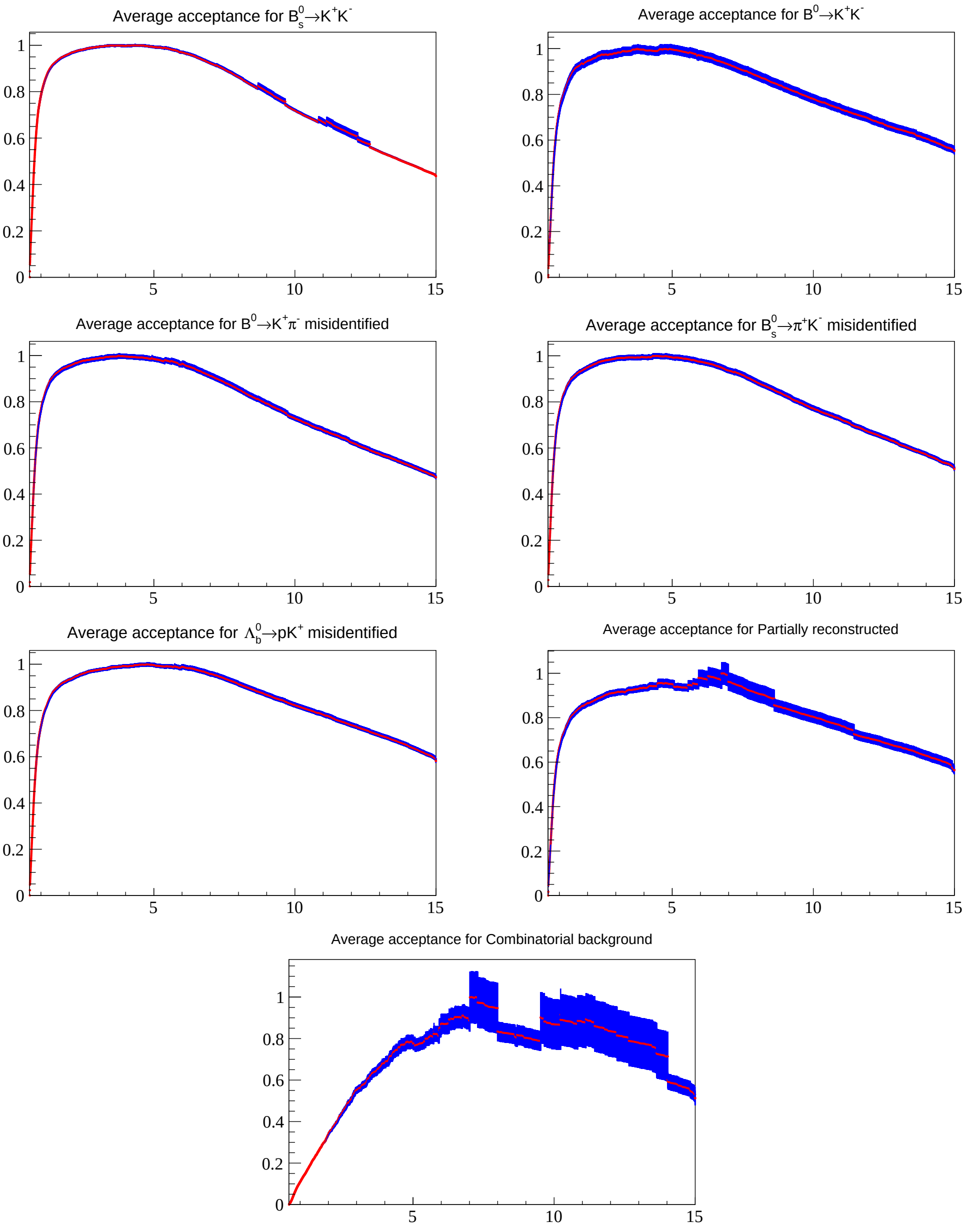

Figure 7.7: Acceptance functions used in the decay-time fit to the K^+K^- final state. The red line represents the function and the blue area represents the statistical uncertainty on the function.

7.3.2 Decay-time fit to the $K^+\pi^-$ final state

The decay-time distribution of the $K^+\pi^-$ final state candidates is fitted over a range of 0.6 - 12 ps, which is shown in Figure 7.8. This fit measures the $B^0 \to K^+\pi^-$ lifetime as

$$\tau_{B^0\to K^+\pi^-} = 1.504 \pm 0.006 \pm 0.029 \text{ ps},$$

and measures the $B_s^0 \to \pi^+K^-$ lifetime as

$$\tau_{B_s^0\to \pi^+K^-} = 1.548 \pm 0.028 \pm 0.029 \text{ ps}.$$

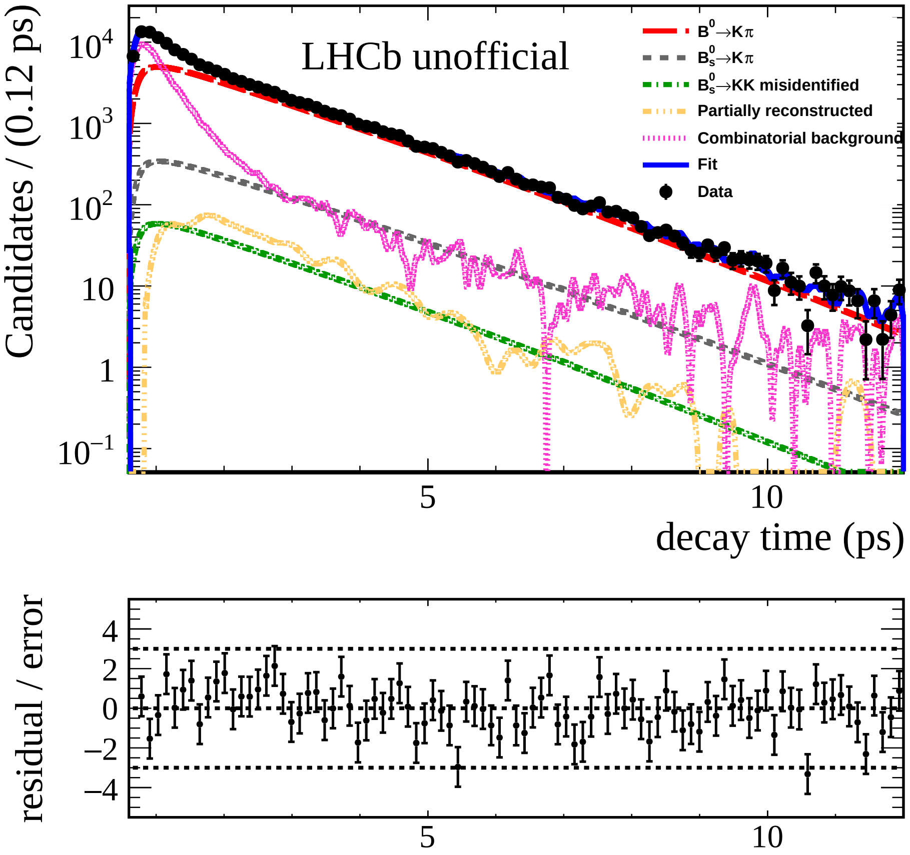

Figure 7.8: Decay-time distribution and fit to the $K^+\pi^-$ final state. The upper plot shows the fit to the decay-time distribution in a log scale. The lower plot shows the binned residuals. The black points represent the data points and the blue line shows the full fit.

Figure 7.9 shows the acceptance functions for the signal and background channels in the $K^+\pi^-$ distribution, which have been evaluated with the swimming algorithm.

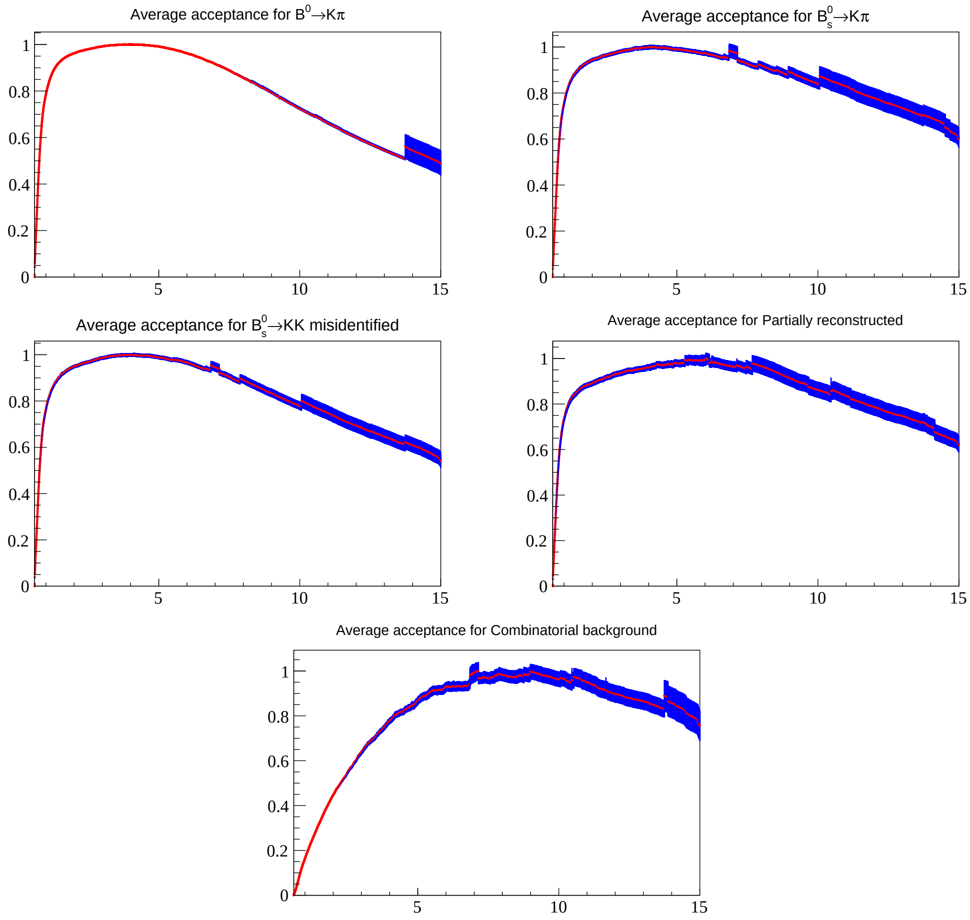

Figure 7.9: Acceptance functions used in the decay-time fit to the $K^+\pi^-$ final state. The red line represents the function and the blue area represents the statistical uncertainty on the function.

7.3.3 Decay-time fit to the $\pi^+\pi^-$ final state

The decay-time distribution of the $\pi^+\pi^-$ final state candidates is fitted over a range of 0.6 - 12 ps, which is shown in Figure 7.10. This fit measures the $B^0 \to \pi^+\pi^-$ lifetime as

$$\tau_{B^0\to\pi^+\pi^-} = 1.495 \pm 0.012 \pm 0.012 \text{ ps},$$

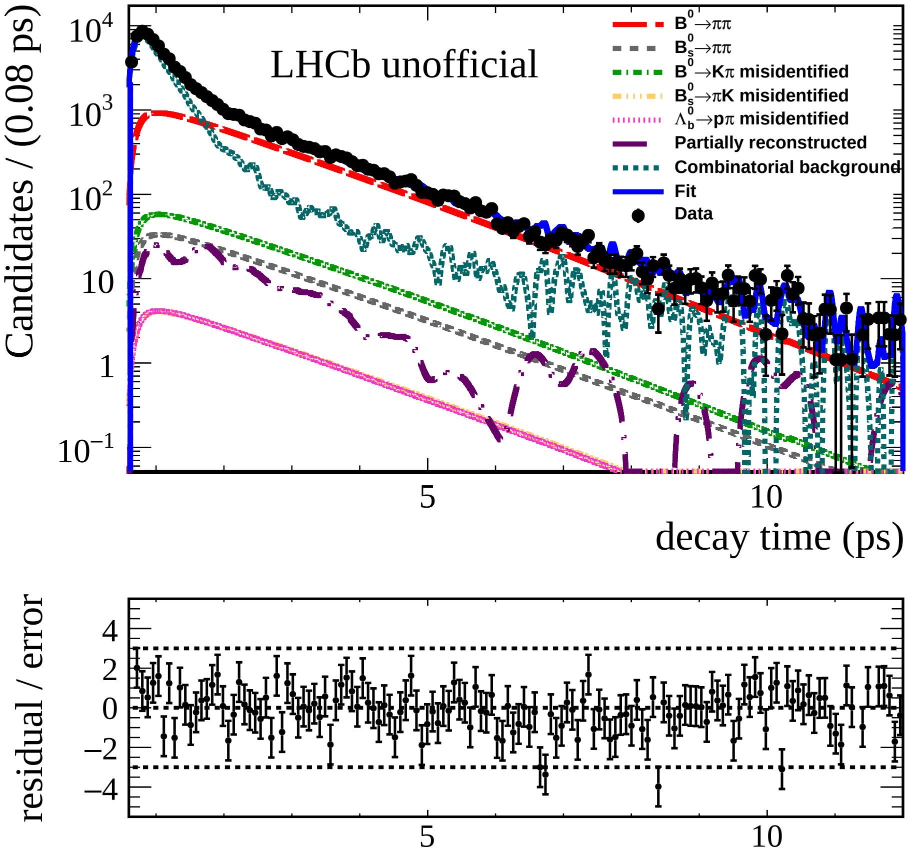

Figure 7.10: Decay-time distribution and fit to the $\pi^+\pi^-$ final state. The upper plot shows the fit to the decay time distribution in a log scale. The lower plot shows the binned residuals. The black points represent the data points and the blue line shows the full fit.

Figure 7.11 shows the acceptance functions for the signal and background channels in the $\pi^+\pi^-$ distribution, which have been evaluated with the swimming algorithm.

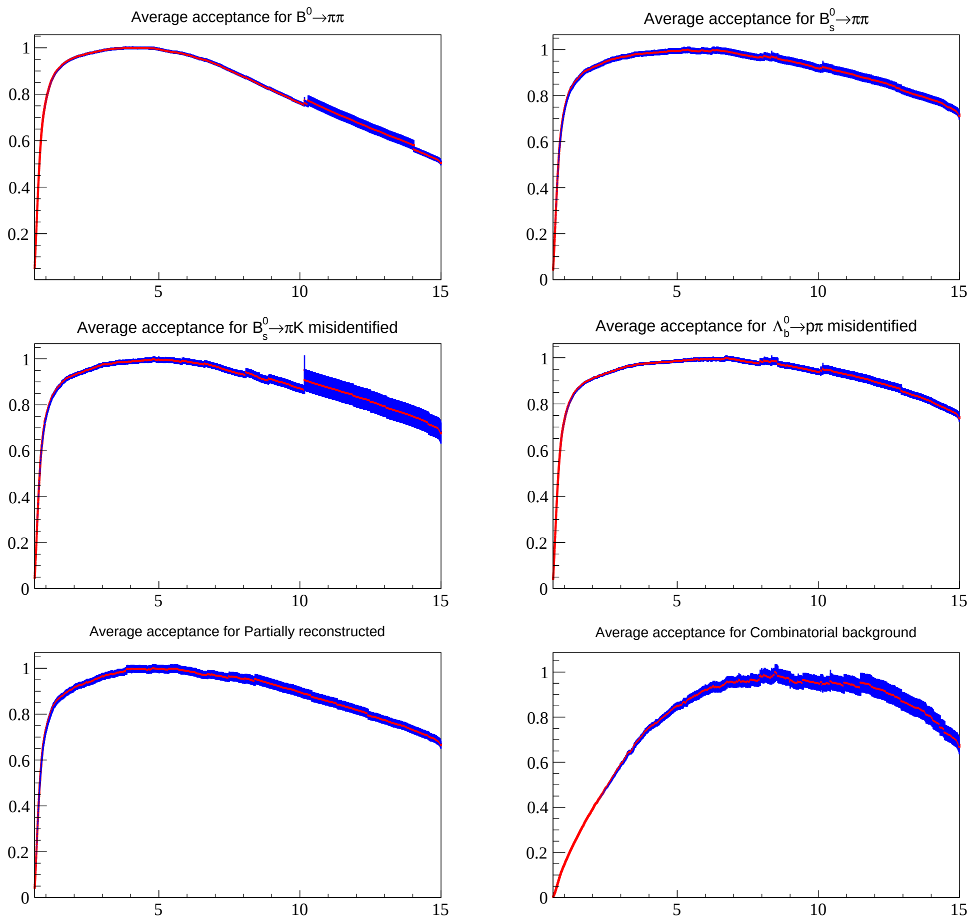

Figure 7.11: Acceptance functions used in the decay-time fit to the $\pi^+\pi^-$ final state. The red line represents the function and the blue area represents the statistical uncertainty on the function.

7.3.4 Decay-time fit to the $p\pi^-$ final state

The decay-time distribution of the $p\pi^-$ final state candidates is fitted over a range of 0.6 - 10 ps, which is shown in Figure 7.12. The fit models the data very well apart from a small deviation in the first decay time bin. This fit measures the $\Lambda_b^0 \to p\pi^-$ lifetime as

$$\tau_{\Lambda_b^0 \to p\pi^-} = 1.511 \pm 0.028 \pm 0.039 \text{ ps},$$

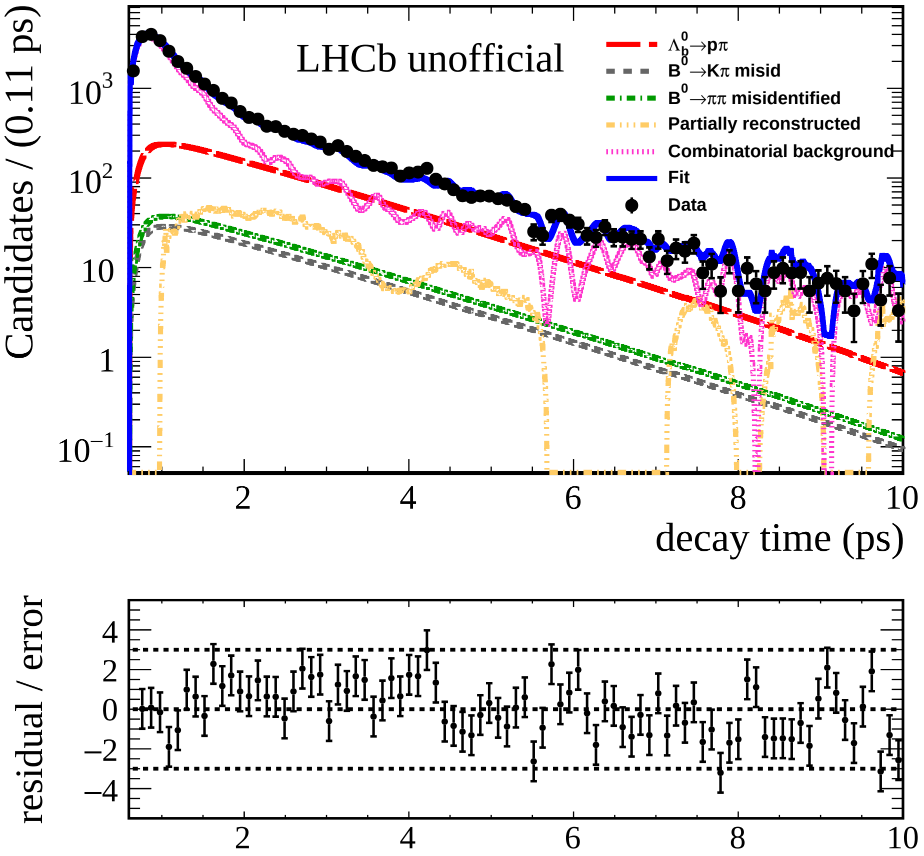

Figure 7.12: Decay-time distribution and fit to the $p\pi^-$ final state. The upper plot shows the fit to the decay-time distribution in a log scale. The lower plot shows the binned residuals. The black points represent the data points and the blue line shows the full fit.

Figure 7.13 shows the acceptance functions for the signal and background channels in the $p\pi^-$ distribution, which have been evaluated with the swimming algorithm.

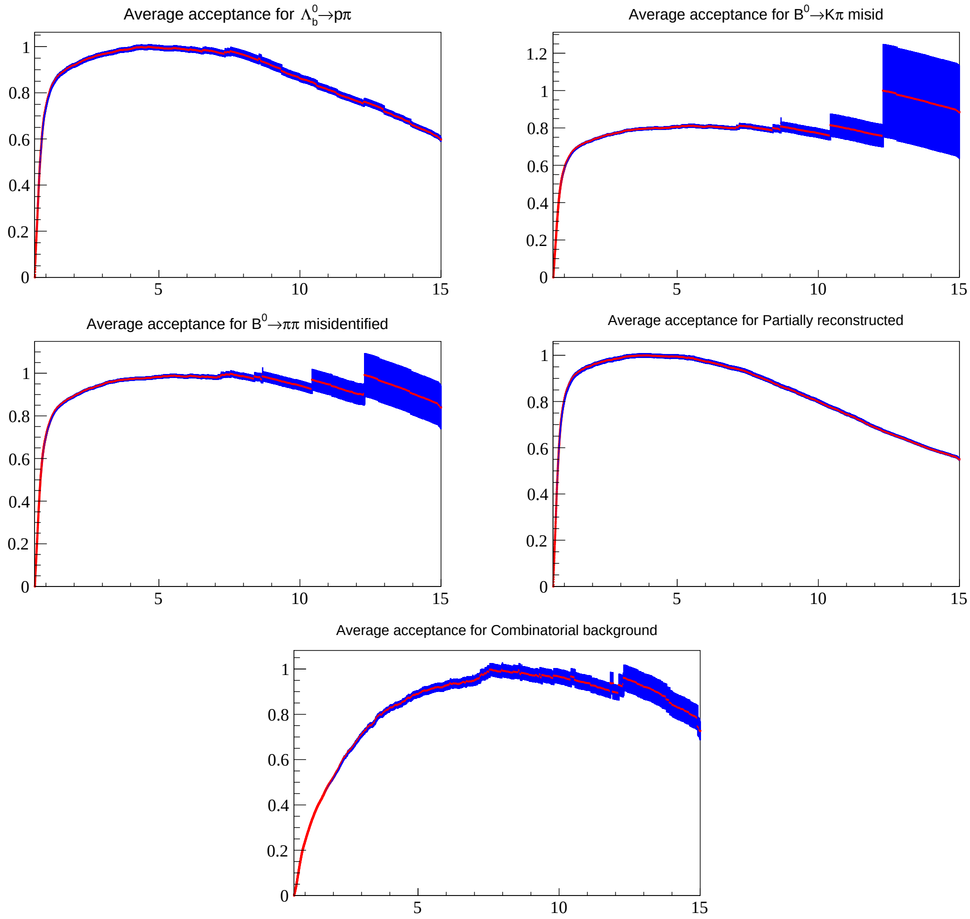

Figure 7.13: Acceptance functions used in the decay-time fit to the $p\pi^-$ final state. The red line represents the function and the blue area represents the statistical uncertainty on the function.

7.3.5 Decay-time fit to the pK^- final state

The decay-time distribution of the pK^- final state candidates is fitted over a range of 0.6 - 10 ps, which is shown in Figure 7.14. The fit models the data very well apart from a small deviation in the first two-decay time bins. This fit measures the $\Lambda_b^0 \to pK^-$ lifetime as

$$\tau_{\Lambda_b^0 \to pK^-} = 1.477 \pm 0.022 \pm 0.029 \text{ ps},$$

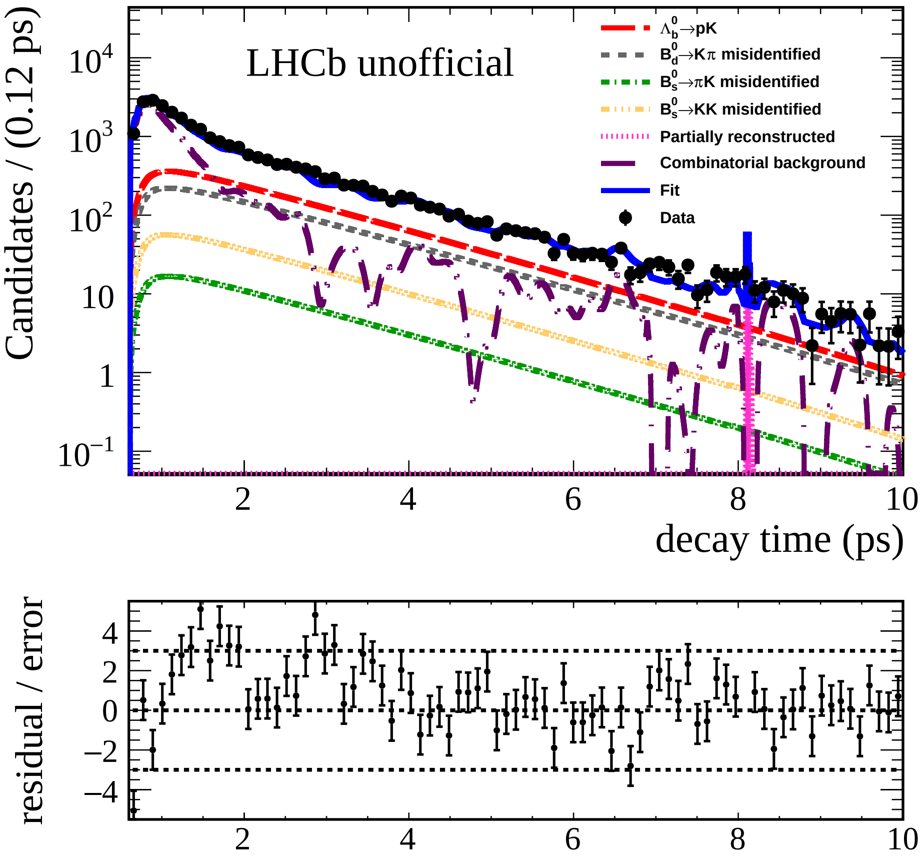

Figure 7.14: Decay-time distribution and fit to the pK^- final state. The upper plot shows the fit to the decay time distribution in a log scale. The lower plot shows the binned residuals. The black points represent the data points and the blue line shows the full fit.

Figure 7.15 shows the acceptance functions for the signal and background channels in the pK^- distribution, which have been evaluated with the swimming algorithm.

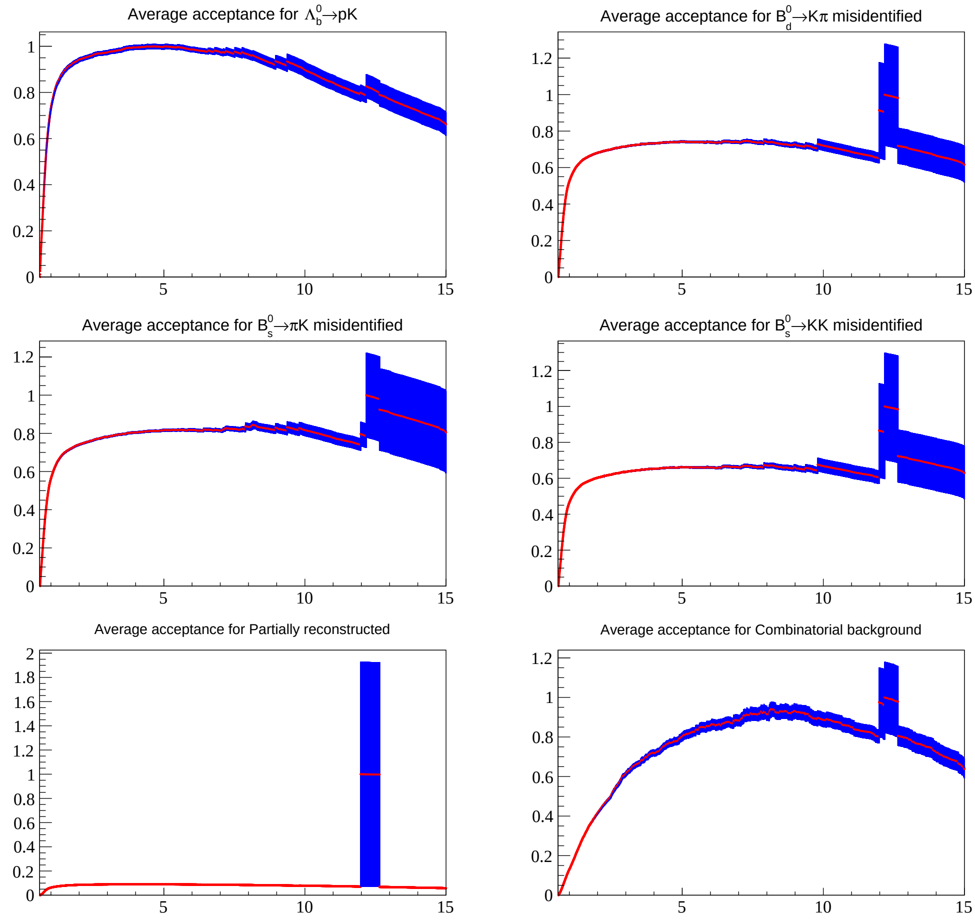

Figure 7.15: Acceptance functions used in the decay-time fit to the pK^- final state. The red line represents the function and the blue area represents the statistical uncertainty on the function.

7.4 Analysis of results

7.4.1 Calculation of $A_{\Delta\Gamma}$

The value of the decay-rate asymmetry can be calculated using Equations 1.42 and 1.43. Together they result in the expression

$$A_{\Delta\Gamma} = \frac{2\Gamma_s^2}{\Delta\Gamma_s}\tau_{B_s^0\to K^+K^-} - \frac{2\Gamma_s}{\Delta\Gamma_s}. \tag{7.1}$$

Inputing in the known values of $\Gamma_s = 0.6645 \pm 0.0022\,\mathrm{ps}^{-1}$, $\Delta\Gamma_s = 0.086 \pm 0.006\,\mathrm{ps}^{-1}$ from [34] and $\tau_{B_s^0\to K^+K^-}$ measured in the analysis presented in this thesis, results in

$$A_{\Delta\Gamma} = -0.975 \pm 0.092\ (stat) \pm 0.113\ (syst) \pm 0.082\ (ext),$$

where the first uncertainty comes from the statistical uncertainty on $\tau_{B_s^0\to K^+K^-}$, the second uncertainty comes from the systematic uncertainty on $\tau_{B_s^0\to K^+K^-}$ and the third uncertainty comes from the uncertainty on Γ_s and $\Delta\Gamma_s$. The result is consistent with the SM prediction of $A_{\Delta\Gamma}^{SM} = -0.972^{+0.014}_{-0.009}$ [38] and is consistent with the indirect measurement of $A_{\Delta\Gamma} = 0.947 \pm 0.021$ from the time-dependent analysis of $B_s^0 \to K^+K^-$ [31].

Combining this with the measured $C_{K^+K^-} = 0.24 \pm 0.06 \pm 0.02$ and $S_{K^+K^-} = 0.22 \pm 0.06 \pm 0.02$ [31], gives

$$(S_f)^2 + (C_f)^2 + (A_{\Delta\Gamma})^2 = 1.06 \pm 0.329,$$

which is consistent with 1.

7.4.2 Calculation of Average B_d^0 and Λ_b^0 Lifetimes

The combined measurements of the $B^0 \to K^+\pi^-$ and $B^0 \to \pi^+\pi^-$ lifetimes result in an average B_d^0 lifetime of

$$\tau_{B^0} = 1.501 \pm 0.005\text{ ps (stat)}\ {}^{+0.026}_{-0.020}\text{ ps (syst)},$$

and the combined measurements of the $\mathit{\Lambda}_b^0 \to p\pi^-$ and $\mathit{\Lambda}_b^0 \to pK^-$ lifetimes result in an average Λ_b^0 lifetime of

$$\tau_{\Lambda_b^0} = 1.496 \pm 0.017\text{ ps (stat)}\ {}^{+0.027}_{-0.041}\text{ ps (syst)}.$$

The statistical errors of each lifetime are assumed to be uncorrelated and are combined as such. The systematic errors are conservatively taken as the largest spread in decay time allowed by errors on the individual B^0 and Λ_b^0 lifetimes.

7.5 Summary

To summarise, this chapter has presented results of the six dominant $B \to h^+h^{'-}$ decay modes using $3\,\mathrm{fb}^{-1}$ of run 1 LHCb data. The measured lifetimes are

$$\begin{aligned}
\tau_{B^0_s\to K^+K^-} &= 1.410 \pm 0.009 \text{ ps (stat)} \;\pm 0.011 \text{ ps (syst)},\\
\tau_{B^0\to K^+\pi^-} &= 1.504 \pm 0.006 \text{ ps (stat)} \;\pm 0.023 \text{ ps (syst)},\\
\tau_{B^0_s\to \pi^+K^-} &= 1.548 \pm 0.028 \text{ ps (stat)} \;\pm 0.023 \text{ ps (syst)},\\
\tau_{B^0\to \pi^+\pi^-} &= 1.495 \pm 0.012 \text{ ps (stat)} \;\pm 0.007 \text{ ps (syst)},\\
\tau_{\Lambda^0_b\to p\pi^-} &= 1.511 \pm 0.028 \text{ ps (stat)} \;\pm 0.012 \text{ ps (syst)},\\
\tau_{\Lambda^0_b\to pK^-} &= 1.477 \pm 0.022 \text{ ps (stat)} \;\pm 0.022 \text{ ps (syst)}.
\end{aligned}$$

All the values agree with each other and the current world average lifetimes, which are $\tau_{B^0_s\to K^+K^-} = 1.408 \pm 0.017$, $\tau_{B^0_s} = 1.516 \pm 0.014$, $\tau_{B^0} = 1.520 \pm 0.004$ and $\tau_{\Lambda^0_b} = 1.470 \pm 0.010$ [34]. The measured $\tau_{B^0_s\to K^+K^-}$, $\tau_{B^0\to K^+\pi^-}$, $\tau_{B^0_s\to \pi^+K^-}$ and $\tau_{\Lambda^0_b\to pK^-}$ agree within 1σ of these world averages. The measured $\tau_{B^0\to\pi^+\pi^-}$ and $\tau_{\Lambda^0_b\to p\pi^-}$ agrees within 2σ. The $B^0_s \to K^+K^-$ lifetime is used to calculate the decay rate asymmetry $A_{\Delta\Gamma} = -0.975 \pm 0.092\ (stat) \pm 0.113\ (syst) \pm 0.082\ (ext)$. This value agrees with the SM prediction of $A^{SM}_{\Delta\Gamma} = -0.972^{+0.014}_{-0.009}$ [38]. Improved lifetime fits to the low decay times could decrease the difference between the measured lifetimes and the world average values. Work on this will continue, with the aim of reducing the systematic uncertainties to produce world-best measurements of the $B^0_s \to K^+K^-$ effective lifetimes and competitive measurements of the B^0 and Λ^0_b lifetimes that will improve the world average of these measurements.

Chapter 8

Conclusions and Outlook

This thesis presents lifetime measurements of charmless two-body decays of B hadrons, specifically the six decay modes with the highest branching fractions in the category of decays labelled $B \to h^+h'^-$. These are $B_s^0 \to K^+K^-$, $B^0 \to K^+\pi^-$, $B_s^0 \to \pi^+K^-$, $\Lambda_b^0 \to p\pi^-$ and $\Lambda_b^0 \to pK^-$. The measurements are performed using LHCb data with an integrated luminosity of $3\,\text{fb}^{-1}$ collected at centre of mass energies of 7 TeV and 8 TeV. The candidates were selected using a boosted decision tree trained with kinematic variables and particle identification selections were used to separate between final daughter states. One of the main features of the fit method is the event-by-event determination of decay-time acceptance, known as the swimming algorithm, which involves artificially moving the primary vertex along the momentum vector of the mother particle. This identifies intervals in decay-time where an event is accepted based on the selections applied to the candidates.

The results of this analysis are

$$\begin{aligned}
\tau_{B_s^0 \to K^+K^-} &= 1.410 \pm 0.009 \text{ ps (stat)} \ \pm 0.011 \text{ ps (syst)}, \\
\tau_{B^0 \to K^+\pi^-} &= 1.504 \pm 0.006 \text{ ps (stat)} \ \pm 0.023 \text{ ps (syst)}, \\
\tau_{B_s^0 \to \pi^+K^-} &= 1.548 \pm 0.028 \text{ ps (stat)} \ \pm 0.023 \text{ ps (syst)}, \\
\tau_{B^0 \to \pi^+\pi^-} &= 1.495 \pm 0.012 \text{ ps (stat)} \ \pm 0.007 \text{ ps (syst)}, \\
\tau_{\Lambda_b^0 \to p\pi^-} &= 1.511 \pm 0.028 \text{ ps (stat)} \ \pm 0.012 \text{ ps (syst)}, \\
\tau_{\Lambda_b^0 \to pK^-} &= 1.477 \pm 0.022 \text{ ps (stat)} \ \pm 0.022 \text{ ps (syst)}.
\end{aligned}$$

The lifetime measurements of $\tau_{B_s^0 \to K^+K^-}$, $\tau_{B^0 \to K^+\pi^-}$ and $\tau_{B_s^0 \to \pi^+K^-}$ are systematics dominated, the lifetime measurements of $\tau_{B^0\to\pi^+\pi^-}$ and $\tau_{\Lambda_b^0\to p\pi^-}$ are statistically dominated and the lifetime measurement of $\tau_{\Lambda_b^0\to pK^-}$ has a statistical and systematic error of equal size. The systematics are much larger than expected due to the fact that for samples of fully simulated MC data, the generated lifetimes could not be recovered. The cause of this discrepancy is unknown and further work on understanding this discrepancy is required to improve precision. A reduction on the systematic uncertainties could produce the worlds most precise $B_s^0\to K^+K^-$ effective lifetime measurement.

The decay rate asymmetry calculated with the measurement of the $B_s^0 \to K^+K^-$ effective lifetime presented in this thesis is

$$A_{\Delta\Gamma} = -0.975 \pm 0.092\ (stat) \pm 0.113\ (syst) \pm 0.082\ (ext),$$

which agrees with the Standard Model prediction.

The combined lifetime measurements of $B^0 \to K^+\pi^-$ and $B^0 \to \pi^+\pi^-$ result in an average B_d^0 lifetime of $\tau_{B^0} = 1.501 \pm 0.005$ ps (stat) $^{+0.026}_{-0.020}$ ps (syst), and the combined lifetimes measurements of $\Lambda_b^0\to p\pi^-$ and $\Lambda_b^0\to pK^-$ result in an average Λ_b^0 lifetime of $\tau_{\Lambda_b^0} = 1.496 \pm 0.017$ ps (stat) $^{+0.027}_{-0.041}$ ps (syst).

This thesis also presents a study on the performance of the RICH subdetector by measuring the photoelectron yields, N_{pe}, in RICH1 and RICH2 for the run 1 (2012) and run 2 (2015 and 2016) data-taking periods. The photoelectron yield directly affects the LHCb particle identification (PID) algorithm and any changes over run 1 and run 2 would indicate a deterioration on the PID performance. A statistically-driven method is used with low track multiplicity $pp \to pp\mu^+\mu^-$ events and higher track multiplicity D^* tagged $D^0 \to K^-\pi^+$ events. RICH1 N_{pe} measurement was shown to have increased between run 1 and run 2 by ~ 3 photoelectrons, which is predicted due to the removal of the aerogel radiator in the RICH 1 over the long shut down between 2012 and 2015. The RICH2 N_{pe} measurement remains approximately the same between run 1 and run 2. The effects of dust on the RICH 1 up box mirrors was also evaluated and causes a small reduction in N_{pe} for the top HPD box compared to the bottom HPD box. This will need to be monitored in future LHCb run 2 data taking, as the levels of dust on the RICH 1 mirrors could increase.

Further work on $B\to h^+h'^-$ lifetimes can be performed by using data collected during run 2. There has been $3\,\mathrm{fb}^{-1}$ of data collected at LHCb during 2015, 2016 and 2017. This can be combined with the run 1 data to improve the precision on the lifetimes measured in this thesis and also could be used to measure the lifetimes of $B \to h^+h^{'-}$ channels with smaller branching fractions.

Appendix A

D^* tagged $D^0 \to K^-\pi^+$ Event Selection in N_{pe} Studies

Selection Type	Selection
Daughter selections on π^+ and K^- from $D^0 \to K^-\pi^+$	$p_T > 800\,\text{MeV}$ $\chi^2_{IP} > 9.0$ $p > 5000$ MeV Track $\chi^2/d.o.f. < 3.0$
Combination selections on π^+ and K^- from $D^0 \to K^-\pi^+$	$p_T > 2000\,\text{MeV}$ $DOCAZ > 0.007$ mm $1765\ \text{MeV}/c^2 > m_{combination} > 1965\ \text{MeV}/c^2$
Selections on K^-	$DLL_{K\pi} > 5$ $\chi^2_{IP} > 16.0$
Selections on D^0	$p_T > 1500\,\text{MeV}$ Vertex $\chi^2/d.o.f. < 10.0$ Flight distance $\chi^2 > 49$ $IP\chi^2 < 30$ Track $\chi^2/d.o.f. < 5.0$ $DIRA > 0.9999$
Selections on π^+_{slow}	$p_T > 150\,\text{MeV}$ Track $\chi^2/d.o.f. < 5.0$
Selections on D^{*+}	Vertex $\chi^2/d.o.f. < 13.0$

Table A.1: Requirements on $D^{*+} \to D^0(\to K^-\pi^+)\pi^+$ 2012 data used for N_{pe} measurements.

Table A.1 shows the requirements on $D^{*+} \to D^0(\to K^-\pi^+)\pi^+$ 2012 data used for photon yield studies. The pion originating from the D^{*+} decay is referred to as a slow pion, π^+_{slow} , due to its lower momentum. Table A.2 shows the requirements on $D^{*+} \to D^0(\to K^-\pi^+)\pi^+$ 2015 data used for photon yield studies. The selections are different from the 2012 data due to availability of stripped data with information needed to perform photon yield measurements.

Selection Type	Selection
Daughter selections on π^+ and K^- from $D^0 \to K^-\pi^+$	$p_T > 250\,\mathrm{MeV}$ $\chi^2_{IP} > 9.0$ $p > 2000$ MeV $IP\chi^2 > 16$
Combination selections on π^+ and K^- from $D^0 \to K^-\pi^+$	p_T^π OR $p_T^K > 1000\,\mathrm{MeV}$ 1780 MeV/$c^2 > m_{combination} > 1950$ MeV/c^2
Selections on D^0	$p_T > 1500\,\mathrm{MeV}$ Vertex $\chi^2/d.o.f. < 10.0$ Flight distance $\chi^2 > 49$ $IP\chi^2 < 30$ $DIRA > 0.9999$
Selections on D^{*+}	$IP\chi^2/d.o.f. < 20.0$ Vertex $\chi^2/d.o.f. < 15.0$

Table A.2: Requirements on $D^{*+} \to D^0(\to K^-\pi^+)\pi^+$ 2015 data used for N_{pe} measurements.

Appendix B

Dependence of N_{pe} on Charged Track Multiplicity

Linear fits to the distributions of N_{pe} in bins of charged track multiplicity are shown in Figure B.1 and the values that the fit parameters converged to are listed in Table B.1.

Data sample	y-intercept	slope
RICH 1 2012 MC	22.85 ± 0.16	$(-2.23 \pm 0.54) \times 10^{-3}$
RICH 1 2012 data	22.27 ± 0.08	$(-0.81 \pm 0.21) \times 10^{-3}$
RICH 1 2015 data	25.35 ± 0.04	$(-4.13 \pm 0.12) \times 10^{-3}$
RICH 2 2012 MC	17.64 ± 0.19	$(2.55 \pm 0.67) \times 10^{-3}$
RICH 2 2012 data	17.29 ± 0.10	$(2.37 \pm 0.27) \times 10^{-3}$
RICH 2 2015 data	17.14 ± 0.03	$(1.95 \pm 0.10) \times 10^{-3}$

Table B.1: Linear fits results of N_{pe} in bins of charged track multiplicity for pion events.

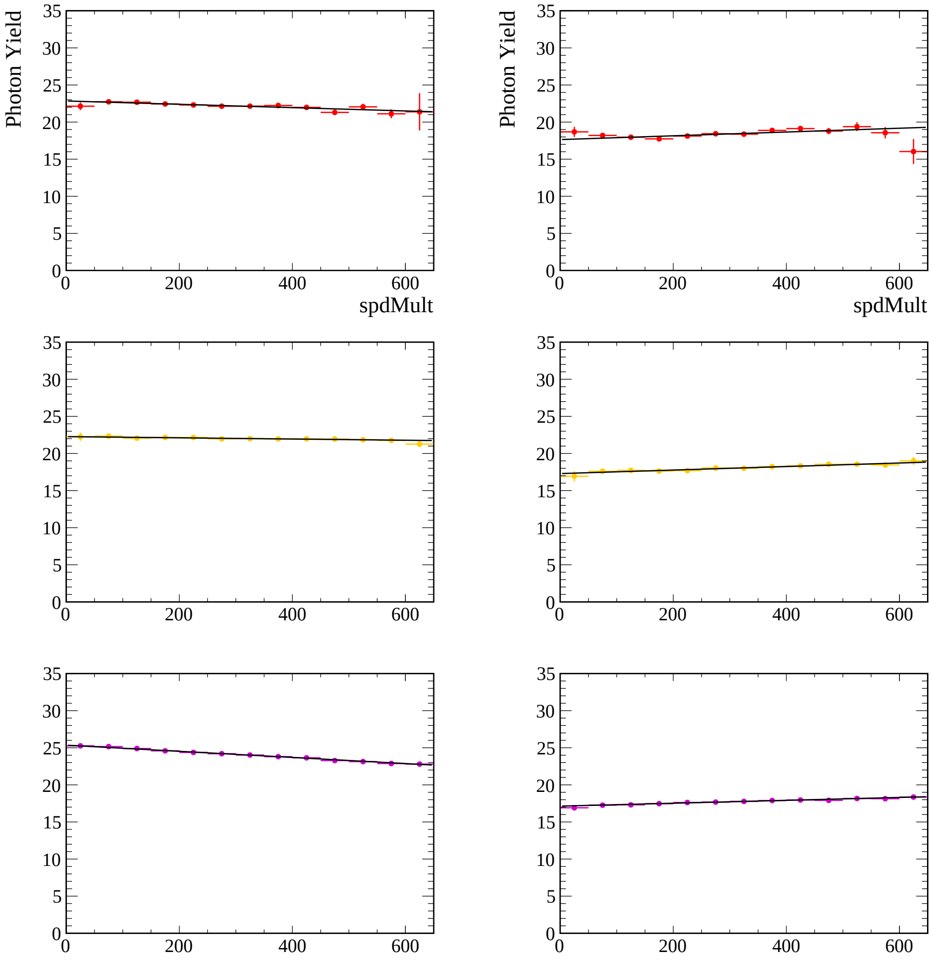

Figure B.1: Charged track multiplicity dependence on N_{pe} with linear fits to the distributions shown in black, for pion events. (Left) RICH 1, (right) RICH 2, (top) 2012 MC sample, (middle) 2012 data sample, (bottom) 2015 data sample.

Appendix C

Parameters of the $B \rightarrow h^+h^{'-}$ Mass Fits

This Appendix contains the parameters the mass-fits converge to for all $B \rightarrow h^+h^{'-}$ final states (K^+K^-, $K^+\pi^-$, $\pi^+\pi^-$, $p\pi^-$ and pK^-) with the run 1 data sample, listed in Tables C.1-C.5.

Parameter	Value
$f_{B^0_s\rightarrow K^+K^-}$	0.627 ± 0.003
$f_{B^0\rightarrow K^+K^-}$	0.008 ± 0.001
$f_{B^0\rightarrow K^+\pi^-}$	0.038 ± 0.003
$f_{B^0_s\rightarrow \pi^+K^-}$	0.005 ± 0.003
$f_{\Lambda^0_b\rightarrow pK^-}$	0.012 ± 0.005
f_{part}	0.033 ± 0.002
$\mu_{B^0_s}$	5372.17 ± 0.16 MeV/c^2
$\sigma_{B^0_s}$	20.11 ± 0.15 MeV/c^2
∇_{comb}	$(-5.738 \pm 1.919) \times 10^{-7}$ (MeV/c^2)$^{-1}$

Table C.1: Parameters of the converged mass fits to the LHCb run 1 data sample for the K^+K^- invariant mass spectrum.

Parameter	Value
$f_{B^0 \to K^+\pi^-}$	0.610 ± 0.002
$f_{B_s^0 \to \pi^+ K^-}$	0.044 ± 0.001
$f_{B_s^0 \to K^+ K^-}$	0.009 ± 0.001
f_{part}	0.008 ± 0.001
$\mu_{B_d^0}$	5284.84 ± 0.09 MeV/c^2
$\sigma_{B_d^0}$	20.23 ± 0.08 MeV/c^2
$\mu_{B_s^0}$	5371.38 ± 0.59 MeV/c^2
$\sigma_{B_s^0}$	20.58 ± 0.09 MeV/c^2
∇_{comb}	$(-1.126 \pm 0.059) \times 10^{-6}$ (MeV/$c^2)^{-1}$

Table C.2: Parameters of the converged mass fits to the LHCb run 1 data sample for the $K^+\pi^-$ invariant mass spectrum.

Parameter	Value
$f_{B^0 \to \pi^+\pi^-}$	0.290 ± 0.003
$f_{B_s^0 \to \pi^+\pi^-}$	0.011 ± 0.002
$f_{B^0 \to K^+\pi^-}$	0.019 ± 0.002
$f_{B_s^0 \to \pi^+ K^-}$	0.001 ± 0.002
$f_{\Lambda_b^0 \to p\pi^-}$	0.002 ± 0.002
f_{part}	0.007 ± 0.001
$\mu_{B_d^0}$	5284.44 ± 0.21 MeV/c^2
$\sigma_{B_d^0}$	20.82 ± 0.22 MeV/c^2
$\mu_{B_s^0}$	5369.94 ± 3.46 MeV/c^2
$\sigma_{B_s^0}$	21.18 ± 0.23 MeV/c^2
∇_{comb}	$(-6.548 \pm 0.531) \times 10^{-7}$ (MeV/$c^2)^{-1}$

Table C.3: Parameters of the converged mass fits to the LHCb run 1 data sample for the $\pi^+\pi^-$ invariant mass spectrum.

Parameter	Value
$f_{\Lambda_b^0 \to p\pi^-}$	0.152 ± 0.004
$f_{B^0 \to K^+\pi^-}$	0.029 ± 0.018
$f_{B^0 \to \pi^+\pi^-}$	0.029 ± 0.015
f_{part}	0.031 ± 0.023
$\mu_{\Lambda_b^0}$	5624.53 ± 0.61 MeV/c^2
$\sigma_{\Lambda_b^0}$	21.05 ± 0.67 MeV/c^2
∇_{comb}	$(-1.250 \pm 0.377) \times 10^{-6}$ (MeV/$c^2)^{-1}$

Table C.4: Parameters of the converged mass fits to the LHCb run 1 data sample for the $p\pi^-$ invariant mass spectrum.

Parameter	Value
$f_{\Lambda_b^0 \to pK^-}$	0.245 ± 0.005
$f_{B^0 \to K^+\pi^-}$	0.132 ± 0.018
$f_{B_s^0 \to \pi^+K^-}$	0.043 ± 0.062
$f_{B_s^0 \to K^+K^-}$	0.010 ± 0.035
f_{part}	0.044 ± 0.052
$\mu_{\Lambda_b^0}$	5624.85 ± 0.41 MeV/c^2
$\sigma_{\Lambda_b^0}$	19.97 ± 0.46 MeV/c^2
∇_{comb}	$(-1.055 \pm 0.359) \times 10^{-6}$ (MeV/c^2)$^{-1}$

Table C.5: Parameters of the converged mass fits to the LHCb run 1 data sample for the pK^- invariant mass spectrum.

Appendix D

2012 Monte Carlo Data Samples Used in the $B \rightarrow h^+h^{'-}$ Analysis

Table D.1 lists all 2012 MC samples used in the $B \rightarrow h^+h^{'-}$ lifetime analysis, with the branching ratios and size of initial sample included. These values are used to determine the partially reconstructed 3-body backgrounds in the $B \rightarrow h^+h^{'-}$ lifetime measurements.

Decay mode	Sample size	$\mathcal{B}\times(10^{-6})$
$B^0 \to K^+\pi^-$	1 529 495	$19.57\ ^{+0.53}_{-0.52}$
$B^0 \to \pi^+\pi^-$	3 067 742	5.10 ± 1.9
$B^0 \to K^+K^-$	2 035 242	$0.13\ ^{+0.06}_{-0.05}$
$B^0_s \to K^+K^-$	3 052 242	24.8 ± 1.7
$B^0_s \to \pi^+\pi^-$	2 030 741	0.76 ± 0.13
$B^0_s \to \pi^+K^-$	3 067 739	5.5 ± 0.5
$\Lambda^0_b \to p\pi^-$	1 509 492	3.5 ± 1.0
$\Lambda^0_b \to pK^-$	1 513 745	5.5 ± 1.4
$B^0 \to \pi^+\pi^-\pi^0$	2 554 495	50 (*)[a]
$B^0 \to K^+\pi^-\pi^0$	1 540 497	37.8 ± 3.2
$B^0 \to K^+K^-\pi^0$	2 554 490	2.17 ± 0.65
$B^0 \to K^0_s\pi^+\pi^-$	4 058 986	25.9 ± 1.0
$B^0 \to K^0_sK^\mp\pi^\pm$	4 034 487	3.3 ± 0.4
$B^0 \to K^0_sK^+K^-$	4 062 988	26.3 ± 1.5
$B^+ \to \pi^+\pi^-\pi^+$	2 029 494	15.2 ± 1.4
$B^+ \to \pi^+\pi^-K^+$	1 020 995	16.3 ± 2.0
$B^+ \to \pi^+K^-K^+$	1 024 197	5.0 ± 0.7
$B^+ \to K^+K^-K^+$	2 032 993	34.0 ± 1.0
$B^+ \to p\overline{p}\pi^+$	1 525 246	$1.62\ ^{+0.21}_{-0.20}$
$B^+ \to p\overline{p}K^+$	1 038 747	5.14 ± 0.25
$B^0_s \to K^-\pi^+\pi^0$	2 523 492	5 (*)
$B^0_s \to K^+K^-\pi^0$	1013498	20 (*)
$B^0_s \to K^0_s\pi^+\pi^-$	4 069 987	10 ± 3
$B^0_s \to K^0_sK^+K^-$	4 058 489	3.5 (*)[b]± 3
$B^0_s \to K^0_sK^\mp\pi^\pm$	4 046 483	49 ± 8
$\Lambda^0_b \to \Lambda^+_c\pi^-$	2 519 745	$4300\ ^{+360}_{-350}$
$\Lambda^0_b \to pK^-\eta$	6 130 488	3.5 (*)
$\Lambda^0_b \to pD^0\pi^-$	542 499	660 ± 70
$\Lambda^0_b \to pD^0K^-$	535 000	47 ± 8

Table D.1: MC 2012 samples for two- and three-body decays that could be reconstructed as $B \to h^+h'^-$. These samples are used to model the shapes of to signal and background classes. All branching fractions values are taken from [97] except the decays marked with (*), where the branching ratio is not known and the value for a similar decay is used. Sample size is the number of events in a sample before any event selection is applied. Footnotes: a) Listed as $< 720\times10^{-6}$ @ 90% C.L. in [104], b) Listed as $< 3.5\times10^{-6}$ @ 90% C.L. in [104].

Appendix E

Hadronisation Fractions

Measured quantity	Experimental result
f_u/f_d	1 (assumed)
f_s/f_d	0.259 ± 0.013
$f_s/(f_u + f_d)$	0.223 ± 0.004
$f_{\Lambda_b^0}/(f_u + f_d)$	0.223 ± 0.022
f_q	Used value
$f_d = f_u$	0.406
f_s	0.106
$f_{\Lambda_b^0}$	0.210

Table E.1: Hadronisation fractions used in the $B \to h^+h^{'-}$ lifetime analysis, measured quantities are taken from [97].

The b-hadron production fractions f_q represent the hadronisation probability to the b-hadron final state. In the $B \to h^+h^{'-}$ lifetime measurements the values of f_q are taken from [97], which uses the LHCb measurements [105, 106] to determine average values, and are list in Table E.1. These hadronisation fractions are used to predict the levels of background contamination for the two- and three-body backgrounds.

Appendix F

Mass Models of Simulated Monte-Carlo Data

This Appendix contains extra information on the fits to simulated Monte-Carlo data that is used to determine the shapes of signal and background classes in the $B \rightarrow h^{+}h^{'-}$ mass fits.

$B \rightarrow h^{+}h^{'-}$ Signal MC Fits

Figures F.1-F.4 show 2012 and 2011 simulated Monte-Carlo data fits with double crystal ball functions (DCB) [84]. The tail parameters from these fits are extracted and fixed in the fit to data in the $B \rightarrow h^{+}h^{'-}$ lifetime analysis. Table F.1 lists the tail parameters of the converged fits.

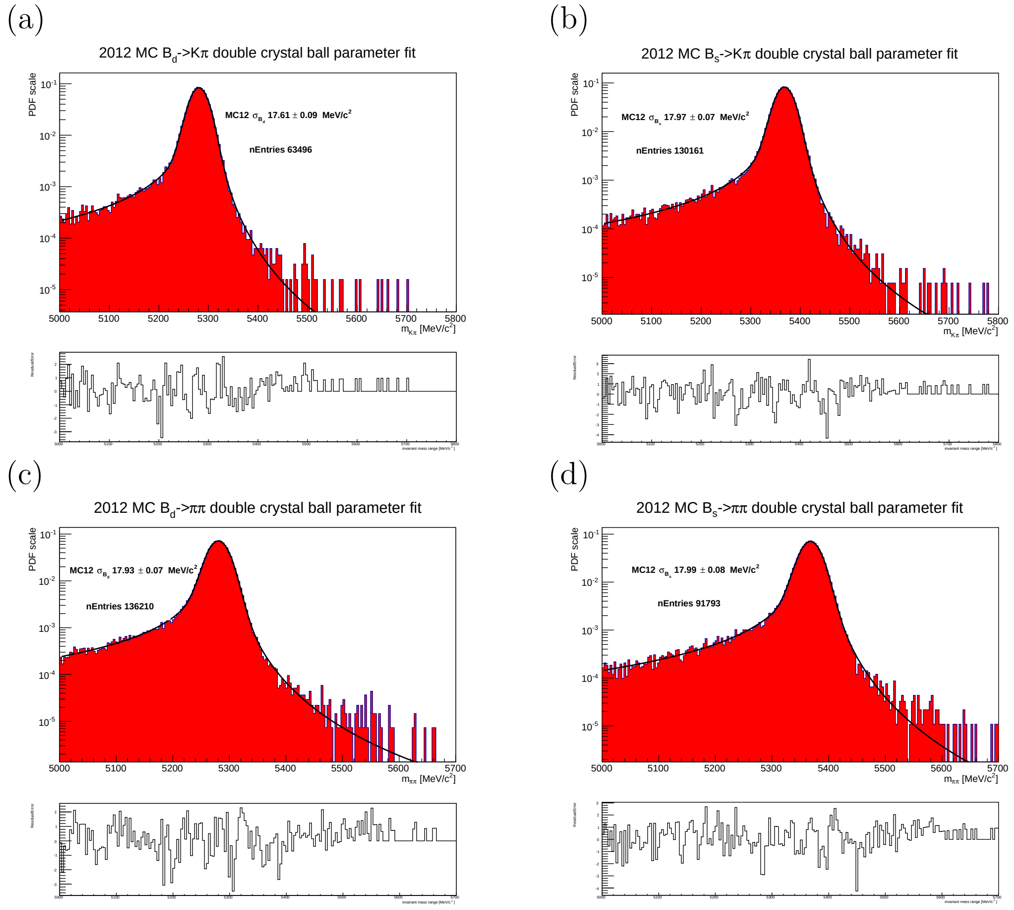

Figure F.1: Mass distributions and fit residuals of $B \to h^+h^{'-}$ signal 2012 MC with the full event selection applied. The distributions are fitted with double crystal ball functions [84], generalised from Equation 5.12. The radiative tails in the data, where mass regions are lower and higher than the central peak, are well described by the fits. (a) shows the $B^0 \to K^+\pi^-$ mass peak, (b) shows the $B_s^0 \to \pi^+K^-$ mass peak, (c) shows the $B^0 \to \pi^+\pi^-$ mass peak, (d) shows the $B_s^0 \to \pi^+\pi^-$ mass peak.

Three Body Partially Reconstructed Backgrounds

Table F.2 lists the parameters from the partially reconstructed background fits converged to, in all cases the fit was performed on a weighted samples of 2012 MC reconstructed as $B \to h^+h^{'-}$ events.

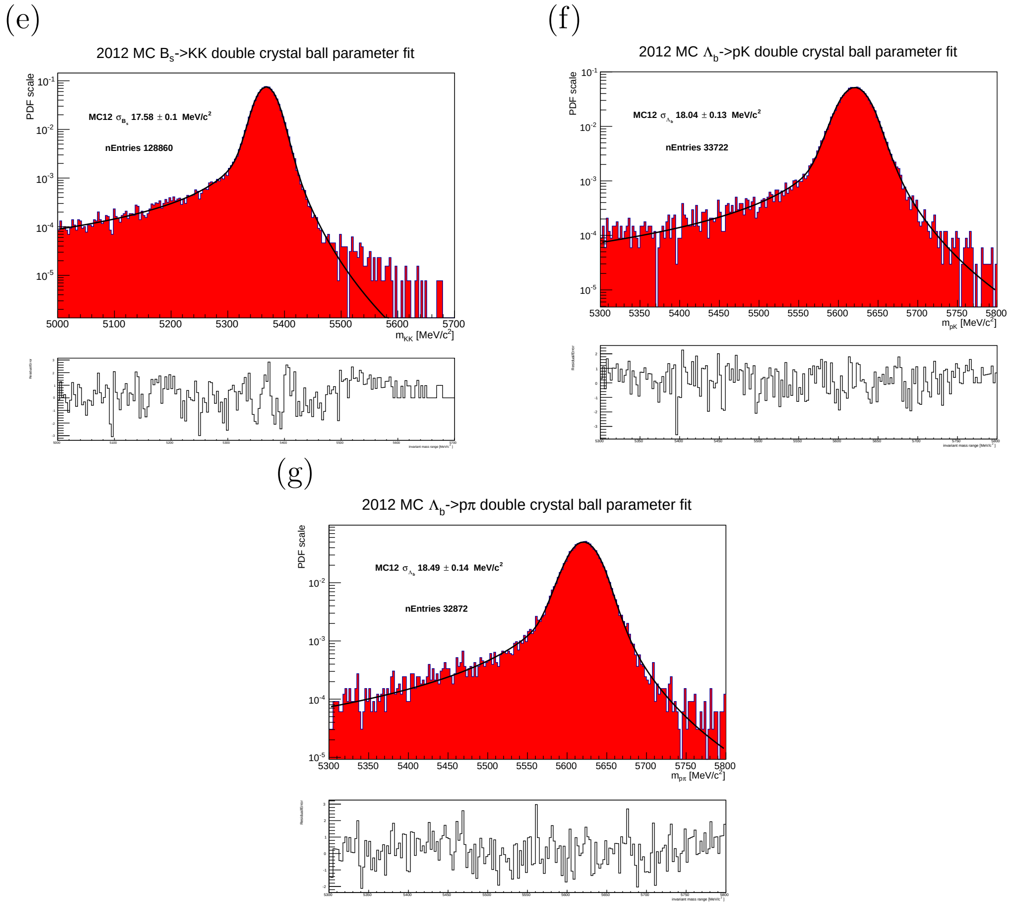

Figure F.2: Mass distributions and fit residuals of $B \to h^+h^{'-}$ signal 2012 MC with the full event selection applied. The distributions are fitted with double crystal ball functions [84], generalised from Equation 5.12. The radiative tails in the data, where mass regions are lower and higher than the central peak, are well described by the fits. (e) shows the $B_s^0 \to K^+K^-$ mass peak, (f) shows the $\Lambda_b^0 \to pK^-$ mass peak, (g) shows the $\Lambda_b^0 \to p\pi^-$ mass peak.

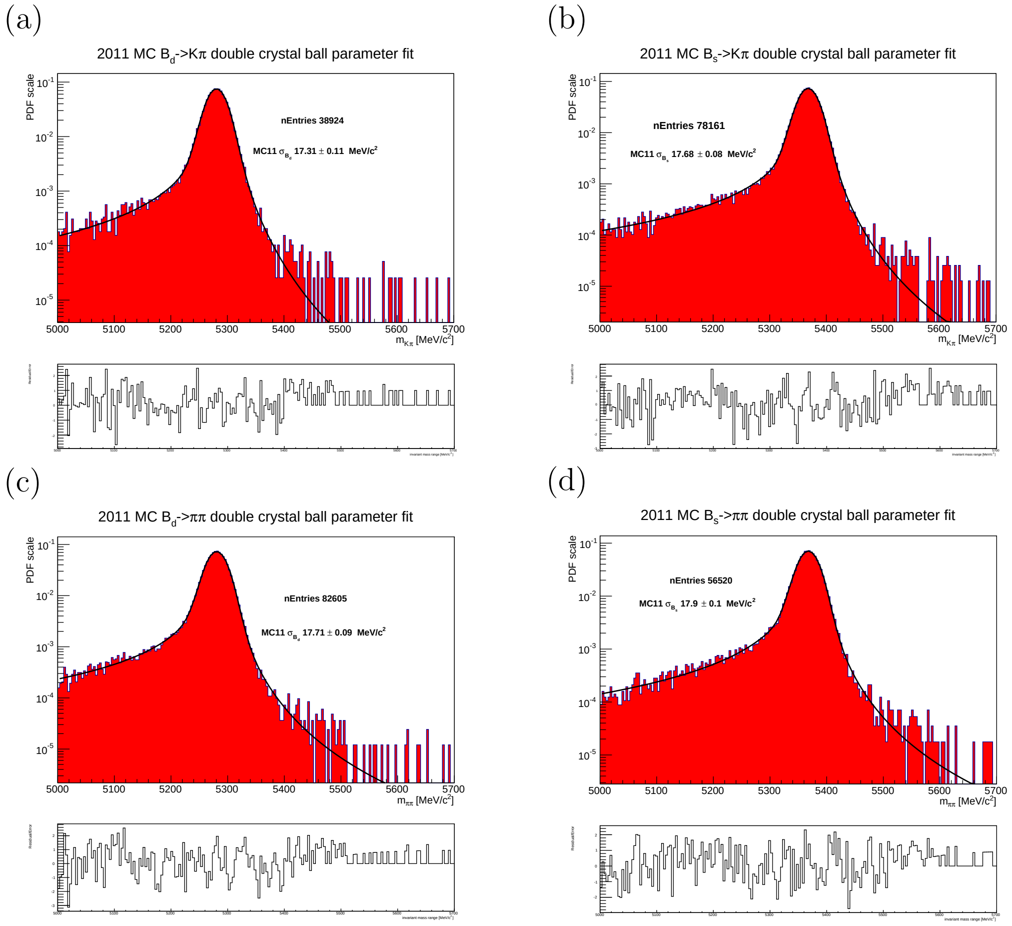

Figure F.3: Mass distributions and fit residuals of $B \to h^+ h^{'-}$ signal 2011 MC with the full event selection applied. The distributions are fitted with double crystal ball functions [84], generalised from Equation 5.12. The radiative tails in the data, where mass regions are lower and higher than the central peak, are well described by the fits. (a) shows the $B^0 \to K^+\pi^-$ mass peak, (b) shows the $B^0_s \to \pi^+ K^-$ mass peak, (c) shows the $B^0 \to \pi^+\pi^-$ mass peak, (d) shows the $B^0_s \to \pi^+\pi^-$ mass peak.

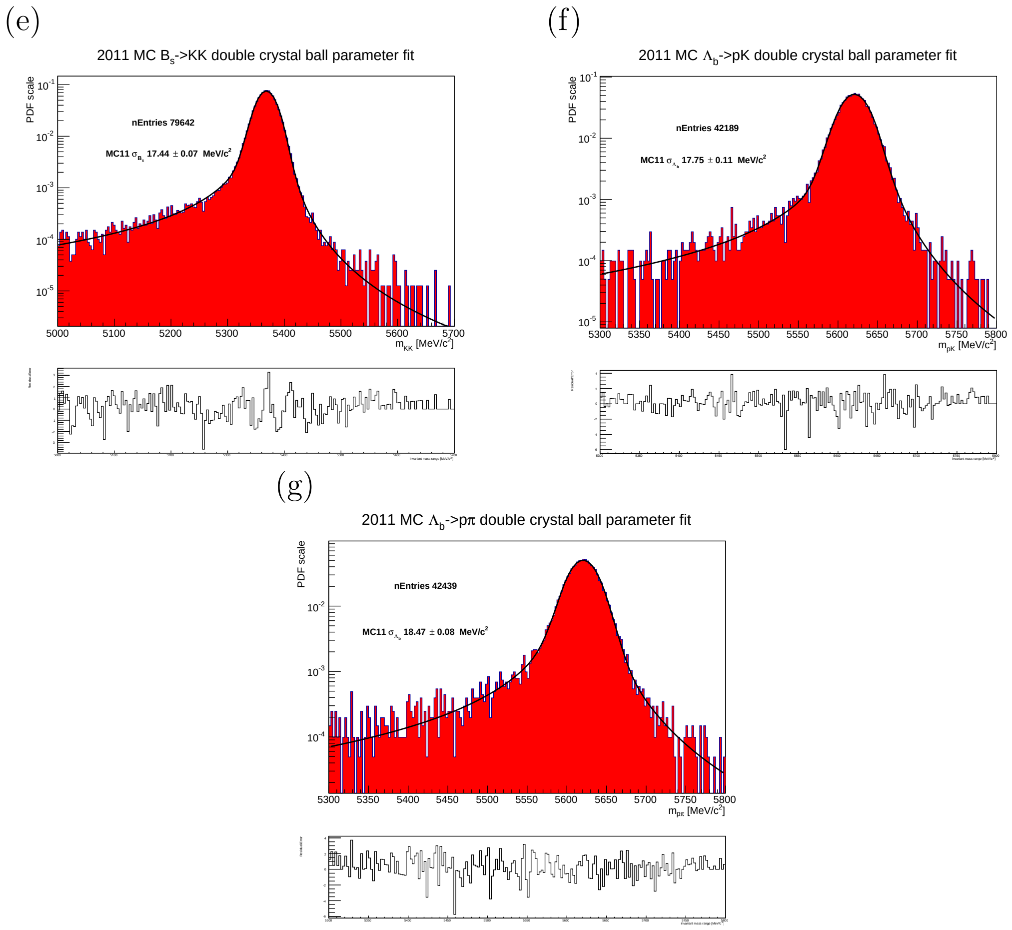

Figure F.4: Mass distributions and fit residuals of $B \to h^+h^{'-}$ signal 2011 MC with the full event selection applied. The distributions are fitted with double crystal ball functions [84], generalised from Equation 5.12. The radiative tails in the data, where mass regions are lower and higher than the central peak, are well described by the fits. (e) shows the $B_s^0 \to K^+K^-$ mass peak, (f) shows the $\Lambda_b^0 \to pK^-$ mass peak, (g) shows the $\Lambda_b^0 \to p\pi^-$ mass peak.

Paramter	Value
$B_s^0 \to K^+K^-$	
α_{CBL}	1.631 ± 0.113
α_{CBH}	1.731 ± 0.081
n_{CBL}	1.468 ± 0.053
n_{CBH}	7.225 ± 1.259
fraction	0.4307 ± 0.0825
$B^0 \to K^+\pi^-$	
α_{CBL}	1.276 ± 0.112
α_{CBH}	1.969 ± 0.079
n_{CBL}	1.545 ± 0.082
n_{CBH}	4.395 ± 0.677
fraction	0.3008 ± 0.510
$B_s^0 \to \pi^+K^-$	
α_{CBL}	1.422 ± 0.087
α_{CBH}	1.917 ± 0.056
n_{CBL}	1.551 ± 0.050
n_{CBH}	4.357 ± 0.417
fraction	0.3915 ± 0.0535
$B^0 \to \pi^+\pi^-$	
α_{CBL}	1.430 ± 0.070
α_{CBH}	1.866 ± 0.061
n_{CBL}	1.464 ± 0.043
n_{CBH}	3.754 ± 0.290
fraction	0.4798 ± 0.0518

Paramter	Value
$B_s^0 \to \pi^+\pi^-$	
α_{CBL}	1.261 ± 0.078
α_{CBH}	1.854 ± 0.062
n_{CBL}	1.608 ± 0.053
n_{CBH}	4.436 ± 0.512
fraction	0.3873 ± 0.0465
$\Lambda_b^0 \to p\pi^-$	
α_{CBL}	1.517 ± 0.090
α_{CBH}	1.763 ± 0.083
n_{CBL}	1.615 ± 0.065
n_{CBH}	3.367 ± 0.290
fraction	0.4947 ± 0.0730
$\Lambda_b^0 \to pK^-$	
α_{CBL}	1.371 ± 0.095
α_{CBH}	1.823 ± 0.063
n_{CBL}	1.725 ± 0.080
n_{CBH}	4.015 ± 0.455
fraction	0.331 ± 0.050

Table F.1: Parameters of the converged double crystal ball fits to 2012 $B \to h^+h^{'-}$ MC.

K^+K^-	Exponentially modified gaussian
mean μ	5239 ± 1
width σ	17.49 ± 1.33
decay rate λ	$(8.41 \pm 2.04) \times 10^{-3}$
$K^+\pi^-$	2 Exponential functions
decay rate 1 λ_1	9.577 ± 0.910
decay rate 2 λ_2	50.855 ± 3.820
$\pi^+\pi^-$	2 Exponential functions
decay rate 1 λ_1	10.985 ± 1.004
decay rate 2 λ_2	35.39 ± 2.635
$p\pi^-$	Exponentially modified gaussian
mean μ	5316 ± 15
width σ	240 ± 59
decay rate λ	$(0.44 \pm 0.20) \times 10^{-3}$
pK^-	Exponentially modified gaussian
mean μ	4897 ± 18
width σ	227 ± 3
decay rate λ	$(4.07 \pm 0.11) \times 10^{-3}$

Table F.2: Parameters of the partially reconstructed 2012 MC fits.

Appendix G

Pull Distributions of the Mass Fitter

Figures G.1-G.7 show the pull distributions for the free parameters in the mass fitter. It can be seen the mass fitter introduces no bias.

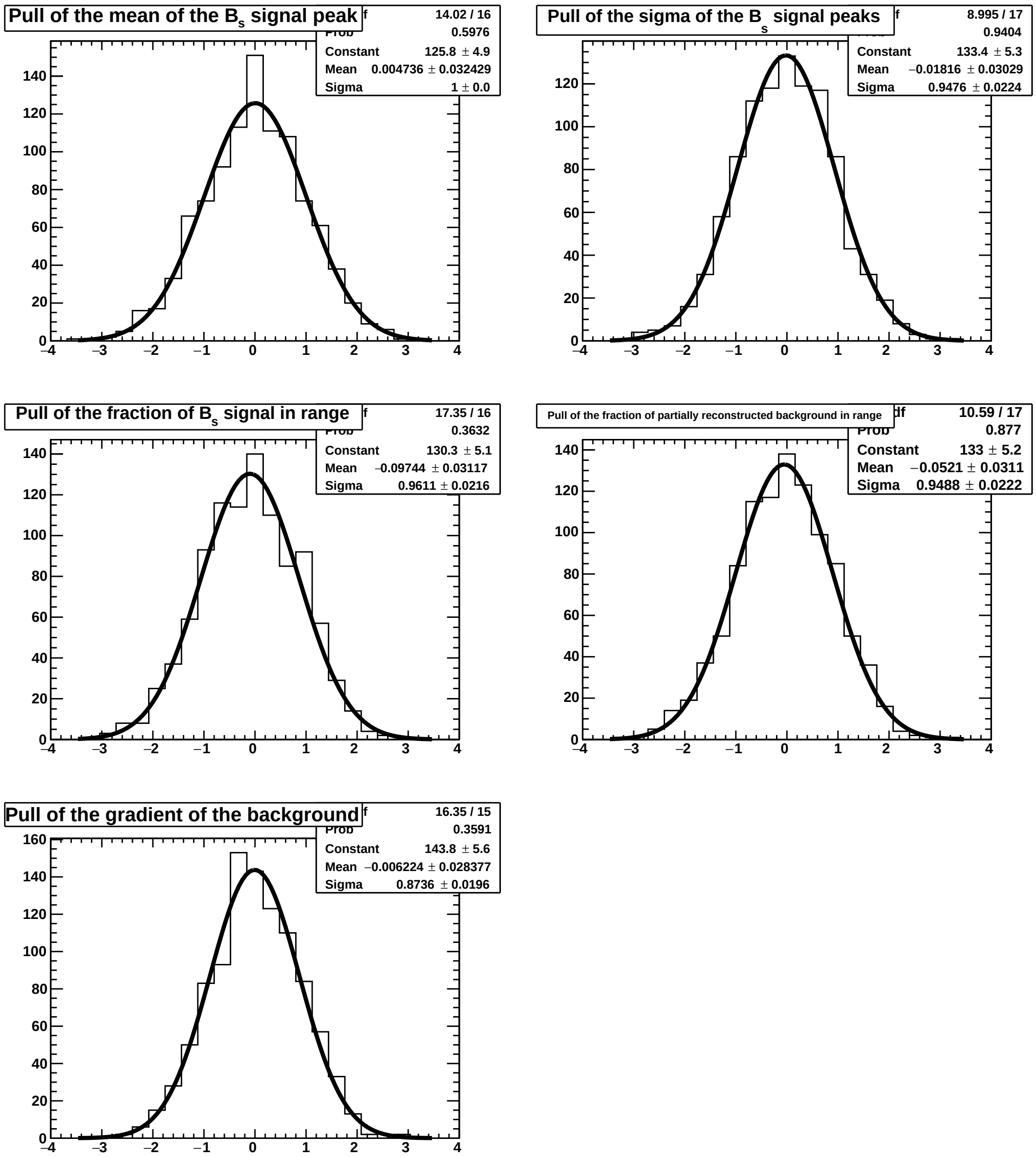

Figure G.1: Pull distributions from the mass fitter for the K^+K^- final state.

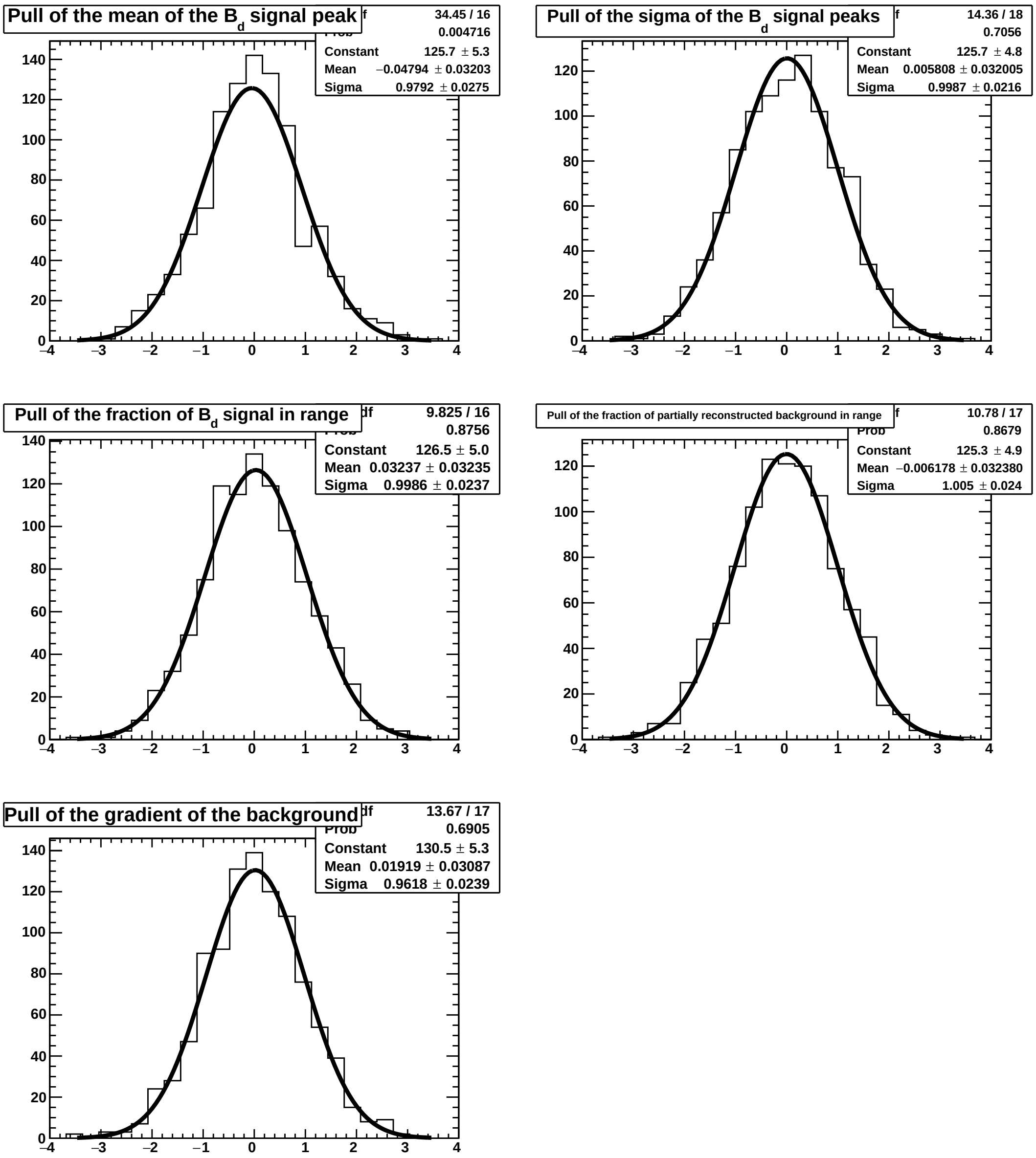

Figure G.2: Pull distributions from the mass fitter for the $K^+\pi^-$ final state.

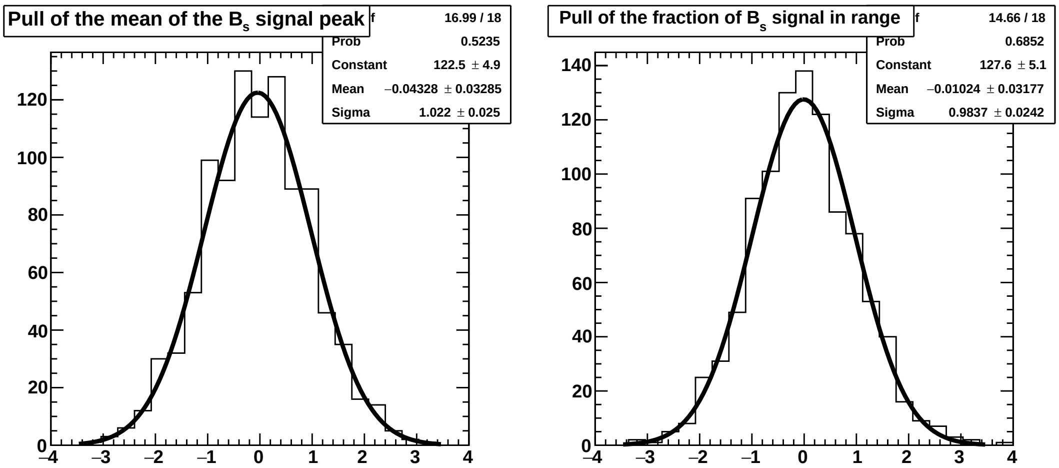

Figure G.3: Pull distributions from the mass fitter for the $K^+\pi^-$ final state.

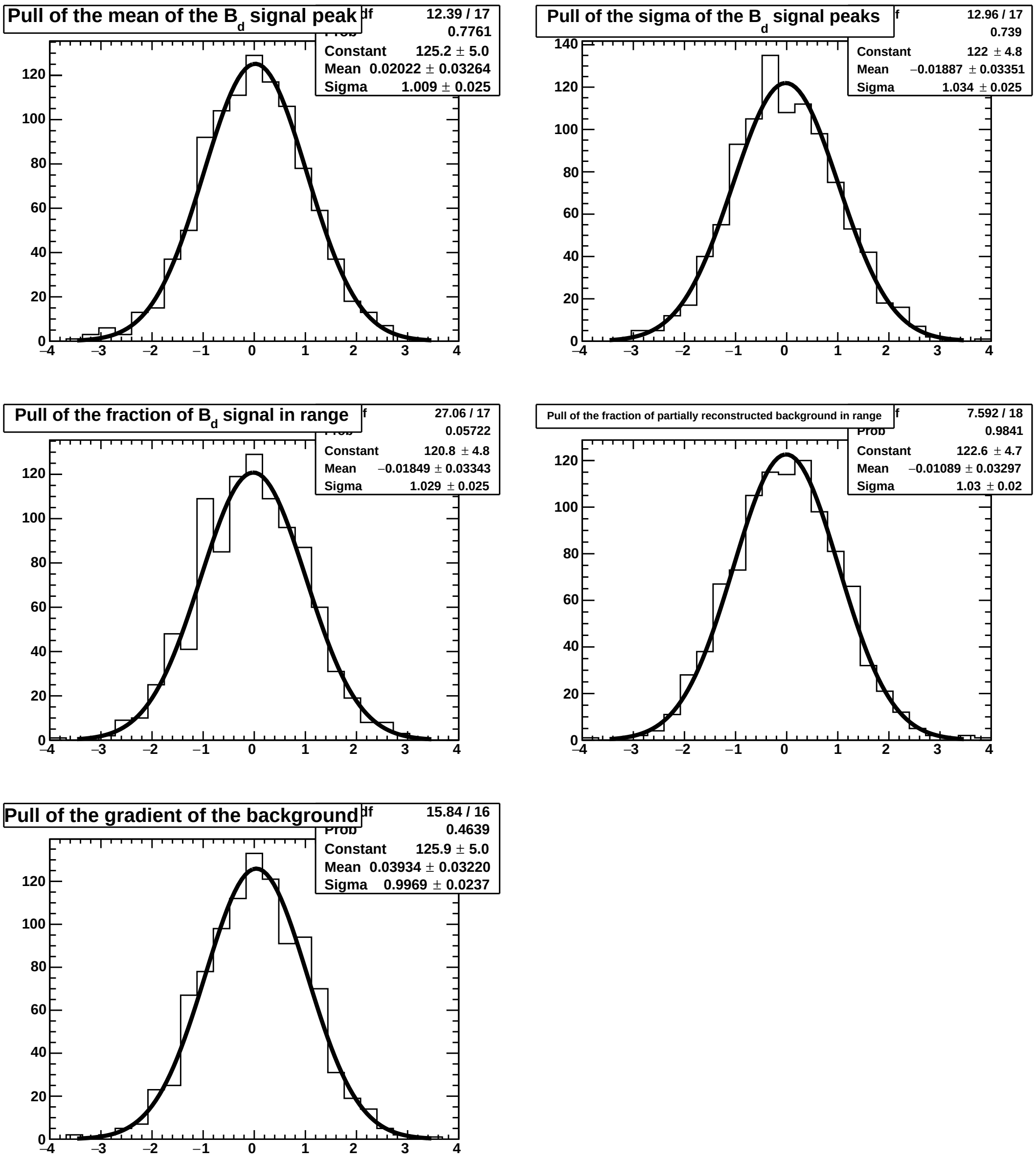

Figure G.4: Pull distributions from the mass fitter for the $\pi^+\pi^-$ final state.

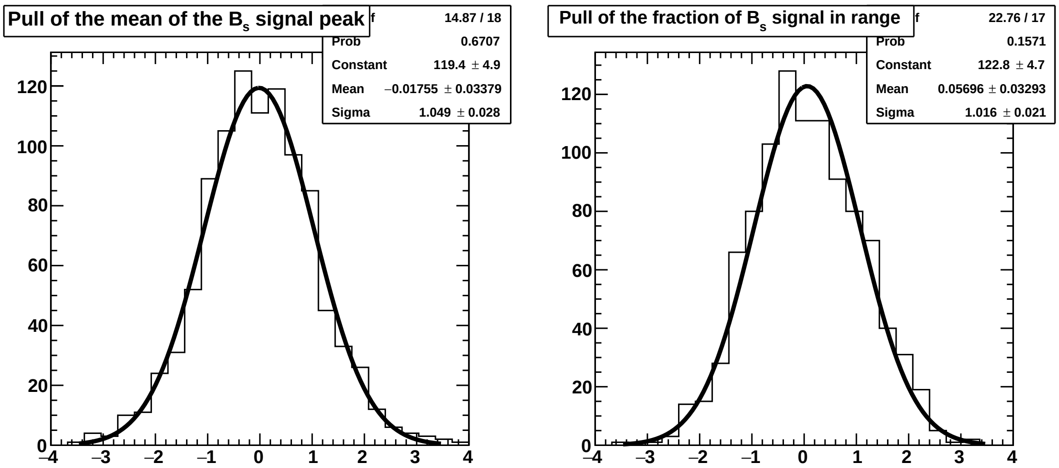

Figure G.5: Pull distributions from the mass fitter for the $\pi^+\pi^-$ final state.

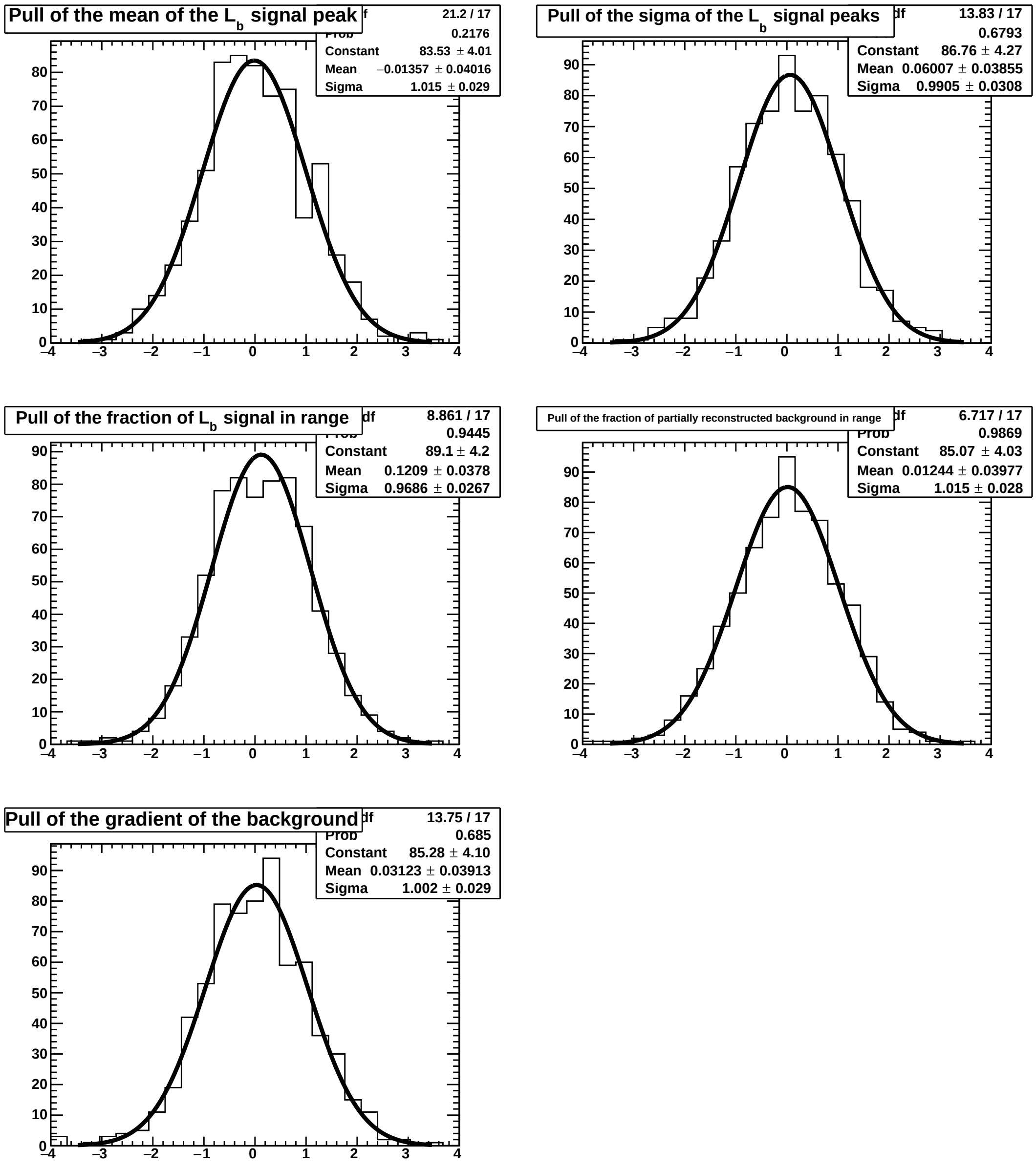

Figure G.6: Pull distributions from the mass fitter for the $p\pi^-$ final state.

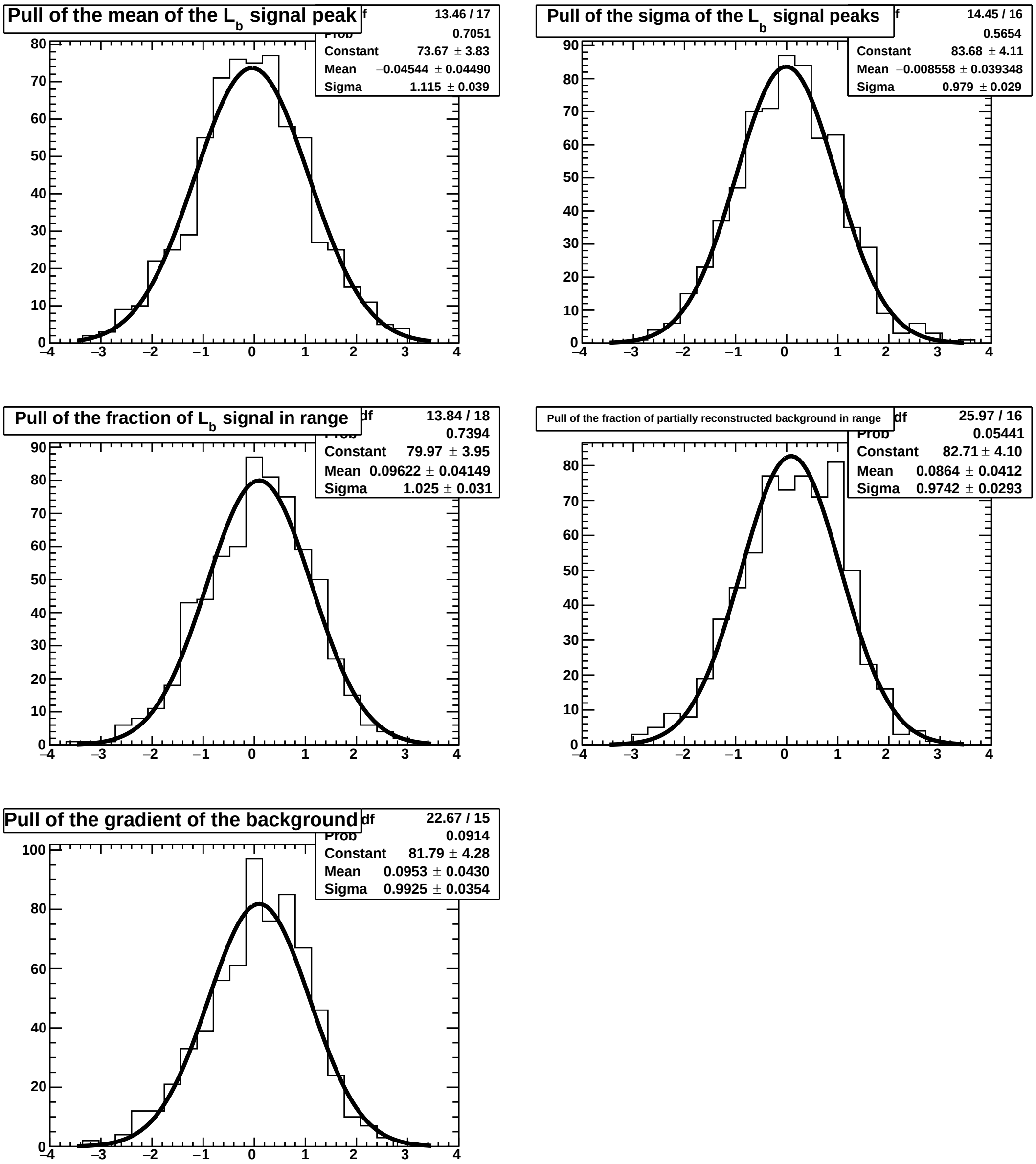

Figure G.7: Pull distributions from the mass fitter for the pK^- final state.

Bibliography

[1] UA1, G. Arnison *et al.*, *Experimental Observation of Isolated Large Transverse Energy Electrons with Associated Missing Energy at s**(1/2) = 540-GeV*, Phys. Lett. **122B** (1983) 103.

[2] UA1, G. Arnison *et al.*, *Experimental Observation of Lepton Pairs of Invariant Mass Around 95-GeV/c**2 at the CERN SPS Collider*, Phys. Lett. **126B** (1983) 398.

[3] CDF, F. Abe *et al.*, *Observation of top quark production in $\bar{p}p$ collisions*, Phys. Rev. Lett. **74** (1995) 2626, `arXiv:hep-ex/9503002`.

[4] D0, S. Abachi *et al.*, *Observation of the top quark*, Phys. Rev. Lett. **74** (1995) 2632, `arXiv:hep-ex/9503003`.

[5] DONUT, K. Kodama *et al.*, *Observation of tau neutrino interactions*, Phys. Lett. **B504** (2001) 218, `arXiv:hep-ex/0012035`.

[6] ATLAS, G. Aad *et al.*, *Observation of a new particle in the search for the Standard Model Higgs boson with the ATLAS detector at the LHC*, Phys. Lett. **B716** (2012) 1, `arXiv:1207.7214`.

[7] CMS, S. Chatrchyan *et al.*, *Observation of a new boson at a mass of 125 GeV with the CMS experiment at the LHC*, Phys. Lett. **B716** (2012) 30, `arXiv:1207.7235`.

[8] Particle Data Group, C. Patrignani *et al.*, *Review of Particle Physics*, Chin. Phys. **C40** (2016), no. 10 100001.

[9] M. E. Peskin and D. V. Schroeder, *An Introduction to quantum field theory.* Addison-Wesley, Reading, USA, 1995.

[10] P. Higgs, *Broken symmetries, massless particles and gauge fields*, Physics Letters **12** (1964), no. 2 132 .

[11] F. Englert and R. Brout, *Broken symmetry and the mass of gauge vector mesons*, Phys. Rev. Lett. **13** (1964) 321.

[12] Super-Kamiokande, Y. Fukuda *et al.*, *Evidence for oscillation of atmospheric neutrinos*, Phys. Rev. Lett. **81** (1998) 1562, `arXiv:hep-ex/9807003`.

[13] Planck, P. A. R. Ade *et al.*, *Planck 2015 results. XIII. Cosmological parameters*, Astron. Astrophys. **594** (2016) A13, `arXiv:1502.0158`.

[14] C. S. Wu *et al.*, *Experimental test of parity conservation in beta decay*, Phys. Rev. **105** (1957) 1413.

[15] V. Fanti *et al.*, *A new measurement of direct CP violation in two pion decays of the neutral kaon*, Physics Letters B **465** (1999), no. 14 335.

[16] KTeV Collaboration, A. Alavi-Harati *et al.*, *Observation of direct CP violation in* $K_{s,l} \to \pi\pi$ *decays*, Phys. Rev. Lett. **83** (1999) 22.

[17] BaBar, B. Aubert *et al.*, *Observation of direct CP violation in* $B^0 \to K^+\pi^-$ *decays*, Phys. Rev. Lett. **93** (2004) 131801, `arXiv:hep-ex/0407057`.

[18] Belle, Y. Chao *et al.*, *Evidence for direct CP violation in* $B^0 \to K^+\pi^-$ *decays*, Phys. Rev. Lett. **93** (2004) 191802, `arXiv:hep-ex/0408100`.

[19] M. Kobayashi and T. Maskawa, *CP Violation in the Renormalizable Theory of Weak Interaction*, Prog. Theor. Phys. **49** (1973) 652.

[20] N. Cabibbo, *Unitary Symmetry and Leptonic Decays*, Phys. Rev. Lett. **10** (1963) 531, [,648(1963)].

[21] U. Nierste, *Three Lectures on Meson Mixing and CKM phenomenology*, in *Heavy quark physics. Proceedings, Helmholtz International School, HQP08, Dubna, Russia, August 11-21, 2008*, pp. 1–38, 2009. `arXiv:0904.1869`.

[22] J. C. et al., *CKMfitter Group, updated results and plots available at: http://ckmfitter.in2p3.fr*, Eur. Phys. J. **C41** (2005) 1, `arXiv:hep-ph/0406184`.

[23] ARGUS, H. Albrecht *et al.*, *Observation of B0 - anti-B0 Mixing*, Phys. Lett. **B192** (1987) 245.

[24] CDF, A. Abulencia *et al.*, *Observation of $B_s^0 - \bar{B}_s^0$ Oscillations*, Phys. Rev. Lett. **97** (2006) 242003, `arXiv:hep-ex/0609040`.

[25] Belle, M. Staric *et al.*, *Evidence for D^0 - $\bar{D}^0$ Mixing*, Phys. Rev. Lett. **98** (2007) 211803, `arXiv:hep-ex/0703036`.

[26] J. H. Christenson, J. W. Cronin, V. L. Fitch, and R. Turlay, *Evidence for the 2π Decay of the K_2^0 Meson*, Phys. Rev. Lett. **13** (1964) 138.

[27] LHCb, B. Adeva *et al.*, *Roadmap for selected key measurements of LHCb*, `arXiv:0912.4179`.

[28] LHCb, R. Aaij *et al.*, *Observation of the annihilation decay mode $B^0 \to K^+K^-$*, `arXiv:1610.0828`.

[29] LHCb, R. Aaij *et al.*, *First observation of the rare purely baryonic decay $B^0 \to p\bar{p}$*, `arXiv:1709.0115`.

[30] M. Gronau, O. F. Hernández, D. London, and J. L. Rosner, *Decays of b mesons to two pseudoscalars in broken SU(3) symmetry*, Phys. Rev. D **52** (1995) 6356.

[31] LHCb Collaboration, *Measurement of time-dependent CP-violating asymmetries in $B^0 \to \pi^+\pi^-$ and $B_s^0 \to K^+K^-$ decays at LHCb* , Tech. Rep. LHCb-CONF-2016-018. CERN-LHCb-CONF-2016-018, CERN, Geneva, Jan, 2017.

[32] K. Hartkorn and H.-G. Moser, *A new method of measuring $\frac{\Delta\Gamma}{\Gamma}$ in the $B_s^0 - \bar{B}_s^0$ system*, The European Physical Journal C - Particles and Fields **8** (1999), no. 3 381.

[33] R. Fleischer and R. Knegjens, *In Pursuit of New Physics With $B_s^0 \to K^+K^-$*, Eur. Phys. J. **C71** (2011) 1532, `arXiv:1011.1096`.

[34] Y. Amhis *et al.*, *Averages of b-hadron, c-hadron, and τ-lepton properties as of summer 2016*, , `arXiv:1612.07233`.

[35] M. Donega, *Measurement of the* $B_s \to K^+K^-$ *lifetime and extraction of the* $\Delta\Gamma_{CP}/\Gamma_{CP}$ *at CDF Run II and development of the ATLAS-SCT endcap modules*, PhD thesis, presented 2006.

[36] R. Aaij *et al.*, *Measurement of the effective* $B_s^0 \to K^+K^-$ *lifetime*, Phys. Lett. **B707** (2012) 349, `arXiv:1111.0521`.

[37] R. Aaij *et al.*, *Measurement of the effective* $B_s^0 \to K^+K^-$ *lifetime*, Phys. Lett. B **716** (2012) 393, `arXiv:1207.5993`.

[38] LHCb, R. Aaij *et al.*, *Effective lifetime measurements in the* $B_s^0 \to K^+K^-, B^0 \to K^+\pi^-$ *and* $B_s^0 \to \pi^+K^-$ *decays*, Phys. Lett. **B736** (2014) 446, `arXiv:1406.7204`.

[39] LHCb collaboration, R. Aaij *et al.*, *Measurement of* CP *violation and the* B_s^0 *meson decay width difference with* $B_s^0 \to J/\psi K^+K^-$ *and* $B_s^0 \to J/\psi\pi^+\pi^-$ *decays*, Phys. Rev. D 87, **112010** (2013) , `arXiv:1304.2600`.

[40] O. S. Brning *et al.*, *LHC Design Report.* CERN Yellow Reports: CERN-2004-003-V1 Monographs. CERN, Geneva, 2004.

[41] *LEP Design Report: Vol.2. The LEP Main Ring*, .

[42] CERN press, *CERN releases analysis of LHC incident, (https://press.cern/press-releases/2008/10/cern-releases-analysis-lhc-incident/)*, 2008.

[43] *CERN Accelerators and Technology Sector*, `https://espace.cern.ch/acc-tec-sector/default.aspx`, February, 2016.

[44] ALICE, K. Aamodt *et al.*, *The ALICE experiment at the CERN LHC*, JINST **3** (2008) S08002.

[45] ATLAS, G. Aad *et al.*, *The ATLAS Experiment at the CERN Large Hadron Collider*, JINST **3** (2008) S08003.

[46] CMS, S. Chatrchyan *et al.*, *The CMS experiment at the CERN LHC*, JINST **3** (2008) S08004.

[47] LHCb Collaboration, A. A. Alves *et al.*, *The LHCb Detector at the LHC*, JINST **3** (2008), no. LHCb-DP-2008-001. CERN-LHCb-DP-2008-001 S08005.

[48] TOTEM Collaboration, G. Anelli *et al.*, *The TOTEM experiment at the CERN Large Hadron Collider*, JINST **3** (2008) S08007.

[49] LHCf Collaboration, O. Adriani *et al.*, *The LHCf detector at the CERN Large Hadron Collider*, JINST **3** (2008) S08006.

[50] *LHCb : Technical Proposal.* Tech. Proposal. CERN, Geneva, 1998.

[51] LHCb, R. Aaij *et al.*, *Measurement of* $\sigma(pp \to b\bar{b}X)$ *at* $\sqrt{s} = 7$ TeV *in the forward region*, Phys. Lett. **B694** (2010) 209, `arXiv:1009.2731`.

[52] LHCb, R. Aaij *et al.*, *Measurement of the b-quark production cross-section in 7 and 13 TeV pp collisions*, Phys. Rev. Lett. **118** (2017), no. 5 052002, `arXiv:1612.0514`.

[53] LHCb, R. Aaij *et al.*, *LHCb Detector Performance*, Int. J. Mod. Phys. **A30** (2015), no. 07 1530022, `arXiv:1412.6352`.

[54] R. L. G. Federico Alessio, Richard.Jacobsson, *LHCb operations plots webpage. (http://lhcb-operationsplots.web.cern.ch/lhcb-operationsplots/index.htm)*, 2016.

[55] LHCb Collaboration, P. R. Barbosa-Marinho *et al.*, *LHCb VELO (VErtex LOcator): Technical Design Report.* Technical Design Report LHCb, CERN-LHCC-2001-0011. CERN, Geneva, 2001.

[56] R. Aaij *et al.*, *Performance of the LHCb Vertex Locator*, JINST **9** (2014) 09007, `arXiv:1405.7808`.

[57] LHCb Collaboration, S. Amato *et al.*, *LHCb RICH: Technical Design Report.* Technical Design Report LHCb, CERN-LHCC-2000-037. CERN, Geneva, 2000.

[58] LHCb RICH group, M. Adinolfi *et al.*, *Performance of the LHCb RICH detector at the LHC*, Eur. Phys. J. C **73** (2012) 2431. 25 p.

[59] LHCb Collaboration, S. Amato *et al.*, *LHCb magnet: Technical Design Report.* Technical Design Report LHCb, CERN-LHCC-2000-007. CERN, Geneva, 2000.

[60] LHCb Collaboration, *LHCb silicon tracker - material for publications. (http://lhcb.physik.uzh.ch/st/public/material/index.php)*, 2016.

[61] LHCb Outer Tracker group, R. Arink *et al.*, *Performance of the LHCb Outer Tracker*, JINST **9** (2013) P01002. 30 p.

[62] LHCb Collaboration, P. R. Barbosa-Marinho *et al.*, *LHCb muon system: Technical Design Report.* Technical Design Report LHCb, CERN-LHCC-2001-010. CERN, Geneva, 2001.

[63] LHCb MuonID group, F. Archilli *et al.*, *Performance of the Muon Identification at LHCb*, J. Instrum. **8** (2013) P10020. 17 p.

[64] LHCb Collaboration, *The Brunel project. (http://lhcb-release-area.web.cern.ch/lhcb-release-area/doc/brunel/)*, 2016.

[65] LHCb Collaboration, *The DaVinci project. (http://lhcb-release-area.web.cern.ch/lhcb-release-area/doc/davinci/)*, 2016.

[66] T. Sjöstrand, S. Mrenna, and P. Skands, *A brief introduction to PYTHIA 8.1*, Comput. Phys. Commun. **178** (2008) 852, `arXiv:0710.3820`.

[67] D. J. Lange, *The EvtGen particle decay simulation package*, Nucl. Instrum. Meth. **A462** (2001) 152.

[68] Geant4 collaboration, S. Agostinelli *et al.*, *Geant4: a simulation toolkit*, Nucl. Instrum. Meth. **A506** (2003) 250.

[69] Geant4 collaboration, J. Allison *et al.*, *Geant4 developments and applications*, IEEE Trans. Nucl. Sci. **53** (2006) 270.

[70] LHCb RICH, A. Papanestis and C. D'Ambrosio, *Performance of the LHCb RICH detectors during the LHC Run II*, `arXiv:1703.0815`.

[71] S. Eisenhardt, *Operating hybrid photon detectors in the LHCb RICH counters at high occupancy*, Nuclear Instruments and Methods in Physics Research Section A: Accelerators, Spectrometers, Detectors and Associated Equipment **766** (2014) 217 , *RICH2013 Proceedings of the Eighth International Workshop on Ring Imaging Cherenkov Detectors Shonan, Kanagawa, Japan, December 2-6, 2013.*

[72] I. Sepp, Using Rare Decays to Probe the Standard Model at LHCb*, PhD thesis, Imperial Coll., London, Feb, 2014, Presented 25 Mar 2014.*

[73] *M. G. Albrow, T. D. Coughlin, and J. R. Forshaw, Central Exclusive Particle Production at High Energy Hadron Colliders, Prog. Part. Nucl. Phys.* **65** *(2010) 149,* `arXiv:1006.1289`.

[74] *A. G. Shamov and V. I. Telnov, Precision luminosity measurement at LHC using two photon production of mu+ mu- pairs, Nucl. Instrum. Meth.* **A494** *(2002) 51,* `arXiv:hep-ex/0207095`.

[75] *LHCb, R. Aaij* et al.*, Measurement of $D^0 - \overline{D^0}$ Mixing Parameters and Search for CP Violation Using $D^0 \to K^+\pi^-$ Decays, Phys. Rev. Lett.* **111** *(2013), no. 25 251801,* `arXiv:1309.6534`.

[76] *L. Collaboration, LHCb PID Upgrade Technical Design Report, Tech. Rep. CERN-LHCC-2013-022. LHCB-TDR-014, Nov, 2013.*

[77] *A. Puig, The LHCb trigger in 2011 and 2012, Tech. Rep. LHCb-PUB-2014-046. CERN-LHCb-PUB-2014-046, CERN, Geneva, Nov, 2014.*

[78] *L. Anderlini* et al.*, The PIDCalib package, Tech. Rep. LHCb-PUB-2016-021. CERN-LHCb-PUB-2016-021, CERN, Geneva, Jul, 2016.*

[79] *A. Hocker* et al.*, TMVA - Toolkit for Multivariate Data Analysis, PoS* **ACAT** *(2007) 040,* `arXiv:physics/0703039`.

[80] *L. Breiman, J. H. Friedman, R. A. Olshen, and C. J. Stone,* Classification and regression trees*. Wadsworth international group, Belmont, California, USA, 1984.*

[81] *B. P. Roe* et al.*, Boosted decision trees as an alternative to artificial neural networks for particle identification, Nucl. Instrum. Meth.* **A543** *(2005) 577,* `arXiv:physics/0408124`.

[82] *Minuit (https://seal.web.cern.ch/seal/snapshot/work-packages/mathlibs/minuit/), 2017.*

[83] *M. Pivk and F. R. Le Diberder, sPlot: a statistical tool to unfold data distributions, Nucl. Instrum. Meth.* **A555** *(2005) 356,* `arXiv:physics/0402083`.

[84] *T. Skwarnicki,* A study of the radiative cascade transitions between the Upsilon-prime and Upsilon resonances*, PhD thesis, Institute of Nuclear Physics, Krakow, 1986, DESY-F31-86-02.*

[85] *K. S. Cranmer, Kernel estimation in high-energy physics, Comput. Phys. Commun.* **136** *(2001) 198,* `arXiv:hep-ex/0011057`.

[86] *R. Bailey* et al.*, Measurement of the lifetime of charged and neutral D mesons with high resolution silicon strip detectors, Z. Phys.* **C28** *(1985) 357.*

[87] *DELPHI, W. Adam* et al.*, Lifetimes of charged and neutral B hadrons using event topology, Z. Phys.* **C68** *(1995) 363.*

[88] *J. Rademacker, Reduction of statistical power per event due to upper lifetime cuts in lifetime measurements, Nucl. Instrum. Meth.* **A570** *(2007) 525,* `arXiv:hep-ex/0502042`.

[89] *CDF, T. Aaltonen* et al.*, Measurement of the B^- lifetime using a simulation free approach for trigger bias correction, Phys. Rev.* **D83** *(2011) 032008,* `arXiv:1004.4855`.

[90] *LHCb, R. Aaij* et al.*, Measurement of mixing and CP violation parameters in two-body charm decays, JHEP* **04** *(2012) 129,* `arXiv:1112.4698`.

[91] *V. V. Gligorov* et al.*, Swimming: A data driven acceptance correction algorithm, J. Phys. Conf. Ser.* **396** *(2012) 022016.*

[92] *M. Alexander,* Constraints on Mixing and CP-Violation in the Neutral Charmed Meson System at LHCb*, PhD thesis, Glasgow, Univ. Glasgow, Glasgow, 2012.*

[93] *J. Mikusiński,* Operational calculus*, vol. 8. CUP Archive, 1967.*

[94] *LHCb, R. Aaij* et al.*, Measurement of the track reconstruction efficiency at LHCb, JINST* **10** *(2015), no. 02 P02007,* `arXiv:1408.1251`.

[95] *F. Dordei and S. Hansmann-Menzemer,* Lifetime measurements of beauty hadrons at the LHCb experiment*, PhD thesis, Heidelberg U., Nov, 2014, Presented 19 May 2015.*

[96] *LHCb, R. Aaij* et al., *Measurement of J/ψ production in pp collisions at $\sqrt{s} = 7$ TeV, Eur. Phys. J.* **C71** *(2011) 1645,* `arXiv:1103.0423`.

[97] *Heavy Flavor Averaging Group (HFAG), Y. Amhis* et al., *Averages of b-hadron, c-hadron, and τ-lepton properties as of summer 2014,* `arXiv:1412.7515`.

[98] *A. Roodman, Blind analysis in particle physics, eConf* **C030908** *(2003) TUIT001,* `arXiv:physics/0312102`.

[99] *LHCb Collaboration, The Moore project. (http://lhcb-release-area.web.cern.ch/lhcb-release-area/doc/moore/), 2017.*

[100] *Particle Data Group, J. Beringer* et al., *Review of particle physics, Phys. Rev.* **D86** *(2012) 010001, and 2013 partial update for the 2014 edition.*

[101] *LHCb, R. Aaij* et al., *Precision measurement of the B_s^0-$\bar{B}_s^0$ oscillation frequency with the decay $B_s^0 \to D_s^- \pi^+$, New J. Phys.* **15** *(2013) 053021,* `arXiv:1304.4741`.

[102] *LHCb, R. Aaij* et al., *Observation of the Decay $B_c^+ \to B_s^0 \pi^+$, Phys. Rev. Lett.* **111** *(2013), no. 18 181801,* `arXiv:1308.4544`.

[103] *F. Ferrari, Measurement of B^0, B_s^0, B^+ and Λ_b^0 production asymmetries in 7 and 8TeV pp collisions at LHCb, Nuovo Cim.* **C40** *(2017), no. 1 39.*

[104] *Particle Data Group, K. Olive* et al., *Review of Particle Physics, Chin. Phys.* **C38** *(2014) 090001.*

[105] *LHCb, R. Aaij* et al., *Measurement of the fragmentation fraction ratio f_s/f_d and its dependence on B meson kinematics, JHEP* **04** *(2013) 001,* `arXiv:1301.5286`.

[106] *LHCb, R. Aaij* et al., *Study of the kinematic dependences of Λ_b^0 production in pp collisions and a measurement of the $\Lambda_b^0 \to \Lambda_c^+ \pi^-$ branching fraction, JHEP* **08** *(2014) 143,* `arXiv:1405.6842`.